UNIVERSITY OF TECHNOLOGY SYDNEY

Enhancement of the UV Emission in Metal Nanoparticle-Coated ZnO

by
Saskia FIEDLER

A thesis submitted in partial fulfilment for
the degree of Doctor of Philosophy

in the

School of Mathematical and Physical Sciences
Faculty of Science

2018

Declaration of Original Authorship

I, Saskia FIEDLER, declare that this thesis titled, "Enhancement of the UV Emission in Metal Nanoparticle-Coated ZnO ", is submitted in fulfilment of the requirements for the award of Doctor of Philosophy, in the School of Mathematical and Physical Sciences, Faculty of Science at the University of Technology Sydney.

This thesis is wholly my own work unless otherwise reference or acknowledged. In addition, I certify that all information sources and literature used are indicated in the thesis. This document has not been submitted for qualifications at any other academic institution.

Signature: Production Note: Signature removed prior to publication.

Date: 04/10/2018

Abstract

Large emission enhancement factors resulting from orders of magnitude increases in ultra-violet (UV) luminescence in ZnO have been reported, due to the presence of a surface coating of either Au or Al nanoparticles. Two significantly different models have been proposed to explain the observed increase in the UV light output. One involving the decay of metal nanoparticles localised surface plasmons (LSP) into hot carriers and their radiative recombination following injection into the ZnO conduction and valence bands. The other describes the creation of an additional fast relaxation pathway via a dipole-dipole coupling mechanism between excitons in ZnO and the metal nanoparticle LSPs, resulting in an improved ZnO UV spontaneous emission rate. This work specifically addresses this significant discrepancy in the existing literature, that reports metal nanoparticle-induced light emission in ZnO.

The UV emission enhancement mechanism between *a*-plane ZnO single crystals and ZnO nanorods coated with Al and Au nanoparticles were systemically investigated in this thesis, using cathodoluminescence (CL) and photoluminescence (PL) spectroscopy in conjunction with ellipsometry, optical absorption and synchrotron valence band spectroscopy measurements. Significantly novel concurrent CL-PL techniques were also employed in this study. The presence of both metal surface films was found to enhance the ZnO UV emission. Moreover, changes to the surface band bending induced by the metal coating was confirmed and their effect on visible deep level (DL) defect related ZnO emission and surface electronic properties was considered.

For 5 nm-Au nanoparticle-coated ZnO nanorods, an up to 3.8-fold enhanced UV emission with no change in the intensity of the visible defect luminescence due to deep level recombination: quenching of the DL is hallmark characteristic of the hot carrier model. The underlying UV enhancement effect was found to be excitation depth-dependent with the largest enhancement being observed with light generation at the surface, closest to the ZnO-Au interface. Concurrent CL-PL showed that UV emission of the Au nanoparticle-coated ZnO samples under simultaneous electron beam and laser irradiation is identical to the electron beam excitation alone, confirming that while LSPs are created in the Au nanoparticles, hot electrons are not injected into the conduction band of the ZnO. Furthermore, time-resolved PL measurements at 10 K revealed that the presence of the Au nanoparticle surface coating on ZnO nanorods produced a 40 ps reduced lifetime compared with the uncoated side of the sample. The corresponding Purcell enhancement

factor of only 1.4 is much lower than the observed UV enhancement of up to 3.8, indicating that the LSP-exciton coupling is not the cause of the UV enhancement. The findings collectively confirm that that neither of the two reported models can be responsible for the observed UV enhancement in these samples. Consequently an alternate mechanism is proposed which is consistent with all of the experimental results. This model suggests that the interband transitions in Au in the UV spectral range, from the 5d band to the partly filled 6sp conduction band, can be excited by the exciton emissions in ZnO via a resonance energy transfer mechanism. The creation of this additional, faster relaxation channel increases the exciton spontaneous emission rate, enhancing the observed UV emission of Au nanoparticle-coated ZnO.

In the case of the Al-coating, *a*-plane ZnO single crystals and ZnO nanorods were coated with a 2 nm thin Al film, resulting in an up to 12-fold enhancement of the UV PL emission. The increase was attributed to a strong Al LSP-exciton coupling mechanism. Additionally, below 80 K, the in-diffusion of the Al into the ZnO was found to contribute to measured increase in the total UV emission by increasing the Al I_6 bound exciton luminescence. The maximum UV enhancement was found at 80 K, where the bound excitons (BX) in ZnO are mostly thermally dissociated and the luminescence spectra are dominated by the free exciton (FX) emission. The LO-phonon replicas of the FX were also highly-enhanced by the Al-coating, indicating that the LSPs in the Al nanoparticles couple more favourably to the FX in the ZnO than to the BX. It was also found that the LSP-coupling to one of the three A, B and C FXs in ZnO is dependent on the ZnO crystal orientation and thereby the polarisation of the FX in ZnO with respect to the incident laser light. Furthermore, the strength of the LSP-exciton coupling was found to be dependent on the carrier density of ZnO with samples having higher carrier densities exhibiting a greater UV enhancement.

In conclusion, ZnO planar and nanorod samples coated with both Au and Al nanoparticles thin films in this work resulted in a large UV enhancement, arising from two different processes. The UV enhancement of the Au nanoparticle-coated ZnO samples was attributed to interband transitions in the Au nanoparticles, while the origin of the UV enhancement of the Al-coated ZnO samples was assigned to LSP-exciton coupling to preferably the FX in ZnO. The results of this thesis provide insight into why different explanations for the observed metal nanoparticle-induced emission enhancement in ZnO exist in the literature and why comprehensive characterisation of the structural and physical properties of both the ZnO and the metal nanoparticle ZnO composite is essential to establish the exact identity of the primary enhancement mechanism.

To my family — Mama, Papa and Nils.

Acknowledgements

I would like to sincerely thank my supervisor Prof. Matthew R. Phillips for his excellent guidance, support and motivation throughout the 3.5 years at UTS. I am truly grateful that he shared his knowledge and so many stories, particularly on traveling, with me in our weekly meetings! Thanks for helping me to get through the difficult and stressful times — you were always my point of reference.
I would also like to express my thanks to my co-supervisor Assoc. Prof. Cuong Ton-That for his comments and suggestions, particularly on the XPS data.
Special thanks to Dr. Olivier Lee Cheong Lem, who has been a constant source of motivation and great support — I could not have done it without you!
Furthermore, I would like to thank my great colleagues at UTS, especially Dr. Sejeong Kim for her help with the plasmonic simulations, and Dr. Carlo Bradac — you are a true source of inspiration.
Many thanks for the exceptional assistance and support at the UTS Microstructural Analysis Unit, particularly Katie McBean — thanks for proofreading my thesis in a very stressful time, as well as being a great boxing partner. Additionally, I wish to thank Geoff McCredie and Dr. Angus Gentle for their help with all technical issues I encountered during my time at UTS and their excellent support with ellipsometry, UV-Vis spectroscopy and the deposition of metals.
Furthermore, I would like to thank Marie Wintrebert-Fouquet from BluGlass for taking her time to help me with the Hall effect measurements.
I would like to extend my thanks to the great technical support at the Australian Synchrotron and Christian Clarke for collecting last minute XPS data for my thesis.
Special thanks to Markus Schleuning for spending so much time on collecting the time-resolved PL spectra in Berlin, as well as Prof. Axel Hofmann and his group for technical assistance at the Technische Universität Berlin, Germany.
To Prof. Igor Aharonovich for many stimulating discussions and fantastic scuba diving at Gordon's Bay.
In addition, I wish to thank the Australian Research Council for the financial support during my time at UTS (DP150103317).

Finally, I would like to thank all my friends for being the best I could wish for. In particular, my friends back home for always being supportive, although being on the other

side of the globe, Constanze Matthai, Isabelle Hoffmann, Jacqueline Heu, Nadine Roche, Uta-Pari Kohlhoff and Valentina Ellinghaus.
Thanks for proofreading, Nina Schwarz and being a wonderful friend and dive buddy.
Special thanks to Yvonne Bartling, who has become one of my best friends in Sydney in no time; thanks for not only sharing the horse love with me but also Jersey and Lulu.
Steve van den Berg, I am very grateful for your love and great support, especially during the very stressful times. Thanks for being the amazing person you are!
Last but not least, I would like to thank my family, my dad Michael Jansen, my mum Renate Fiedler and my brother Nils Fiedler, for always supporting me and my goals in life, although being 16 000 km away from home. I wish to thank my dad for being supportive in many ways; and I am very grateful for endless conversations on the phone with my mum, her kindness and love. Thanks to my loving brother for always being there for me and for traveling the world together.

List of Publications

S. Fiedler, L. O. Lee Cheong Lem, C. Ton-That and M. R. Phillips. "Mechanism behind enhanced UV emission of metal nanoparticle-coated ZnO ", E-MRS Fall 2018

S. Fiedler, L. O. Lee Cheong Lem, C. Ton-That and M. R. Phillips. "Investigation of Plasmonic UV Emission Enhancement from Au-coated ZnO Nanorods", ICONN 2018

S. Fiedler, L. O. Lee Cheong Lem, C. Ton-That and M. R. Phillips. "Plasmonic Coupling Mechanism behind UV Enhancement of Au-Coated ZnO Nanorods", MRS Fall 2017

A. M. Berhane, K. -Y. Jeong, Z. Bodrog, S. Fiedler, T. Schröder, N. V. Triviño, T. Palacios, A. Gali, M. Toth, D. Englund and I. Aharonovich. "Bright Room-Temperature Single-Photon Emission from Defects in Gallium Nitride". Advanced Materials, 2017.

S. Fiedler, C. Ton-That and M. R. Phillips. "Enhanced UV emission of Au-coated nanorods via plasmon polariton-exciton coupling", E-MRS Fall 2016

S. Fiedler, C. Ton-That and M. R. Phillips. "Investigation of the optical properties of ZnO nanorods coated with Au nanoparticles", ICONN 2016

Contents

List of Figures

List of Tables

List of Abbreviations

ABX	Neutral **A**cceptor **B**ound e**X**citon
AFM	**A**tomic **F**orce **M**icroscopy
ALD	**A**tomic **L**ayer **D**eposition
ASF	**A**tomic **S**ensitivity **F**actor
BSE	**B**ack **S**cattered **E**lectrons
BX	**B**ound e**X**citon
CCD	**C**harge-**C**oupled **D**evice
CL	**C**athodo**L**uminescence
DBX	**D**onor **B**ound e**X**citon
DAP	**D**onor-**A**cceptor **P**air
DL	**D**eep **L**evel
EL	**E**lectro**L**uminescence
EQE	**E**xternal **Q**uantum **E**fficiency
FDTD	**F**inite-**D**ifference **T**ime-**D**omain
FWHM	**F**ull **W**idth at **H**alf **M**aximum
FX	**F**ree e**X**citon
GL	**G**reen **L**uminescence at 2.3 eV
GL$_1$	**G**reen **L**uminescence at 2.45 eV
HMT	**H**exa**M**ethylene**T**etramine
IQE	**I**nternal **Q**uantum **E**fficiency
LED	**L**ight **E**mitting **D**iode
LEE	**L**ight **E**xtraction **E**fficiency
LO	**L**ongitudinal **O**ptical
LSP	**L**ocalised **S**urface **P**lasmon
LSPR	**L**ocalised **S**urface **P**lasmon **R**esonance
MFP	**M**ean **F**ree **P**ath
MQW	**M**ultiple **Q**uantum **W**ell
NBE	**N**ear **B**and **E**dge
ND	**N**eutral **D**ensity
OL	**O**ange **L**uminescence
PL	**P**hoto**L**uminescence
RL	**R**ed **L**uminescence
sccm	**s**tandard **c**ubic **c**entimetres per **m**inute
SE	**S**econdary **E**lectrons
SER	**S**pontaneous **E**mission **R**ate
SEM	**S**canning **E**lectron **M**icroscopy
SPP	**S**urface **P**lasmon **P**olariton
SX	**S**urface e**X**citon
TES	**T**wo-**E**lectron **S**atellite

TE	**T**ransverse **E**lectric
TEM	**T**ransmission **E**lectron **M**icroscopy
TM	**T**ransverse **M**agnetic
TR-PL	**T**ime-**R**esolved **P**hoto**L**uminescence
UV	**U**ltra-**V**iolet
UV-Vis	**U**ltra-**V**iolet **Vis**ible
XPS	**X**-Ray **P**hotoelectron **S**pectroscopy

1 Introduction

Since the invention of high-brightness blue LEDs by Nakamura in the 1990s, the use of LEDs in daily life has grown rapidly with the development and commercialisation of high-efficiency, low-cost and long-lasting white LEDs [1]. In 2014, Nakamura, Akasaki and Amano were awarded the Nobel Prize in Physics for their seminal work on the GaN-based blue light emitting diode [2]. In particular, their development of the $\mathrm{In}_x\mathrm{Ga}_{1-x}\mathrm{N}$ material system provided the opportunity to shift the LED emission wavelength from near-ultraviolet (UV) to green with increasing indium content [3]. However, growing thick layers of $\mathrm{In}_x\mathrm{Ga}_{1-x}\mathrm{N}$ introduces additional challenges due to strain-related effects. To overcome these issues and to increase the internal quantum efficiency (η_{IQE}), multiple quantum well (MQW) sandwich structures were introduced. They consisted of stacks of alternating nanometre thick $\mathrm{In}_x\mathrm{Ga}_{1-x}\mathrm{N}$ and GaN layers [3]. Despite their commercial success, the resulting planar MQW LED-structure inherently introduces a number of performance limitations that are yet to be resolved [4, 5]. Of particular concern is the poor light extraction efficiency (η_{LEE}), which is currently limited to approximately 4% [6] and is the main reason for the low external quantum efficiency (η_{EQE}) of these planar structures [6].

The poor η_{LEE} is mainly due to the abrupt change of the refractive index at the device to air interface, causing strong internal reflection. To overcome this issue, various anti-reflection coatings have been fabricated and demonstrated to successfully increase the η_{LEE} of the GaN-based LEDs. Particularly, nanostructured metal films have been used to enhance the UV emission via plasmonic effects in the metal nanoparticles. However, the physical mechanism behind the enhanced UV emission due to a metal nanoparticle-coating is still a subject of controversy.

Although GaN has been widely used for optoelectronic devices, the fabrication is typically relatively expensive and the growth of nanostructures can still be challenging. Another wide bandgap semiconductor with similar structural and optical properties is ZnO, and accordingly has attracted much interest for the fabrication of UV LEDs and lasers in the recent years [7–14]. Even though ZnO is relatively cheap and can be easily grown in a great variety of nanostructures, the fabrication of stable *p*-type doping of ZnO is still a challenge, which eliminates the production of homostructural *pn* optoelectronic devices based on ZnO.

Nevertheless, ZnO is an ideal platform material to systematically investigate the η_{LEE}

of wide bandgap semiconductors coated with nanostructured metal films. Furthermore, anti-reflection composite coatings consisting of nanostructured ZnO and metal nanoparticles can possibly be used to increase the the light extraction for GaN-based LEDs and lasers, as well as to improve the light injection in solar cells. Here, a graded refractive index via the ZnO nanorods and waveguiding effect with the ZnO nanorods can help to effectively increase the η_{LEE}, by combining the interaction between the semiconductor and the metal nanoparticles. The origin of the first two enhancement mechanisms are well studied and comprehended, while the fundamental mechanisms involving the metal nanoparticles is still not fully understood yet. However, two different models have been proposed in the literature, surprisingly based on the results from samples that are reported to be identical. The first involves the direct coupling of excitons with Localised Surface Plasmons (LSPs) while the second, the transfer of energetic electrons from the metal nanoparticles via plasmon decay into the semiconductor material, thereby enhancing the UV emission [15–26]. This inconsistency in the reported underlying mechanism of the UV enhancement of ZnO coated with nanostructured metal films found in the literature, will be addressed in this thesis. A systematic study was conducted on the two types of ZnO — single crystals and nanorods with different carrier densities — coated with Al and Au nanoparticles. The results show that the comprehensive characterisation of the electrical and optical properties is essential to understand the physical mechanisms in these samples, that are responsible for the enhanced light emission.

1.1 Aim and Objectives

The overall aim of this research is to elucidate the physical mechanisms involved in the enhancement of the UV emission of nanostructured metal coated ZnO, specifically to clarify the discrepancy reported on apparently identical samples in the literature.
Two different types of ZnO samples will be investigated — single crystals and nanorods — coated with two different types of nanostructured metal films, Au and Al. The origin of the large enhancement factors of the UV emission in ZnO due to the metal nanoparticle-coating is systematically studied, allowing for direct comparison between the different ZnO morphologies and metal nanoparticle-coatings.
The key objectives of this research project are summarised below:

- Investigate the effect of different ZnO sample morphologies and carrier densities, as well as different types of metal nanoparticle-coatings on the UV emission enhancement.
- Fabricate high quality specimens, which enable the systemic study the emission enhancement in nanostructured metal coated ZnO samples.

- Design of bespoke experimental techniques to comprehensively study the two different metal nanoparticle-induced UV enhancement mechanisms, reported in the literature.
- Study the reported UV enhancement mechanism in Au nanoparticle-coated ZnO, as well as the enhancement via interband transitions in Au.
- Investigate the coupling mechanisms of the excitons in ZnO to the LSPs in the Al nanoparticles, including the observed polarisation dependence on the laser excitation.

1.2 Thesis Structure

The main focus of this thesis is the investigation and systematic characterisation of the electronic and optical properties of Al and Au NP-coated *a*-plane ZnO and ZnO nanorods, while the core aim is to elucidate the fundamental processes involved in the metal nanoparticle-induced light emission enhancement.
The structure of this work can be divided into five main sections:

- Introduction and aims — Chapter 1
- Literature review and theoretical background — Chapter 2
- Experimental details — Chapter 3
- Experimental results — Chapter 4 and 5
- Conclusions — Chapter 6

Chapter 1 gives a succinct introduction on the motivation and the main focus of this work. It also provides the background to place the research into context with previous work.
Chapter 2 contains a comprehensive review of the current, relevant literature, including the different reported UV enhancement mechanisms of ZnO coated with nanostructured metal films with an emphasis on the clear inconsistency between the two models. Furthermore, this chapter also covers the theoretical background of the physical concepts used in the literature and in this work.
Chapter 3 describes the experimental details of the sample preparation, as well as the various utilised characterisation techniques.
Chapter 4 focuses on the characterisation and analysis of the electronic and optical properties of the ZnO samples coated with Au nanoparticles.
Chapter 5 analyses the Al surface coatings on the ZnO samples and examines the origin

of the resulting UV enhancement, as well as the effect of carrier densities in ZnO on the UV enhancement.

Chapter 6 summarises the results and conclusions of the previous two chapters and offers suggestions for future research directions.

2 Theoretical Background and Literature Review

2.1 Planar GaN-based LEDs

Although GaN-based devices, such as LEDs, have been used and studied for many years, the light extraction efficiency (η_{LEE}) is still as low as $\sim 4\%$, which is mainly due to an abrupt change in refractive index at the semiconductor-air interface, which leads to total internal reflections and Fresnel loss [6]. This can be explained by Snell's Law, which describes the relationship between the incident and refracted light passing through the interface of two media with different refractive indices n_{i}.

$$\frac{\sin(\theta_{\mathrm{in}})}{\sin(\theta_{\mathrm{out}})} = \frac{n_{\mathrm{air}}}{n_{\mathrm{GaN}}}, \tag{2.1}$$

where θ_{in} is the angle of the incoming light, more precisely the photons generated in the

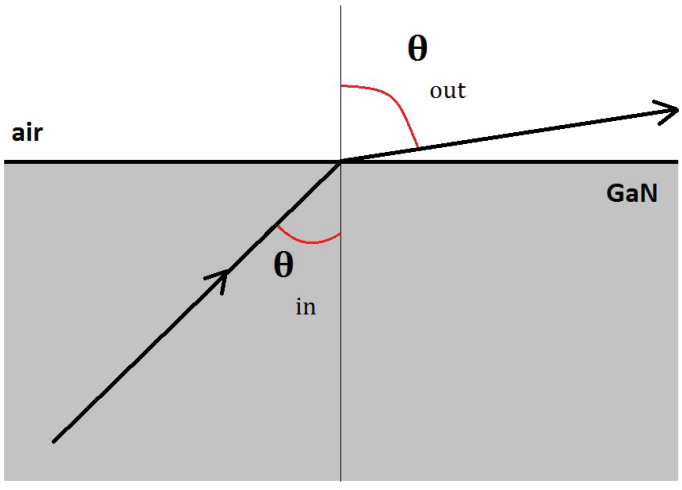

Fig. 2.1: Illustration of Snell's Law.

active region of the LED, while θ_{out} is the angle of the outgoing light. The quantities n_{air} and n_{GaN} are the refractive indices of air and GaN, respectively (cf. fig. 2.1).
If the difference in refractive indices is larger than the critical angle of incidence, the light is totally reflected at the interface and not refracted into the adjacent medium. The critical

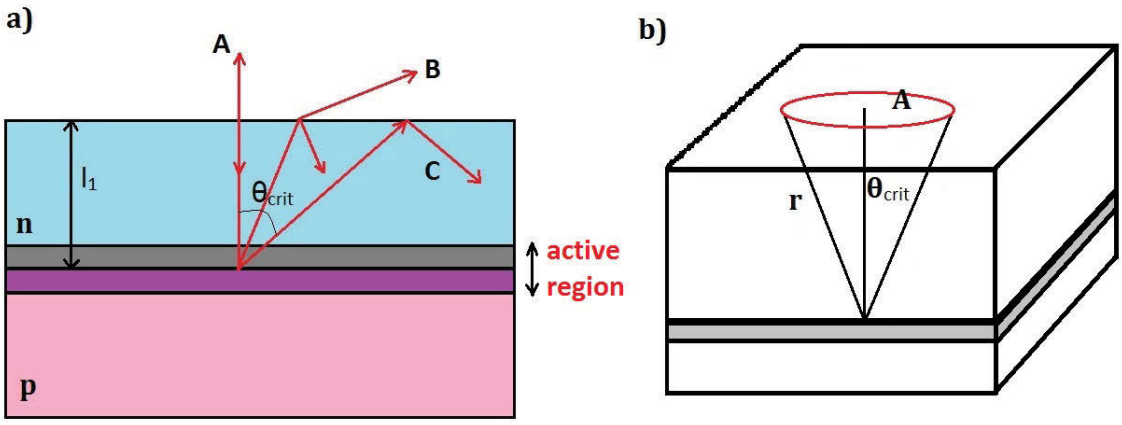

Fig. 2.2: (a) Simplified planar LED with generated light rays showing the limited light extraction and (b) the resulting escape cone.

angle for the GaN-air interface is around 23°, as the refractive index of GaN is $n_{\text{GaN}} \sim 2.5$ and that of air is $n_{\text{air}} = 1.0$:

$$\theta_{\text{crit}} = \arcsin\left(\frac{\theta_{\text{in}}}{\theta_{\text{out}}}\right) = \arcsin\left(\frac{1.0}{2.5}\right) \sim 23^{\circ}. \tag{2.2}$$

For LEDs, θ_{crit} defines the light escape cone. The photons generated spontaneously in the active region of the LED are radiated uniformly in all directions (cf. fig. 2.2 a). Rays at normal incidence, such as ray A, are attenuated by the factor, η_1:

$$\eta_1 = \exp\left(-\alpha(\lambda) l_1\right), \tag{2.3}$$

where $\alpha(\lambda)$ is the absorption coefficient at the wavelength λ and l_1 the distance from the active layer to the surface of the device. Furthermore, some of the generated light is reflected at the semiconductor-air boundary, which is known as the Fresnel loss:

$$\eta_2 = 1 - \frac{(n-1)^2}{(n+1)^2} = \frac{4n}{(n+1)^2}, \tag{2.4}$$

where n is the refractive index of the semiconductor. The overall transmittance of ray A is the product of η_1 and η_2:

$$\eta_A = \eta_1 \times \eta_2. \tag{2.5}$$

Ray B has a longer path through the semiconductor and therefore suffers from a larger absorption:

$$\eta_B < \eta_A. \tag{2.6}$$

While ray C is outside of the cone of critical angle θ_{crit}, and therefore is totally internally reflected. The above mentioned escape cone is defined by the fraction of light coming from a point source that can be extracted (η_{LEE}) from the LED, as depicted in fig. 2.2b

$$\frac{A}{4\pi r^2} = \frac{2\pi r^2(1 - cos(\theta_{\text{crit}})}{4\pi r^2} = \frac{1 - cos(\theta_{\text{crit}})}{2} \sim \frac{1}{4n^2} = \eta_{\text{LEE}}. \tag{2.7}$$

The performance of a LED is characterised by the external quantum efficiency (EQE), which is equal to the number of photons emitted divided by the number of electrons injected. The EQE can also be expressed as the product of the internal quantum efficiency (IQE) and the light extraction efficiency (LEE). The IQE is defined as the ability to produce photons under carrier injection in the active region, while the LEE is the ability to extract the generated photon to the surroundings:

$$\eta_{\text{EQE}} = \eta_{\text{LEE}} * \eta_{\text{IQE}}. \tag{2.8}$$

In the case of GaN-based LEDs, the IQE has reached approximately 80% [27]. In contrast, the LEE is still as low as 4%, which leaves considerable room for improvement in EQE of GaN-based planar devices [6].
This can be realised by developing anti-reflection coatings, which increase the angle of the escape cone. A promising candidate is nanostructured zinc oxide (ZnO), as it is a transparent material that can possibly be used as charge transport layer, replacing the existing ITO as well as exhibiting interesting optical properties — discussed in section 2.2. Furthermore, the structural and optoelectric properties of ZnO are very similar to that of GaN, allowing for both, the growth of high quality epitaxial films of ZnO onto GaN and the use of ZnO as platform to study wide bandgap semiconductors.

2.2 Zinc Oxide

Zinc oxide (ZnO) is a wide band-gap (3.37 eV) semiconductor with a large exciton binding energy of 60 meV at room temperature and it mostly occurs in hexagonal wurtzite structure [28]. Its outstanding optical and geometrical properties make ZnO a promising candidate for applications in optoelectronics and for the fabrication of waveguides, particularly as a transparent oxide conductor.

2.2.1 Optical Properties of ZnO

Luminescence spectra can reveal the intrinsic optical and electrical properties of ZnO, as well as information about crystal quality, concentration of defects, impurities and dopants. The typical luminescence spectrum of ZnO— shown in fig. 2.3a — is dominated by sharp emission peaks in the UV range ($\sim$ 3.3 eV [28]) and broad emission bands

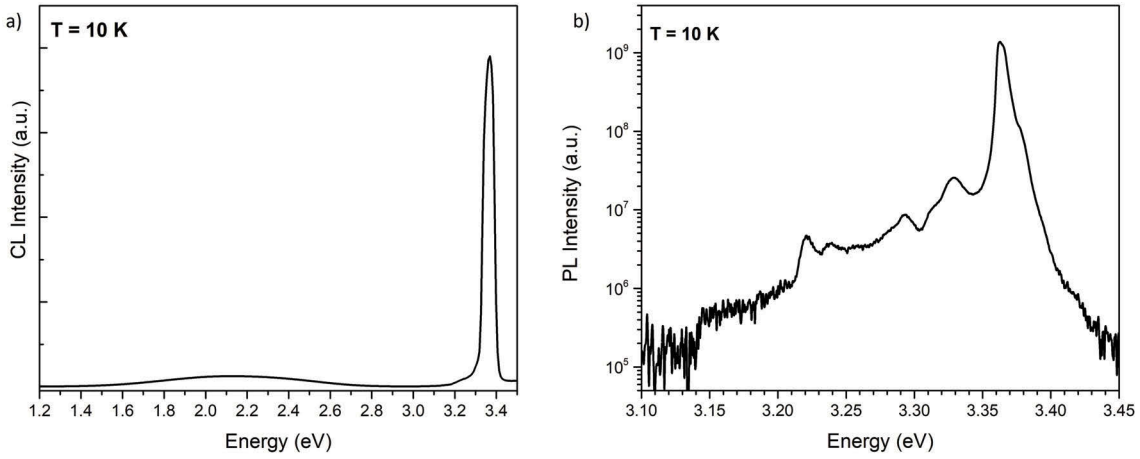

Fig. 2.3: (a) Typical 10 K-CL spectrum of ZnO nanorods, showing near-band edge (NBE) emission at 3.37 eV and defect-related deep-level (DL) emission centered at 2.1 eV. HV = 5 kV, P =17.5 µW, scan area 15 µm x 15 µm. (b) High resolution PL-spectrum of the NBE emission of *a*-plane ZnO at 10 K and P =22.4 mW.

in the visible spectral range (1.5 eV to 3.0 eV [29]).

The emission in the UV region, the near-band-edge (NBE), originates from the recombination of free excitons (FX), located at an energy of 3.376 eV at 4 K, and donor bound exciton (DBX) and acceptor bound exciton (ABX) transitions [30], cf. table 2.1. In high-quality materials, the longitudinal optical phonon replicas of the FX and bound excitons are also observed with a 73 meV spacing.

The typical luminescence spectrum of the near-band edge (NBE) — cf. fig. 2.3b — region of ZnO contains information on the various recombination channels, which can be radiative — with the emission of a photon, usually with an energy up to the bandgap of the investigated material — or non-radiative, through phonon and Auger energy loss mechanisms, see fig. 2.4.

Here, the band-to-band transitions — the radiative recombination of a free electron at the conduction band minimum with a free hole at the valence band maximum — are not necessarily the most efficient radiative recombination channel. The emission energy, reduced from the band gap of the material by excitonic transitions, can have a greater luminescence intensity.

Excitons can be formed when electrons and holes are attracted via electrostatic Coulomb forces, resulting in bound electron-hole pairs. These quasi-particles can travel through the crystal lattice without net charge disruptions and a binding energy, E_X, for example E_X = 60 meV for ZnO. A exciton has quantised energy states that are hydrogen-like, defined by the quantum number n:

$$E_X = \frac{m_r^* e^4}{2\hbar^2 \epsilon^2} \frac{1}{n^2}. \tag{2.9}$$

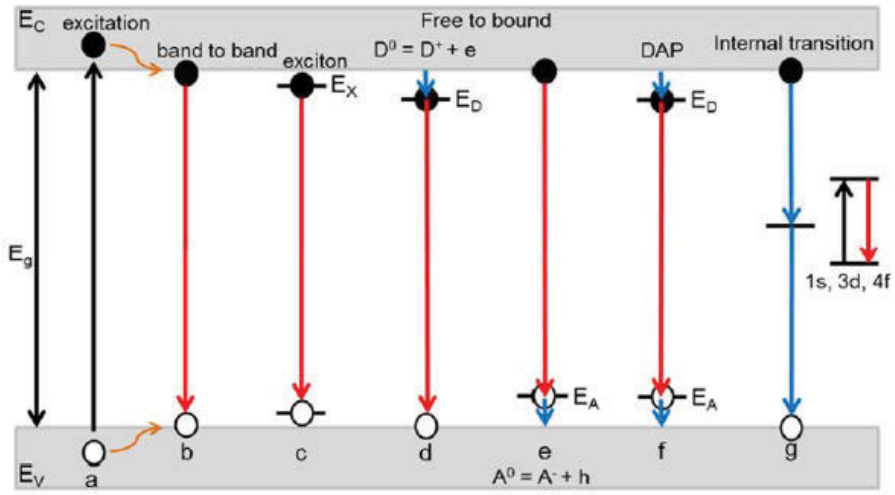

Fig. 2.4: Various recombination channels in a semiconductor, where the black arrow indicates electron beam or laser excitation of electrons from valence band to conduction band.

Where m_r^* is the reduced mass of the exciton, e the elementary charge, $\hbar$ the reduced Planck's constant and ϵ the dielectric constant [31]. The number of created excitons is dependent on E_X, as well as on the electron and hole effective masses of the material, and temperature. It can be calculated by using the Saha equation [32]:

$$\frac{n_{\text{eh}}^2}{n_X} = \frac{k_B T}{2\pi\hbar^2} m_r^* exp\Big(\frac{-E_X}{k_B T}\Big). \tag{2.10}$$

Where n_{eh} and n_X are the number of free carriers and excitons, respectively.
In the case of ZnO, three free excitons (FX) are observed in the luminescence spectras, labelled A, B and C, arising from the valence band splitting into three levels due to crystal field and spin orbit effects. While the A- and B-excitons are perpendicular polarised to the c-axis of the crystal, the energetically higher C-exciton is parallel polarised [33–35].
Excitons can be trapped by defects or scattered by phonons, when traveling through the crystal, which can lead to bound exciton (DBX) radiative recombination emission. The bound excitons emissions in ZnO are reduced by their localisation energy E_{loc}:

$$E_{\text{BX}} = E_{\text{FX}} - E_{\text{loc}}, \tag{2.11}$$

where E_{loc} is equal to the exciton binding energy to the donor or acceptor. The corresponding signature excitonic emission energies in ZnO are listed in table 2.1, which will be used to identify the origin of the emission peaks of the NBE spectra of the uncoated and metal-coated ZnO, in this work.
Broad emission bands in the visible spectrum are also observed in ZnO, cf. fig. 2.3a,

Table 2.1: Recombination energies of the NBE in ZnO.

Line	E (eV)	Chemical identity	References
$LO - I_5$	3.2895	-	[36]
$LO - I_4$	3.298	-	[36]
$LO - FX - A$	3.3061	-	[37]
$LO - FX - B$	3.3136	-	[37]
$TES - I_6(2p)$	3.3215	-	[36]
$TES - I_6(2s)$	3.323	-	[36]
$TES - I_4$	3.329	-	[36]
I_10	3.3531	-	[36]
I_9	3.3567	In	[36]
I_8	3.3598	Ga	[36]
I_7	3.3600	-	[36]
I_6	3.3608	Al	[36]
I_5	3.3615	-	[36]
I_4	3.3628	H	[36]
I_3	3.3660	-	[36]
SX	3.369	-	[38]
I_2	3.3674	-	[36]
I_0	3.3727	-	[36]
I_{0b}	3.3741	-	[36]
I_{0a}	3.3745	-	[36]
$FX - A$	3.3781	-	[37]
$FX - B$	3.3856	-	[37]
$FX - C$	3.4262	-	[37]

which have been associated with a large number of overlapped deep level (DL) emission peaks. Their origin is still controversial, however, the different emission peaks reported in the literature are listed in table 2.2.

2.2.2 ZnO Nanostructures

Many nanostructures often have interesting optical and mechanical properties that make them unique and very different from their bulk material counterparts. Consequently, tailored nanomaterials have opened the door for the fabrication of novel devices with improved functionalities and efficiencies. However, it is essential to study and fully understand the physics and chemistry of these nanostructured materials to fully exploit many of their potential applications [59].

In general, the luminescent characteristics of ZnO nanostructures are similar to that of bulk crystalline ZnO material [60]. However, in nano-sized ZnO particles a new UV emission is observed which is ascribed to a surface exciton (SX) recombination, $E_{\mathrm{SX}} =$

Table 2.2: DL defects in ZnO.

Peak position (eV)	Defect assignment	Colour	References	Type of defect
2.53, 2.5, 2.48, 2.45, 2.36, 2.35	Oxygen vacancy, V_0	Green	[39], [40], [41], [42], [43], [44]	Donor-like
2.53, 2.4*, 2.35, 2.30	Zinc vacancy, V_{Zn}	Green	[40], [45], [39], [41]	Acceptor-like
2.45, 2.43, 2.42	Substitutional Copper, Cu_{Zn}	Green	[45], [46], [43], [47]	
2.26	Oxygen interstitial, O_{i}	Green	[48]	Acceptor-like
2.1, 2.06, 2.03, 1.98, 1.95	Oxygen interstitial, O_{i}	Orange	[49], [50], [51], [52], [53]	Acceptor-like
1.79	Oxygen interstitial, O_{i}	Red	[54]	Acceptor-like
1.69	Oxygen interstitial, O_{i}	Red	[55], [56]	Acceptor-like
2.17, 2.07, 1.93	Substitutional Lithium, Li_{Zn}	Yellow	[40], [57], [58]	Acceptor-like

3.369 eV [38, 61] and is often strongly enhanced due to the high surface-to-volume ratio exhibited by nanostructures [29, 62–65]. The intensity of the SX peak relative to the DBE emission is dependent on the dimensions of the nanowire [63] where the SX emission increases with decreasing size. However, Bai et al. reported that photoluminescence excitation conditions, such as sample temperature, wavelength and intensity can change the intensity of the SX peak [29, 62–64, 66, 67]. The origin of the SX peak is still under considerable debate, as it has also been attributed to absorbates on the ZnO surface and the presence of surface fields [38, 65]. Blue shifting of the luminescence due to quantum confinement is exhibited in ZnO nanostructures, however, the effect is only observed below 10 nm and consequently is not relevant to this work [68].

ZnO can be grown as a variety of different nanostructures, such as nanowires, nanosprings [70], nanobelts, nanoflowers and nanorods [71, 72], that can confine and guide incident and excited light (fig. 2.5). Nanorods have recently attracted great research interest for anti-reflection coating applications for solar cells with increased light absorption and LEDs with increased light extraction. Different methods have been used to fabricate these nanostructures, such as vapour–liquid–solid [73], metal organic vapour-phase epitaxy [74] and pulsed laser deposition [75, 76]. Although these techniques produce high-quality ZnO nanostructured films, they are unsuitable for deposition onto nitride

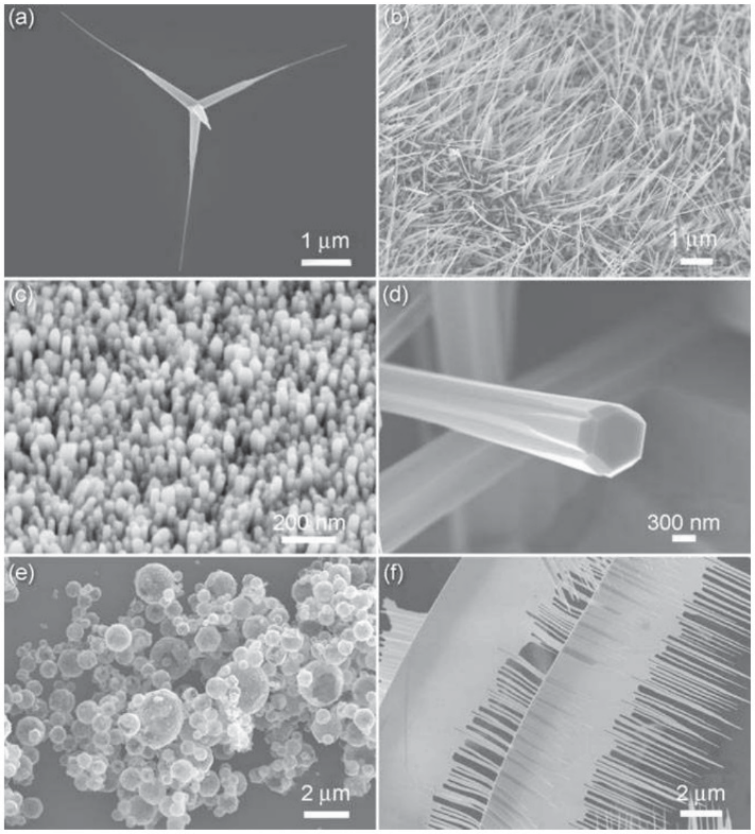

Fig. 2.5: Various ZnO nanostructures, taken from [69].

device structures because their growth is conducted above 650 °C. At these elevated temperatures, ionised Mg acceptors can be passivated by residual, mobile hydrogen in the *p*-type GaN, which lowers the hole density after annealing. Furthermore, implementation of these techniques in a typical commercial LED fabrication process would involve the addition of expensive and complex instrumentation [77]. Conversely, low-temperature (< 100 °C) hydrothermal growth methods are more attractive as they will not affect the electrical properties of the nitride LED devices and they are cost-effective and adaptable to large-scale production [78]. Accordingly, hydrothermal ZnO coatings were employed and studied in this thesis.

2.2.3 Hydrothermal Growth of ZnO Nanorods

Vayessieres et al. and Greene were the first to show that the growth of vertically aligned ZnO nanorod arrays via a hydrothermal method is possible [79–81]. In this process an equimolar mixture of zinc nitrite dihydrate dissolved in deionized water and hexamethylenetetramine (HMT) in aqueous solution is mixed in a stainless steel autoclave. The substrate is positioned upside-down, floating on the surface before sealing the flask and is held at a growth temperature of < 100 °C for a few of hours.

The chemical mechanism with NH_3 as a buffer was determined by Xu et al. and is shown below [82]:

$$\begin{aligned} (CH_2)_6N_4 + 6H_2O &\rightleftharpoons 4\,NH_3 + 6\,HCHO \\ NH_3 + H_2O &\rightleftharpoons NH_3 \cdot H_2O \\ NH_3 \cdot H_2O &\rightleftharpoons {NH_4}^+ + OH^- \\ Zn^{2+} + 2\,OH^- &\rightleftharpoons Zn(OH)_2 \\ Zn(OH)_2 &\xrightarrow{\Delta} ZnO + H_2O. \end{aligned} \tag{2.12}$$

Zn^{2+} ions required for producing ZnO nanorods are provided by the zinc nitrite salts while oxygen ions (O^{2-}) are provided by the water in the growth solution. HMT plays a crucial role in the growth process for hydroxylation, even though its exact function is still unclear [71, 82]. Some groups also add sodium hydroxide ($NaOH$) to adjust the pH value of the solution, which enables the ZnO morphology to be varied in a systematic way [82, 83]. Additionally, changing the growth temperature and time as well as the relative concentration of the precursors can lead to different morphologies [72]. It has been reported that these parameters also vary the length and diameter of the ZnO nanorods [83–89]. However, it is still unclear which of these parameters tunes the spatial dimensions of the nanorods.

Most reports suggest that the length of the nanorod increases with longer growth times. Takanezawa et al. stated that the length increases almost linearly with growth time [84]. Tay et al. on the other hand demonstrated that the length and density of the nanorods is changed by the growth temperature and the precursor concentration [85]. Specifically lower temperatures elongate the rods, while the maximised density is reached by increasing the growth temperature and minimising the solubility of zinc. Conversely, Al-lami et al. showed that the growth temperature as well as the concentration of the reactants is responsible for the morphology of the ZnO nanostructures [72]. The authors managed to grow branched and prism-like shaped nanostructures. These previous results clearly indicate that tuning the length, diameter and density of ZnO nanorods independently of each other by varying the growth parameters is still difficult to achieve in practice.

To grow the ZnO nanorods independently of the substrate, Greene et al. suggested the use of a simple deposited seed layer by adapting an existing method for forming ZnO colloids and nanocrystals in aqueous solution, so that a layer of nanocrystals is directly formed on a substrate [81, 90, 91]. In this approach zinc acetate dissolved in ethanol was drop-cast onto the substrate's clean surface and then thermally decomposed at 200 °C to 350 °C. Pacholski et al. developed a similar method in 2002, which seems to have been adopted by Greene [92]. This simple method using the seed layer deposition enables the

use of any flat surface as a substrate. For example, several groups have already fabricated ZnO nanorods on a broad range of substrates, such as paper or plastic (PET), that will facilitate a range of applications, most importantly disposable optoelectronic devices [93–95].

2.3 Existing Anti-Reflection Coatings

To maximise the light output from planar GaN-based LED structures anti-reflection coatings for enhanced light extraction efficiency are essential. Several studies have been conducted with different approaches, such as surface texturing or roughening [96–99], to randomly scatter the generated photons out of the device. Also, conductive omnidirectional reflectors [100, 101], graded-refractive-index indium tin oxide (ITO) layers [102, 103] and periodic patterns, such as photonic crystals, have been fabricated [104–109]. Even though all of these methods achieved an increase in the light extraction efficiency, they have not been optimised, and most approaches are not suitable for up-scaling for mass LED production, as the required implementation technology is complex and costly. Additionally, as discussed previously, the use of elevated temperatures in some of these techniques excludes their use in this application due to thermal degradation of the electrical properties of the LEDs.
Mimicking nature, such as the imitation of the moth's eye structure, is another approach for the development of anti-reflection coatings. Moths as well as some butterflies are nocturnal and therefore possess night vision. Their eyes have a particular structure, which is a hierarchical combination of a microstructure and a nano-sized corneal nipple arrays [110]. A number of research groups have implemented moth-eye structures in functional thin films to suppress light reflection. Han et al., for instance, fabricated an anti-reflection coating consisting of ZnO nanorods on top of a solar cell [111]. These hydrothermally grown ZnO nanorods reduced the reflectance of the incident light significantly, which was attributed to a graded refractive index at the interface between the topmost layer of the solar cell and air. The gradient in refractive index can be explained by the effective medium theory, proposed by Clapham et al. [112]. Here, the nanostructure can be treated as a homogeneous medium with an effective refractive index since the geometric size of the nanorod arrays is smaller than the wavelength of the incident light. Specifically:

$$n_{\text{eff}}(f) = f * n_{\text{sc}} + (1 + f) * n_{\text{air}}, \tag{2.13}$$

where n_{eff} is the resulting effective refractive index, f the filling factor of the semiconductor nanostructure (here: ZnO nanorods) and n_{sc} the refractive index of the semiconductor [110].
Jeong et al. fabricated a ZnO nanorod array on top of the current spreading layer of

ITO of a GaN-based LED [113]. This device showed a 30% enhancement in light output power at an injection current of 20 mA and an increased transmittance. Both could be attributed to the smooth graded refractive index transition from GaN ($n_{\mathrm{GaN}} = 2.49$) to ITO ($n_{\mathrm{ITO}} = 2.04$) to the ZnO nanorod array ($n_{\mathrm{eff}} = 1.85$ to 1.65) and finally air ($n_{\mathrm{air}} = 1.0$). Also, Lin et al. grew ZnO nanorods hydrothermally on a GaN-based solar cell [88], resulting in an increased light extraction and a reduced reflection, which was also attributed to a graded refractive index.

Lee et al. demonstrated that the length and morphology of ZnO nanorods can influence the reflection reduction significantly [114]. Tapering the top end of the rods was achieved by adding DAP (1,3-diaminopropane) into the growth solution, which improved antireflection performance. The broadband suppression of reflectance was ascribed to the gradual reduction of the effective refractive index from the silicon solar cell surface to the air.

According to Chao et al., a pyramidal microstructure combined with ZnO nanorods on top can change the angle between the incident light and the surface via the textured surface [115]. Furthermore, a reflection reduction was achieved by creating a longer path length for the incident light and a gradient in the refractive index between the air and the surface. Song et al. could demonstrate a significant reduction in reflectance ($< 5\%$ at an incident wavelength of 635 nm) with the microstructural etched pits in the p-GaN layer of the LED and a ZnO nanorods array on top [116]. The improved light extraction was attributed to the elimination of Fresnel reflection by the nanorod arrays and the reduction of the total internal reflection by the microstructure.

Tian et al. fabricated a pyramidal arrays of ZnO with sizes of 0.8 µm to 1.1 µm in the base and 1.5 µm to 2 µm in height and achieved a reflectance of less than 2.5% for the visible and near-infrared spectral range, which was ascribed to the graded refractive index as well [117, 118]. These authors found that the low reflectance of these optically black ZnO pyramidal nanostructures also resulted in increasing film temperature, which was attributed to light absorption by confined electrons.

Other groups attributed the enhanced light output to greater transmission of the incident light via waveguiding effects in the nanostructured ZnO film. Hsiao et al. fabricated a syringe-like ZnO array on a GaN-based LED device and achieved a 10.5% light output power enhancement at an injection current of 20 mA [3]. The tapered tip of the nanorods wave-guided the generated light through the rods out of the device which also supressed side-wall emission. This was confirmed experimentally using single nanorods illuminated with laser light, and a graded refractive index was suggested as a possible explanation for the enhancement. Son et al. produced etched GaN pits in the micrometre scale, decorated with hydrothermally-grown ZnO nanorods, which led to a 3.5-time increase in the electroluminescence signal [119]. This improvement was attributed to a waveguiding effect by the nanorods and a widening of the critical angle, which increased the escape

probability and the scattering probability of the emitted light. Another hybrid approach was proposed by Kim et al. [120]. They fabricated nickel-cobalt oxide nanoparticles and ZnO nanorod composite arrays to reduce the Fresnel reflection at the LED surface; they attributed this reduction to an enlargement of the escape cone and the graded refractive index from the device surface to the surrounding air medium.
To summarise, many different anti-reflection coatings have already been developed to improve light extraction in LEDs and absorption in photo voltaic devices respectively, several of which are based on ZnO nanorod arrays. The improved performance has been tentatively attributed to a graded refractive index between the topmost layer and the surrounding air medium. Some groups also suggested the possibility of light output enhancement due to waveguiding effects within the nanorods. From these studies it is clear that a systematic investigation of the experimentally observed optical effects must be conducted to fully understand and optimise the underlying processes.
Interestingly, the use of a composite of ZnO nanorods with metal nanostructures is an intriguing and potentially powerful approach to further enhance light extraction from planar LED structures. Moreover, these nanocomposite structures are an ideal test-bed to evaluate another interesting effect: light extraction in LEDs owing to plasmon-coupling, as discussed below (section 2.4). This is relevant as whilst critical to determine the ultimate performance of these anti-reflection structures, the phenomenon itself is poorly understood [121].

2.4 Plasmonics: A Theoretical Background

Plasmonics studies the interaction of light with charges, mainly electrons in metals, allowing Abbe's diffraction limit to be broken by the localisation of light into subwavelength dimensions [122, 123], which leads to strongly enhanced and localised electromagnetic fields.

2.4.1 Maxwell's Equations and Bulk Plasmons

The fundamental equations and their derivations are adapted from Maier [124].
The properties of electromagnetic fields can be described by the macroscopic Maxwell's

Equations:

$$\begin{aligned}
\vec{\nabla} \cdot \vec{D} &= \rho_{\text{ext}} \\
\vec{\nabla} \cdot \vec{B} &= 0 \\
\vec{\nabla} \times \vec{E} &= -\frac{\partial \vec{B}}{\partial t} \\
\vec{\nabla} \times \vec{H} &= \vec{J_{ext}} + \frac{\partial \vec{D}}{\partial t}.
\end{aligned} \tag{2.14}$$

The four macroscopic fields in these equations are $\vec{D}$, the dielectric displacement, $\vec{E}$, the electric field, $\vec{H}$, the magnetic field and $\vec{B}$, the magnetic flux density. The quantity ρ_{ext} is the external charge density and $\vec{J_{\text{ext}}}$ is the external current density, while the total charge density and total current density are $\rho_{\text{tot}} = \rho_{\text{int}} + \rho_{\text{ext}}$ and $\vec{J_{\text{tot}}} = \vec{J_{\text{int}}} + \vec{J_{\text{ext}}}$, respectively. The dielectric displacement is defined in terms of the polarisation $\vec{P}$ and the dielectric function ε as:

$$\vec{D} = \varepsilon_0 \vec{E} + \vec{P} = \varepsilon \varepsilon_0 \vec{E}. \tag{2.15}$$

The magnetic field $\vec{H}$ is defined in terms of magnetisation $\vec{M}$ as:

$$\vec{H} = \frac{1}{\mu_0} \vec{B} - \vec{M}. \tag{2.16}$$

In the case of absence of magnetic fields, the first Maxwell Equation can be rewritten as:

$$\vec{\nabla} \cdot \vec{E} = \frac{\rho_{\text{tot}}}{\varepsilon_0}. \tag{2.17}$$

Furthermore, the current density is proportional to the conductivity σ of the metal:

$$\vec{J} = \sigma \cdot \vec{E}. \tag{2.18}$$

This gives the fundamental relationship between the conductivity and the dielectric function, $\varepsilon(\omega)$, which is, in the case of light interaction, only dependent on the angular frequency of light, ω, if the wavelength of the incident light is significantly longer than characteristic dimensions of the electron, such as the mean free path:

$$\varepsilon(\omega) = 1 + \frac{i\sigma(\omega)}{\varepsilon_0 \omega}. \tag{2.19}$$

Both, σ and ε are complex valued functions of the angular frequency:

$$\sigma(\omega) = \sigma_1 + i\sigma_2 \tag{2.20}$$

$$\varepsilon(\omega) = \varepsilon_1 + i\varepsilon_2. \tag{2.21}$$

At optical frequencies, ε can be experimentally determined via the material's complex refractive index, $\widetilde{n}(\omega)$:

$$\widetilde{n}(\omega) = n(\omega) + i\kappa(\omega) = \sqrt{\varepsilon}, \tag{2.22}$$

where κ is the extinction coefficient that determines the absorption of the electromagnetic wave through the material.

At optical frequencies, metals can be characterised by employing the *Drude model*, where the valence electrons can move freely through stationary positive ion cores, analogous to the kinetic theory of neutral dilute gas. Electron-electron interactions and the lattice potential are neglected; collisions are taken into account by the damping factor $\gamma = \frac{1}{\tau}$, where τ is the relaxation time of a free electron gas.

To derive the plasma frequency, the equation of a free electron in an electric field needs to be solved:

$$m\frac{d^2\vec{x}}{dt^2} + m\gamma\frac{d\vec{x}}{dt} = -e\vec{E}. \tag{2.23}$$

Assuming a harmonic time dependence of the electric field $\vec{E}(t) = \vec{E_0} \cdot e^{-i\omega t}$, eq. (2.23) can be solved:

$$\vec{x}(t) = \frac{e}{m\omega^2 + i\gamma\omega}\vec{E}(t). \tag{2.24}$$

Inserting this into the polarisation $\vec{P}$, which is defined as the dipole moment per unit volume, gives:

$$\vec{P} = -ne\vec{x}(t) = -\frac{ne^2}{m(\omega^2 + i\gamma\omega)}\vec{E}(t). \tag{2.25}$$

Applying this to eq. (2.15) leads to:

$$\vec{D} = \varepsilon_0\Big(1 - \frac{\omega_\mathrm{P}^2}{\omega^2 + i\gamma\omega}\Big)\vec{E}, \tag{2.26}$$

with ω_P the plasma frequency of the free electron gas. That gives a new expression for the dielectric function:

$$\varepsilon(\omega) = 1 - \frac{\omega_\mathrm{P}^2}{\omega^2 + i\gamma\omega}. \tag{2.27}$$

In the range of the metallic character of the metal ($\omega < \omega_\mathrm{P}$), the dielectric function is mainly real and can be rewritten as:

$$\varepsilon(\omega) + 1 - \frac{\omega_\mathrm{P}^2}{\omega^2}. \tag{2.28}$$

In this regime, the metals are predominantly absorbing with the absorption coefficient a:

$$a = \sqrt{\frac{2\omega_\mathrm{P}^2\tau\omega}{c^2}}. \tag{2.29}$$

The electric field falls off exponentially into the metal as:

$$exp(-\frac{z}{\delta}), \tag{2.30}$$

with z the depth into the material and δ being the skin depth:

$$\delta = \frac{2}{a} = \frac{c}{\kappa\omega}. \tag{2.31}$$

2.4.2 Surface Plasmons

Surface Plasmon Polaritons (SPPs) are electromagnetic excitations that are created and travel along the planar interface between a dielectric and a metal. The evanescent field of a SPP is confined perpendicular to the interface, falling off exponentially into both media. By applying Maxwell's Equations (eq. (2.14)) to a planar interface between a dielectric and a conducting material, it can be shown that SPPs can exist only in transverse magnetic (TM) polarisation. The dispersion relation of SPPs traveling along the interface of dielectric and metal is given by:

$$\beta = k_0\sqrt{\frac{\varepsilon_{\mathrm{m}}\varepsilon_{\mathrm{metal}}}{\varepsilon_{\mathrm{m}} + \varepsilon_{\mathrm{metal}}}}, \tag{2.32}$$

with ε_{m} and $\varepsilon_{\mathrm{metal}}$ being the dielectric function of the dielectric medium and of the metal, respectively. The quantity β is the propagation constant of the traveling waves and $k_0 = \omega/c$ the wave vector of the propagating wave in vacuum. SPPs can therefore only be excited by light with phase-matching techniques, such as prism configurations, gratings or surface roughening [125–127].
By inserting eq. (2.32) in eq. (2.27), the surface plasmon frequency, ω_{SP}, is given by:

$$\omega_{\mathrm{SP}} = \frac{\omega_{\mathrm{P}}}{\sqrt{1 + \varepsilon_{\mathrm{metal}}}}. \tag{2.33}$$

2.4.3 Localised Surface Plasmons

In contrast to propagating SPPs, Localised Surface Plasmons (LSPs) are non-propagating excitations of electrons in metallic nanostructures coupled to an electromagnetic field [124].
For small particle sizes with a diameter *d* smaller than the wavelength of the incident light ($d \ll \lambda$), it can be assumed that the phase of the harmonically oscillating electromagnetic field is constant over the volume of the nanoparticle (quasi-static approximation). To calculate the electric field $\vec{E} = -\nabla\phi$, the Laplace equation $\Delta\phi = 0$ needs to be solved for the electrostatic case. The simplest geometry is shown in fig. 2.6, where a homogeneous, isotropic sphere with dielectric function $\varepsilon(\omega)$ and radius *a* is surrounded by a dielectric

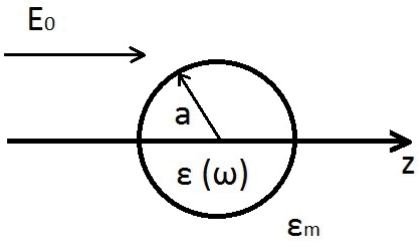

Fig. 2.6: Metal sphere with radius a and dielectric function $\varepsilon(\omega)$ surrounded by dielectric medium with dielectric constant ε_m. Electric field lines are oriented along the z-axis.

material with dielectric constant ε_m. The electric field lines are parallel to the z-direction. By satisfying the boundary conditions, this leads to:

$$\phi_\mathrm{in} = -\frac{3\varepsilon_\mathrm{m}}{\varepsilon + 2\varepsilon_\mathrm{m}} E_0 r\cos(\theta) \tag{2.34}$$

$$\phi_\mathrm{out} = -E_0 r\cos(\theta) + \frac{\varepsilon - \varepsilon_\mathrm{m}}{\varepsilon + 2\varepsilon_\mathrm{m}} E_0 a^3 \frac{\cos(\theta)}{r^2} \tag{2.35}$$

$$= -E_0 r\cos(\theta) + \frac{\vec{p}\cdot\vec{r}}{4\pi\varepsilon_0\varepsilon_\mathrm{m} r^3} \tag{2.36}$$

$$\Leftrightarrow \vec{p} = \varepsilon_0\varepsilon_\mathrm{m}\alpha\vec{E_0},$$

with the polarisability $\alpha = (4\pi a^3\varepsilon - \varepsilon_\mathrm{m})/(\varepsilon + 2\varepsilon_\mathrm{m})$. Equation (2.35) shows the superposition of the applied field and the dipole located at the nanoparticle centre while eq. (2.36) describes the induced dipole moment inside the sphere by the applied field.
If the denominator in eq. (2.35) reaches its minimum, the so-called Fröhlich condition is fulfilled [124], where:

$$Re[\varepsilon(\omega)] = -2\varepsilon_\mathrm{m}. \tag{2.37}$$

The polarisability α experiences a resonant enhancement, which is limited as $Im[\varepsilon(\omega)] \neq 0$.
Therefore, the electric field can be calculated ($\vec{E} = -\nabla\phi$):

$$\vec{E_\mathrm{in}} = \frac{3\varepsilon_\mathrm{m}}{\varepsilon + 2\varepsilon_\mathrm{m}} \vec{E_0} \tag{2.38}$$

and

$$\vec{E_\mathrm{out}} = \vec{E_0} + \frac{3\vec{n}(\vec{n}\cdot\vec{p}) - \vec{p}}{4\pi\varepsilon_0\varepsilon_\mathrm{m}} \cdot \frac{1}{r^3}. \tag{2.39}$$

It can be seen that an enhancement of the internal and dipolar field occurs at resonance of α. This enhancement comes with increased scattering and absorption of light by the metal nanoparticle, which are desirable attributes for many optical applications.

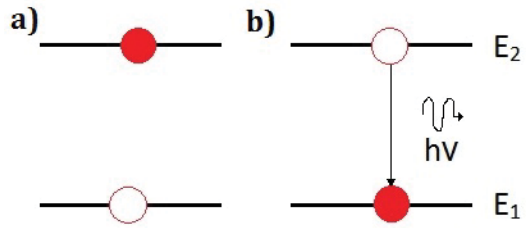

Fig. 2.7: Illustration of the spontaneous emission. (a) atom in excited state, (b) atom decays to a lower energy level, releasing a photon with energy $E_2 - E_1 = h\nu_{photon}$.

2.4.4 Spontaneous Emission Rate and Purcell Enhancement Factor

The spontaneous emission rate (SER) of a semiconductor can be understood when looking at an atomic system that is initially in an excited state, decaying to a lower energy level, with the emission of a photon. If an atom is in an excited state with energy E_2, it will spontaneously decay to a lower level of energy E_1, e.g. the ground state. During this process, it releases a photon with the energy that separates these two energy levels (cf. fig. 2.7):

$$E_{\text{photon}} = E_2 - E_1 = h\nu_{\text{photon}}, \tag{2.40}$$

with h being Planck's constant.
The number of atoms in the excited state at a given time t is $N(t)$, which decays with time:

$$\frac{\partial N(t)}{\partial t} = -A_{21}N(t), \tag{2.41}$$

where A_{21} is the Einstein coefficient for spontaneous emission. This differential equation can be solved:

$$N(t) = N(0)\exp(-A_{21}t) = N(0)\exp(-\Gamma_{\text{R}}t). \tag{2.42}$$

Where $N(0)$ is the number of atoms that were initially in the excited state and Γ_{R} the radiative decay rate.
The SER Γ_{R} is the reciprocal of the lifetime, τ_{21}, of an excited atom, which is defined by the decay to $1/e$ of its original value $N(0)$.

$$A_{21} = \Gamma_{\text{R}} = \frac{1}{\tau_{\text{R}}}. \tag{2.43}$$

In real systems, the lifetime τ_{tot} usually consists of a radiative recombination component τ_{R} as well as a non-radiative one τ_{NR}, which is attributed to surface states and trapping:

$$\frac{1}{\tau_{\text{tot}}} = \frac{1}{\tau_{\text{R}}} + \frac{1}{\tau_{\text{NR}}}. \tag{2.44}$$

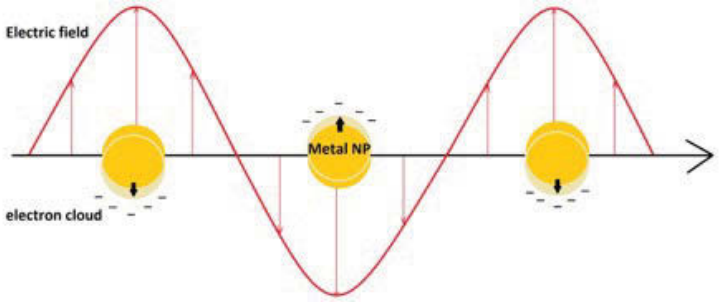

Fig. 2.8: Illustration of Localised Surface Plasmons.

One possible way to increase the SER is by applying a metal nanoparticle film to the semiconductor, creating a new recombination path by coupling with their LSPs. As discussed in section 2.4.3, LSPs are surface bound charge oscillations of free electrons in metal nanoparticles in resonance with the electromagnetic field (cf. fig. 2.8). The local surface electric field of the nanoparticles can be greatly enhanced when excited resonantly. This can be achieved by external illumination such as laser light or by resonant coupling to excitons in the semiconductor. The latter is known as LSP-exciton coupling which is a direct, resonant dipole-dipole coupling between the LSPs in metal nanoparticles and the excitons of a semiconductor. Here, excitons, when their transition dipole moment collapses, can transfer electromagnetic energy into LSP modes instead of free space, which significantly enhances the SER of the surroundings [128]. The increased SER originates from an additional, faster recombination channel through the LSPs, associated with lifetime, τ_{LSP}, which consequently reduces the total carrier lifetime

$$\frac{1}{\tau^*_{\mathrm{tot}}} = \frac{1}{\tau^*_{\mathrm{R}}} + \frac{1}{\tau^*_{\mathrm{NR}}} + \frac{1}{\tau^*_{\mathrm{LSP}}}. \tag{2.45}$$

Therefore, a shorter lifetime due to metal nanoparticle decoration is considered to be strong evidence for LSP-exciton coupling [129, 130]. The coupling strength depends on the plasmon resonance frequency of the metal nanoparticles with respect to the frequency of the incident light or emission, being highest at resonance.
The Purcell enhancement factor (F_P) quantifies the increased SER in analogy to the Purcell effect in cavity quantum electrodynamics where excitons are coupled to cavity photons [131]. It can be calculated using the recombination rates of electron-hole pairs which are inversely proportional to the carrier lifetimes:

$$F_P = \frac{\Gamma^*_{\mathrm{R}} + \Gamma^*_{\mathrm{NR}} + \Gamma^*_{\mathrm{LSP}}}{\Gamma_{\mathrm{R}} + \Gamma_{\mathrm{NR}}} = \frac{\tau_{\mathrm{R}} + \tau_{\mathrm{NR}}}{\tau^*_{\mathrm{R}} + \tau^*_{\mathrm{NR}} + \tau^*_{\mathrm{LSP}}}. \tag{2.46}$$

In summary, an enhanced luminescence with a shorter lifetime due to the presence of a metal nanoparticle coating is a strong indicator for LSP-exciton coupling, which can be quantified by the Purcell enhancement factor.

2.5 Literature Review on Plasmonic Coupling

The following sections will present an overview of the existing state-of-the-art plasmonic structures incorporated in GaN-based LEDs as well as plasmonic interactions between ZnO and metal thin films and nanostructures.

2.5.1 Surface Plasmons in GaN-LEDs

As mentioned in section 2.4.2, surface plasmon energy can be extracted as light if the metal film is rough or nanostructured, which allows scattering and coupling of the surface plasmons into radiated light. Metal films incorporated in GaN-based LEDs showed an increase of spontaneous emission rate (SER) due to the large field enhancement at the interface of the metal and the semiconductor [132, 133]. Hence, it is desirable to increase the SER to enhance the internal quantum efficiency of the LED by producing more luminescence.
Okamoto et al. fabricated a silver coated GaN-based LED that showed a 12-time increased photoluminescence (PL) emission [133]. The enhancement was attributed to the coupling of the surface plasmons to the electron-hole pairs in the multiple quantum wells (MQWs) of the LED. The increased spontaneous emission rate resulted in a higher internal quantum efficiency (IQE). Cho et al. were able to achieve an increased IQE due to an enhancement in the spontaneous recombination rate through coupling of excitons of the MQWs with the LSPs in the incorporated silver nanoparticles [134]. Kao et al. and Kwon et al. showed similar results [135, 136] as well as Cho et al., who integrated gold and aluminium nanoparticles [134, 137]. Many other recent articles are found in the literature providing experimental evidence that inserting a nanostructured metal film can significantly increase the IQE [132, 133, 138–143]. Furthermore, it has been demonstrated that the distance from the metal film to the MQWs is crucial for strong plasmonic coupling because of the exponential decay of the evanescent field as described above (cf. section 2.4). Lee et al. found that the *p*-GaN topmost layer of the LED with a thickness of 20 nm is favourable [144]. This thickness is sufficient for the operation of the MQW device, but it is thin enough to facilitate strong coupling between the MQWs and LSPs.
Although an increase in light extraction efficiency has been demonstrated using these plasmonic approaches, the physical mechanisms in the improved performance are still not well understood. Strong coupling between the MQWs and the LSPs is used as the common explanation, however, a satisfactory theoretical justification is lacking. To study

and optimise this enhancement of efficiency, further systematic experiments and theoretical modeling are needed. In particular, the interaction of LSPs with the dielectric media is not fully understood yet. Furthermore, the existing literature has focussed on the research to exploit these plasmonic interactions to increase the IQE of the GaN-based LEDs. However, as these devices have a transparent conductive ITO capping layer, internal reflection losses are still significant and in this case enhancement of the light extraction efficiency is more critical than the IQE.
Therefore, nanostructured ZnO films and their metal nanoparticle composites are the focus of this work as they can in principle act as the conductive capping layer electrode as well as enhancing the light extraction efficiency.

2.5.2 LSP-Exciton Coupling in ZnO with Various Metals

As stated above, coupling between LSPs and excitons is strongly dependent on the overlap of the plasma resonance frequency of the metal nanoparticles and that of the excitonic emission. Therefore, it is favourable to use metal nanoparticles with plasma resonance frequency close to the near-band-edge (NBE) emission of ZnO to enhance the local field, resulting in an enhanced UV emission.
Gold and silver are the most commonly used metals for plasmonic applications. Gold in particular is a widely-used plasmonic metal as it is inert and stable, making it easy to deposit and handle, whereas silver easily sulphonates and oxidises when exposed to air [145, 146]. However, the plasmon resonance frequency, ω_{SP}, is in the green and blue spectral range, for Au and Ag respectively. By varying shapes and sizes of nanoparticles, ω_{SP} is tunable to some degree but resonant coupling to ZnO's UV emission cannot be realised.
Aluminium is a promising plasmonic candidate for ZnO as its resonance frequency is in the UV, which is widely tunable by nanoparticle sizes and shapes [147]. However, it is easily oxidised and a well-known dopant for ZnO, enhancing the NBE emission with a signature Al donor bound exciton emission at 3.3608 eV (cf. I_6 line in table 2.1). Thus, using elevated temperatures may unintentionally incorporate Al, leading to a similar effect of UV emission enhancement.
A greatly enhanced UV emission of metal nanoparticle coated ZnO has been reported in literature as well as a reduced carrier lifetime which has been attributed to plasmonic coupling (cf. section 2.4.3). For instance, Guidelli et al. reported a shortened lifetime of ZnO-Ag core-shell nanostructures from 1570 ps to 1045 ps as well as enhanced PL UV emission while the DL emission was decreased [148]. Zang et al. showed a greatly enhanced CL UV emission of Ag-coated ZnO hollow nanospheres with unchanged DL emission [128]. The carrier lifetime decreased from 60 ps to 28 ps for Ag-coated ZnO nanospheres, indicating an improved recombination rate for excitons in ZnO after Ag

decoration. Similarly, Yin et al. reported an increased UV emission for Ag nanoparticle-coated ZnO nanorods and a reduced lifetime from 552 ps to 22 ps [149]. Additionally, a silicon dioxide (SiO_2) layer was inserted to suppress charge transfer between ZnO and Ag that showed a similarly short lifetime of 44 ps. This result was used to suggest that the underlying enhancement mechanism is due to LSP-exciton coupling. Similar results have been reported by Liu et al. showing a 7-fold enhancement of UV emission of Ag nanoparticle-coated ZnO nanorods separated by a thin SiO_2 charge blocking layer [150]. An optimal thickness of 12 nm of SiO_2 between ZnO nanorods and 10 nm Ag nanoparticle coating showed a decreased lifetime from 79 ps to 52 ps while the lifetime increased to 86 ps for ZnO nanorods coated with SiO_2 only. These measurements were used as evidence for direct LSP-exciton coupling between ZnO and Ag, creating an additional, faster recombination channel. A Purcell enhancement factor of 1.52 and an approximate 3.5-fold increased IQE were calculated, matching the 7-fold PL enhancement in the UV.
However, these lifetimes are very close to the typical laser response, which is not specified in the relevant publications, and therefore reliability and significance can be questioned. Furthermore, evidence that the employed metal films are continuous as well as results demonstrating the material's quality are missing. Similarly, the continuity and quality of the dielectric spacer layers is not given, despite being essential to effectively block charge transfer.
Nevertheless, the presented results show that Ag can be used to enhance ZnO's NBE emission through LSP-exciton coupling despite Ag not being resonantly excited by either laser light or ZnO's NBE emission. The Purcell enhancement factor can be calculated from carrier lifetimes of pristine, uncoated and coated ZnO, which gives insight in the coupling strength between excitons and LSPs. However, enhanced luminescence and Purcell factors typically do not line up, demonstrating that a deeper physical understanding is required supported by systematic experiments addressing this particular inconsistency.
Similar results have been reported for Al-coated ZnO, allowing theoretically stronger plasmonic coupling due to Al plasma resonance frequency being widely tunable in the UV and visible spectrum. Therefore, in principle, larger enhancement factors should be achievable.
Lu et al. fabricated ZnO microrods coated with large Al nanoparticles, which led to an 170-fold UV emission enhancement as well as a shortened lifetime from 1.23 ns to 0.98 ns [130]. This was attributed to the creation of an additional recombination path through LSPs. Clearly, the resulting Purcell enhancement factor of approximately $F_P = 1.25$ does not explain such large enhancement of the UV emission. For thicker Al films, the nanoparticles had coalesced, which resulted in a red-shift of the plasmon resonance frequency and a reasonably reduced plasmonic coupling strength. While the UV emission enhancement was ascribed to LSP-exciton coupling, the accompanying suppression of the DL

emission was attributed to its absorption by Al nanoparticles, creating hot electron in Al nanoparticles. Their transfer to the conduction band of ZnO resulted in a further enhanced UV emission. The absorption mechanism here is not clear, as the plasmon resonance frequency of Al is very close to ZnO's NBE emission, which is strongly blue shifted from the DL energy.
Similar structures have been grown by Lu et al., which showed a PL UV emission, which was enhanced by 40 times and in electroluminescence (EL) by 30 times — attributed to direct LSP-exciton coupling [151]. Furthermore, a decreased carrier lifetime from 1282 ps to 203 ps was observed, leading to a Purcell enhancement factor of 6.3, which alone cannot explain the reported 30-40 time increase in UV emission. Similar enhancements from coating ZnO with nanostructured Al have also been reported in literature [152].
These reports show that Al coatings can greatly enhance the UV emission of ZnO, which is typically attributed to direct LSP-exciton coupling. However, the results vary widely in lifetime reduction and enhancement factors, although the samples appear to be identical by their description. Furthermore, the Purcell enhancement factors resulting from lifetime measurements generally do not agree with the UV enhancement, indicating insufficient understanding of the underlying coupling mechanism.
Despite Al being known for oxidising easily, evidence for its metallic character is typically missing. Furthermore, Al incorporation in ZnO can enhance the DBX emission by doping, which has not been further investigated in literature. In the case of Al, a more detailed and systematic study of LSP-exciton coupling is needed.

In summary, many reports have been published on LSP-exciton coupling of ZnO and metal nanoparticles, showing significant enhancement factors in UV emission. A shortened carrier lifetime of the excitonic emission as well as enhanced UV emission despite an inserted charge blocking layer are considered as strong indicators for LSP-exciton coupling. Nevertheless, the coupling mechanism for non-matching plasma resonance frequencies with ZnO's NBE emission is not fully understood yet. In addition, the fabrication of high quality Ag and Al nanoparticle surface coatings are not trivial, as they easily oxidise and Al is a well-known donor dopant in ZnO.

2.5.3 Plasmonic Coupling between Au and ZnO

Contrary to Ag and Al, gold is a very stable and inert metal, which allows for simple fabrication methods for plasmonic coatings. Interestingly, great enhancement factors of ZnO's UV emission have been reported using Au nanoparticle coating despite the plasmon resonance frequency of Au being in the green spectral range [15–26]. Although the enhancement mechanism is presently not fully understood, two different models have

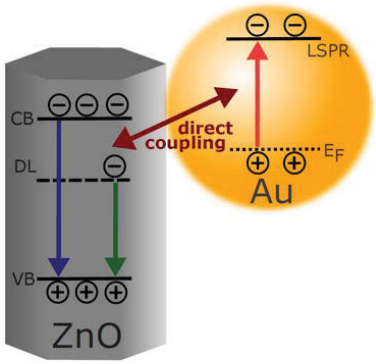

Fig. 2.9: Illustration of the LSP-exciton dipole-dipole coupling mechanism.

been put forward to explain the increased light emission from what are reported to be identical specimens:

1. Direct coupling between excitons of ZnO and LSPs of Au, which is illustrated in fig. 2.9.

2. Charge transfer mechanism from Au to the conduction band of ZnO, depicted in fig. 2.10.

As mentioned before, the LSP-exciton coupling mechanism explains the increased UV emission of Au-coated ZnO by resonant dipole-dipole coupling between ZnO's excitons and LSPs in Au. This leads to an increased density of optical states, and consequently, an enhanced spontaneous emission rate by creating an additional, faster recombination channel via LSPs (cf. section 2.4.4).
In the charge transfer mechanism, the LSPs in Au are directly excited by the DL emission of ZnO, which is known to be close to the plasma resonance frequency of Au [18, 23, 24]. LSPs can then decay into hot carriers, allowing hot electrons to transfer from Au to the conduction band of ZnO. Recombination with holes in the valence band results in enhanced NBE emission. However, the migration of electrons from defect states of ZnO to Au is also possible as their energy levels are close to each other. The increase of electron density in Au creates high-energy electrons that can relax into the conduction band of ZnO, enhancing the NBE emission [15, 16, 20].
Lin et al. fabricated ZnO nanorods of an average diameter of 90 nm to 160 nm sputter-coated with Au that exhibit an increased NBE PL emission and suppressed DL emission compared to uncoated ZnO nanorods [153]. They propose the aforementioned charge transfer mechanism where the DL emission is absorbed by the Au via LSP resonance (LSPR) followed by a non-radiative transfer of electrons from higher energy levels in the Au to the conduction band of ZnO to explain the enhanced NBE emission as well as the suppressed DL emission.

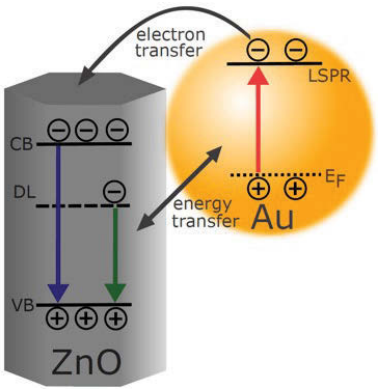

Fig. 2.10: Illustration of the charge transfer mechanism, where the defect-related emission from ZnO is absorbed by the Au nanoparticles to create Localised Surface Plasmons. The decay into hot carriers allows for charge transfer of hot electrons from the Au to the conduction band of ZnO.

Increasing sputter-coating times of Au led to different UV enhancement factors, which was attributed to two competing effects. For longer sputtering times, the UV emission intensity was further enhanced until it dropped at $t = 50\,\mathrm{s}$, which is due to stronger scattering as the density of Au nanoparticles increased. The optimum density was reached for $t = 60\,\mathrm{s}$ with highest UV emission, which is the most efficient way to transfer excited electrons from Au into the conduction band of ZnO, according to the authors. Further increase in sputtering time led to densely-shadowed ZnO nanorods with decreased NBE emission. Furthermore, the authors repeated the same experiment with a ZnO nanorod sample with negligible DL emission, showing a decrease in NBE emission. That was attributed to missing LSP excitation by DL emission of ZnO nanorods and, consequently, electron transfer from the ZnO's conduction band to Au rather than the other way around. The formation of a Schottky barrier at the interface between ZnO and Au, preventing charge flow from ZnO's conduction band to Au, was not discussed. These two experiments were used to underline the charge transfer mechanism, although remaining holes in the Au nanoparticles were not taken into account.
Other groups have conducted similar experiments showing enhanced UV and suppressed DL emission, reasoning to explain their observations [15, 154–156].
For instance, Li et al. fabricated ZnO films decorated with Au nanoparticles [16]. PL measurements at room temperature show an enhanced UV emission of 18 times compared to uncoated ZnO, while the DL emission is suppressed. Here, electrons in defect states are transfered to the Au as their energy level is close to the Au's Fermi level. The resulting increased electron density in Au nanoparticles creates energetic electrons in higher energy states which can then transfer to the conduction band of ZnO, enhancing the NBE emission. Varying nanoparticle densities and sizes shift the LSPR differently, leading to different enhancement factors of the NBE emission. This model has been adapted by

other authors, which showed similar results using ZnO nanorods and Au nanoparticles [21–23]. However, this mechanism does not account for the remaining holes in defect levels which are likely to recombine with electrons from the conduction band of ZnO.
Mahanti et al. reported a 2-fold PL enhancement of the NBE emission and a suppressed DL emission of ZnO nanorods grown on a Au nanoparticle layer [157]. According to the authors, the defect-related emission excites the LSPs in Au, which decay into hot electrons, which can subsequently migrate into the conduction band of ZnO. Thus, the increased NBE and decreased DL emission can be explained. Furthermore, they inserted a SiO_2 spacer layer that increased the UV emission up to 6 times, depending on the layer thickness. For layers thicker than 42 nm the intensity of UV emission decreased due to reduced plasmonic coupling strength of the DL emission of ZnO with LSPs in Au. The further enhanced UV emission was attributed to preventing charge transfer from the conduction band of ZnO to the Fermi level of Au, which they assigned as a competing effect to excitonic recombination without the SiO_2 spacer. However, it is questionable how hot electrons from Au can still transfer into ZnO's conduction band despite the presence of a 42 nm SiO_2 layer. In addition, it is unclear how remaining hot holes in Au would relax.
Interestingly, another article by the same group showed the opposite trend of a similar structure, ZnO nanorods sputter coated with Au nanoparticles [158]. Here, the UV photoresponse was enhanced while the room-temperature PL was decreased due to Au nanoparticle decoration. According to the authors, a Schottky junction is formed at the interface of ZnO and Au, which leads to surface band bending. Therefore, the increased UV sensitivity can be attributed to a separation of electrons and holes. Nevertheless, the question arises why those very similar samples show very different results.
Charge blocking layers have also been used by other groups such as Wang et al., who inserted a thin SiO_2 spacer layer between a Au nanoparticle layer and a single ZnO nanorod [159]. It has been shown that the optimal spacer thickness is 5 nm, resulting in the greatest enhancement in UV emission using CL spectroscopy.
A more systematic study has been reported by Zhang et al. [25]. The authors inserted an Al_2O_3 spacer layer of increasing thickness between ZnO and Au, which led to a further increase in NBE emission than that of ZnO and Au in direct contact. These results were explained using three competing effects:

1. *Quenching*, which is described as an energy transfer from ZnO to the metal, resulting in a decreased NBE emission. Dipole oscillations are damped by the nearby Au nanoparticles.

2. *Space charge*, which affects the magnitude of surface plasmons and therefore changes the NBE emission of ZnO.

3. *Surface plasmons*, which increase the local incident field on the Au nanoparticles, enhancing the NBE emission.

With an Al_2O_3 spacer of 25 nm optical thickness, the surface plasmons are still able to couple, but quenching is no longer allowed due to strong exponential decay with distance. Therefore, a stronger enhancement of the UV emission can be achieved.
Polarisation of the incident laser light showed a linearly decreasing of the UV emission of the uncoated ZnO, while Au coated ZnO exhibited a polarisation-dependent behaviour. For polarisation angles from $0°$ to $42°$, the NBE emission showed monotonic enhancement, which then slowly decreased for greater angles. As the surface plasmons are an electromagnetic excitation, which can be modulated by the polarisation of incident light, the authors concluded that the polarisation dependence of the Au-coated ZnO is due to plasmonic interaction.
Cheng et al. suggested a combination of the two LSP excitation mechanisms — electron transfer from the DL to Au and energy absorption of the DL emission by the Au nanoparticles [18]. PL spectra showed a 6-fold enhancement of the NBE emission while the DL emission was quenched.
By introducing an Al_2O_3 spacer layer between ZnO and Au, the charge transfer between ZnO and Au is no longer allowed. However, the NBE emission of ZnO was still increased compared to the uncoated nanorods. Time-resolved PL measurements exhibited a shortened lifetime for Au coated ZnO nanorods ($\tau \sim 30\,\mathrm{ps}$ to $35\,\mathrm{ps}$) compared to the uncoated ones ($\tau \sim 230\,\mathrm{ps}$), indicating an increase in the spontaneous emission rate. The authors assume that exciton-LSP coupling is the underlying mechanism for the UV emission enhancement while a charge transfer from the DL to the Au explains the quenched DL emission as well as the further increase in UV emission by hot electron migration from high energy levels in Au to the conduction band of ZnO. It is unclear whether the Al_2O_3 spacer layer changed the DL emission of the Au-coated ZnO nanorods. Furthermore, evidence that the Al_2O_3 layer is continuous is missing and the possibility of Al doping has not been discussed.
Similar experiments have been conducted by Liu et al., using PL spectroscopy to study ZnO nanorods coated with Al_2O_3 spacer layers of different thicknesses and sputtered Au nanoparticles [160]. The Au nanoparticle coating increased the NBE emission, while the DL emission was quenched. The Al_2O_3 layer can passivate competitive non-radiative surface state recombination channels in the ZnO nanorods, which was reflected by a slightly enhanced NBE emission. The quenching of DL emission was independent of the Al_2O_3 thickness ($t = 0\,\mathrm{nm}$ to 25 nm), indicating that the underlying effect is not LSP-related. The UV enhancement was assigned to two competing effects, (i) enhanced spontaneous emission rate with decreasing spacer thickness and (ii) monotonically-increasing

coupling probability with thicker spacer layers. The resulting Purcell enhancement factor is the product of those two effects and the optimal Al_2O_3 thickness was found to be $t = 65\,\mathrm{nm}$.

Summarising, large enhancement factors of ZnO's NBE emission with Au have been reported in literature. The increased UV emission has been attributed to one of the two existing models; one involving direct, resonant exciton-LSP coupling and the other charge transfer of hot carriers from LSP decay. Although the proposed models offer an explanation for the enhanced UV as well as the decreased DL emission, some important factors have not been taken into account:

1. Electrons transfered from the DL of ZnO to Au nanoparticles will leave holes in the DL states. They are possibly re-populated by electrons from the conduction band of ZnO.

2. LSPs in Au decay into hot carriers, but only the hot electrons are transferred to ZnO, which does not explain how the hot holes would relax.

3. It is not clear how direct, resonant LSP-exciton coupling between ZnO and Au nanoparticles is possible as the Au's plasmon resonance frequency is far from the excitonic emission of ZnO.

4. It is questionable how dielectric spacer layers can block the electron transfer in only one direction, while hot electrons from Au can still relax into ZnO's conduction band. Furthermore, it is unclear why the quenching of the DL emission is unaffected by the charge blocking layer.

Accordingly, it is clear that an in-depth systematic study is needed to provide a comprehensive understanding of the underlying coupling mechanism between ZnO and metal nanoparticles, in particular Au.

3 Experimental Details

This chapter describes the synthesis of the zinc oxide nanorods and metal nanoparticle coatings used in this investigation, as well as the characterisation methods utilised to study them.

3.1 ZnO Samples

In this work, two different ZnO samples were used — in-house hydrothermally-grown ZnO nanorods and commercially available *a*-plane ZnO single crystals.

3.1.1 Hydrothermally-Grown ZnO Nanorods

The synthesis of ZnO nanorods consists of two main steps, in this work: the seed layer deposition and the hydrothermal growth of the ZnO nanorods. The process is based on a technique developed by Greene and collaborators [80, 81, 161].

3.1.1.1 Seed Layer Deposition for ZnO Nanorod Growth

In Greene's procedure, silicon (Si(110)) was used as the growth substrate. The substrates were cleaned by a standard cleaning process, consisting of consecutive ultrasonication steps in acetone, isopropanol and deionised water, each for 15 minutes.
To obtain a uniform growth, a zinc acetate seed layer was deposited before the synthesis of the ZnO nanorods. This was achieved using 5 mM zinc acetate dissolved in ethanol, drop-casted onto a clean Si substrate and rinsed with pure ethanol after ten seconds. After repeating this process five times, the substrate was annealed in air in a conventional oven at 250 °C for 20 minutes. This procedure was carried out twice to ensure a uniform ZnO seed layer.

3.1.1.2 Hydrothermal Growth of ZnO Nanorods

The substrate with the seed layer was positioned upside-down on the surface of the growth solution in a stainless steel autoclave with an inner lining of Teflon, see fig. 3.1. The growth solution contained 25 ml of 0.025 M hexamethylenetetramine (HMT) and 25 ml of 0.025 M zinc nitrite, both dissolved in deionised water. The synthesis was carried

Fig. 3.1: Picture of stainless steel autoclave with lining of Teflon.

out in a conventional oven at a temperature of 90 °C for 3 hours. After the growth, the sample was rinsed with deionised water several times and dried in air.

3.1.2 ZnO Crystals

In addition to ZnO nanorods, planar ZnO single crystals were purchased from the MTI Corporation, USA to act as reference standard. These crystals were also used to study the plasmonic coupling mechanism between ZnO and Al. The hydrothermally-grown *a*-plane ZnO crystals were as pure as >99.99 $wt\%$ with the main impurities being Mg (5 ppm), Al (30 ppm), Si (30 ppm), Ti (10 ppm), Cu (30 ppm), Fe (5 ppm), Ca (5 ppm) and Ag (2 ppm).
The as-received ZnO crystals were manually polished, using a Leco SS1000 polishing unit with a Leco lecloh polishing pad. An alkaline 50 nm colloidal silica suspension was used to ensure a clean surface with a consistent roughness of less than one nanometre, which was determined by AFM (cf. section 3.2.1).
The standard cleaning process – described in section 3.1.1.1 – was subsequently applied before coating the surface with metal nanoparticles (cf. section 3.1.3).

3.1.3 Metal Nanoparticle Coating

The ZnO samples were then coated with three different nanostructured metals – Au, Al and Ag – to investigate their plasmonic interaction.
Uniform gold nanoparticles were formed using a simple DC sputtering and annealing process. An Au film was directly sputtered onto the ZnO nanorods with a nominal thickness of one nanometre, using argon as the working gas and a chamber base pressure of 6-10$\times 10^{-3}$ mbar. This process was carried out in a Leica EM ACE600 that automatically

calculates the layer thickness by measuring the change of resonance frequency in a quartz crystal. Similarly, Au layers were produced in a home-built deposition chamber, using a base pressure of 1.3×10^{-3} mbar, DC power of 30 W and argon gas flow of 60 sccm. Subsequent annealing of the sample at 300 °C for 30 minutes was carried out, resulting in the formation of a uniform distribution of Au nanoparticles with an average diameter of 5 nm — imaged by a Zeiss 55VP Supra Scanning Electron Micropscope (SEM) (cf. section 3.2.3).
The aluminium (Al) nanostructured films were produced, using the previously mentioned home-built deposition chamber. By varying the deposition parameters, three different layers were fabricated:

1. A thin Al film of a nominal thickness of 2 nm using argon as working gas with a flow of 60 sccm, resulting in a randomly-distributed nanostructured Al film covered in aluminium oxide (Al_2O_3). This sample will be assigned as sample *Al*.

2. A thin Al film deposited under same conditions (nominal thickness 2 nm) but at an elevated temperature of 300 °C. The coating consisted of small Al nanoparticles embedded in Al_2O_3, which will be referred to as sample *Al hot*.

3. A thin Al film deposited in gas mixture of 58 sccm argon and 30 sccm oxygen, leading to a smooth Al_2O_3 thin film (nominal thickness 2 nm). This is sample *Al oxide*.

The Ag nanoparticle-coatings were similarly sputter-coated onto ZnO, but subsequently abandoned due to significant oxidation effects.
The morphology and composition of the resulting Al films were characterised by Atomic Force Microscopy (AFM) and ellipsometry – discussed in section 3.2.1 and section 3.2.2.
Note that ZnO nanorods were only coated with 2 nm film at room temperature, while the planar *a*-plane ZnO single crystals were separately coated with all three variation of Al coatings, mentioned above.

3.2 Sample Characterisation

The characterisation of the size and shape of the synthesised nanostructures was performed using scanning electron microscopy (SEM) and atomic force microscopy (AFM) at high spatial resolution, as well as ellipsometry. Cathodoluminescence (CL) and photoluminesence (PL) spectroscopy and CL imaging were utilised to investigate the optical and electronic bulk and surface properties of the fabricated nanostructures, as well as defect structures using depth-resolved and temperature-resolved methods. Time-resolved PL was used to obtain an insight into the charge carrier dynamics, specifically lifetime measurements to confirm Purcell enhancement and increased SER, in the ZnO crystals and nanorods with and without a surface coating. X-ray photoelectron spectroscopy (XPS)

was performed to understand the band structure of the fabricated ZnO-Au nanocomposite and the Al-coated *a*-plane ZnO.
In order to simulate the plasmonic interaction between ZnO and the metal nanoparticles, Finite-Difference Time-Domain (FDTD) method was used.
The following section describes these characterisation techniques.

3.2.1 Atomic Force Microscopy

High-resolution images of the sample surface can be achieved using Atomic Force Microscopy (AFM). This technique uses a sharp tip at the end of a cantilever, with a typical radius of a few nanometres. It is raster-scanned across the sample's surface, creating a high-resolution image of the topography. By lowering the tip down to the sample surface, using piezoelectric elements, small changes in inter-atomic force between the tip and the sample can be used to track the surface topography by maintaining a specific deflection of the cantilever. This is achieved by a laser which is focussed onto the end of the cantilever, reflecting back onto a quadrant photodiode. The difference in outputs from the quadrants of the photodiode allows tracking of the angular position of the cantilever. This directly translates into the mapping of the topography of the sample's surface. A schematic diagram of a typical AFM is shown in fig. 3.2.

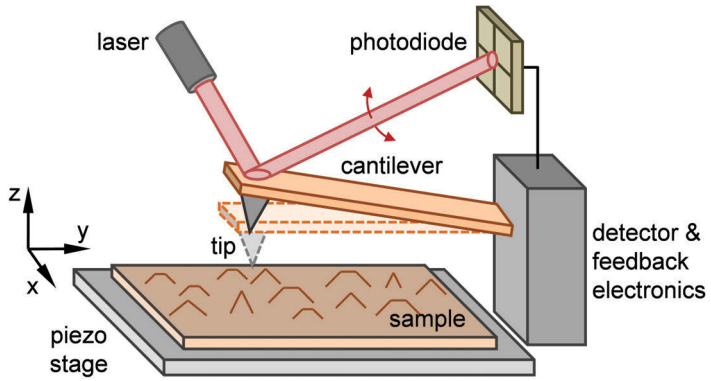

Fig. 3.2: Schematic AFM set-up, showing tapping mode.

In this work, a Bruker Dimension 3100 with IIIA controller was used to study the surface roughness of *a*-plane ZnO crystals and different metal nanoparticle coatings. A NSC15 tip with a force constant of $k = 40\,\mathrm{N\,m^{-1}}$ was used in tapping mode. Here, the tip is oscillated near its resonance frequency; once lowered to the surface, it is intermittently touching the sample ("tapping") as it scans the surface. The tip-to-surface force interaction causes the resonance amplitude to change; it usually decreases as the tip gets closer to the sample surface. This amplitude is typically used to adjust the tip-sample distance, which is kept constant. The resulting "tapping mode" image gives the topography of the sample's surface.

3.2.2 Ellipsometry

Ellipsometry is a surface-sensitive technique which uses polarised light to characterise thin films or sample surfaces with sub-monolayer precision.
Here, the phase change in a light beam of reflected polarised light is analysed. Unlike other optical characterisation techniques, the measured parameters Ψ and Δ are not physical quantities of the sample itself, but they are related to the Fresnel coefficients of s- and p-polarised light, R_s and R_p, respectively:

$$\rho = \frac{R_p}{R_s} = \tan(\Psi)\exp(-i\Delta). \tag{3.1}$$

The measured quantities Ψ and Δ are functions of the incident light beam such as wavelength, angle and polarisation state. P- and s-polarisation can be understood by using an electromagnetic plane wave, derived from Maxwell's Equations (cf. eq. (2.14)). In this case, the electric and magnetic field are perpendicular to each other and to the direction of wave propagation. Therefore, only the electric field and the propagation direction are needed to describe the complete plane wave:

$$\vec{E}(\vec{r},t) = \vec{E_0}\exp\left(\frac{-i2\pi\tilde{n}}{\lambda}\vec{q}\vec{r}\right)\exp(i\omega t). \tag{3.2}$$

Where $\vec{q}$ is the unit vector along the direction of the propagating wave, $\tilde{n}$ the complex refraction index ($\tilde{n} = n - i\kappa$), λ the wavelength of the light in vacuum, ω the angular frequency of the wave, and $\vec{E_0}$ is a complex vector constant specifying the amplitude and polarisation state of the wave.
The polarisation states of a wave are typically described by using the direction and phase of the electric field vector. In terms of ellipsometry, the so-called Jones vector can be used to fully describe the polarisation of the electric field of an isotropic beam:

$$\vec{E} = \begin{pmatrix} \tilde{E_p} \\ \tilde{E_s} \end{pmatrix}. \tag{3.3}$$

Here, the *p*-polarisation is defined as lying in the plane of incidence, with $\tilde{E_p}$ being a complex vector, while the *s*-polarisation is perpendicular to the *p*-direction ($\tilde{E_s}$).
Ψ and Δ can therefore be used to investigate various optical properties of the sample surface. By using a model which includes known parameters of the incident light beam such as polarisation state, angle of incidence and wavelength, and some unknown physical quantities, the generated data can be fitted. This way of solving the inverse problem of modeling, the measured data gives rise to an estimate of physical values of the sample. In order to find a set of optimised modeling parameters, the fit parameters are varied and adjusted to the measured data. Consequently, a best-fit model can be evaluated, whose

parameters have to be unique, physically reasonable and not strongly correlated.
This method is mainly limited by the length scale of the probe, namely the wavelength of incident light. The sample should be uniform and flat within the measured spot, and the surface roughness should be less than 10% of the probe beam wavelength to avoid specular scattering and depolarisation of the reflected light.

3.2.3 Scanning Electron Microscopy

A Scanning Electron Microscope (SEM) scans a focussed energetic electron beam over the sample surface in a raster pattern. The electron beam loses energy within the sample, producing different emissive signals from the material, e.g. secondary electrons (SE), back-scattered electrons (BSE), characteristic X-rays and cathodoluminescence (CL). The secondary electrons have a low energy (1-3 eV) and consequently are only detected from the near surface, giving high-resolution information on the topology of the sample. Conversely, scattering of the primary electrons by the material's atomic nuclei leads to high-energy back-scattered electrons, detected from depths up to the primary electron range (see fig. 3.3). The contrast in the resulting image reveals the compositional information of the material due to differences in the average atomic number. Induced X-rays arising from the ionisation of core shell electrons provide information on the identity and concentrations of elements within the sample (cf. fig. 3.3).

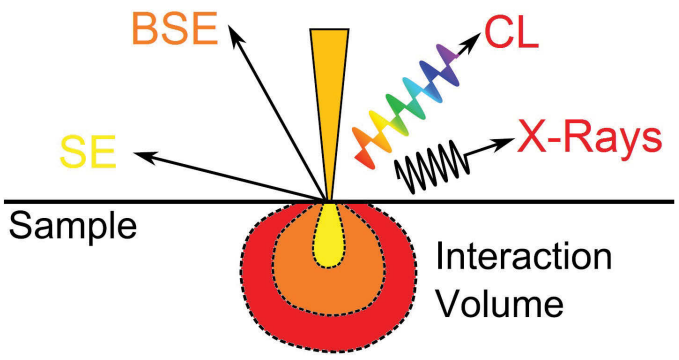

Fig. 3.3: Penetration depth of the primary electron beam indicating the induced processes within the sample.
This figure is adapted from [162].

In this work, a Field Emission Scanning Electron Microscope (Zeiss Supra 55VP) was used to investigate the morphology of the ZnO and Au nanostructures. The instrument has a resolution of 1.0 nm at 15 kV using a high efficiency in-lens detector.

3.2.4 Cathodoluminescence Spectroscopy

Cathodoluminescence (CL) spectroscopy is a non-destructive technique that allows for the investigation of the optical and electronic properties of matter.
A focussed electron beam injects electron-hole pairs in the semiconducting sample by exciting valence band electrons into the conduction band, leaving holes behind. After the thermalisation of electrons and holes to the band edges, they can radiatively recombine, producing CL emission. The resulting CL spectrum carries optical information on the band gap, impurities, dopants, point defects as well as the extended defects in the sample. This is particularly useful for wide band gap semiconductors, where optical excitation is challenging and restricted to the near surface region of the sample.
Furthermore, using electron beam excitation, rather than photons, allows for sub-50 nm high spatial resolution, well below that of the diffraction limit of light. The CL spatial resolution is strongly dependent on the interaction volume and spot size of the electron beam, the carrier recombination length and the sample composition. The simulation of the electron beam with a semiconducting sample will be discussed in section 3.2.4.2.

In this work, CL spectroscopy was carried out using an FEI Quanta 200 ESEM, which has a spatial resolution of 1.0 nm at 30 kV and 3.0 nm at 3 kV.
As depicted in fig. 3.4, the electron beam passes through a small hole in the top of a parabolic mirror positioned above the sample, inducing CL. The emitted light is collected by the parabolic mirror which guides it to the detector via optical fibres. A range of different detectors were available. Two Ocean Optics spectrometers (QE6500 and QEPro) covering a wide spectral range; 200 nm to 1100 nm with a spectral resolution of 5 nm for the QE6500, and 350 nm to 1100 nm with a spectral resolution down to 1.6 nm, depending on the slit size, for the QEPro, each consisting of a 1024×54 active pixel area. For high resolution CL, a Hamamatsu S7011-1007 CCD sensor in a Hamamatsu C7021 detector head with an active area of 1044×124 pixels was used. The dispersion of the collected light is achieved with an Oriel MS 257 $\frac{1}{4}$ m monochromator equipped with a 1200 lines/mm grating. A spectral resolution of 0.1 nm over a range of 53 nm can be achieved.
CL spectra at low temperatures were collected by using two different cooling stages. A Gatan C1002 liquid nitrogen cold stage allows the sample to be cooled down to a temperature of 80 K, while the Gatan CF302 continuous flow liquid helium cold stage reaches temperatures down to 5 K. Furthermore, a home-built hot stage allows to heat the sample to up to 600 K.
The different CL techniques, used in this work, will be shown in the following sections (section 3.2.5).

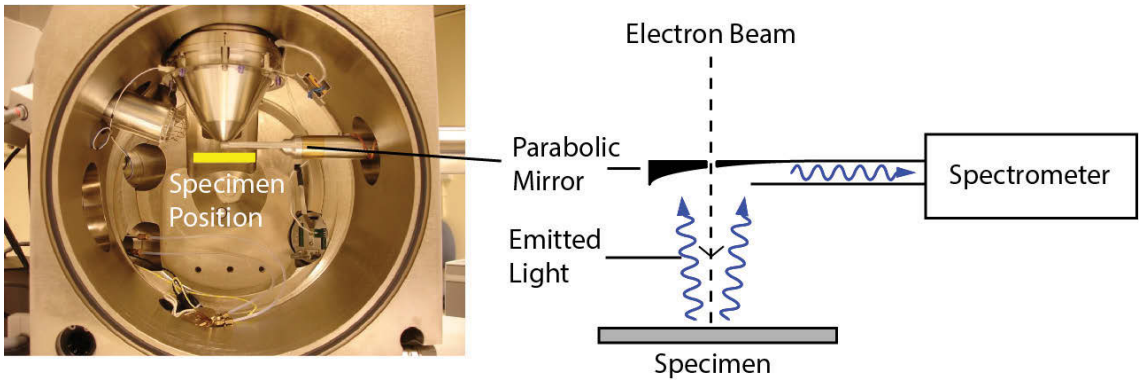

Fig. 3.4: Picture of the SEM chamber (left) and schematic of the CL set-up (right).

3.2.4.1 CL System Correction

All CL spectra were corrected for the total response of the collection system, using an Oriel 63358 45 W QTH calibrated lamp. The intensity-corrected spectra were obtained by using the following equation:

$$\text{corrected spectrum} = \text{measured spectrum} \times \text{correction curve}. \tag{3.4}$$

The wavelength correction for high resolution CL spectra was obtained by measuring the atomic spectral lines of a mercury lamp. The calibrated wavelength is subsequently converted from nm to eV by using the equation:

$$E_{\text{photon}}(\text{eV}) = \frac{1239.841856}{\lambda(\text{nm})}. \tag{3.5}$$

CL intensities are converted to energy space, using the following equation:

$$I(\text{eV}) = \lambda^2 I(\text{nm}). \tag{3.6}$$

The fitting software *Peak-o-mat* was used to analyse the peak positions and shapes of the calibrated CL spectra (see latest version: http://lorentz.sourceforge.net/).

3.2.4.2 CL Modeling via CASINO Simulations

The electron-hole pair distribution before and after generation, can be modeled for specific excitation voltages and spot diameters, allowing prediction of the penetration range of electrons depending on the acceleration voltage [163]. CASINO (Monte **CA**rlo **SI**mulation of electro**N** trajectory in s**O**lids) simulations apply a single scattering Monte Carlo

simulation specifically developed for low energy electron beam interactions, which allows for the approximation of the maximum range (R_e) of the injected electrons.
Figure 3.5a shows a CASINO simulation of ZnO at an acceleration voltage of 5 kV. The blue lines represent the primary electrons scattered within the sample, while the red lines indicate the backscattered electrons. The corresponding energy lost within the samples is shown in fig. 3.5b.
In fig. 3.6, the CL generation as a function of depths and radius at a fixed acceleration voltage of 5 kV is depicted.

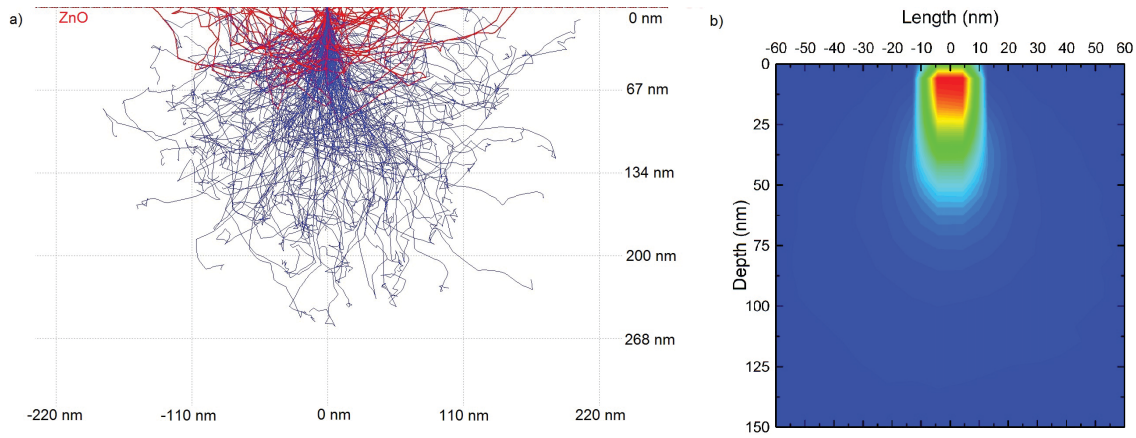

Fig. 3.5: CASINO simulation of ZnO at $HV = 5$ kV, showing (a) the trajectories of the primary (blue) and backscattered electrons (red) as they scatter within the sample, and (b) the energy loss.

The simulated CL generation depths into ZnO at various acceleration voltages with a fixed area are shown in fig. 3.7. The intensity of the CL emission is proportional to the

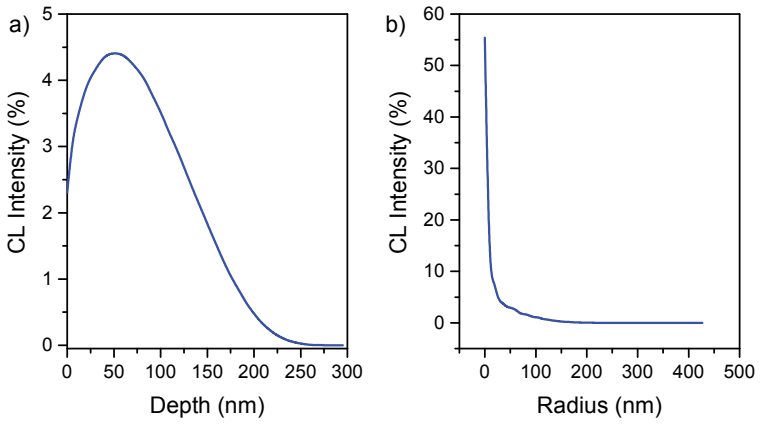

Fig. 3.6: 5 kV-CASINO simulation of ZnO, showing the CL generation as a function of (a) depths and (b) radius.

number of free carriers generated by the primary electrons of the electron beam, which can be estimated by the energy loss profiles, as simulated from CASINO [164]. Thus, the

interaction volume can be used to estimate the CL generation depth, depending on the acceleration voltage of the electron beam.

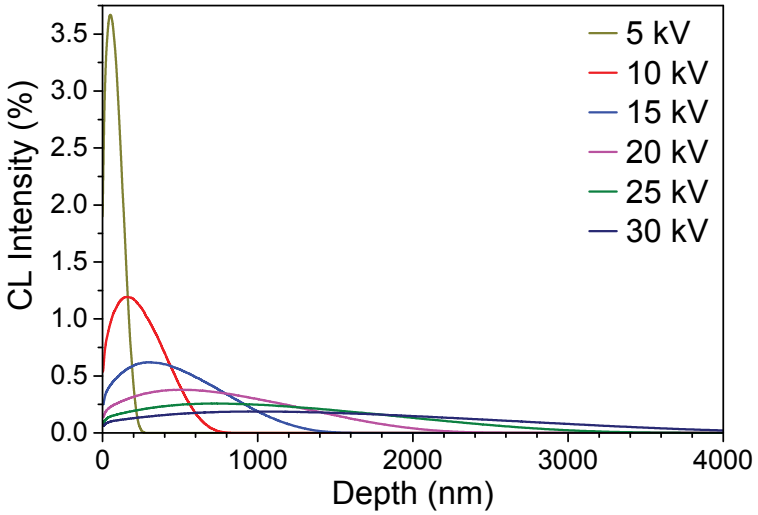

Fig. 3.7: CASINO simulations of CL depths into ZnO at acceleration voltages HV = 5 kV to 30 kV.

Here, the number of free electrons (N_{P}) created by the primary electrons (n_{e}) can be calculated:

$$N_{\mathrm{P}}(n_{\mathrm{e}}) = n_{\mathrm{e}}(1-\eta)\frac{E_{\mathrm{B}}}{E_{\mathrm{f}}}. \tag{3.7}$$

Where E_{f} is the average formation energy, which is required to generate an electron-hole pair, defined as:

$$E_{\mathrm{f}} = 2.8E_{\mathrm{g}} + E' \tag{3.8}$$

with E_{g} being the band gap energy and $0.5 < E' < 1.0$ eV. E_{B} is the energy of the primary electron beam, while η is the backscatter coefficient, accounting for the energy loss through electron back scattering.

For ZnO ($E_{\mathrm{g}} = 3.37$ eV), one 5 kV-electron generates approximately 350 electron-hole pairs, using $\eta = 0.26$ from CASINO simulations. This can be compared with the laser excitation, where a single photon can at best produce one electron-hole pair.

For low energy electron beam excitation, the diffusion length of free carriers has to be taken into account, as they have a certain lifetime before they recombine. This can increase the CL generation depth and width significantly. The diffusion length L is determined by the minority charge carriers and can be calculated by:

$$L = \sqrt{D\tau} = \sqrt{\frac{k_{\mathrm{B}}T}{m_e}\mu(T)\tau}. \tag{3.9}$$

Where D is the diffusion coefficient, τ the lifetime, m_e the electron mass and $\mu(T)$ the mobility of the free carriers, which is dependent on the temperature T (Kelvin). The diffusion length is independent of the excitation voltage, which is why it only affects CL spatial resolution at low acceleration voltages — when the interaction volume is smaller than the diffusion length. If L is known, CASINO allows simulation of in-depth and in-plane energy loss post diffusion.

3.2.5 CL Techniques

The samples can be comprehensively characterised by different CL techniques, such as depth-resolved, temperature-dependent and power-resolved CL. The measurement techniques used in this work, will be discussed in the following sections.

3.2.5.1 Depth-Resolved CL Spectroscopy

Depth-resolved CL spectroscopy can provide non-destructive information on the optical properties at different distances from the sample's surface by varying the electron beam energy. Since the number of electron-hole pairs generated in the sample is proportional to the electron beam power (cf. eq. (3.7)), the CL generation depth can be varied by changing the beam energy. The electron-hole generation rate can be fixed by adjusting the beam current to keep the excitation power constant:

$$P = I_{\mathrm{B}} E_{\mathrm{B}}. \tag{3.10}$$

Where I_{B} and E_{B} are the current and the acceleration voltage of the electron beam, respectively. This technique is specifically used to study the defect-related emissions of the surface as well as the bulk of the sample.
For higher electron beam energies, the higher-energy tail of the band-edge emission can be re-absorbed by the sample itself. The self-absorption results in a red-shifted luminescence, whose light intensity can be described by the Beer-Lambert relation:

$$I(\lambda) = I_0 \exp\left(-\alpha(\lambda) d\right). \tag{3.11}$$

Here, d the photon generation depth and α the wavelength-dependent absorption coefficient of the sample material, which is greater for higher energies closer to the materials band edge, results in a red-shifted luminescence. As described above (cf. section 3.2.4.2), the CL generation depths can be modeled by CASINO simulations. [165]

3.2.5.2 Power-Resolved CL Spectroscopy

Varying the electron beam current over a few orders of magnitude at a constant acceleration voltage allows for the investigation of the power-dependent behaviour of the sample's emissions. Therefore, power-resolved CL spectroscopy can give insight into the saturation effects of electronic states.
The change of emission intensity with I_B can be expressed by the power law:

$$I_{CL}(P) = AI_B^n. \tag{3.12}$$

Where I_{CL} is the emission intensity, A a constant and n is a power-law exponent. A and n can be determined from the CL data, by drawing a linear fit of $\log(I_{CL})$ versus $\log(I_B)$ graph [166]:

$$\log(I_{CL}) = \log(A) + n\log(I_B). \tag{3.13}$$

[166] A power-law exponent with $n = 1$ is typical for excitonic emission with a short lifetime (ps), while sublinear, $n < 1$, is characteristic of strongly lattice coupled defects with slow recombination lifetimes of µs to ms. Super-linear saturation rates, $n > 1$, are mainly observed for stimulated emission, such as lasing and can also arise from the saturation of competitive non-radiative recombination channels.

3.2.5.3 Temperature-Dependent CL Spectroscopy

As mentioned above, the sample can be cooled down to as low as 5 K, using a liquid helium stage, and heated up to 600 K with a home-built hot stage, which allows for temperature-dependent CL spectroscopy. This gives the possibility to study the temperature-dependent nature of the defects and of the excitonic behaviour.
In general, with increasing temperature, a broadening of the CL emission peaks can be observed due to an increased phonon interaction in the recombination transition. Furthermore, the average atomic spacing and electron-phonon scattering effect increases as the temperature rises, resulting in a narrowing of the band gap and a corresponding redshift of the position of the NBE emission peaks, FX and DBX [167].
The DBX dominates the NBE-spectrum of ZnO at 5 K due to their high capture cross-sections and quenches at higher temperature, as the excitons thermally dissociate from donors and acceptors. As the DBX and FX are competitive radiative recombination channels, the FX emissions become more intense with increasing temperatures towards 100 K and above. Additionally, non-radiative recombination pathways due to defects also activate at elevated temperature, quenching the luminescence signal.
The activation energy of these recombination channels can be calculated by using the

Arrhenius equation:

$$I(T) = I_0\Big[1 + A\exp\Big(\frac{E_\mathrm{A}}{k_\mathrm{B}T}\Big)\Big]^{-1}. \tag{3.14}$$

Where A is a constant and E_A the activation energy of the recombination channel.

3.2.6 Photoluminescence Spectroscopy

Photoluminescence (PL) spectroscopy is a non-destructive and surface-sensitive technique that can be used to investigate the optical and electronic properties of semi-conductive materials.

PL is the spontaneous emission of photons in a semiconductor induced by a focussed laser (photoexcitation), typically with an energy higher than the energy band gap of the investigated material ($E_\mathrm{exc} > E_\mathrm{g}$). In this case, electrons from the valence band can absorb the incoming light, which are subsequently excited to the conduction band, leaving holes behind. The excited electrons in the conduction band recombine spontaneously with the holes in lower energy states, emitting photons of energy equal to the difference in energy between those levels. The nature of the the PL signal can be either excitonic or defect-related, identical to the CL recombination pathways, shown in fig. 2.4. The created electron-hole pairs can recombine through various radiative or non-radiative recombination paths. The PL excitation spectra at a specific emission energy provide detailed information on electronic energy levels, binding energies and chemical origin of the defects of the near-surface layers of the sample.

In comparison to CL spectroscopy, excitation with laser light can at best generate one electron-hole pair per photon, while one energetic electron can create 10^2-10^3 electron-hole pairs, depending on the energy of the electron beam (cf. eq. (3.7)).

Furthermore, the penetration depth of the laser light is fixed by the excitation wavelength and the absorption coefficient (α) of the investigated material, as shown in the Beer-Lambert equation (eq. (3.11)). α is typically large for above band gap excitation, which makes this a near-surface probing technique. Therefore, the excitation density in PL and CL can be significantly different.

In the case of ZnO, the laser excitation density can be calculated, using the Beer-Lambert equation stated above (eq. (3.11)), with $\lambda_\mathrm{exc} = 325\,\mathrm{nm}$, $I_0 = 1 - R$, where $R = 0.06936$ is the reflectivity of ZnO, and $\alpha = 0.0165\,\mathrm{nm}^{-1}$ the extinction coefficient[168, 169]:

$$I(\lambda_\mathrm{exc}) = (1 - R)\exp\left(-\alpha(\lambda_\mathrm{exc})d\right). \tag{3.15}$$

As the CL mirror is used to focus the laser light and collect the excited PL (cf. section 3.2.6.1), the effective circular collection area of the mirror can be used to determine the laser spot size, see fig. 3.8. The laser penetration depth at which 80% of the excitation energy is lost in ZnO is determined to be $d = 110\,\mathrm{nm}$.

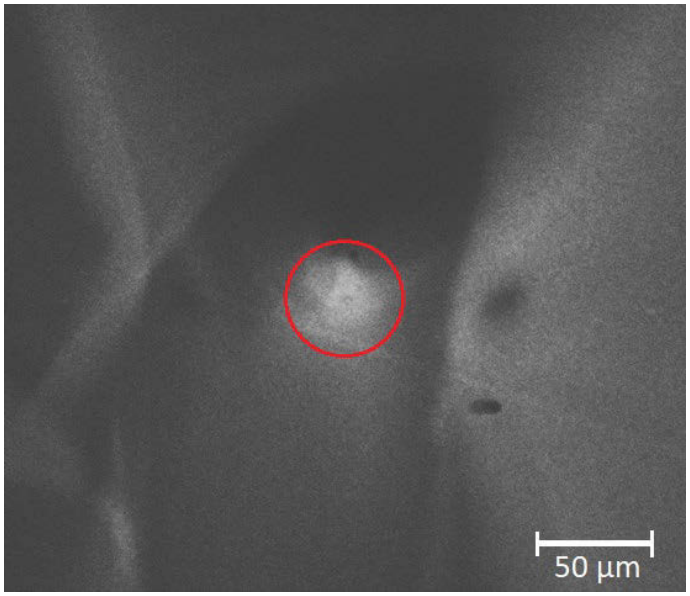

Fig. 3.8: Panchromatic CL image, showing the CL collection area through the mirror aperture with an approximate spot of 30 µm.

Using a typical laser power of 1 mW and the corresponding photon energy of $E_{\text{photon}} = 6.1 \times 10^{-19}$ J/photon, the number of photons per second can be calculated:

$$N_{\text{PL}} = \frac{hc}{\lambda} E_{\text{photon}} = 1.63 \times 10^{15} s^{-1}. \tag{3.16}$$

With the volume, determined as followed using the laser spot radius of $r = 15\,\mu\text{m}$, the electron-hole-pair generation per second per volume $N_{\text{eh, PL}}$ can be calculated.

$$V = \pi r^2 I(80\%) = 7.77 \times 10^{10} \text{nm}^3. \tag{3.17}$$

$$N_{\text{eh, PL}} = N_{\text{PL}}/V = 2.10 \times 10^{4} \text{nm}^{-3} s^{-1}. \tag{3.18}$$

Note that the number of generated electron-hole-pairs was calculated, assuming that each incoming photon creates one electron-hole-pair, and consequently provides the maximum value for $N_{\text{eh, PL}}$. In reality, this number can be lower due to scattering and absorption effects.

$N_{\text{eh, PL}}$ is substantially different to the number electron-hole-pair generated by the electron beam, $N_{\text{eh, CL}}$. For an acceleration voltage of 5 kV, the CL and PL probing depths are commensurate. The CASINO simulations of the in-depth and in-plane energy loss profiles at 5 kV provide a depth of 88 nm and a radius of 35 nm, respectively, for 80% energy loss.

As per section 3.2.4.2 with the electron-hole-pair formation energy in ZnO of 10.6 eV and

the backscatter coefficient $\eta = 0.26$ allows the calculation of the number of electron-hole-pairs per second: $N_{\mathrm{CL}} = 7.63 \times 10^{12} s^{-1}$ for a typical I_{B} of 3.5 nA. The corresponding cylindrical energy loss volume is calculated, using the radius of 35 nm and the depth of $z = 88\,\mathrm{nm}$:

$$V = \pi r^2 z = 3.4 \times 10^5 \mathrm{nm}^3. \tag{3.19}$$

Similarly to eq. (3.18), the electron-hole-pair generation per second per volume can be subsequently determined:

$$N_{\mathrm{eh,\,CL}} = N_{\mathrm{CL}}/V = 2.25 \times 10^7 \mathrm{nm}^{-3} s^{-1}. \tag{3.20}$$

It is also important to note that the PL maximum energy os always at the the sample's surface and conversely, the CL maximum energy loss is at a depth of $\sim \frac{R_{\mathrm{e}}}{3}$ (see fig. 3.6). It can be seen that $N_{\mathrm{eh,\,CL}}$ is approximately four orders of magnitude larger than that with the laser excitation. However, the CL generation depth — at an acceleration voltage of 5 kV — is very similar to the probing depth of the HeCd-laser, which allows for comparison between CL and PL.
Neutral-density (ND) filters allow for attenuation of the laser power for power-dependent PL measurements and to set electron-hole-pair injection density similar to those excited with CL.
Furthermore, sub-bandgap laser excitation allows probing the defect-related emissions through the entire film thickness without exciting bandgap emissions, which is impossible with electron excitation.
In addition, polarisation effects can be studied with laser excitation, which is very difficult to realise for CL. Non-conductive or poorly electrically conductive samples can be investigated with laser illumination, without strong charging effects that can occur with electron beam excitation.
Thus, PL and CL spectroscopy are highly complementary tools used to investigate the samples in this work.

3.2.6.1 Combined CL and PL Spectroscopy

To investigate the difference between electron beam and laser excitation, a light injection setup was designed for this project and attached to the existing CL system (see fig. 3.10). This allows collection of CL or PL from spatially-equivalent regions of the sample, excited by the electron beam or the laser separately, or simultaneous excitation. Three different excitation laser wavelengths were accessible, allowing excitation of ZnO above and sub-bandgap. A schematic is shown in fig. 3.9.
A HeCd laser from Melles Griot allows direct switching between two different wavelengths: 325 nm ($P = 42\,\mathrm{mW}$) and 442 nm ($P = 110\,\mathrm{mW}$) or a combined output of

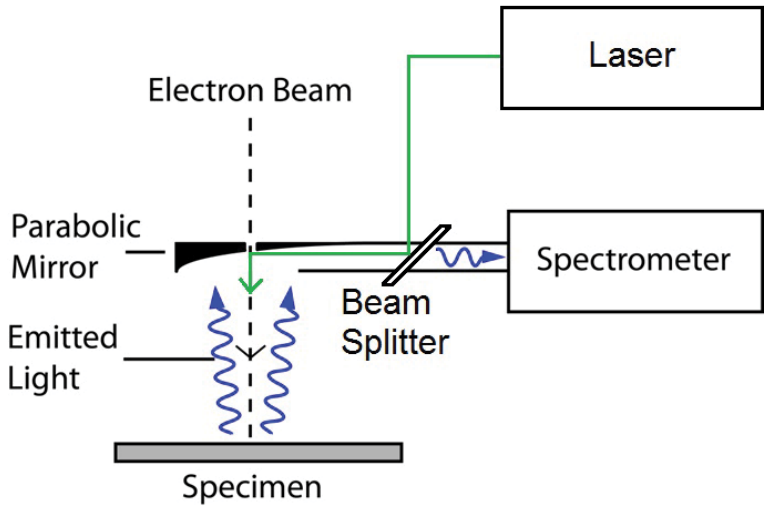

Fig. 3.9: Schematic of light injection into CL chamber.

$P = 152\,\mathrm{mW}$. A LambdaPro laser with a power output of $P = 20\,\mathrm{mW}$ at a wavelength of $\lambda = 532\,\mathrm{nm}$ was used for sub-bandgap excitation of ZnO and direct excitation of Localised Surface Plasmons in Au.

Figure 3.10 shows the experimental setup of the light injection. The UV light coming from the laser is coupled into a 100-µm multimode fibre, allowing to compensate the height offset between the laser and the SEM chamber. UV-specific mirrors and a dichroic beam splitter are used to guide the laser beam into the SEM chamber, where it is focussed onto the sample by the parabolic mirror, which also collects the PL emission. The laser-illuminated area of the sample can be excited by the electron beam, which allows for concurrent PL and CL spectroscopy.

The PL is transmitted by the dichroic beam splitter if it is above 336 nm (reflection band from 300 nm to 325 nm with $R_{\mathrm{abs}} > 94\%$; $T_{\mathrm{avg}} > 90\%$ for the range 336 nm to 1200 nm) to ensure collection only of the luminescence coming from the sample. Subsequently, the spectrum is collected via an optical fibre connected to one of the spectrometers.

Similarly, the blue and the green laser ($\lambda_{\mathrm{exc}} = 442\,\mathrm{nm}$ and $\lambda_{\mathrm{exc}} = 532\,\mathrm{nm}$, respectively) are focussed onto the sample allowing sub-band gap excitation of ZnO. A different optical path allows the use of appropriate mirrors and a notch dichroic beam splitter blocking the transmitted light of the excitation wavelength only (reflection band from 439 nm to 457.9 nm with $R_{\mathrm{abs}} > 94\%$, $T_{\mathrm{avg}} > 93\%$ for the blue laser and for the green laser: 507.5 nm to 570 nm with $R_{\mathrm{abs}} > 98\%$; $T_{\mathrm{avg}} > 90\%$). The luminescence is subsequently collected and detected via the aforementioned spectrometers (cf. section 3.2.4).

Furthermore, the use of a set of neutral density filters allows to adjust the laser power for power-dependent PL measurements.

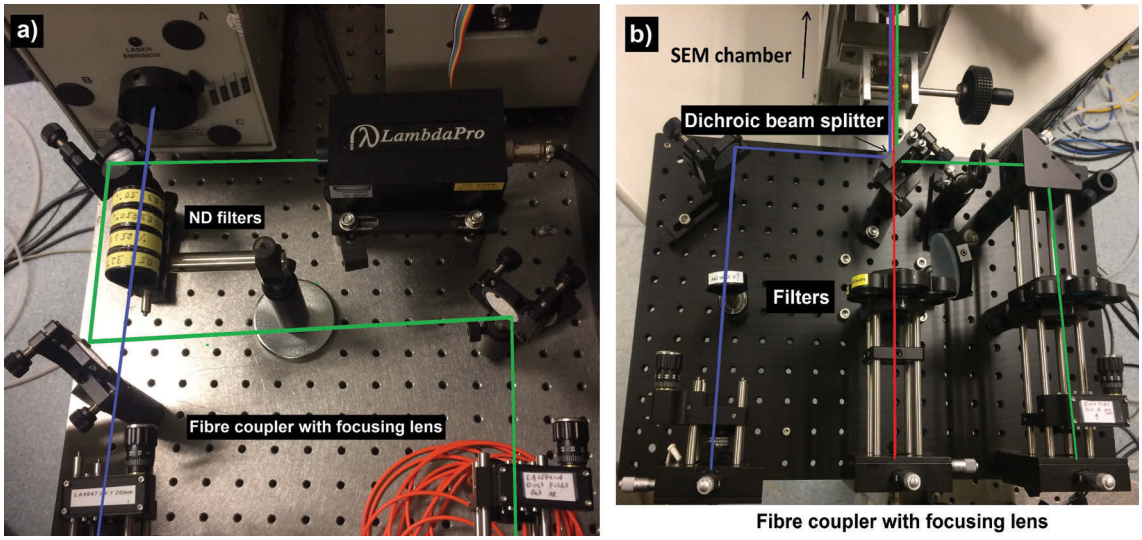

Fig. 3.10: Light injection for PL setup, allowing selection of three different excitation wavelengths. The blue line indicates the light path of the 325 nm laser, while the green line shows light paths of the 532 nm laser and the 442 nm. The red line indicates the collection of the resulting luminescence through attached optical fibres.

3.2.7 Time-Resolved PL Spectroscopy

Time-resolved PL (TR-PL) is a surface-sensitive, contact-less technique to study the charge carrier dynamics in a semiconductor.

Contrary to the steady-state PL, where the PL signal is integrated over time, TR-PL allows to measure the lifetimes of the minority charge carriers in the sample which is typically in the range of ps to ns. To achieve measurements of PL intensity decay as a function of such short times, pulsed laser excitation is required. After the excitation pulse, the PL is measured as a function of time.

The TR-PL spectroscopy was performed at Technische Universität Berlin, Germany.

There, a pulsed fibre laser is used for excitation, with a fundamental wavelength of $\lambda = 1031\,\mathrm{nm}$ which is internally halved ($\lambda = 515.5\,\mathrm{nm}$) and subsequently frequency-doubled to $\lambda_{\mathrm{exc}} = 258\,\mathrm{nm}$. The laser has a pulse repetition rate of 76 MHz and a pulse duration of approximately 5.5 ps. The luminescence decay was recorded by a standard photon counting technique, using a Becker & Hickl SPC-130 photon counting card. The temporal resolution was ~ 30 ps which can be further improved by deconvolution techniques [170].

The experimental set-up is shown in fig. 3.11.

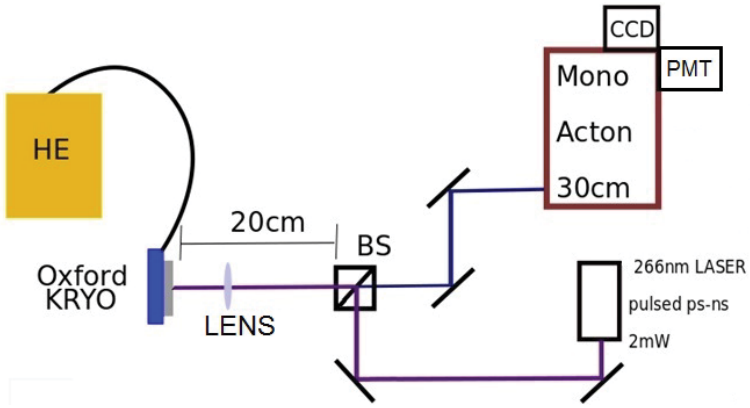

Fig. 3.11: Schematic of the time-resolved PL set-up, showing the principle light path.

3.2.8 X-Ray Photoelectron Spectroscopy

X-ray photoelectron spectroscopy is a surface-sensitive technique to investigate the chemical identity and element concentrations in a sample by irradiation with monochromatic X-ray photons. The resulting emission of electrons from the sample can be analysed by using the following equation:

$$E_{\mathrm{b}} = \hbar\omega - E_{\mathrm{kin}} - \phi_d. \tag{3.21}$$

The quantity E_{b} is the binding energy of the elements in the sample, E_{kin} the energy of the emitted electrons, $\hbar\omega$ the energy of the X-ray photon and ϕ_d the work function of the detector.
A typical laboratory setup utilises aluminum or magnesium targets as X-ray sources with energies, 1486.6 eV ($\mathrm{Al}K_\alpha$) and 1253.6 eV ($\mathrm{Mg}K_\alpha$), respectively.
In this work, the XPS data of the Au-coated ZnO samples were taken at the Soft X-Ray Spectroscopy beam line at the Australian Synchrotron, Victoria, Australia. At the Synchrotron, high speed electrons (99.9997% of the speed of light) are deflected by a magnetic field resulting in electromagnetic radiation known as the synchrotron light. This radiation is highly polarised and has a wide energy spectrum from infrared light to hard X-rays. Using soft X-rays provides the possibility to fine-tune the appropriate energy of those X-ray photons between 90 eV to 2500 eV. Even though the X-ray photons penetrate 1 µm to 10 µm into the material, the electron mean free path is only of the order of tens of Angstrom due to a high electron-matter interaction (escape depth for ZnO ∼1.8 nm), making XPS a surface characterisation technique.
The Al-coated ZnO samples were analysed with a laboratory XPS setup at the University of New South Wales, Australia.

3.2.9 Finite-Difference Time-Domain Simulation Method for Modeling of Plasmonic Structures

The Finite-Difference Time-Domain (FDTD) method is a numerical analysis technique which can model a wide variety of electrodynamic problems by solving Maxwell's Equations (see eq. (2.14)).
It approximates the derivatives in the Maxwell's curl equations by finite differences, which allows for a second-order accuracy. Here, the electric and magnetic fields are discretised in both, space and time, so that a non-uniform rectilinear mesh (voxel) is formed. In 1966, Kane Yee [171] reported on this numerical method, using spatial and temporal staggering of the discretised electric and magnetic fields. This allows to solve the resulting differential equations and obtain "updated equations", which reflect future fields in terms of past fields. A time-stepping scheme, the so-called leap-frog algorithm, was used for marching in time. In this case, the repetitive evaluation of the individual electric and magnetic fields one step into the future allows the slow build up of continuous electromagnetic waves in space and time, propagating in the aforementioned numerical mesh over the desired duration.
Since FDTD is a time domain method, a wide range of frequencies can be covered by a single simulation, as Fourier techniques can be used to convert from the time into the frequency domain. Furthermore, models can be evaluated, as the electric and magnetic fields are calculated in the computational domain, allowing for the display of the electromagnetic field movement through the model.
On the other hand, a fine spatial grid must be created in the computational domain to resolve the smallest geometrical features in the model as well as the smallest electromagnetic wavelength, which can result in long computational times. In this work, the software package *Lumerical* was used.

4 Characterisation of Gold Nanoparticle-Coated ZnO

In this chapter, the results of a comprehensive characterisation study of planar *a*-plane ZnO single crystals and hydrothermally grown ZnO nanorods coated with Au nanoparticles will be shown. Their morphology will be discussed, as well as the optical properties of the uncoated and Au nanoparticle-coated planar and nanostructured ZnO. Here, the Au was directly deposited onto the ZnO, resulting in a large enhancement of the excitonic UV emission. These optical data provide new understanding of the coupling mechanism between ZnO and Au nanoparticle surface coating. Furthermore, the work presented in this chapter will address the discrepancy in the literature.

4.1 Morphology of the ZnO Nanorods and the Au Coating

The morphology of the hydrothermally grown ZnO nanorods, synthesisedusing the protocol described in section 3.1.1, was determined by SEM. In fig. 4.1a, a typical SEM image of as-grown nanorods is depicted, showing a continuous and dense film of hexagonal ZnO nanorods. They are randomly oriented at different angles to the direction of the substrate, with an average diameter of (40 ± 10) nm and an approximate length of 700 nm.

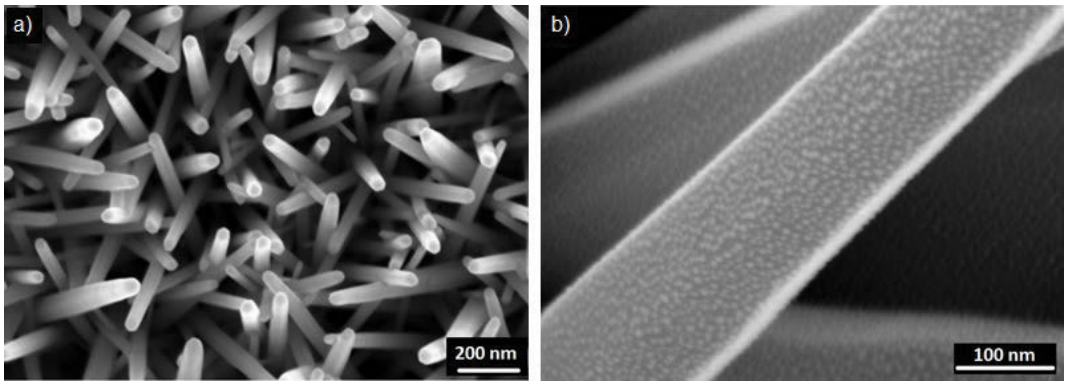

Fig. 4.1: SE image of (a) as-grown hexagonal ZnO nanorods with an approximate diameter of 40 nm and length of 700 nm, (b) ZnO nanorod decorated with uniform 5 nm Au nanoparticle film. $HV = 10$ kV.

Note that for all optical characterisation techniques, such as CL and PL spectroscopy, the

area of interest on each side of the sample — with and without metal coating — was carefully chosen to ensure the same morphology of the ZnO nanorods. This allows for direct spectral comparison between the uncoated and metal nanoparticle-coated side of the ZnO nanorod-samples.

A SEM image of the Au nanoparticle-coating is presented in fig. 4.1b, showing a single nanorod decorated with uniformly-distributed and well-separated Au nanoparticles of an average diameter of 5 nm. This is comparable with the results of Au deposition onto Si substrates, shown in fig. 4.2a, indicating that the sputter-coating and annealing process is reproducible regardless of the type of the substrate. Here, increasing the nominal Au thickness from 1 nm to 6 nm not only increased the size of the Au nanoparticles, but also changed the shape from spherical to more faceted with elongated shapes, see fig. 4.2b-d. It can be seen that the annealing of the 1 nm thin Au film results in a uniform Au nanoparticle-coating, while thicker deposited layers of Au show a larger distribution of sizes and shapes; at 6 nm most of the nanoparticles merge to form larger, irregularly shaped particles. To achieve a narrow Localised Surface Plasmon resonance (LSPR) from Au nanoparticles, a film of uniformly distributed and well separated nanoparticles is desirable. Furthermore, a smaller size of the Au nanoparticles results in a LSPR closer to the excitonic UV emission of ZnO, which will be shown in section 4.3.

In this work, the CL and PL studies focus on ZnO coated with an annealed 1 nm thin Au film, resulting in round Au nanoparticles with a diameter of 5 nm. Note that the ZnO

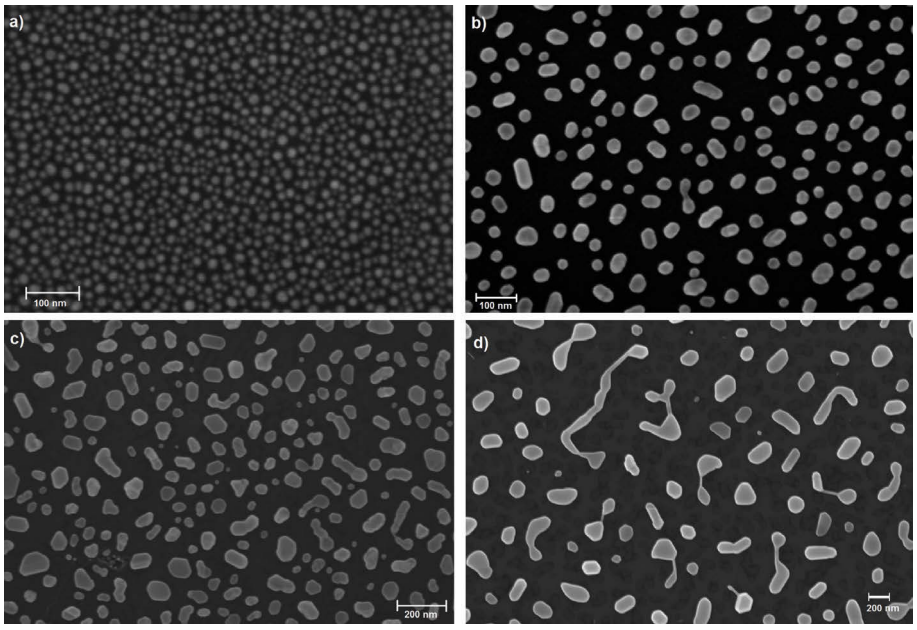

Fig. 4.2: SE image of Si sputter-coated with increasing nominal thicknesses of Au from (a) 1 nm, (b) 2 nm, (c) 4 nm and (d) 6 nm, leading to increased Au nanoparticle sizes and different shapes after annealing.

nanorod samples are only half coated with Au nanoparticles, leaving the other uncoated side as an internal reference. The *a*-plane ZnO single crystal samples were similarly half-coated with Au, with the Au NPs exhibiting the same morphology as on Si and ZnO nanorods.

4.2 Valence Band X-Ray Photoemission Spectroscopy of ZnO Nanorods Coated with Au Nanoparticles

As described in section 3.2.8, valence band X-ray photoemission spectroscopy (VB-XPS) of the uncoated and the Au nanoparticle-coated ZnO nanorods was performed at the Australian Synchrotron, allowing for the determination of the surface band bending.

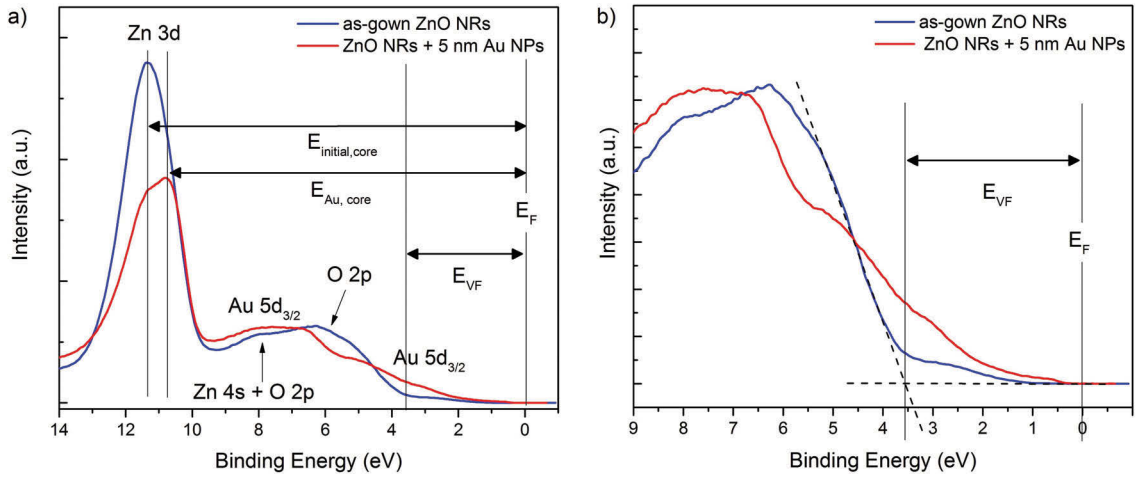

Fig. 4.3: (a) Valence band XPS spectra of uncoated (blue) and Au nanoparticle-coated ZnO nanorods (red), and (b) close-up of the valence band.

The VB-XPS spectra are presented in fig. 4.3a, consisting of the Zn $3d$ peak at ~ 11 eV and two peaks in the near-band edge near the valence band maximum, which are centered at 7 eV and 5 eV, attributed to hybridised Zn $4s$-O $2p$ and O $2p$ states, respectively [172–176]. From the spectrum of the uncoated ZnO nanorods, the surface band bending (V_{BB}) can be calculated using the valence band onset, shown in fig. 4.3b. Here, the intercept of a linear fit of the leading edge of the valence band with the XPS background determines the position of the valence band maximum. The energy difference from this valence band maximum to the Fermi energy at $E = 0$ is labeled as E_{VF}. The surface band bending can be calculated using the following equation:

$$V_{\mathrm{BB}} = E_{\mathrm{g}} - E_{\mathrm{VF}} - E_{\mathrm{CF}}. \tag{4.1}$$

Where E_g is the bandgap energy of ZnO ($E_g = 3.37\,\text{eV}$ at $300\,\text{K}$) and E_{CF} the energy difference between the Fermi level and the conduction band minimum of ZnO, which can be calculated by:

$$E_{CF} = \frac{k_B T}{e} \ln\left[\frac{N_C}{n_e}\right]. \tag{4.2}$$

Here, k_B is the Boltzmann constant and N_C the conduction band effective density of states, which is equal to 2.94×10^{18} cm^{-3} for the effective mass of $m_e^* = 0.24\, m_e$ in ZnO. n_e is the bulk carrier density, which is estimated to $\sim 10^{18}$ cm^{-3} as a typical value in the literature for ZnO nanorods of similar morphology and growth methods, as in this work [55, 56, 177]. Thus, the quantity E_{CF} is estimated to be 0.03 eV.

For the uncoated ZnO nanorods, the surface band bending was calculated to $V_{BB} = -0.20\,\text{V}$, indicating a downward bending. This is typical of adsorbed donor species,

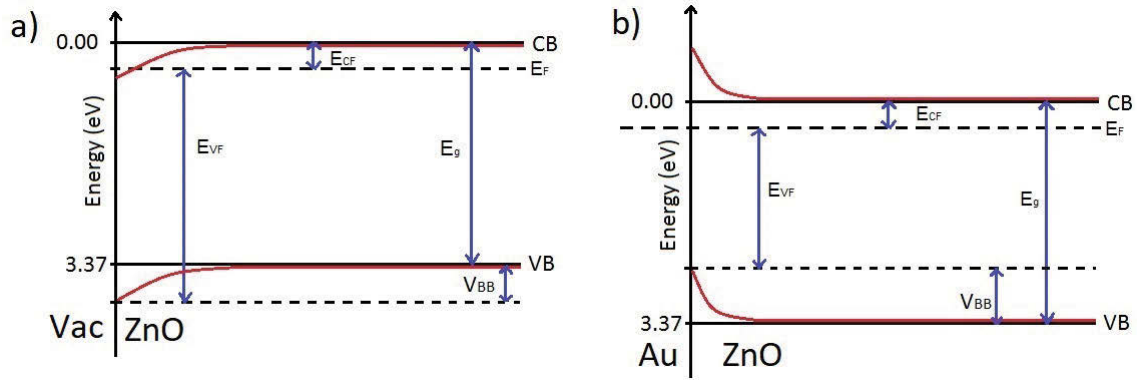

Fig. 4.4: Band diagram of (a) the uncoated ZnO nanorods, showing downward band bending of −0.20 V and (b) the Au nanoparticle-coated ZnO nanorods, showing upward band bending of 0.24 V.

which leads to electron accumulation at the surface of the ZnO nanorods [176–178]. The corresponding band diagram is depicted in fig. 4.4a.

The comparison with the Au nanoparticle-coated ZnO nanorod side of the sample, presented in fig. 4.3a, shows a change in the valence band onset, as well as a shift of the Zn $3d$ peak to lower binding energies. This shifted peak is overlapped with the Zn $3d$ peak of the underlying ZnO, which can be explained by the high surface sensitivity of the technique. In the case of ZnO, the penetration depth of the X-rays is approximately 10 nm, which results in a mixture of binding energies of both the ZnO and the Au surface coating.

Due to the Au $5d$ states close to the Fermi level in the Au-coated ZnO nanorods, the linear fit of the valence band onset cannot be drawn anymore. Alternatively, the shift in the Zn $3d$ peak position, indicated by two vertical lines in fig. 4.3a, can be used to determine the surface band bending. The equation below has been used in the literature by Das et al.

[179, 180].

$$V_{\mathrm{BB}} = E_{\mathrm{g}} - E_{\text{initial VF}} + E_{\text{initial core}} - E_{\text{Au core}} = +0.24V. \tag{4.3}$$

This result indicates an upward band bending of 0.24 V. This effect can be explained by an electron depletion layer at the surface due to electron transfer from ZnO to Au, forming a Schottky barrier at the ZnO-Au interface. The corresponding band diagram is shown in fig. 4.4b. The upward band bending between ZnO and Au is in accordance with the difference in the electron affinity of ZnO (4.7 eV) and the work function of Au (5.1 eV)[31, 181].
Furthermore, the width of the electron depletion layer can be calculated, using the following equation of the full depletion model [182, 183].

$$W = \sqrt{\frac{2\varepsilon_{\mathrm{r}}\varepsilon_0 V_{\mathrm{BB}}}{q n_{\mathrm{e}}}}. \tag{4.4}$$

Where $\varepsilon_0 = 8.85 \times 10^{-14}$ C/Vcm is the vacuum permittivity, $\varepsilon_{\mathrm{r}} = 8.66$ the relative permittivity of ZnO, and $q = 1.6 \times 10^{-19}$ C the electric charge. With the upward band bending of 0.24 V of the Au nanoparticle-coated ZnO nanorods, the width of the depletion layer can be determined to 15 nm, which is already close to the average diameter of the ZnO nanorod of 40 nm. The accumulation layer width of the uncoated ZnO nanorods can be calculated for the downward band bending of −0.20 V to 14 nm. For both, the uncoated and the Au nanoparticle-coated ZnO nanorods, a large electric field at the surface, E_{S}, is a result from the surface band bending.

$$E_{\mathrm{S}} = \frac{q n_{\mathrm{e}} W}{\varepsilon_{\mathrm{r}}\varepsilon_0}. \tag{4.5}$$

For the uncoated ZnO nanorods, an electric field at the surface of 2.9×10^5 V cm^{-1} can be determined, while it is slightly larger for the Au nanoparticle-coated ZnO nanorods with $E_{\mathrm{S}} = 3.1 \times 10^5$ V cm^{-1}. The results for the calculations are listed in table 4.1.

Table 4.1: Electric parameters calculated from the VB-XPS data under the assumption that $n_{\mathrm{e}} \sim 10^{18}$ cm^{-3}.

Sample	V_{BB} (V)	W (nm)	E_{S} (V cm^{-1})
Uncoated ZnO nanorods	−0.20	14	2.9×10^5
Au nanoparticle-coated ZnO nanorods	+0.24	15	3.1×10^5

In summary, the uncoated ZnO nanorods exhibited a downward band bending (−0.20 V) due to adsorbed species at the surface of the ZnO nanorods, such as water-molecules

or OH-groups. The Au nanoparticle-coating on the ZnO nanorods resulted in a upward band bending of 0.24 V, indicating the formation of a Schottky barrier. The depletion layer width was calculated to $\sim$ 15 nm with an electric field at the surface of $3.1 \times 10^5\,\mathrm{V\,cm^{-1}}$.

4.3 Optical Spectroscopy of Gold-Coated ZnO

Transmission spectroscopy can provide insight in the absorption of light over a great range of the electromagnetic spectrum. Transmission spectroscopy was performed to determine the plasmon resonance (LSPR) of the Au nanoparticle-coating.
To perform transmission spectroscopy on the ZnO nanorods, the opaque Si substrate was replaced by transparent quartz glass. The growth was conducted under the same condition as described in section 3.1.1, and resulted in an equivalent ZnO nanorod film. However, the random orientation of the ZnO nanorods with respect to the substrate caused high scattering loss at the air-ZnO nanorod-interface for top-down illumination, leading to inconclusive transmission spectroscopy results. Similarly, reflectance spectroscopy of the ZnO nanorods grown on Si did not give any conclusive results due to the low signal-to-noise ratio.
Therefore, an *a*-plane ZnO single crystal, half coated with Au nanoparticles, was used as a reference sample. The corresponding transmission spectra are presented in fig. 4.5, showing the expected absorption edge in the UV spectral range, representing the near-band edge of ZnO. The Au nanoparticle-coated *a*-plane ZnO single crystal has an additional, broad absorption band centered at $E_{SP} = 2.25\,\mathrm{eV}$, which extends into the UV. This dip is characteristic for the localised plasmon resonance (LSPR) energy of spherical Au nanoparticles with a diameter of 5 nm [184–186], providing evidence for plasmonic effects in this sample. The UV tail is typically attributed to interband transitions of electrons in the occupied $5d$ band in Au to the hybridised $6sp$ band. The energy threshold for these transitions is approximately 2.4 eV with an extension into the UV. The overlap of these interband transitions with the LSPR of the Au nanoparticles are responsible for the characteristic, asymmetric shape of the LSPR absorption.
Conversely, the transmission spectrum of an as-deposited 1 nm thin Au film exhibits a very broad transmission dip around 1.8 eV, as well as a reduction in transmission over the entire measured range. This can be explained by the presence of Au nanoparticles with a wide distribution of sizes and shapes.
These results show that a uniformly distributed 5 nm-Au nanoparticle film is needed to create a sharper plasma absorption band, which can be attributed to the formation of Localised Surface Plasmons.
Since the Au nanoparticle coating shows the same morphology on planar and nanostructured ZnO surfaces, it is expected that the behaviour of optical transmission of the

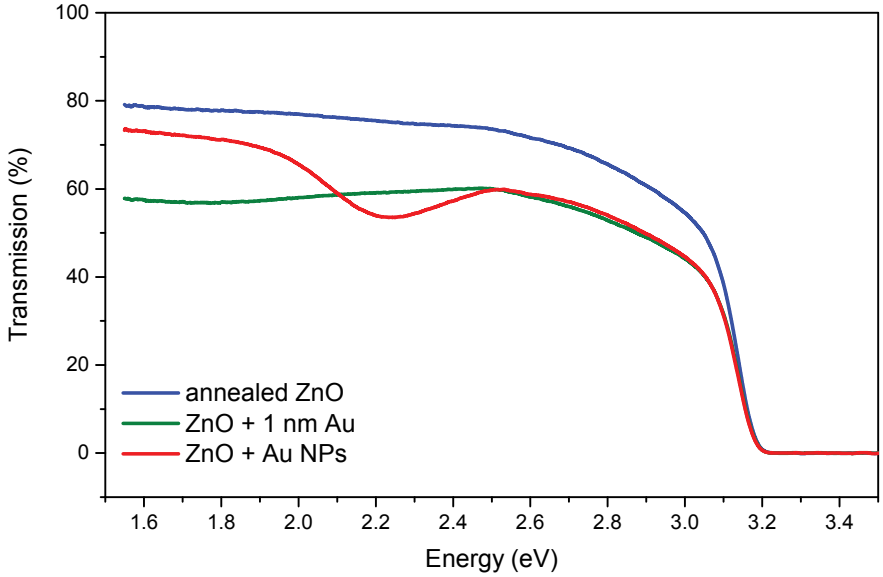

Fig. 4.5: Transmission spectroscopy of uncoated (blue), 1 nm Au thin film-coated (green) and Au nanoparticle-coated (red) *a*-plane ZnO single crystal, showing plasmonic absorption band centered at $E_{\mathrm{LSP}} = 2.25\,\mathrm{eV}$.

Au nanoparticle-coated *a*-plane ZnO single crystal is indicative of the Au nanoparticle-coated ZnO nanorod sample. Thus, the same 5 nm Au nanoparticle plasmon resonance energy of $E_{LSP} = 2.25\,\mathrm{eV}$ is used throughout this work.

4.4 CL and PL Study of Gold-Nanoparticle Coated ZnO Nanorods

The optical properties of uncoated and Au nanoparticle-coated ZnO nanorods were investigated by depth-resolved CL, temperature- and excitation power-dependent PL, as well as a concurrent CL-PL technique and time-resolved PL. Particularly, the resulting UV enhancement due to the presence of the Au nanoparticles was systematically studied to gain more insight in the underlying enhancement mechanism. The results of the uncoated and the Au nanoparticle-coated ZnO nanorods are shown and discussed in this section.

4.4.1 Depth-Resolved CL of Au Nanoparticle-Coated ZnO Nanorods

To investigate the luminescence properties of uncoated ZnO nanorods and the effect of the Au nanoparticle-coating, CL and PL studies were conducted on Au nanoparticle-coated ZnO nanorods. An enhancement of up to 3.8 times of the UV luminescence is demonstrated and its origin comprehensively studied. The two plasmonic coupling mechanisms of ZnO nanorods with Au nanoparticles, mentioned in section 2.5.3, are investigated as well as other possible effects explaining the observed enhancement of the UV emission.

A typical 80 K-CL spectrum of annealed ZnO nanorods is depicted in fig. 4.6. It shows a

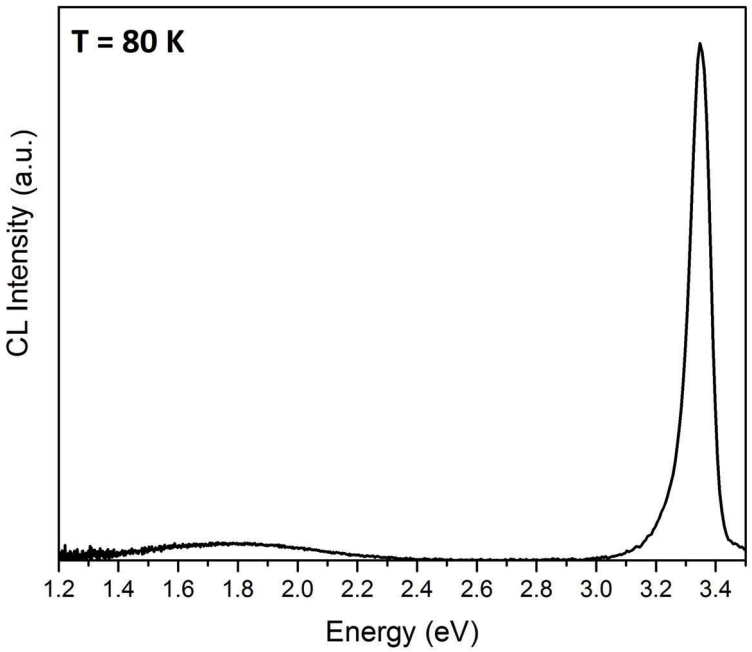

Fig. 4.6: CL spectrum of uncoated ZnO nanorods, showing NBE emission at 3.35 eV and DL emission centered at 1.8 eV.
$T = 80$ K, $HV = 5$ kV, $P = 17.5$ µW, scan area 10 µm $\times$ 10 µm.

relatively sharp peak in the UV spectral region centered at 3.35 eV, assigned to the excitonic emissions of the near-band edge (NBE) of ZnO ($E_g = 3.37$ eV). A broader, comparatively weak defect-related emission in the orange and red part of the visible spectrum, centered at 1.8 eV, can be attributed to the aforementioned deep levels (DL), cf. section 2.2.1. The green luminescence at an energy of 2.45 eV, which is commonly found in ZnO nanostructures and typically ascribed to V_O, is not present in these samples. However, the red and orange emissions (OL and RL) are typically assigned to intrinsic point defects, yet their chemical origin is still under discussion in the literature. In other work, it has been shown that the OL at 1.95 eV and the RL at 1.69 eV from similarly grown ZnO

nanorods can be attributed to native acceptor-like centres involving V_{Zn} and O_{i}, respectively (cf. table 2.2). Therefore, it can be assumed that the present ZnO nanorods are oxygen-rich rather than depleted in oxygen. However, the focus of this work is on the NBE emission and its enhancement from nanostructured metal coatings; thus, the effects of the metal films on DL emission will be reported and only discussed when relevant to the UV enhancement.

To spectrally resolve individual emission peaks of ZnO's NBE, the spectra have to be collected at low temperature, which typically leads to higher charging effects under electron beam irradiation, particularly at 10 K. This is due to increased electron trapping, which accumulates electrons from the primary electron beam, creating charging effects, such as beam drift, flash-over and anomalous SEM image contrast. This issue can be circumvented by using laser excitation ($\lambda_{\mathrm{exc}} = 325\,\mathrm{nm}$), which does not introduce additional charges and allows for higher excitation power.

A comparison of PL and CL at 80 K, displayed in fig. 4.7, shows a change in the defect-related DL emission. This can be explained by a different level of injected electron-hole pairs into the ZnO sample by electron beam and laser, leading to non-equivalent defect saturation, as well as a slightly different probing depth.

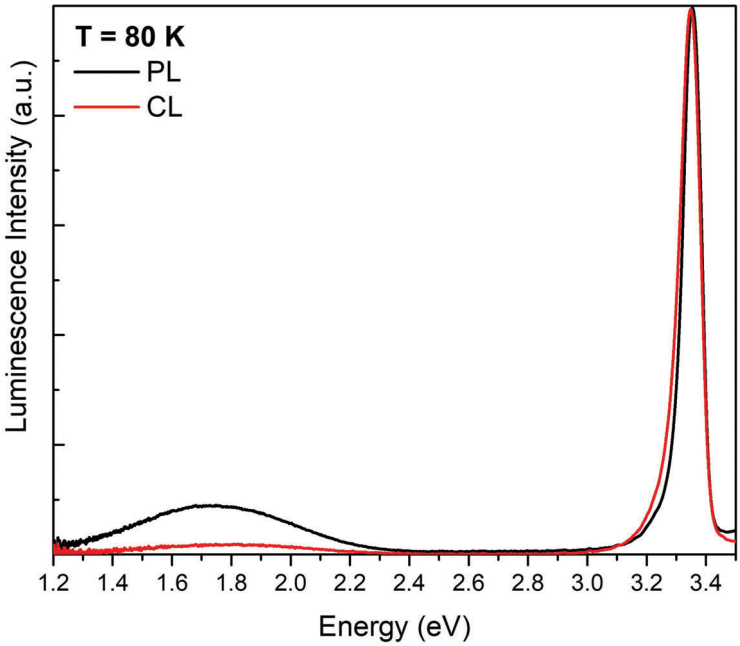

Fig. 4.7: Normalised 80 K-PL and -CL spectrum of the uncoated ZnO nanorods, showing changes in the DL emission due to different excitation power density of the electron beam and laser light.
CL: $HV = 5\,\mathrm{kV}$, P =45 µW, scan area 15 µm × 15 µm.
PL: $\lambda_{\mathrm{exc}} = 325\,\mathrm{nm}$, $P = 35\,\mu\mathrm{W}$, spot size $\sim 30\,\mu\mathrm{m}$.

While the CL excitation depth is determined by the acceleration voltage of the electron

beam, the penetration depth of the HeCd-laser is limited by the absorption coefficient of ZnO at the excitation wavelength ($\lambda_{exc} = 325\,nm$). As shown in section 3.2.6, a similar CL excitation depth of 88 nm to the PL penetration depth of 110 nm can be achieved when using an acceleration voltage of 5 kV. However, the number of generated electron-hole-pairs per second per volume — calculated in eq. (3.20) and eq. (3.18) for electron beam and laser excitation, respectively — is substantially higher for CL than for PL, with a difference of approximately four orders of magnitude. This increase can justify the decreased DL emission for CL compared to PL, as the defect-related emission with longer recombination lifetimes can be saturated under electron beam excitation, resulting in a lower DL and therefore increased UV emission. The DL saturation using laser excitation occurs to a much lesser extent due to smaller injected electron-hole pair density [187].

A typical high-resolution PL spectrum of the NBE of the ZnO nanorods is displayed in fig. 4.8. It shows relatively broad emission peaks, which is due to the poorer crystal quality of the hydrothermally-produced ZnO nanorods compared to the commercially available planar hydrothermally-grown single crystals, shown in fig. 2.3b. Here, the spectrum is dominated by donor bound transitions, which are at an energy of 3.36 eV — cf. table 2.1. The LO-phonon replica, as well as the two-electron satellite emissions at 3.32 eV are visible. However, the 3.36 eV peak is too broad to allow its assignment to a specific DBX I line (see table 2.1).

To study the distribution of luminescence from the surface into the bulk of the ZnO nanorods, depth-resolved CL was performed, whereby the power was held constant at 17.5 µW by adjusting the electron beam current at each acceleration voltage (cf. section 3.2.5.1). The acceleration voltage was varied from 2 to 20 kV, which translates to CL excitation depths ranging from approximately 30 nm for $HV = 2\,kV$ to $\sim 900\,nm$ for $HV = 20\,kV$, using the CASINO simulations shown in fig. 3.7.

Figure 4.9a shows the depth-resolved CL spectra of uncoated ZnO nanorods, using this range of acceleration voltages. It can be seen that the intensity of the NBE emission increased between 2 and 3 kV due to surface recombination effects, followed by a slow decrease; this trend is graphed in fig. 4.10a, showing the integrated NBE emission as a function of acceleration voltage. This intensity decrease of the NBE emission can be explained by self-absorption of the higher-energy tail by the sample (see section 3.2.5.1). Furthermore, a slight red-shift in the NBE peak position with increasing depth is apparent, as the optical absorption coefficient is higher on the blue side of the NBE emission compared with its red side. This self-absorption-related effect can be illustrated by normalising the NBE emission and is shown in fig. 4.9c. In this work, only CL data up to 10 kV was collected. In this region, the red-shift is negligibly small.

The DL emission in fig. 4.9a decreases as the electron beam penetrates deeper into the sample, resulting in less CL signal coming from the surface-related defects. A better crystal quality inside the nanorod is assumed to be the origin of the decreased DL emission

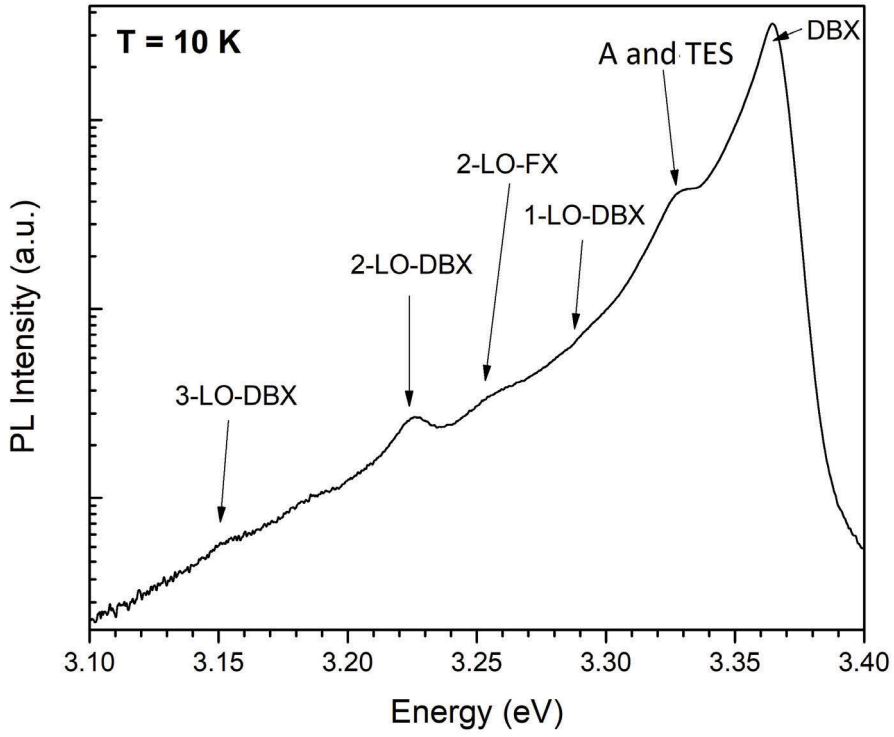

Fig. 4.8: High-resolution PL spectrum of NBE of the ZnO nanorods at T =10 K, P =17.5 µW, scan area 10 µm × 10 µm.

at higher acceleration voltages, as well as band flattening away from the surface possibly changing defect charge states in the bulk compared with the surface. Furthermore, a slight red-shift with increasing acceleration voltage can be seen, which indicates the presence of two peaks, with one quenching faster with increasing acceleration voltage. The integrated DL emission as a function of acceleration voltage is depicted in fig. 4.10b. A similar trend can be observed for Au nanoparticle-coated ZnO nanorods, shown in fig. 4.9b, and the normalised UV emission of Au nanoparticle-coated ZnO nanorods in fig. 4.9d.

To study the effect of the Au nanoparticle coating, a direct spectral comparison of the uncoated and Au nanoparticle-coated ZnO nanorods is critical. In fig. 4.11a, the 10 K-CL spectra at three increasing acceleration voltages of 3 kV, 5 kV and 10 kV of uncoated and Au nanoparticle-coated ZnO nanorods are displayed. It can be seen that the Au nanoparticle-coating enhanced the UV emission, while the weak DL emission was unchanged. The comparison of the UV intensity of the Au nanoparticle-coated and the

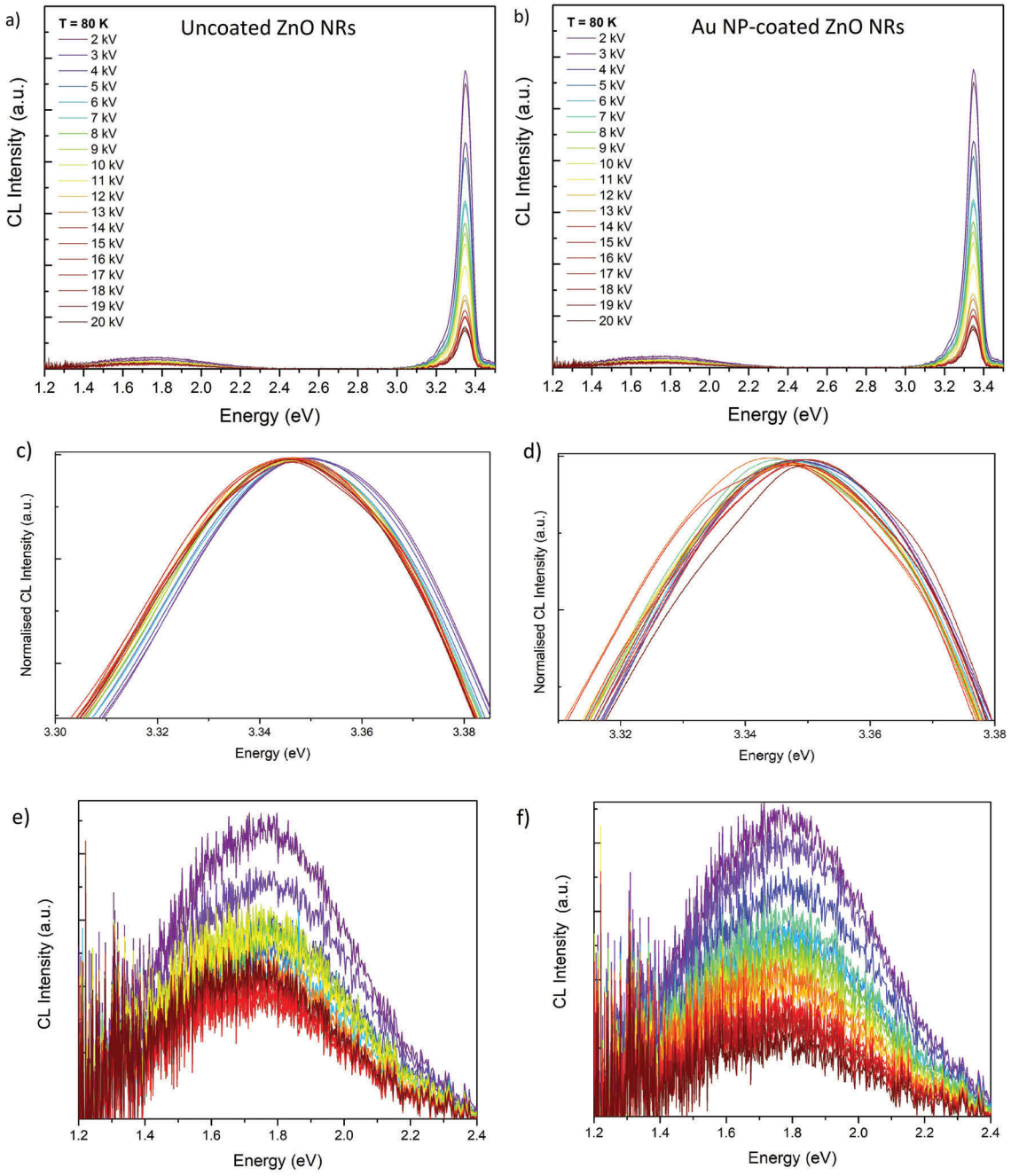

Fig. 4.9: Depth-resolved CL spectra of (a) uncoated and (b) Au nanoparticle-coated ZnO nanorods, showing typical self-absorption of NBE emission and slightly increased DL emission with depth. (c) and (d) depict the normalised, slightly red-shifted NBE emission. (e) and (f) depict the increased DL emission of uncoated and Au nanoparticle-coated ZnO nanorods, respectively.
$HV = 2\,\text{kV}$ to $20\,\text{kV}$, $T = 80\,\text{K}$, $P = 17.5\,\mu\text{W}$, scan area $10\,\mu\text{m} \times 10\,\mu\text{m}$.

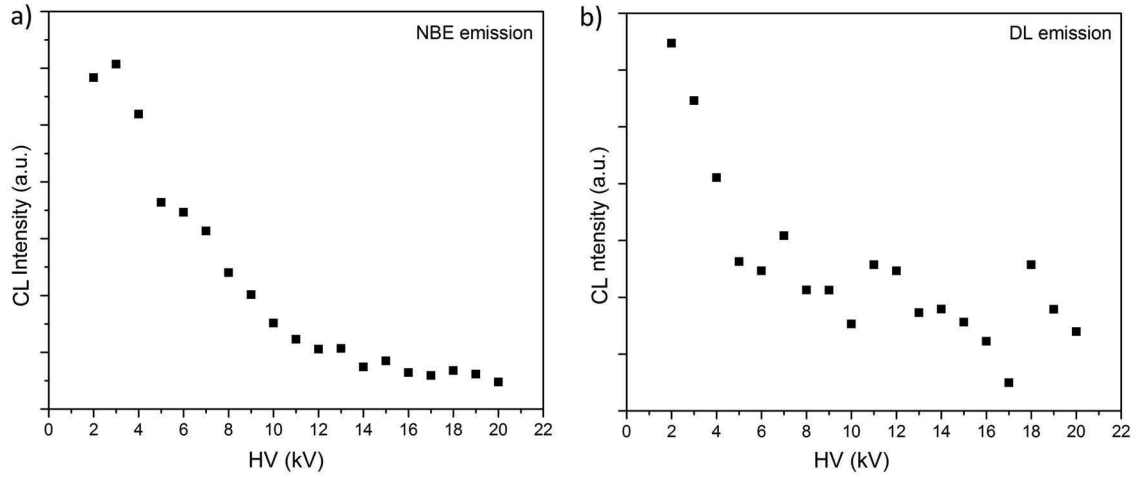

Fig. 4.10: CL intensity of (a) NBE and (b) DL emission of annealed ZnO nanorods as a function of acceleration voltage.
$T = 80\,\text{K}$, $HV = 5\,\text{kV}$, $P = 17.5\,\mu\text{W}$, scan area $10\,\mu\text{m} \times 10\,\mu\text{m}$.

uncoated ZnO nanorods suggests a depth-dependent enhancement factor, as listed in table 4.2 at the temperatures of 10 K, 80 K and 300 K. Here, the third column represents the UV enhancement factors, calculated by dividing the maximum intensity of the Au nanoparticle-coated ZnO nanorods by that of the uncoated ones. The fourth column shows the ratio of the integrated UV intensity from 3.10 eV to 3.45 eV of the Au nanoparticle-coated and uncoated ZnO nanorods.

Table 4.2: UV enhancement factors of the hydrothermally-grown ZnO nanorods coated with Au, at three different acceleration voltages at 10 K, 80 K and 300 K. The third column shows the UV enhancement calculated by diving the maximum intensity of the Au nanoparticle-coated ZnO nanorods by the that of the uncoated ZnO nanorods. The fourth column illustrates the ratio of the UV emission integrated from 3.10 eV to 3.45 eV.

HV (kV)	T (K)	UV enhancement (I)	UV enhancement (Int)
3	10	2.4	1.5
5	10	3.8	3.6
10	10	6.6	6.3
3	80	1.5	1.6
5	80	2.3	2.4
10	80	2.4	2.5
3	300	2.1	2.1
5	300	1.1	1.0
10	300	1.1	1.0

At 10 K, the UV enhancement increases from 2.4-fold at 3 kV, which corresponds to a CL excitation depth of approximately 50 nm, to 6.3-times at 10 kV (∼350 nm CL excitation

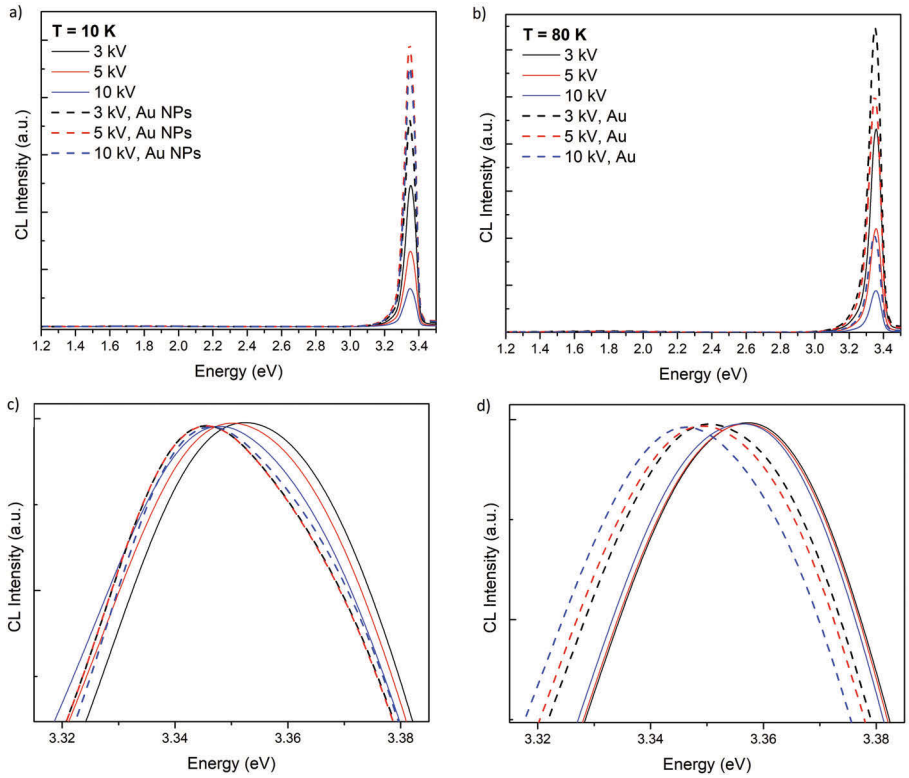

Fig. 4.11: Depth-resolved CL spectra of uncoated and Au nanoparticle-coated ZnO nanorods at (a) $T = 10\,\mathrm{K}$ and (b) $T = 80\,\mathrm{K}$. Owing to the Au nanoparticle coating, the NBE emission was increased with highest enhancement factor at 10 kV, while the DL emission was unchanged. (c) and (d) show the normalised NBE emission at $T = 10\,\mathrm{K}$ and $T = 80\,\mathrm{K}$, respectively. A red-shift of 8 meV from 3.353 eV to 3.245 eV. $P = 17.5\,\mu\mathrm{W}$, scan area $10\,\mu\mathrm{m} \times 10\,\mu\mathrm{m}$.

depth). While at 80 K (fig. 4.11b) this depth dependence is less pronounced, it changes to the opposite behaviour at room temperature with the highest enhancement of 2.1 at 3 kV, which reduces to 1.0 at 5 kV and 10 kV.

Although the UV enhancement is greater at deeper excitation depths, the Au nanoparticle-coating can possibly have a larger effect closest to the ZnO-Au interface. This can be explained by the CL excitation of a larger surface area of the ZnO nanorods by the 10 kV-electron beam, compared with that at 3 kV, as the diameter of the ZnO nanorods is as small as approximately 40 nm and they are randomly oriented with respect to the substrate. This is illustrated in fig. 4.12, showing the CASINO simulation of the energy loss within ZnO coated with 1 nm thin Au film at 3 kV, 5 kV and 10 kV. The diameter of the excited surface area by the 3 kV-electron beam is only approximately 25 nm, while it is substantially larger at 10 kV with ~ 350 nm. Therefore, more Au nanoparticle-coated ZnO nanorod side wall surfaces can be excited at 10 kV, compared to 3 kV, which can possibly result in a greater overall UV enhancement. Furthermore, forward scattered electrons

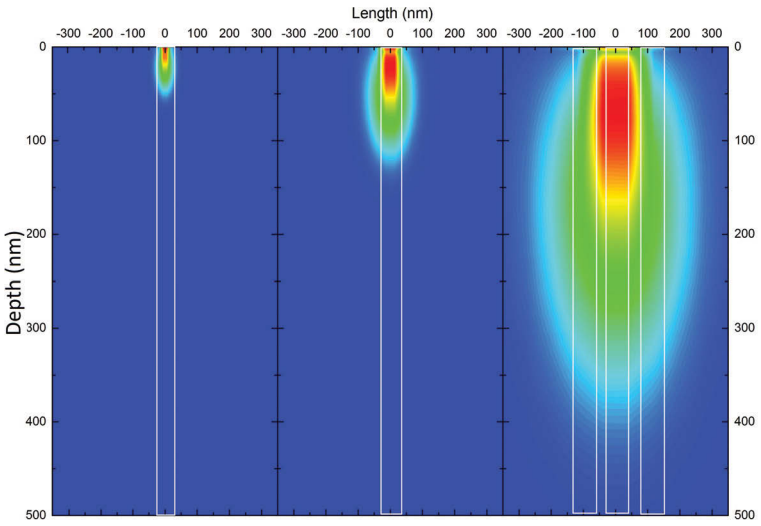

Fig. 4.12: CASINO simulation of the energy loss within ZnO coated with a 2 nm thin Al film at 3 kV (left), 5 kV (centre) and 10 kV (right). The grey bar on the left indicates an average ZnO nanorod with a diameter of 40 nm, showing that all electrons are injected into single nanorod at 3 kV and more ZnO nanorods are excited by higher acceleration voltages.

can possibly excite side wall surfaces of neighbouring ZnO nanorods. Therefore, it can be assumed that the UV enhancement of the Au-coated ZnO nanorods is surface-related, which is consistent with the depth-resolved CL results of the Au nanoparticle-coated *a*-plane ZnO, discussed in section 4.5.1.

Note that the uncoated ZnO nanorods were substantially more affected by charging effects than the Au nanoparticle-coated side of the sample. This trend was more pronounced at 10 K than at 80 K or at room temperature. This behaviour results in an apparently larger UV enhancement factor at 10 K than at higher temperatures. Therefore, temperature-dependent PL spectra of the uncoated and the Au nanoparticle-coated ZnO nanorods were collected, as shown in section 4.4.2. As the laser light does not introduce any additional charges, no charging effects can occur and a more reliable UV enhancement as a function of temperature can be achieved.

The normalised NBE emission in fig. 4.11c shows a slight red-shift, following the Au nanoparticle-coating. This can be explained by the a larger enhancement of certain emission peak in the NBE, such as individual *I* lines in the DBX, than others, resulting in an apparent red-shift of the NBE. To investigate this effect, a higher spectral resolution is needed, which is further discussed below (section 4.4.2).

A similar depth-dependent CL-enhancement can be observed at a higher temperature of 80 K, which is shown in fig. 4.11b. However, the enhancement factors are slightly reduced to 1.5, 2.4 and 2.5 at 3 kV, 5 kV and 10 kV, respectively. The normalised NBE emission is depicted in fig. 4.11d, also showing a red-shift of the Au nanoparticle-coated ZnO

nanorods, which is more pronounced than that at 10 K. A larger change in enhancement factors of the individual emission peak lines in the NBE is a possible explanation.

4.4.2 Temperature-Dependent PL of Au Nanoparticle-Coated ZnO Nanorods

To study the possible temperature dependence of the uncoated and the Au nanoparticle-coated ZnO nanorods, as discussed above, PL spectroscopy was performed over a larger range of temperatures from 10 K to 250 K. Figure 4.13a shows the temperature-dependent

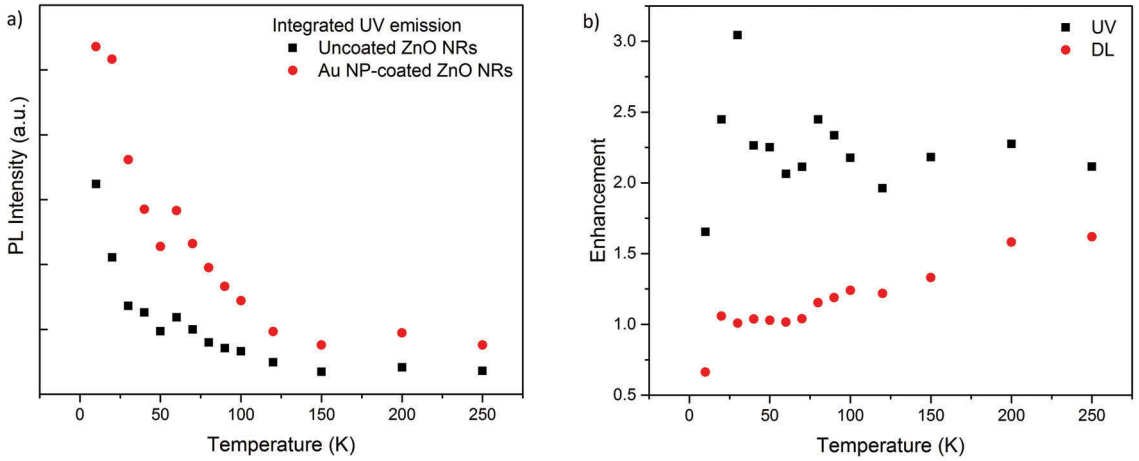

Fig. 4.13: (a) PL integrated from 3.0 eV to 3.45 eV of uncoated (black) and Au nanoparticle-coated (red) ZnO nanorods as a function of temperature. (b) temperature-dependent PL enhancement of Au nanoparticle-coated ZnO nanorods, UV emission in black and DL emission in red. $\lambda_{\text{exc}} = 325\,\text{nm}$, $P = 22.4\,\text{mW}$, spot size $\sim 30\,\mu\text{m}$.

PL intensity of the UV emission, integrated from 3.0 eV to 3.45 eV, of the uncoated and the Au nanoparticle-coated ZnO nanorods. Due to thermalisation, the integrated UV intensity significantly decreases with increasing temperature for both samples.
The corresponding activation energies can be determined from the temperature-dependent PL measurements and be represented in an Arrhenius plot, shown in fig. 4.14. The activation energies of the uncoated and Au nanoparticle-coated ZnO nanorods can be calculated by using eq. (3.14) (cf. section 3.2.5.3); they are as listed in table 4.3 below. Here,

Table 4.3: Activation energies E_{a} of the uncoated and Au nanoparticle-coated ZnO nanorods.

Sample	$E_{\text{a}}(1)$ (meV)	$E_{\text{a}}(2)$ (meV)
Uncoated ZnO nanorods	(10.3 ± 0.8)	(4.2 ± 0.2)
Au nanoparticle-coated ZnO nanorods	(14 ± 1)	(4.6 ± 0.3)

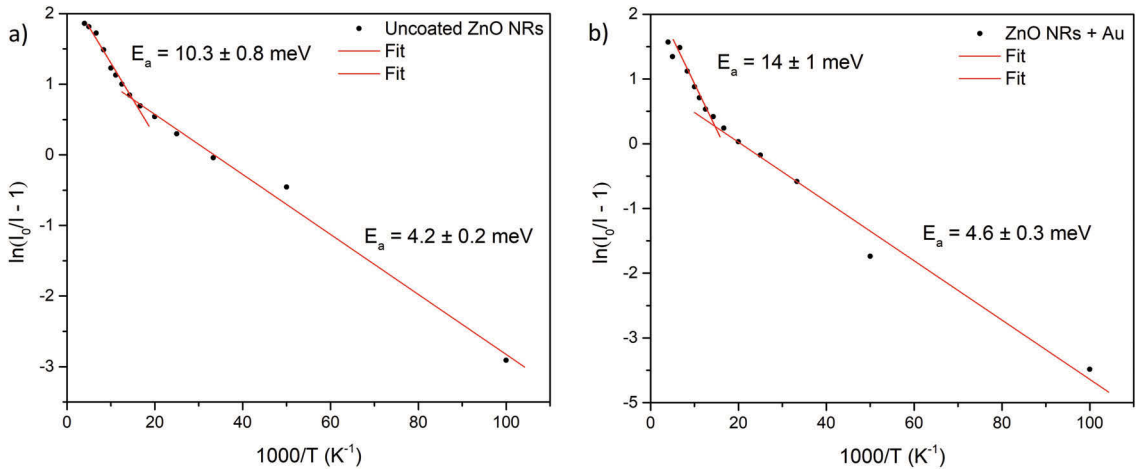

Fig. 4.14: Arrhenius plot of (a) the uncoated and (b) the Au nanoparticle-coated ZnO nanorods, showing an increased activation energy for Au nanoparticle-coated ZnO nanorods.

the activation energy for the Au nanoparticle-coated ZnO nanorods of $E_a(1) = (14 \pm 1)$ meV is higher than that of the uncoated ZnO nanorods, $E_a(1) = (10.3 \pm 0.8)$ meV, while the lower activation energy $E_{1a}(2)$ is similar for both sides of the sample, which is possibly due to the thermalisation of the DBX between 10 K and 20 K. From these results it can be concluded that non-radiative recombination processes in the Au nanoparticle-coated ZnO nanorods become active at higher temperature, indicating that the Au nanoparticle-coating has affected the radiative recombination properties of the ZnO nanorods. Note that the activation energies were calculated for the DBX, which could include more than one emission peak. However, E_a will be dominated by the DBX with the largest binding energy.

Furthermore, the UV enhancement factor can be graphed as a function of temperature by dividing the integrated UV intensity of the Au nanoparticle-coated ZnO nanorods by that of the uncoated ZnO nanorods. This is displayed in fig. 4.13b, as well as the similarly obtained enhancement of the DL emission. The UV emission is approximately 2.3 times enhanced over the entire range of temperatures, while the DL enhancement negligibly increased from 1.1 to 1.5 at higher temperatures. Note that DL emission is possibly comprised of two peaks — OL and RL (table 2.2) — which can behave differently with increasing temperature, resulting in an apparent enhancement at elevated temperatures. Finally, it can be concluded that the UV enhancement of the Au nanoparticle-coated ZnO nanorods is temperature-independent.

Interestingly, the direct spectral comparison of Au nanoparticle-coated ZnO nanorods with that of the uncoated ones at low temperature shows a strong dependence on energy. The corresponding spectra are shown in fig. 4.15, where the bottom figure displays the high-resolution PL spectra of both samples and the top figure their enhancement as

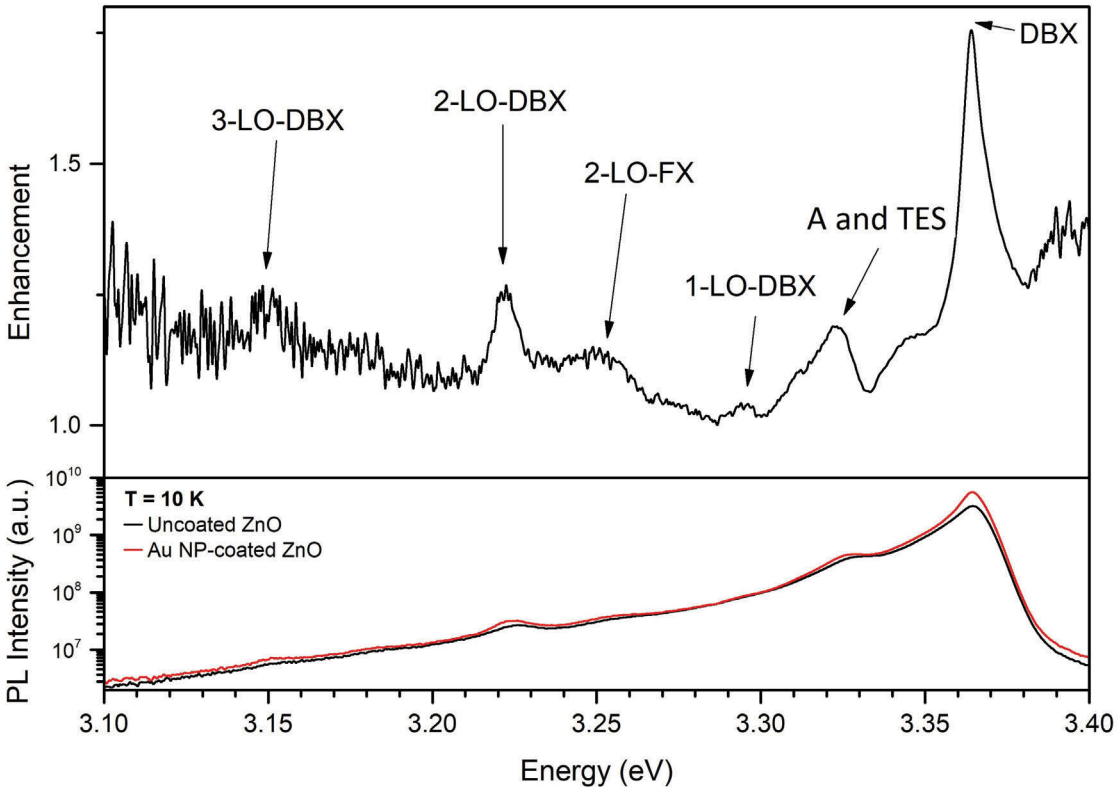

Fig. 4.15: Top: 10 K-PL enhancement factor of Au nanoparticle-coated ZnO nanorods as a function of energy.
Bottom: high-resolution PL of uncoated (black) and Au nanoparticle-coated ZnO nanorods (red), graphed on a semi-logarithmic scale.
$\lambda_{\text{exc}} = 325\,\text{nm}$ and $P = 22.4\,\text{mW}$, spot size $\sim 30\,\mu\text{m}$.

a function of energy. The highest enhancement factor is achieved over the energy range typically associated with donor bound excitons and the DBX-related TES and LO-phonon replica. However, there is a small red-shift for the Au nanoparticle-coated ZnO nanorods, which could be due to a changed ratio in the DBX emission peaks. As those emission peaks are broad, this shift cannot be unequivocally identified or assigned to a specific DBX I line.

As mentioned above, at $T = 10\,\text{K}$ the free exciton emission is very weak; only a shoulder at 3.38 eV is visible which might explain why no apparent enhancement peak from the FX can be found.

4.4.3 Excitation Power-Dependent PL and CL of Au Nanoparticle-Coated ZnO Nanorods

To investigate a possible laser excitation power dependence of the UV enhancement factor of the Au nanoparticle-coated ZnO nanorods, the PL spectra of both the uncoated and

the Au nanoparticle-coated ZnO nanorods were collected as a function of laser excitation power. The UV emission of both sides of the samples were integrated from 3.00 eV to 3.54 eV as a function of laser excitation power, shown as a log-log plot in fig. 4.16a. The ratio was subsequently calculated and used to graph the UV enhancement as a function of laser excitation, as depicted in fig. 4.16b. The corresponding power law exponent of

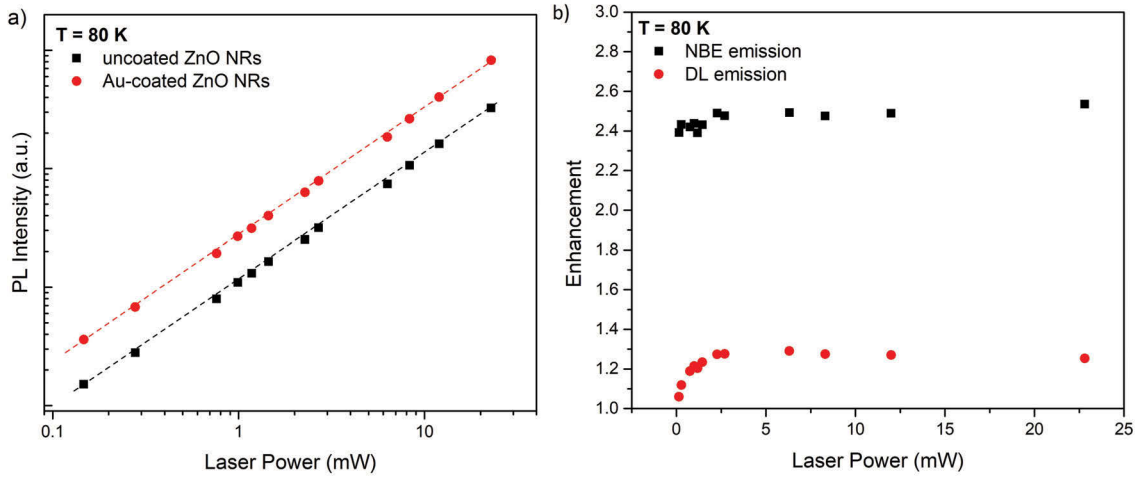

Fig. 4.16: (a) Integrated UV emission from 3.00 eV to 3.54 eV as a function of laser excitation power of uncoated (black) and Au nanoparticle-coated ZnO nanorods (red), plotted logarithmically. The lines serve as a guide of the eye. (b) UV enhancement factor as a function of laser excitation power of the UV (black) and the DL emission (red).
$\lambda_{\mathrm{exc}} = 325\,\mathrm{nm}$, spot size $\sim 30\,\mu\mathrm{m}$ and $T = 80\,\mathrm{K}$.

the uncoated and the Au nanoparticle-coated ZnO nanorods was found to be unchanged with (1.07 ± 0.02) and (1.08 ± 0.01), respectively.
Furthermore, it can be seen that the UV enhancement is slightly increased from 2.4 to 2.5 at very low laser powers, which is negligible. For powers greater than 2 mW, no change in enhancement was observed, indicating that the enhancement is excitation power-independent.
Note that the laser power was measured before the laser light enters the SEM chamber, as it is not possible to measure the exact laser power at the sample position. It is assumed that the power is approximately reduced by 10-20% due to reflection losses at the UV-silica window of the SEM chamber and the CL collection parabolic mirror surface, which is used to focus the laser light onto the sample surface.

4.4.4 Investigation of the Plasmonic Interaction of Au Nanoparticle-Coated ZnO Nanorods

The above discussed CL and PL results — showing a temperature- and excitation power-independent 2.3-fold UV-PL enhancement, which is mainly affecting the DBX-related

emissions, and a depth-dependent enhanced CL UV-emission of up to 3.8 times — can be interpreted with the plasmonic coupling mechanisms in the literature (cf. section 2.5.3).

1. In the charge transfer mechanism — involving transfer of hot electrons from the LSP decay in Au into the conduction band of ZnO — the enhanced NBE emission is typically accompanied by reduced DL emission. In the literature, this has been attributed to the absorption of DL emission by the Au nanoparticles to excite LSPs, as well as an electron transfer from the DL level of ZnO to the Fermi level of Au, as their energy levels are close to each other, cf. fig. 2.10.
   Here, the investigated samples do not exhibit any change in the DL emission, opposite to results in the literature, which appear to be identical samples.
   Furthermore, the weak DL emission of the examined samples is centered around 1.8 eV, while ZnO nanorod-DL emission is usually reported to have more green luminescence arising from oxygen vacancies in ZnO. The DL emission in those samples can resonantly excite the LSPs in Au nanoparticles, while the DL emission of the ZnO nanorods in this work is not at resonance with the measured LSPR energy of the Au nanoparticle coating at 2.25 eV. Nevertheless, plasmonic coupling in the charge transfer picture would still be possible, as the Au's plasma resonance energy is relatively broad. This will be addressed in section 4.4.4.1, using additional green laser illumination to externally excite the LSPs in the Au nanoparticles.

2. The LSP-exciton coupling — a direct dipole-dipole coupling between the excitons in ZnO and LSPs in Au — is typically used to describe resonant coupling, meaning that the LSP resonance (LSPR) energy of the metal is close to that of the excitons, see fig. 2.9. This is clearly not the case for the presented ZnO nanorods with Au nanoparticle coating, as their energies are separated by 1.2 eV ($E_{\mathrm{LSP}} = 2.25\,\mathrm{eV}$ and $E_{\mathrm{g}} = 3.37\,\mathrm{eV}$). However, LSP-exciton coupling cannot be excluded, as the broad LSPR energy of Au nanoparticle-coated ZnO extends into the UV spectral range. This will be discussed in more detail in section 4.4.4.2, using time-resolved PL.

4.4.4.1 Concurrent CL-PL Spectroscopy of Au Nanoparticle-Coated ZnO Nanorods

To further investigate the charge transfer mechanism, simultaneous excitation of Au nanoparticle-coated ZnO nanorods by the electron beam and a sub-bandgap laser ($\lambda_{\mathrm{exc}} = 532\,\mathrm{nm}$) was performed, using the light injection setup shown in section 3.2.6.1. The rationale of this experiment was to use additional green laser illumination to excite LSPs in the Au nanoparticles, allowing for hot electron transfer into ZnO's conduction band to further enhance the UV emission.
In principle, the separate illumination of Au nanoparticle-coated ZnO nanorods with the green laser can only excite LSPs in the Au nanoparticles as well as DL emission in the

ZnO nanorods — if at all, as its energy is not high enough to excite electrons across the bandgap. The separate electron beam excitation should give rise to the typical ZnO spectrum, shown in fig. 4.9. However, concurrent excitation with the electron beam and the green laser should induce both UV and DL emission of the ZnO nanorods, and LSPs in the Au nanoparticles. The additional green laser excitation can create more LSPs in the Au nanoparticles and subsequently hot electrons, which can technically transfer to ZnO's conduction band, thereby further enhancing the UV emission.

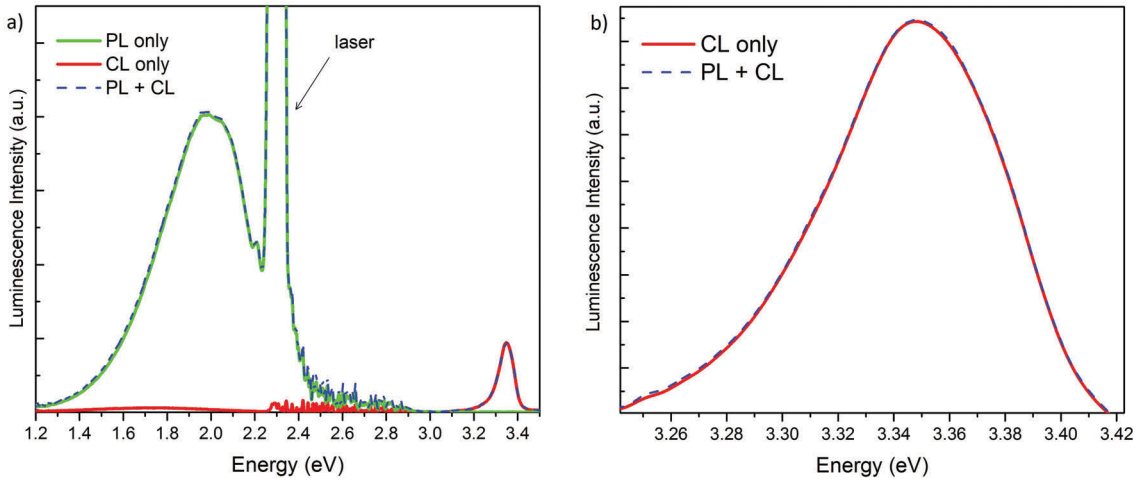

Fig. 4.17: (a) 10 K-concurrent PL-CL spectra of Au nanoparticle-coated ZnO nanorods and (b) large view of the NBE emission, using sub-bandgab illumination at $\lambda_{\text{exc}} = 532\,\text{nm}$ and electron beam acceleration voltage of $HV = 5\,\text{kV}$.
Separate PL and CL spectrum shown in green and red, respectively, while the dashed blue line presents simultaneous excitation by the electron beam and green laser.

The results of this experiment are depicted in fig. 4.17, showing CL only and PL only spectra as well as the spectrum at concurrent CL and PL excitation at a temperature of 10 K. As expected, the electron beam excitation only leads to an intense UV emission ($\sim 3.36\,\text{eV}$) and a weak, broad DL emission centered at 1.8 eV. On the other hand, the laser illumination only strongly excites the green emission of the Au nanoparticle-coated ZnO nanorods with no other emission peaks. Note that the emission at 2.33 eV (equivalent to $\lambda_{\text{exc}} = 532\,\text{nm}$) comes from the incident green laser. It is remarkable that the sub-bandgap illumination alone exhibits a much higher emission in the visible spectrum than that of the CL only, which can be explained by the excitation of an electron in an ionised V_{Zn}^{-} acceptor to the conduction band, which then recombines with the V_{Zn}^{0} centre emitting green luminescence (cf. table 2.2). Furthermore, LSPs in the Au nanoparticles excited by the green laser can possibly emit photons in the visible spectral region when they relax. However, under simultaneous laser and electron beam excitation, the visible part of the spectrum is similar to that of the separate green illumination, while the UV

emission is unchanged to that of the separate electron beam excitation, which can be seen in fig. 4.17b. This indicates that no additional electrons from the Au nanoparticles were injected into ZnO's conduction band to further increase the UV emission, despite LSPs being excited by the green laser illumination.
These results confirm that the charge transfer model cannot be the underlying enhancement mechanism in these samples.

4.4.4.2 Time-Resolved PL of ZnO Nanorods Decorated with Gold Nanoparticles

To understand the carrier dynamics in the uncoated and Au nanoparticle-coated ZnO nanorods, time-resolved PL (TR-PL) was carried out at a fixed collection wavelength of $\lambda = 370\,\text{nm}$ and a temperature of 8 K (see section 3.2.7). In fig. 4.18 the TR-PL data of un-

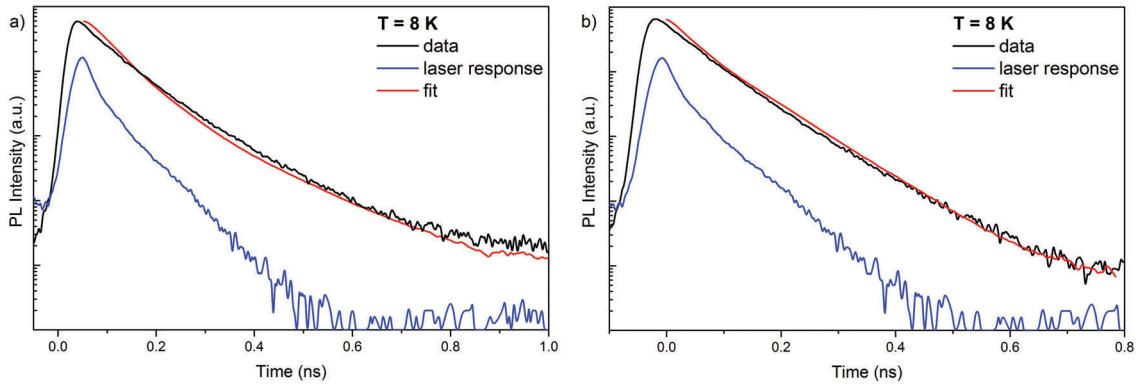

Fig. 4.18: Time-resolved PL of (a) uncoated and (b) Au nanoparticle-coated ZnO nanorods (black), bi-exponentially fitted (red), plotted logarithmically. The system response is shown in blue.
$T = 8\,\text{K}$ and fixed excitation wavelength of $\lambda = 370\,\text{nm}$.

coated and Au nanoparticle-coated ZnO nanorods is shown, as well as the laser response, which was used for de-convolution. Both decays could be fitted using a bi-exponential fit, which can be expressed by the equation [129, 148, 188]:

$$\frac{1}{\tau} = \frac{1}{\tau_\text{R}} + \frac{1}{\tau_\text{NR}}, \tag{4.6}$$

where τ_R is the radiative lifetime and τ_NR the lifetime of non-radiative recombination pathways, such as trapping or surface states [129].
Note that the resulting carrier lifetimes were averaged over five positions on the same sample to eliminate possible nanorod inhomogeneities, leading to different uncertainties for uncoated and Au nanoparticle-coated ZnO nanorods.
The uncoated ZnO nanorods exhibit a bi-exponential decay, one with a short lifetime of $\tau_\text{NR} = (25.2 \pm 3.2)$ ps, which is typically attributed to non-radiative recombination, and the second with a longer lifetime of $\tau_\text{R} = (129.4 \pm 4.5)$ ps. τ_R can be assigned to radiative

excitonic recombination.
The Au nanoparticle-coated side of the ZnO nanorod sample — see fig. 4.18b — shows a similar non-radiative lifetime of $\tau^*_{\mathrm{NR}} = (21.5 \pm 1.5)$ ps. This indicates that surface passivation is not the underlying origin of the enhanced NBE emission of the Au nanoparticle-coated ZnO nanorods, which would lead to a further decreased non-radiative lifetime. However, it should be emphasised that those short lifetimes are close to the system response, i.e. shorter lifetimes cannot be resolved with this experimental setup.
A reduced radiative lifetime was recorded for the Au nanoparticle-coated ZnO nanorods: $\tau^*_{\mathrm{R}} = (91.0 \pm 15.2)$ ps. As discussed in section 2.4.4, a shortened radiative excitonic lifetime due metal nanoparticle coating is considered as evidence for exciton-LSP-coupling. Here, excitons can transfer energy into LSP modes instead of free space, which significantly enhances the spontaneous emission rate (SER) of the ZnO nanorods [128, 130, 189], cf. section 2.4.4. The enhanced SER can be explained by the creation of an additional, faster relaxation channel through the LSPs in the Au nanoparticles, leading to a reduced combined carrier lifetime:

$$\frac{1}{\tau^*} = \frac{1}{\tau^*_{\mathrm{R}}} + \frac{1}{\tau^*_{\mathrm{NR}}} + \frac{1}{\tau^*_{\mathrm{LSP}}}. \tag{4.7}$$

The enhanced SER can be quantified, using the Purcell enhancement factor (F_{P}) which is commonly used for enhanced emissions of two-level systems such as quantum dots in cavities [190, 191]. It has been shown in literature that this can be adopted for the type of samples used in this work to predict the plasmon-assisted enhancement factor [133, 144, 192].
The F_{P} can be calculated using the ratio of the lifetime of the uncoated and Au nanoparticle-coated ZnO nanorods — see section 2.4.4 [131]:

$$F_{\mathrm{P}} = \frac{\tau_{\mathrm{R}} + \tau_{\mathrm{NR}}}{\tau^*_{\mathrm{R}} + \tau^*_{\mathrm{NR}} + \tau^*_{\mathrm{LSP}}} = (1.4 \pm 0.1). \tag{4.8}$$

The comparison with the CL results in section 4.4 shows that the F_{P} of 1.4 is much smaller than the 3.8-fold CL enhancement of the DBX emission at 10 K — cf. fig. 4.11 — or the 2.3 times enhanced integrated NBE emission, measured with the UV-laser excitation (fig. 4.13).

4.4.5 Summary of Au Nanoparticle-Coated ZnO Nanorods

In summary, the maximum UV enhancement of 6.3 of the Au nanoparticle-coated ZnO nanorods was found at the highest CL excitation voltage (10 kV), which can be explained by a larger surface area excited by the electron beam at 10 kV than at 3 kV. Therefore, it can be assumed that the enhancement is surface-related, while an apparent temperature

dependence was mainly attributed to greater charging effects of the uncoated ZnO nanorods than the Au nanoparticle-coated side of the sample, which was most pronounced at 10 K. However, the laser excitation, which does no introduce any charges into the sample, showed a $\sim$ 2.3-fold UV enhancement with no temperature or laser excitation dependence.
The concurrent CL-PL spectroscopy, using additional sub-bandgap laser excitation to the CL, was used to investigate the charge transfer mechanism in the present sample. Although the LSPs in the Au nanoparticles were excited, no hot electrons were injected from the Au nanoparticles into the conduction band of the ZnO nanorods, indicating that this is not the underlying cause of the UV enhancement effect.
Furthermore, an approximately 40 ps-reduced radiative lifetime of the Au nanoparticle-coated ZnO nanorods, compared with that of the uncoated side of the sample, was observed. The corresponding Purcell enhancement factor of $F_{\mathrm{P}} = 1.4$ was found, which is smaller than the observed PL and CL enhancement. Therefore, it can be assumed that an additional, faster recombination pathway via the Au nanoparticles was created. However, a resonant LSP-exciton coupling is unlikely, as the spectral overlap is possibly small. The plasmonic interaction between Au nanoparticles and ZnO nanorods will be further studied by using the FDTD simulations, discussed below in (section 4.6). Therefore, other mechanisms have to be investigated to explain the UV enhancement of Au nanoparticle-coated ZnO nanorods.

4.5 Optical Properties of Au Nanoparticle-Coated *a*-plane ZnO Single Crystals

To obtain a better understanding of the UV enhancement mechanism of Au nanoparticle-coated ZnO nanorods, commercially available *a*-plane ZnO single crystals were used as a reference, having a simpler planar surface.
The *a*-plane ZnO crystals were coated with 5 nm-Au nanoparticles, resulting in a similar surface coating, as well as surface band bending behaviour as the Au nanoparticle-coated ZnO nanorods (cf. section 4.3 and section 4.2).

4.5.1 CL and PL Study of Au Nanoparticle-Coated *a*-plane ZnO

To study the distribution of the luminescence in the uncoated and the Au nanoparticle-coated *a*-plane ZnO with increasing excitation depth, depth-resolved CL spectroscopy at 10 K and 80 K was performed.
The corresponding CL spectra are shown in fig. 4.19. It can be seen that the CL intensity is enhanced due to the Au nanoparticle-coating; at a temperature of 10 K (fig. 4.19a), the CL intensity is 2.0 and 1.3 times enhanced for 5 keV and 10 keV, respectively. At 80 K, shown

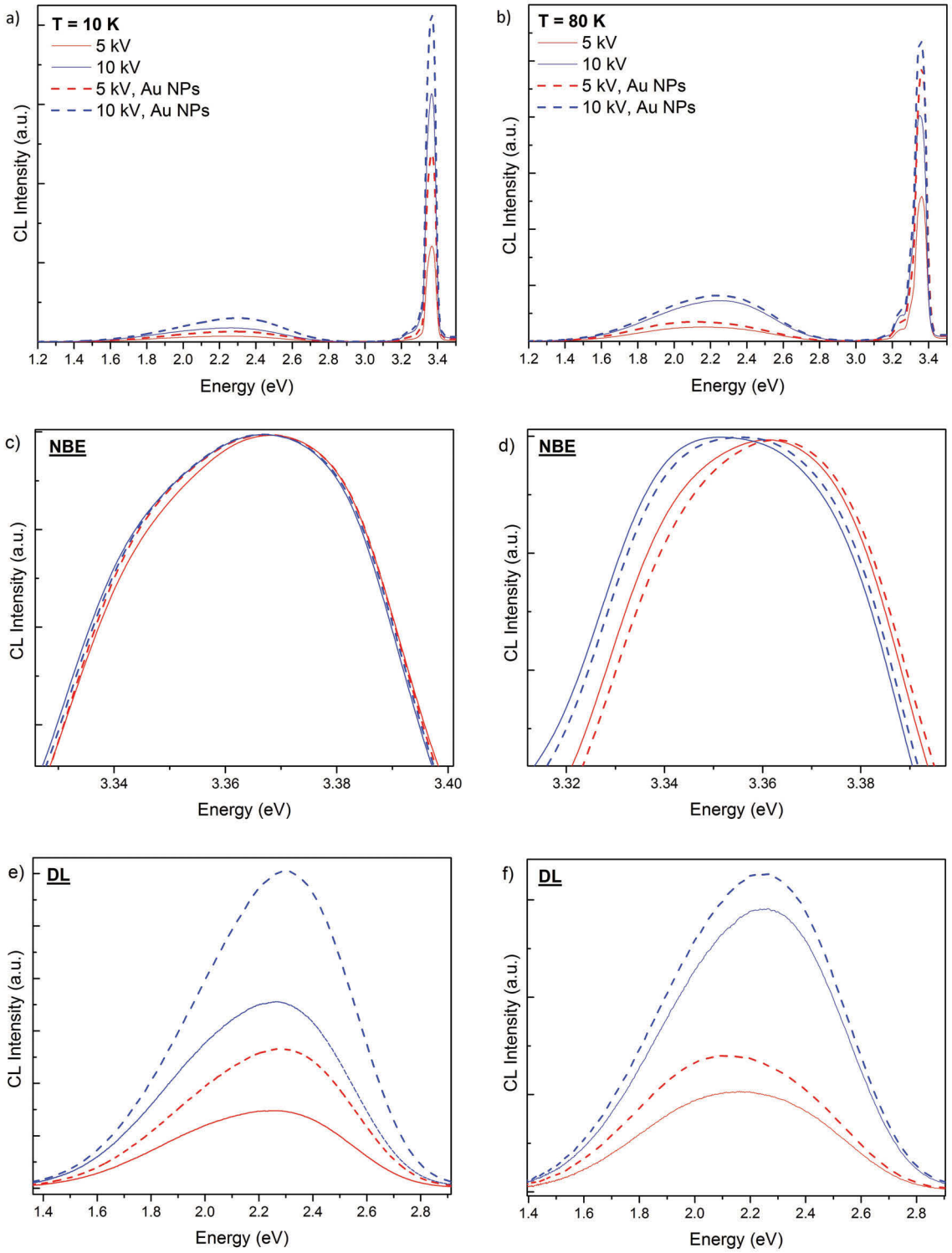

Fig. 4.19: Depth-resolved CL spectra of uncoated (solid lines) and Au nanoparticle-coated *a*-plane ZnO (dashed lines) at (a) 10 K and (b) 80 K. $P = 17.5$ mW and scan area 10 µm × 10 µm.

in fig. 4.19b, the UV enhancement is slightly decreased to 1.9 and 1.3 for 5 kV and 10 kV, respectively. A greater enhancement is achieved at low acceleration voltages, when probing closer to the surface, while the enhancement factor is similar for different temperatures. The UV enhancement factors are presented in the table 4.4 below. The depth

Table 4.4: UV enhancement factors of the Au nanoparticle-coated *a*-plane ZnO at $HV = 5$ kV and 10 kV at a temperature of 10 K and 80 K.
The third column shows the UV enhancement calculated by diving the maximum intensity of the Au nanoparticle-coated *a*-plane ZnO by the that of the uncoated *a*-plane ZnO. The fourth column illustrates the ratio of the UV emission integrated from 3.10 eV to 3.45 eV.

HV (kV)	T (K)	UV enhancement (I)	UV enhancement (Int)
5	10	2.0	2.0
10	10	1.3	1.3
5	80	1.9	1.8
10	80	1.3	1.3

dependence is opposite to that in the Au nanoparticle-coated ZnO nanorods, where the largest enhancement factor was reached at the highest acceleration voltage. However, the maximum UV enhancement was also assumed to be closest to the ZnO-Au interface, as the random orientation of the hydrothermally-grown ZnO nanorods resulted in a larger excited surface area by the electron beam at higher acceleration voltages. However, in the planar sample, the 10 kV-electron beam cannot effectively excite more Au nanoparticles in the sample than at 5 kV, allowing for an actual correlation between the CL excitation depth and the UV enhancement factor. Therefore, it can be concluded that the origin of the UV enhancement is a surface-near effect.

Figure 4.19c and d displays the normalised NBE emission of the uncoated and the Au nanoparticle-coated *a*-plane ZnO at 10 K and 80 K. At 10 K, the shape of the normalised NBE emission is almost unchanged, while a slight blue shift is visible at 80 K. This could be due to an enhancement of individual emission lines in the NBE emission, following the Au nanoparticle-coating. A higher spectral resolution is needed to identify these lines; although the *a*-plane ZnO sample does not show any charging effects, the high-resolution spectra were collected with laser excitation, as shown below.

The DL emission, centered around 2.2 eV of the uncoated and the Au nanoparticle-coated *a*-plane ZnO at 10 K and 80 K is depicted in fig. 4.19e and f, respectively. It can be seen that the DL emission of both sides of the sample is comprised of more than one emission peak. As the defect chemistry in ZnO is still under controversial discussion in the literature, an unequivocal assignment of the defects in this sample is difficult. However, the yellow luminescence (YL), centered at 2.1 eV, which is typically attributed to substitutional Li (Li_{Zn}), as well as the green luminescence (GL) at 2.3 eV, most likely assigned

to zinc vacancies (V_{Zn}), can be found in this sample. A slightly enhanced DL emission, particularly at 10 K can be observed and can possibly be attributed to the passivation of non-radiative relaxation channels. Another possible explanation is change in the charge transfer level due to the surface band bending, resulting from the Au nanoparticle coating forming a Schottky barrier (cf. section 4.2).

To study the difference between electron beam and laser light excitation of the uncoated and the Au nanoparticle-coated *a*-plane ZnO, PL and CL spectra of the same area of the sample were collected at 80 K, as shown in fig. 4.20. To assure similar excitation depths with CL and PL, an acceleration voltage of 5 kV was used in CL, which translates into approximately 88 nm, while the laser penetration depth is ~ 100 nm (cf. section 3.2.6). In fig. 4.20, it can be seen that the DL emission is higher for the laser excitation, as discussed and shown for ZnO nanorods in fig. 4.7. The higher DL emission intensity for laser exci-

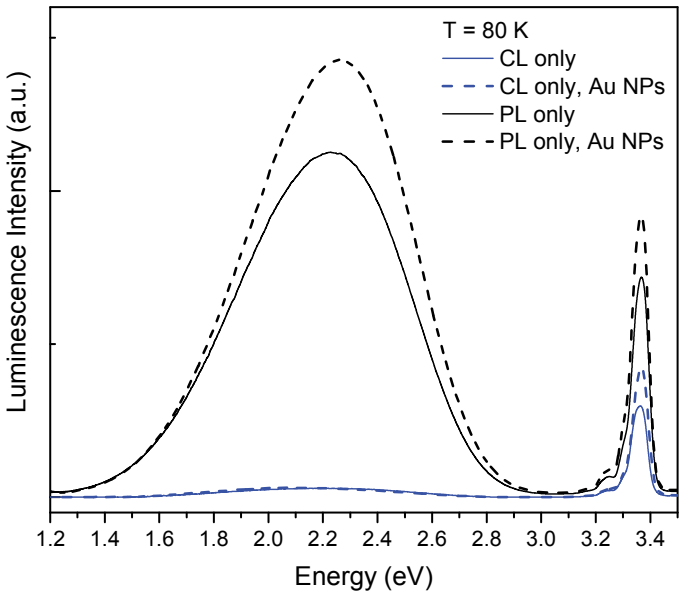

Fig. 4.20: (a) CL and PL spectra of uncoated (solid lines) and Au nanoparticle-coated *a*-plane ZnO (dashed lines) at $T = 80$ K, showing an increased DL emission as well as higher enhancement factor for laser excitation than for electron beam excitation.
CL: $P = 30\,\mu$W, $HV = 5$ kV and scan area of 15 µm $\times$ 15 µm.
PL: $\lambda_{exc} = 325$ nm, $P = 150\,\mu$W, spot size ~ 30 µm.

tation can be explained by a lower excitation power density of the laser, compared to that of the electron beam. As discussed above, the defect recombination channels with longer lifetimes can be saturated by the higher power density of the electron beam, while these effects are less pronounced with lower power density of the laser excitation.
A similar UV enhancement factor of ~ 1.3 times for laser excitation is achieved, while the

CL shows a 1.4-enhanced UV emission. Note that those enhancement factors are calculated, using the maximum intensity of the UV emission only, while the comparison of the integrated UV emission is more suitable, as it takes broadening effects and peak shifts into account, which is illustrated in table 4.5.

Table 4.5: UV enhancement factors of the Au nanoparticle-coated *a*-plane ZnO in PL and CL (5 kV) at a temperature of 80 K.
The third column shows the UV enhancement calculated by diving the maximum intensity of the Au nanoparticle-coated *a*-plane ZnO by the that of the uncoated *a*-plane ZnO. The fourth column illustrates the ratio of the UV emission integrated from 3.10 eV to 3.45 eV.

Type of excitation	T (K)	UV enhancement (I)	UV enhancement (Int)
CL (5 kV)	80	1.4	1.4
PL	80	1.3	1.3

Furthermore, the PL enhancement factor as a function of excitation power was investigated. In fig. 4.21a, the PL, integrated from 3.00 eV to 3.54 eV of the uncoated and the Au nanoparticle-coated *a*-plane ZnO is graphed logarithmically as a function of laser excitation power. The super-linear power law exponent of the uncoated *a*-plane ZnO with (1.10 ± 0.01) is slightly lower than that of the Au nanoparticle-coated side of the sample (1.14 ± 0.01). The corresponding UV enhancement as a function of laser excitation power

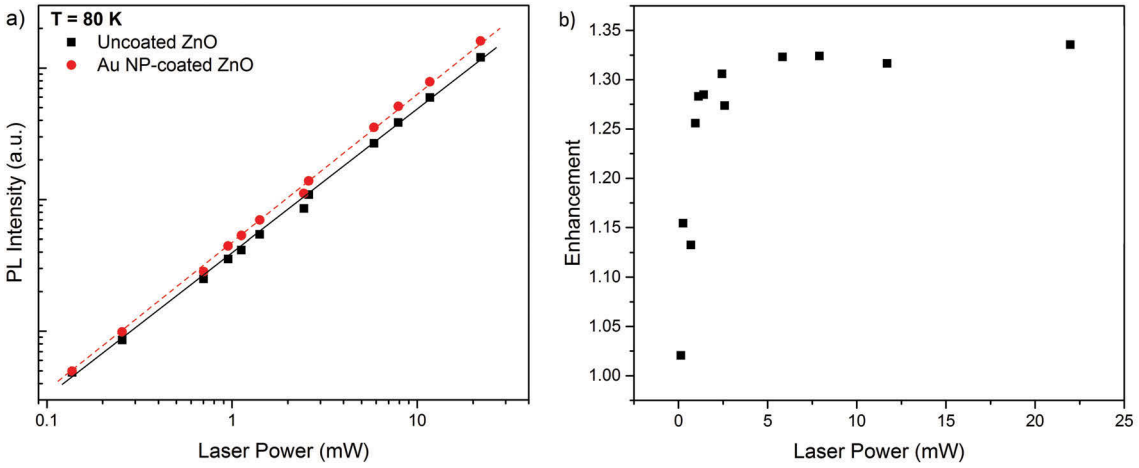

Fig. 4.21: (a) PL integrated from 3.00 eV to 3.54 eV of uncoated (black) and Au nanoparticle-coated (red) *a*-plane ZnO as a function of laser excitation power, plotted logarithmically. The lines serve as a guide of the eye. (b) Power-dependent UV enhancement of Au nanoparticle-coated *a*-plane ZnO.
$\lambda_{exc} = 325$ nm, spot size ~ 30 µm.

is displayed in fig. 4.21b, showing an increased enhancement with increasing power up to approximately $P_{exc} = 3$ mW, while it is saturated for higher laser powers. This saturation

effect of the UV enhancement with increasing laser excitation power can be explained by the saturation of non-radiative defects in the Au nanoparticle-film or band flattening of the electron-hole-pair field in the depletion layer due to the Schottky barrier formed at the Au-ZnO-interface, as discussed in section 4.2.
The PL enhancement in the Au nanoparticle-coated *a*-plane ZnO single crystals is low over the entire range of excitation powers. In comparison, the Au nanoparticle-coated ZnO nanorods showed an overall excitation power-independent enhancement of 2.4 (cf. fig. 4.16). However, the power law exponent of the uncoated ZnO nanorods was found to be unchanged following the Au nanoparticle coating (section 4.4.3); while the super-linear power law exponent of the *a*-plane ZnO sample increases approximately 0.04, resulting in a saturation effect of the UV enhancement with increasing excitation power.

To study the temperature behaviour of the uncoated and Au nanoparticle-coated *a*-plane ZnO, high-resolution PL spectra of the NBE were collected from 10 K to 250 K, which are shown in fig. 4.22a and fig. 4.22b, respectively. The typical red-shift and broadening of the emission peaks with increasing temperature, due to increasing phonon interaction, is observed for both sides of the sample. The spectra clearly show the DBX transitions at low temperature, mainly the I_4 line (cf. table 2.1) and a shoulder around 3.38 eV, which can be assigned to FX transitions. With increasing temperature the spectra are dominated by FX transitions, while the DBX emission intensity is significantly decreased due to thermalisation.

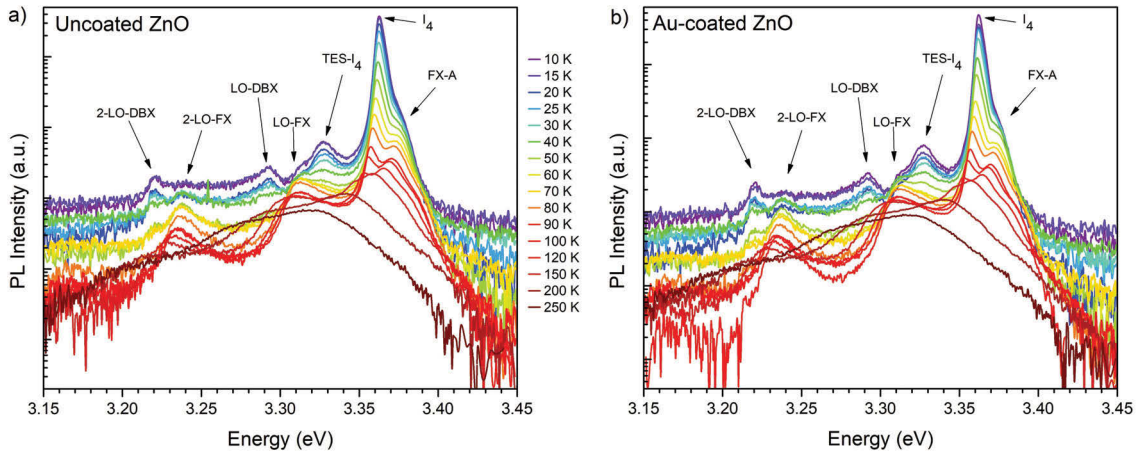

Fig. 4.22: Temperature-dependent PL spectra of (a) uncoated and (b) Au nanoparticle-coated *a*-plane ZnO.
$\lambda_{exc} = 325\,nm$, $P = 2.4\,mW$, spot size $\sim 30\,\mu m$.

The temperature-dependent enhancement as a function of energy was calculated to gain more insight into the enhancement mechanism. Here, the spectrum of the Au nanoparticle-coated *a*-plane ZnO was divided by that of the uncoated for each temperature from

10 K to 100 K, allowing direct comparison of the temperature-dependent UV enhancement as a function of energy, as depicted in fig. 4.23. The data at higher temperatures are omitted due to the large noise contribution. It is striking that the enhancement of the UV emission of the Au nanoparticle-coated *a*-plane ZnO of approximately 1.3 times is smaller than that of the ZnO nanorods with ~ 2.3. Similar to the Au nanoparticle-coated

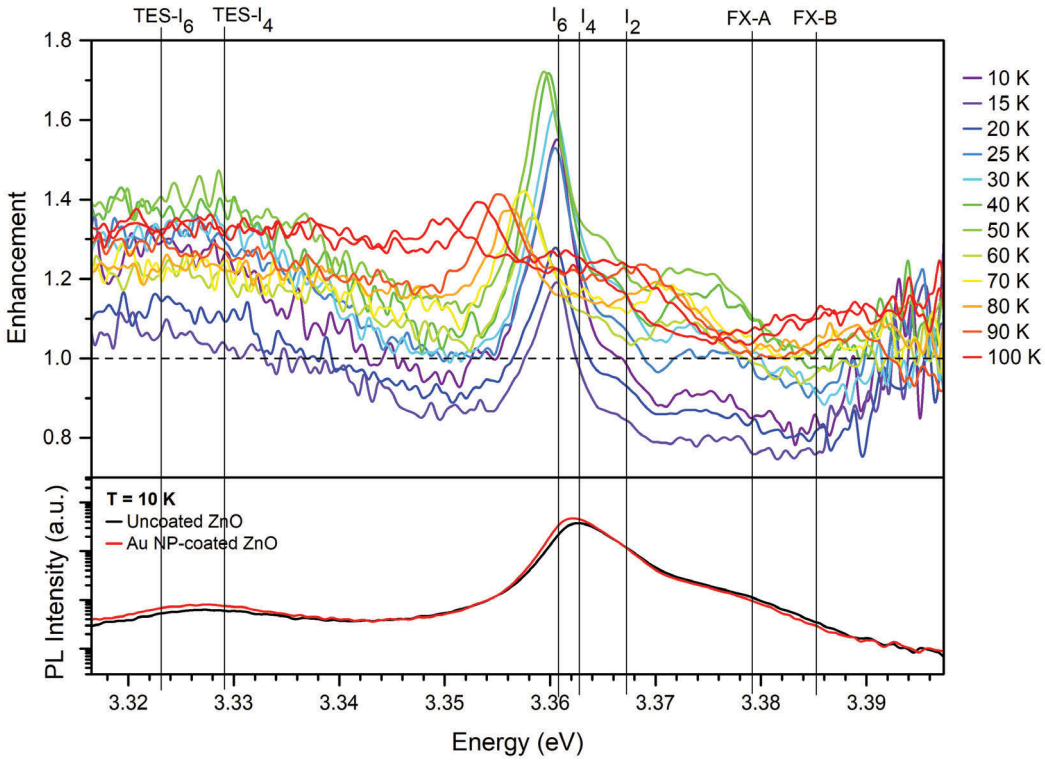

Fig. 4.23: Top: Temperature-dependent PL enhancement factor of Au nanoparticle-coated *a*-plane ZnO as a function of energy, showing that highest enhancement factors are at the DBX-related emissions. The position of the assigned individual emission lines are at 10 K.
Bottom: 10 K-high-resolution PL of uncoated *a*-plane ZnO (black) and Au nanoparticle-coated *a*-plane ZnO (red), plotted on a semi-logarithmic scale. $\lambda_{exc} = 325$ nm, $P = 2.4$ mW, spot size ~ 30 µm.

ZnO nanorods, the Au nanoparticle-coated *a*-plane ZnO shows the greatest enhancement at the DBX and its related emissions — TES and LO-phonon replica. As the DBX thermalises with increasing temperature, it is not surprising that this enhancement gradually reduces at higher temperatures; an equally distributed enhancement over the whole energy range is found for temperatures higher than 100 K. This is comparable to the ZnO nanorods discussed above, indicating that the enhancement mechanism is the same, but more pronounced for Au-ZnO nanostructures. This is most likely due to a larger surface-to-area ratio of the ZnO nanorods.

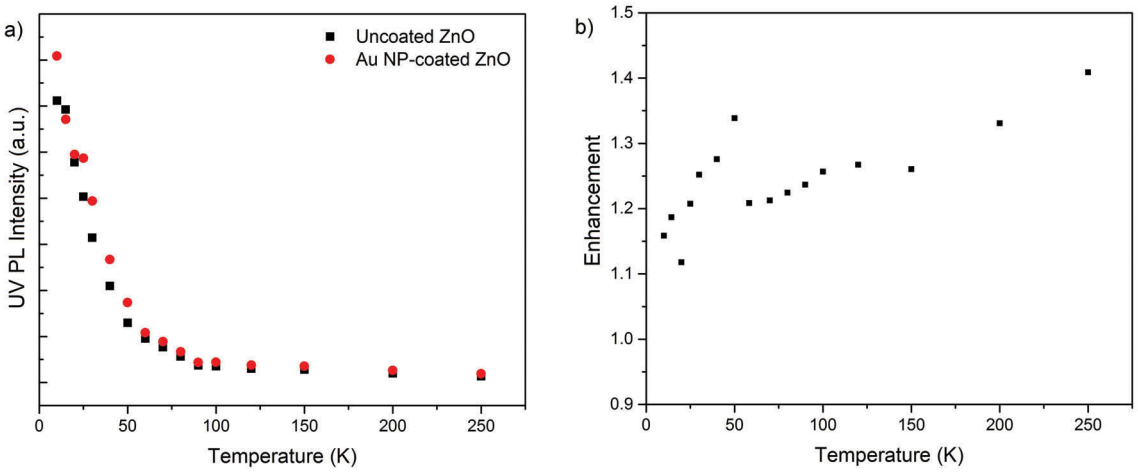

Fig. 4.24: (a) PL integrated from 3.00 eV to 3.54 eV of uncoated (black) and Au nanoparticle-coated (red) *a*-plane ZnO as a function of temperature. (b) Temperature-dependent UV enhancement of integrated PL of Au nanoparticle-coated *a*-plane ZnO.
$\lambda_{exc} = 325\,nm$, $P = 2.4\,mW$, spot size $\sim 30\,\mu m$.

Figure 4.24 shows the integrated PL from 3.00 eV to 3.54 eV as a function of temperature for uncoated and Au nanoparticle-coated *a*-plane ZnO; fig. 4.24b depicts the temperature-dependent UV enhancement factor. The UV emission is roughly 1.3-fold enhanced over the entire temperature range, being similarly temperature-independent as observed with the ZnO nanorods.

4.5.2 Concurrent CL and PL of Au Nanoparticle-Coated *a*-plane ZnO

Similar to the ZnO nanorods coated with Au nanoparticles, the concurrent CL-PL spectroscopy — with additional laser excitation at $\lambda_{exc} = 532\,nm$ — was performed on the Au nanoparticle-coated *a*-plane ZnO single crystals to probe the charge transfer mechanism (cf. fig. 2.10). The corresponding spectra at 10 K can be seen in fig. 4.25, showing no further enhancement of the UV emission with the additional green laser excitation. Note that the emissions at 2.33 eV and 1.75 eV are due to laser artifacts. As expected, the CL shows an increased UV emission due to Au nanoparticle-coating with an approximate enhancement factor of 1.4, while the separate green laser illumination only excites the emissions in the visible. The uncoated side of the sample can only show defect-related emissions, but a slight increase is visible for the Au nanoparticle-coated side. This can be explained by excited LSPs in the Au nanoparticles.
The spectra of simultaneous electron beam and green laser excitation show in an emission in the visible spectral range, which is equal to the sum of the separate CL and PL

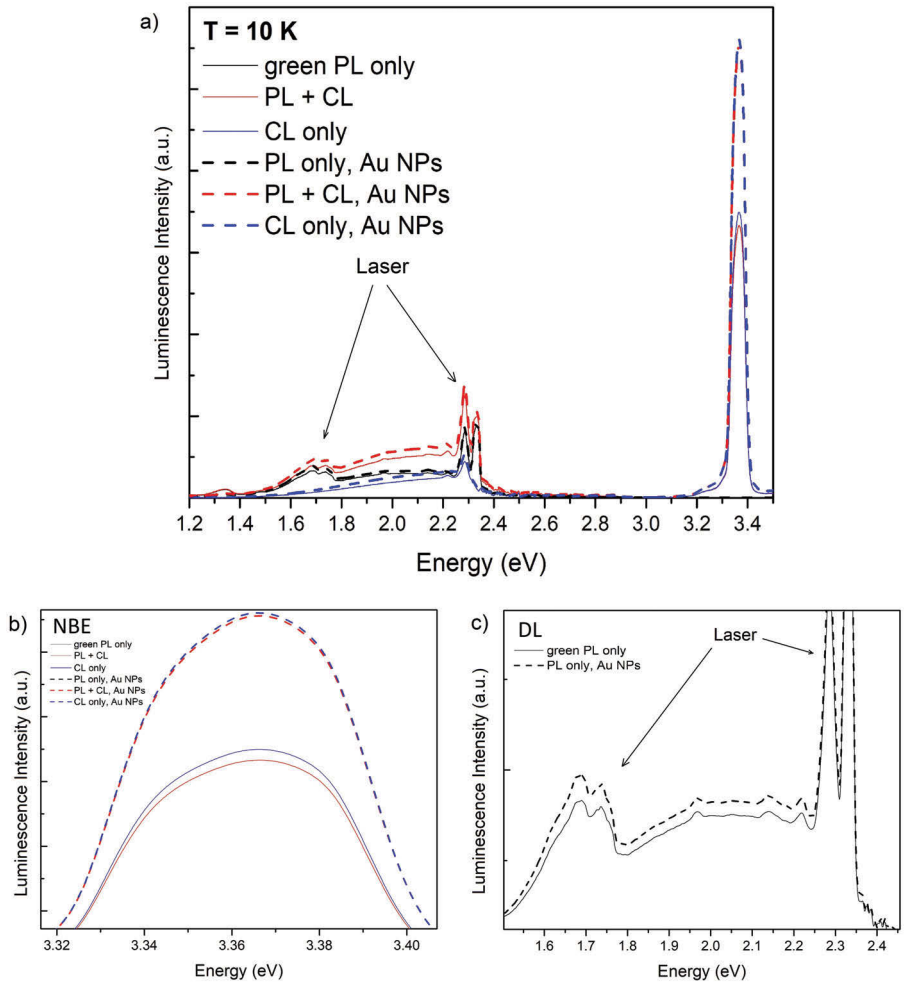

Fig. 4.25: (a) Concurrent CL and PL of the uncoated (solid lines) and Au nanoparticle-coated *a*-plane ZnO (dashed lines) at $T = 10\,\mathrm{K}$. The emissions at 2.33 eV and 1.75 eV are reflections of the incident laser light. (b) NBE emission, showing no further enhancement of the UV emission by the additional green laser excitation. (c) DL emission
CL: $P = 8.6\,\mu\mathrm{W}$, $HV = 5\,\mathrm{kV}$ and scan area $15\,\mu\mathrm{m} \times 15\,\mu\mathrm{m}$.
PL: $\lambda_{\mathrm{exc}} = 532\,\mathrm{nm}$ and $P = 16.0\,\mathrm{mW}$.

for both uncoated and Au nanoparticle-coated *a*-plane ZnO (see fig. 4.25c). The UV emission, shown in fig. 4.25b, is similarly intense for separate electron beam excitation as for the concurrent excitation. This can be seen for both sides of the samples, indicating that the LSPs created in the Au nanoparticles do not enhance the UV emission in this sample. This result is similar to that of the Au nanoparticle-coated ZnO nanorods, although the DL emission of the *a*-plane ZnO single crystals, centered at $\sim 2.2\,\mathrm{eV}$, is much closer to the LSPR of the Au nanoparticles ($E_{\mathrm{LSP}} = 2.25\,\mathrm{eV}$). This indicates that the enhancement in the *a*-plane ZnO-samples, as well as the Au nanoparticle-coated ZnO nanorods, cannot be attributed to the charge transfer mechanism, shown in fig. 2.10, as no hot electrons are

being injected from the Au nanoparticles into the conduction band of ZnO.

4.5.3 Time-resolved PL of Au Nanoparticle-Coated *a*-plane ZnO

TR-PL was used to determine the lifetimes of the minority charge carriers in uncoated and Au nanoparticle-coated *a*-plane ZnO. These were collected at a fixed collection energy of the DBX, at 10 K. Figure 4.26 shows the temporal decays of the uncoated and the Au nanoparticle-coated *a*-plane ZnO at 10 K, respectively, and their bi-exponential fits, which were de-convoluted with the laser response. The corresponding lifetimes for the

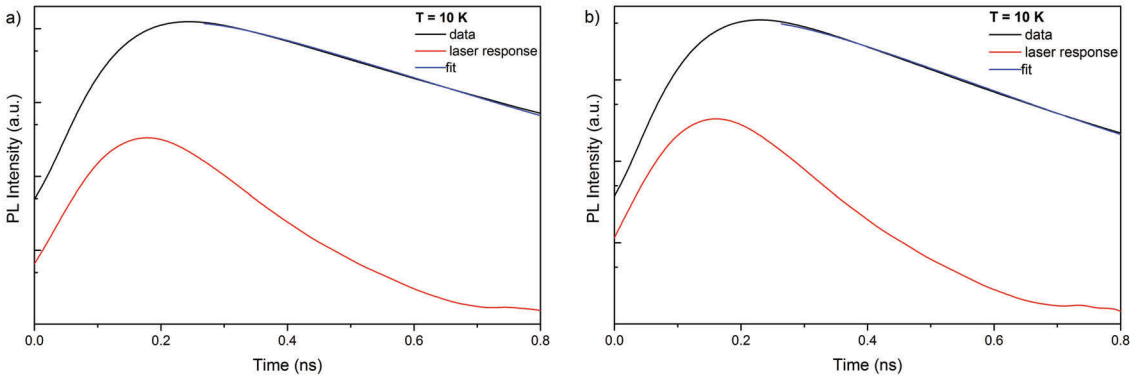

Fig. 4.26: Time-resolved PL of (a) uncoated and (b) Au nanoparticle-coated *a*-plane ZnO at a fixed collection wavelength of 369 nm and a temperature $T = 10\,\mathrm{K}$.
The raw data is shown in black, the laser response in red and the bi-exponential fit in blue.

uncoated *a*-plane ZnO at $T = 10\,\mathrm{K}$, similarly obtained as in eq. (4.6), can be determined to be:
$\tau_{\mathrm{R}} = (190 \pm 5)$ps and $\tau_{\mathrm{NR}} = 24.4\,\mathrm{ps}$.
The shorter lifetime, typically attributed to non-radiative recombination, such as surface states or trapping, is too short to calculate it and its uncertainty. A better time resolution of the experimental setup would be needed to reliably measure the lifetime below 70 ps. The comparison with the TR-PL results of the hydrothermally-grown ZnO nanorods reveals that the radiative lifetime of $\tau_{\mathrm{R,\,ZnO\,NRs}} = (129.4 \pm 4.5)$ ps is slightly lower than that of the *a*-plane ZnO single crystal.
The lifetimes of the Au nanoparticle-coated *a*-plane ZnO are the following:
$\tau^*_{\mathrm{R}} = (166 \pm 5)$ ps and $\tau^*_{\mathrm{NR}} = 23.8\,\mathrm{ps}$. Note that the non-radiative lifetimes are below the resolution of the experimental setup. Note that the non-radiative lifetimes are very similar, suggesting no change in the surface states. However, the measured lifetimes are already at the resolution limit of the experimental setup, which makes it questionable to comment on these results conclusively. Whereas the longer radiative lifetime has obviously shortened for the Au nanoparticle-coated *a*-plane ZnO, which indicates the

formation of an additional, faster relaxation channel.
The Purcell enhancement factor, calculated as per eq. (4.8), is relatively low:
$F_{\mathrm{P}} = (1.14 \pm 0.03)$. This is slightly lower than the CL and PL enhancement of 1.3.
The results of the TR-PL measurements of uncoated and Au nanoparticle-coated *a*-plane ZnO as well as ZnO nanorods are shown in table 4.6 below.

Table 4.6: Summary of measured lifetimes and Purcell enhancement factor, F_{P}, of uncoated and Au nanoparticle-coated *a*-plane ZnO and ZnO nanorods.

Sample	T (K)	τ_{NR} (ps)	τ_{R} (ps)	F_{P}
Uncoated *a*-plane ZnO	10	24.4	(190 ± 5)	N/A
Au-coated *a*-plane ZnO	10	23.8	(166 ± 5)	(1.14 ± 0.03)
Uncoated ZnO nanorods	8	(25.2 ± 3.2)	(129.4 ± 4.5)	N/A
Au-coated ZnO nanorods	8	(21.5 ± 1.5)	(91.0 ± 15.2)	(1.4 ± 0.1)

It can be concluded, that a reduced lifetime is observed due to the presence of the Au nanoparticles, in both type of samples. However, the reduction in lifetime is more pronounced for the ZnO nanorods with $F_{\mathrm{P}} = (1.4 \pm 0.1)$ than that of the Au nanoparticle-coated *a*-plane ZnO ($F_{\mathrm{P}} = (1.14 \pm 0.03)$), which is consistent with the higher UV enhancement factor of 2.3 of the Au nanoparticle-coated ZnO nanorods, compared with that of the *a*-plane ZnO single crystal. The F_{P} of both types of samples obtained from the TR-PL measurements are, however, too low to fully explain the luminescence enhancement.

4.5.4 Summary of the Au Nanoparticle-Coated *a*-plane ZnO Singe Crystals

In summary, the *a*-plane ZnO single crystals coated with Au nanoparticles show a similar behaviour under laser and electron beam excitation with a lower overall UV enhancement of ~ 1.4 in PL and CL, compared to the 2.3-fold enhancement of the Au nanoparticle-coated ZnO nanorods. The greater UV enhancement of the Au nanoparticle-coated ZnO nanorods is most likely due to a greater surface-to-volume ratio, allowing for larger surface area coated with Au nanoparticles compared with that of the *a*-plane ZnO single crystal.
With increasing laser excitation power, the UV enhancement saturated for powers larger than 3 mW, which can be possibly attributed to an increased super-linearity of the power law exponent, following the Au nanoparticle coating. Furthermore, a reduced radiative lifetime of the *a*-plane ZnO from (190 ± 5) ps to (166 ± 5) ps due to the presence of the Au nanoparticles was found, indicating that an additional, faster relaxation channel was created via the Au nanoparticles. The corresponding Purcell enhancement is as small as

(1.14 ± 0.03), which is lower than the actual luminescence enhancement of the UV emission in the Au nanoparticle-coated *a*-plane ZnO. This suggests that the LSPs in the Au nanoparticles do not directly couple to the excitons in the ZnO, which will be further discussed below (section 4.6 and section 4.7). The charge transfer mechanism, shown in fig. 2.10, can also be excluded, as no hot electrons from the Au nanoparticles were injected into the conduction band of the ZnO under concurrent CL and PL ($\lambda_{exc} = 532\,nm$) excitation.

4.6 FDTD simulations of Au Nanoparticle-Coated ZnO

The UV enhancement of the Au nanoparticle-coated ZnO — planar and nanostructured — discussed in the previous sections, can be simulated by using the 3D FDTD methods, introduced in section 3.2.9. The origin of this enhancement can be due to two factors: excitation and Purcell enhancement, which can both contribute to different extents.
Here, the simulation was set with a ZnO ($n = 2.0$) substrate coated with spherical Au nanoparticles of a diameter of 5 nm. Note that a planar ZnO substrate was used, as the diameter of the ZnO nanorods of $\sim 40\,nm$ is much larger than the Au nanoparticle-coating of 5 nm. Thus, this simulation can be used for comparison of the *a*-plane ZnO as well as the ZnO nanorods.

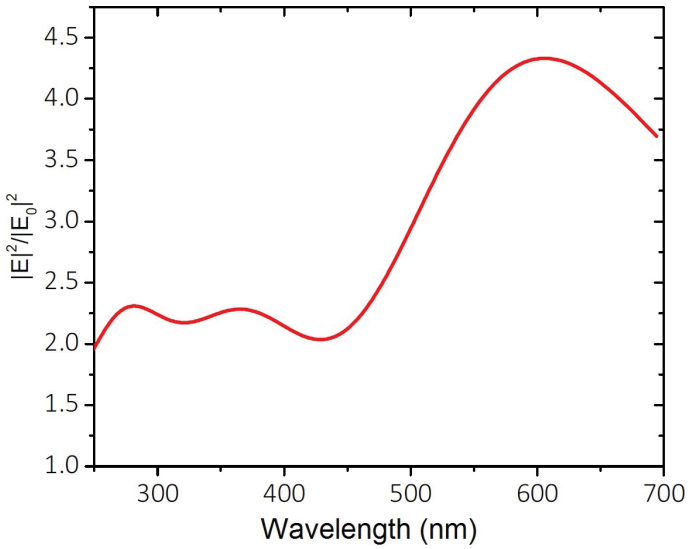

Fig. 4.27: FDTD simulation of ZnO decorated with 5 nm-Au nanoparticles, showing wavelength-dependent excitation enhancement of 2 to 4.

The excitation enhancement as a function of excitation wavelength is depicted in fig. 4.27. It can be seen that the electric field intensity of the ZnO with the Au nanoparticle-coating is higher than that without for all excitation wavelengths. Furthermore, an increase from approximately 2.2 times at 250 nm to 450 nm (2.75 eV to 4.95 eV) to $\sim$ 4.2 times at longer

wavelengths is apparent. This can be explained by the LSPR of the 5 nm-Au nanoparticles in the visible spectral range, which is in accordance with the measured LSPR in fig. 4.5 of approximately 550 nm, which is equivalent to $E_{\mathrm{LSP}} = 2.25\,\mathrm{eV}$.
To simulate the resulting Purcell enhancement of the 5 nm-Au-ZnO structure, a radiating dipole was placed within the ZnO substrate at a wavelength of 370 nm to simulate the excitonic emission of ZnO. This dipole was subsequently moved deeper into the ZnO substrate from 3 nm to 15 nm, simulating excitons at greater distances from the Au-ZnO interface to study the exciton coupling strength to the plasmonic modes in the Au nanoparticles as a function of distance. In fig. 4.28, the total radiated power of the dipole of the

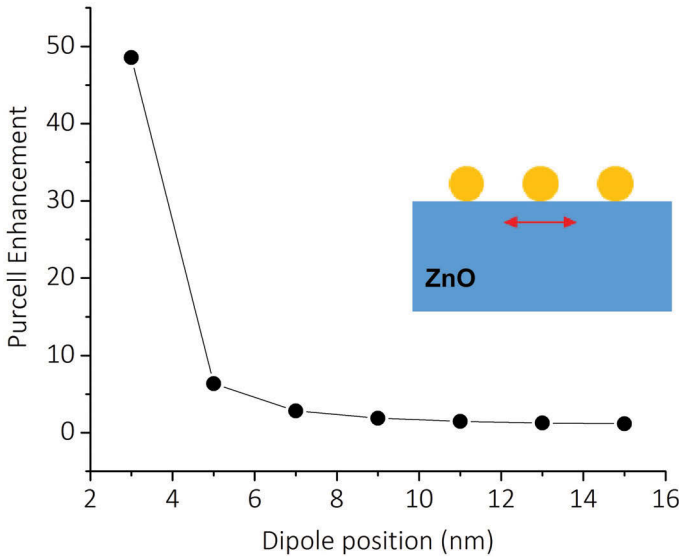

Fig. 4.28: Depth-dependent Purcell enhancement of 5 nm-Au nanoparticle-coated ZnO, simulated by FDTD method. The inset shows the simulated structure of the ZnO substrate in blue, the 5 nm-Au nanoparticles in yellow and the dipole radiation in red.

Au nanoparticle-coated ZnO divided by the uncoated ZnO is shown as a function of the depths of the dipole position from the interface or surface of the ZnO. An increased localised density of states (LDOS) can be found due to the Au nanoparticle-coating, which allows coupling between these plasmonic modes with the emitter, which is known as the Purcell effect.
It is remarkable that the simulated Purcell enhancement factor is as high as 50 for very surface-near plasmonic coupling, while it rapidly reduces to ~ 6 at a dipole depth in ZnO of 3 nm.
A depth dependence of the UV enhancement factor was also found in the depth-resolved CL results (fig. 4.11 and fig. 4.19), but on a larger depth scale. Experimentally, the greatest enhancement was achieved at a depth of approximately 90 nm ($HV = 5\,\mathrm{kV}$), while a less enhanced UV-CL was found at higher acceleration voltages (10 kV, translating to roughly

350 nm CL excitation depth). According to the simulation, no Purcell effect would be taking place at those depths, suggesting that this is not the underlying mechanism for the observed UV enhancement in the samples studied in this work. This is consistent for the comparison of the simulation with the experimentally obtained $F_{\mathrm{P}} = (1.4 \pm 0.1)$ (eq. (4.8)) in the Au nanoparticle-coated ZnO nanorods, indicating a much weaker coupling strength, although the electron-hole-pair excitation depth in TR-PL cannot be taken into account. An even lower F_{P} of $\sim (1.14 \pm 0.03)$ was found for the Au nanoparticle-coated *a*-plane ZnO single crystal.
In addition, the simulated excitation enhancement can be compared with the PL results in fig. 4.13. At an excitation wavelength of 325 nm as used in the experiments, an excitation enhancement of 2.2 can be simulated, as shown in fig. 4.27. This is comparable with the averaged 2.3 times enhanced PL in the Au nanoparticle-coated ZnO nanorods, while the enhancement factor of the Au nanoparticle-coated *a*-plane ZnO samples was as low as 1.3. However, the simulated Purcell enhancement factor is typically substantially larger than the experimentally obtained F_{P}, as no losses are taken into account in the simulations.
Note that the CL results cannot be simulated with the FDTD simulation, as it does not excite the sample at a certain wavelength, the energetic electron beam rather excites all recombination channels in the sample. However, the enhancement factors are simulated for the electric field of the laser light, which cannot be similarly adapted for the electron beam excitation.
In conclusion, both excitation and Purcell enhancement can add up to a comparable enhancement factor observed in the CL and PL results of both, planar and nanostructured ZnO coated with Au nanoparticles. However, both enhancement mechanisms show different simulation and experimental results, which does not allow any of these two mechanisms to fully explain the origin of the UV-enhancement of the Au nanoparticle-coated ZnO.

4.7 Discussion

To discuss and interpret the results of the Au nanoparticle-coated ZnO, a summary of the results presented in this chapter is given below.

- The transmission spectra of Au nanoparticle-coated *a*-plane ZnO shows a LSP absorption band, centered at $E_{\mathrm{LSP}} = 2.25\,\mathrm{eV}$, which is characteristic for spherical Au nanoparticles with a diameter of 5 nm. This is in accordance with the SEM results, showing a uniform film of well separated and uniformly distributed 5 nm-Au nanoparticles.

- VB-XPS spectra show a change in surface band bending, from downward for uncoated ZnO to upward for Au nanoparticle-coated ZnO, indicating the formation of a Schottky barrier at the ZnO-Au interface.
- CL and PL spectra of Au nanoparticle-coated ZnO show enhanced UV-emission, while the DL emission is unchanged.
  - The depth-resolved CL intensity of ZnO nanorods is up to 6.3 times enhanced by Au nanoparticles, with the highest measured enhancement closest to the ZnO-Au interface. Due to the random orientation of the ZnO nanorods, a greater surface area of the ZnO nanorods is excited by the electron beam at 10 K than at 3 kV, resulting in the highest UV enhancement at 10 kV. Increased charging effects at low temperature (10 K) of the uncoated ZnO nanorods compared to the Au nanoparticle-coated side of the sample makes a direct spectral comparison difficult. The unaffected PL spectra, however, showed an average UV enhancement of 2.3, which is independent of temperature and excitation power.
  - Similar results were achieved for Au nanoparticle-coated *a*-plane ZnO single crystals but with lower CL and PL enhancement factors of 2.0 and 1.3, respectively. No temperature dependence was observed in the range of 10 K to 250 K. An increased enhancement with increasing electron beam and laser excitation power of approximately 0.1 was found, which saturates for powers above 100 µW and 3 mW, respectively.
- The simultaneous electron beam and green laser excitation of Au nano-particle-coated ZnO showed an increased visible emission, while the UV emission was unaffected. The increased visible emission can be attributed to both the defect-related DL emission in ZnO and the creation of LSPs in the 5 nm-Au nanoparticles. However, the UV emission under concurrent excitation was unchanged compared to the separate electron beam excitation, indicating that no charge was transfered from the Au nanoparticles to the conduction band of ZnO, as showed in the fig. 2.10.
- The TR-PL measurements show a decreased radiative lifetime for ZnO with Au nanoparticle-coating, indicating the creation of an additional, faster decay pathway through the Au nanoparticles.
  - The Purcell enhancement factor of approximately 1.4 of Au nanoparticle-coated ZnO nanorods cannot fully explain the 3.8-fold and the 2.3 times enhancement in CL and PL, respectively.

– A similar behaviour can be found for the Au nanoparticle-coated *a*-plane ZnO with a smaller $F_{\mathrm{P}} = 1.13$. This is also lower than the CL and PL enhancement factor of 2.0 and 1.3, respectively.

Different mechanisms or a combination of them can be the origin of the UV-enhancement in those samples:

1. **Increased surface roughness** due to the Au nanoparticles.
2. **Change of refractive index** n due to the Au nanoparticle-coating, which can effectively change n (effective medium theory).
3. **Charge transfer mechanism**, where the DL emission of the ZnO excites the LSPs in the Au nanoparticles, which decay into hot carriers. The resulting hot electrons can then transfer to the energetically close conduction band of ZnO, enhancing the UV emission of the Au nanoparticle-coated ZnO. (Figure 2.10)
4. **LSP-exciton coupling**, a direct dipole-dipole coupling between the excitons in ZnO and the LSPs in the Au nanoparticles. This enhances the SER due to the creation of an additional, faster relaxation channel. (Figure 2.9)
5. **Excitation enhancement**, the incident emission is enhanced by the Au nanoparticles, as discussed in fig. 4.27.
6. **Cavity effect** in ZnO nanorods, enhancing the incident radiation by increased reflection off the walls by Au nanoparticles.
7. **Faster, additional relaxation pathway** through transitions in Au, such as interband transitions.

To address the first point in section 4.7, it can be assumed that the surface roughness of 1 nm of the uncoated ZnO might be be increased due to the 5 nm-Au nanoparticles. However, the surface roughness of the 5 nm-Au nanoparticle-coated ZnO surface is too small to result in an enhanced luminescence. Typically, the nanostructured surface has to be in the order of tens to hundreds of nanometres to have the effect of surface roughening [6, 193, 194]. Furthermore, an overall enhanced luminescence is expected for increased surface roughness, which is not in accordance with the enhanced UV and unchanged DL emission of the Au nanoparticle-coated ZnO. Moreover, this effect would not explain the UV-enhancement of the ZnO nanorods decorated with Au nanoparticles. The nanorod film itself can be considered as rough surface, while the Au nanoparticle-coating does presumably not significantly increase the overall roughness.
An Au nanoparticle surface coating can supposedly change the effective refractive index of the sample, but similarly as discussed above, a thicker layer is needed to successfully

apply the effective medium theory. If anything, in this theory, a metallic surface coating is most likely to absorb or reflect light, which would result in the opposite effect to the observed UV enhancement [103, 113].

At first glance, it may appear that the most likely reason for the enhancement of the Au nanoparticle-coated ZnO are the two plasmonic coupling models — the charge transfer mechanism and the LSP-exciton coupling — as a broad LSP absorption band was found in the transmission spectrum of Au nanoparticle-coated *a*-plane ZnO.

However, the charge transfer mechanism can be excluded, as the concurrent CL and PL ($\lambda_{\text{exc}} = 532\,\text{nm}$) generated additional LSPs in the Au nanoparticles, but the UV emission was not further enhanced, which indicates that hot electrons transfer from Au to the conduction band of the ZnO is not the reason for the enhancement. Furthermore, the absorption of the green luminescence in ZnO by the Au nanoparticles is typically used in the literature to explain the resonant excitation of the LSPs in the Au nanoparticles. In the case of the Au nanoparticle-coated ZnO nanorods in this work, only a very weak DL emission, centered at 1.8 eV, is present, which is energetically too far from the Au nanoparticles' LSPR ($E_{\text{LSP}} = 2.25\,\text{eV}$) for resonant excitation. However, the results of the *a*-plane ZnO coated with Au nanoparticles do not show any evidence of hot electron transfer from Au to ZnO's conduction band, despite showing the green defect component in the DL (approximately 1.6 eV to 2.8 eV). Although both samples show different DL emissions, the charge transfer mechanism, probed with concurrent CL-PL, was found to not be responsible for the observed enhancement.

The excitation enhancement, simulated by the FDTD method, showed a similar enhancement as the integrated PL enhancement of approximately 2.2 compared with the measured UV enhancement of 2.5 in the UV region. Although the excitation enhancement can possibly be the origin in PL of both the ZnO nanorods and *a*-plane ZnO coated with Au nanoparticles, the slightly larger CL enhancement cannot be simulated with the FDTD method. Here, the enhancement of the electric field of the incident laser light is simulated, which cannot be adapted for the excitation of all recombination channels with the electron beam. The slightly higher CL enhancement factor is most likely due to an approximately four orders of magnitude higher excitation power density by the electron beam, compared with the laser excitation density. Thus, the excitation enhancement alone cannot explain the enhanced UV emission in CL and PL.

In the case of the Au nanoparticle-coated ZnO nanorods, the enhancement could be explained by a cavity effect, where certain modes are constructively enhanced within a single nanorod. The Au nanoparticle surface coating can act as a semi-reflective mirror, which can further enhance these modes. As no single ZnO nanorods have been investigated in this work, the UV enhancement arising from a cavity effect cannot be excluded. However, similar results were shown from Au nanoparticle-coated *a*-plane ZnO as for

the ZnO nanorods coated with Au nanoparticles, which cannot be explained by the cavity effect because of the larger thickness of the planar *a*-plane ZnO single crystals.
The LSP-exciton-coupling mechanism (cf. fig. 2.9) is unlikely to be responsible for the UV enhancement in PL and CL, due to a low — if any — spectral overlap between the excitonic emission from ZnO and the LSPR in the Au nanoparticles, as they are energetically separated by 1.2 eV (180 nm).
Nevertheless, the TR-PL measurements revealed a shortened lifetime for both types of samples. While a reduced lifetime is a commonly reported indicator of LSP-exciton coupling, the calculated Purcell enhancement factors are too small compared with the enhancement factors in CL and PL. These results, however, suggest that indeed an additional, faster relaxation channel was created through the Au nanoparticles, but not necessarily via the LSPs in Au.
The simulated Purcell enhancement factor in section 4.6 is strongly depth-dependent within the first 10 nm from the Au-ZnO-interface. In this range, the F_P decreases exponentially from 50 to 1. Conversely, the depth-resolved CL results show an increased UV enhancement for CL excitation depths of up to 88 nm, followed by a decrease for greater depths. It is noteworthy, that the Schottky barrier (cf. section 4.2), formed at the interface of Au and ZnO, was not taken into account in the FDTD simulations. However, the upward surface band bending results in an electric field, leading to charge separation at the ZnO-Au interface. An excitation power threshold has to be overcome to effectively enhance the Au nanoparticle-coated ZnO (cf. excitation power saturation in fig. 4.16 and fig. 4.21).
While the charge transfer mechanism can be excluded, as no hot electron transfer from the Au nanoparticles into the conduction band of the ZnO under simultaneous electron beam and green laser ($\lambda_\mathrm{exc} = 532\,\mathrm{nm}$) excitation, LSPs are created. The direct dipole-dipole coupling between the LSPs in the Au nanoparticles and the excitons in the ZnO is unlikely, as the reduction of the lifetime and the resulting F_P are substantially lower than the UV enhancement factor in CL and PL. In addition, little to no spectral overlap between the LSPR in the Au nanoparticles ($E_\mathrm{LSP} = 2.25\,\mathrm{eV}$) and the excitons in the ZnO at 3.37 eV can be assumed. Nevertheless, an additional, faster decay channel was created, indicated by a reduced lifetime due to the presence of the Au nanoparticles. The only requirements for this relaxation pathway are:

1. their energy difference is close to that of the excitonic emission of ZnO (3.36 eV) and
2. this relaxation channel is faster than the excitonic recombination in ZnO.

It is reported in the literature that interband transitions in Au can fulfill both the above requirements [195–198]. The interband transitions in Au are mainly in the UV spectral range and allow excitation of electrons from the occupied $5d$ band to the hybridised $6sp$

conduction band, which is partly filled. The energy threshold of the interband transitions is approximately 2.4 eV with a lower energy tail starting at 1.8 eV. [199, 200] The relativistic band structure calculation in [202] have shown that the lowest energy to promote an electron from the $5d$ to the $6sp$ band is 1.6 eV for the $L^*_{6+5} - L^-_4$ transition [4, 201, 202]. The HeCd-laser with an excitation wavelength of $\lambda_{\text{exc}} = 325\,\text{nm}$ ($\sim 3.81\,\text{eV}$), as well as the excitonic emission from ZnO (3.0 eV to 3.45 eV) allow excitation of the lowest interband transitions in Au ($L^*_{6+5} - L^-_4 \Rightarrow 1.6\,\text{eV}$) and the transition of approximately 3.2 eV ($X^+_7 - X^-_6$). The latter is a transition above the Fermi level, while the lowest interband transition is $\sim 0.8\,\text{eV}$ below the Fermi level of Au. A schematic band diagram of Au is illustrated in fig. 4.29. Therefore, these interband transitions meet the necessary criteria for the additional relaxation channel, stated above.

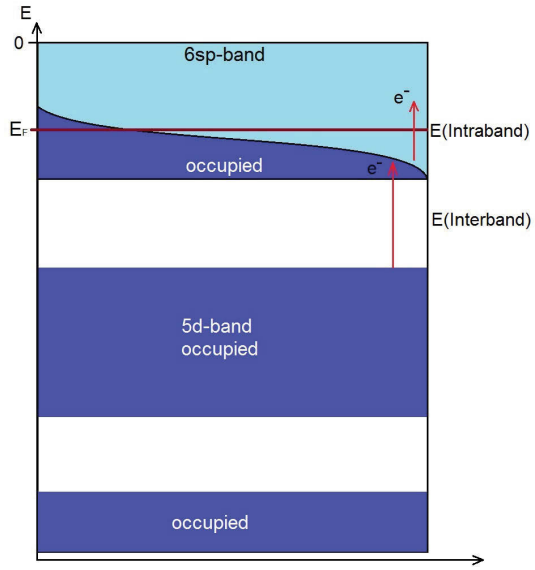

Fig. 4.29: Band diagram of the interband and intraband transitions in Au.

The lifetime of the electron-hole-pairs created by interband transitions can be estimated to be around 200 fs [196, 201, 203], which have been determined by pump-probe experiments in the literature. This can be described by the Fermi liquid theory. Here, an electron excited from the $5d$ to the $6sp$ band, leaving behind a hole in the $5d$ band, thermalises via electron-electron scattering with an approximate lifetime of $> 200\,\text{fs}$. Similarly, the hole thermalises via hole-hole scattering, which is a much faster process at the order of $< 20\,\text{fs}$. Subsequently, the thermalised electron and hole can non-radiately recombine. This relaxation channel is much faster than the radiative recombinations in the DBX of ZnO on the order of tens of ps (cf. table 4.6). Therefore, this additional decay pathway can be used to explain the reduced excitonic lifetime of the Au nanoparticle-coated ZnO, fulfilling the second requirement above.

The above model has some similarities to the interband transition of conduction electrons, which occur due to the excitation of LSPR. In Au, the interband transition lies within the $6sp$ conduction band, which results in an absorption band in the visible spectral range. Their transition process is much faster ($\sim$ 20 fs to 30 fs) than that of the interband transitions, as they only include electron-electron scattering from a non-Fermi distribution. This explains why the reduction in lifetime is so much greater for the LSP-exciton coupling than the for interband transitions [201].

In conclusion, it was shown that the the UV emission of ZnO – hydrothermally-grown ZnO nanorods and *a*-plane ZnO single crystals – can be enhanced by applying an Au nanoparticle surface coating. Different enhancement factors for electron beam and laser excitation of up to 6.3 have been achieved, with CL showing a greater overall enhancement due to the higher excitation power density. The UV enhancement was found to be depth-dependent with its maximum at the surface, closest to the ZnO-Au interface. Furthermore, a reduced carrier lifetime was recorded for Au nanoparticle-coated ZnO, indicating an increased SER due to the formation of an additional, faster relaxation pathway through the Au nanoparticles. In this work, the interband transition in the Au nanoparticles is the most likely decay channel to explain the shortened lifetime, as well as the observed temperature-independent UV-enhancement in PL and CL in both types of samples. The larger enhancement in Au nanoparticle-coated ZnO nanorods was attributed to a higher surface-to-volume ratio, allowing for an effectively higher number of Au nanoparticles to provide non-radiative transitions through interband transitions.

5 Characterisation of ZnO Coated with Aluminium

This chapter discusses the structural and optical properties of *a*-plane ZnO and ZnO nanorods coated with Al. Three differently deposited layers of Al were investigated, resulting in different enhancement factors of the NBE emission of ZnO. The possible origin of the UV enhancement was comprehensively studied using PL and CL spectroscopy as well as surface characterisation methods such as AFM and XPS.

5.1 Morphology of Aluminium-coated *a*-plane ZnO

Three different Al surface coatings were applied onto ZnO to investigate the different structural, electronic and optical properties as well as the underlying physical mechanisms of the different resulting UV enhancement factors.
The Al coatings were produced by DC-sputtering. Here, a nominal thickness of 2 nm was deposited onto half of a manually pre-polished *a*-plane ZnO single crystal (cf. section 3.1.2), leaving the other, uncoated side as a reference. Three different depositions have been used to produce different layers:

1. "*Al* ": Room temperature deposition of Al deposited with a nominal thickness of 2 nm. Argon was used as working gas. This sample was made to study the possible LSP-exciton coupling between the excitons in *a*-plane ZnO and Al. It can be assumed that a small amount of metallic Al is embedded in Al_2O_3, which theoretically should shift the LSPR of the Al nanoparticles from the UV spectral range closer to the excitonic emission in ZnO.

2. "*Al hot* ": Al deposition at 300 °C with a nominal thickness of 2 nm and argon as working gas. The Al-deposition at an elevated temperature should lead to an increased mobility of the Al-atoms to form larger Al nanoparticles within the Al_2O_3 layer, which could allow for a larger spectral overlap between the LSPs in the Al nanoparticles and the excitons in the ZnO, as well as an increase in LSPs for each Al nanoparticle.

3. "*Al oxide* ": Al-deposition at room temperature with a nominal thickness of 2 nm, with argon and oxygen as working gases. Here, the surface coating should consist of an Al_2O_3 layer only with no metallic Al. Due to the presence of oxygen during the deposition, the Al is most likely fully oxidised before the deposition on the *a*-plane ZnO surface. This sample acts a reference to distinguish between possible enhancement effects due to the Al_2O_3 and the investigated LSP-exciton coupling in those three samples.

Various characterisation methods have been used to determine the morphology and the chemical composition of these coatings:

- Optical spectroscopy of the uncoated and the Al-coated *a*-plane ZnO single crystals was performed. No Localised Surface Plasmon-related absorption could be found in the spectral range of ZnO. The LSPR frequency of Al is in the UV spectral range and is known to be widely tunable with particle size and shape [204–206]. To study the transmission properties of the Al-coatings further in the UV, these Al film were deposited under identical conditions used for the *a*-plane ZnO onto UV-quartz, which only absorbs light below 200 nm. The corresponding transmission spectra are shown in section 5.1.3.

- X-ray diffraction (XRD) was conducted to characterise the Al thin films. However, due to the small layer thickness of Al, it was not possible to detect any Al-related diffraction peaks, as this technique does not provide the necessary surface sensitivity.

- SEM techniques used to determine the size of the Au nanoparticles on ZnO were not able to image the nanostructure of the Al film. This could be due to the low SE yield of Al compared with Au [207].
  Another possible explanation is the formation of a Al_2O_3 layer on top of the Al, which is smooth and featureless like the ZnO substrate.

- Transmission electron microscopy (TEM) can image sub-atomic crystalline structures when the investigated samples are transparent to the electron beam. Therefore, the 2 nm-Al-coating, using the standard technique, was deposited onto a holey carbon grid, but the measurements did not show any diffraction patterns or characteristic atomic spacing for Al. This result indicated that the coating is not crystalline or that an Al film does not properly form on the holey carbon grid.

- AFM was used to investigate the surface morphology and roughness of both the *a*-plane ZnO and the Al coatings, which is shown in section 5.1.1.

- Ellipsometry was used to measure and model the composition and the thickness of the sputter-coated Al. For simplicity, the Al-coatings were deposited onto Si-substrates, which were placed next to the *a*-plane ZnO during deposition, assuring identical coating conditions. The results are discussed in section 5.1.2.
- XPS was performed to study the chemical composition and the surface band bending of the uncoated and the Al-coated *a*-plane ZnO single crystals. This will be discussed in section 5.1.4.

5.1.1 Atomic Force Microscopy Al- and Al_2O_3-Coated *a*-plane ZnO

In fig. 5.1, it can be seen that the surface roughness of the uncoated and the Al-coated sides of the *a*-plane ZnO is equivalent. The measured surface roughness of all three samples, as well as the uncoated *a*-plane ZnO is (1.0 ± 0.3) nm, which is within lateral spatial resolution of the AFM. The unchanged, smooth surface morphology of the Al-coated *a*-

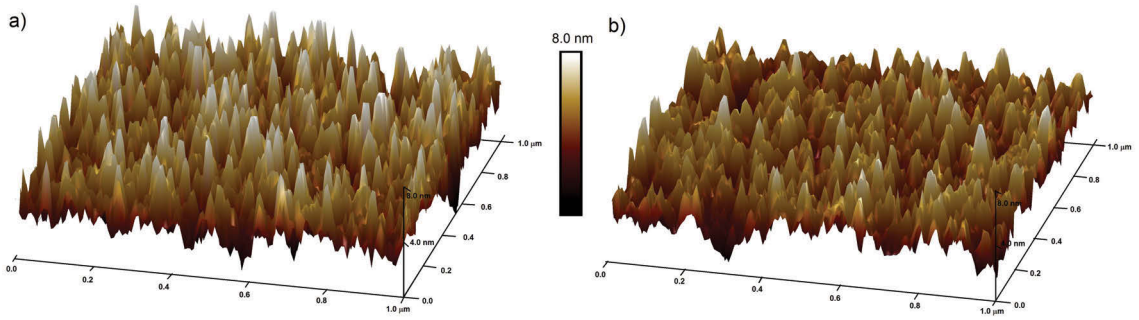

Fig. 5.1: AFM image of (a) the uncoated and (b) the Al-coated *a*-plane ZnO, showing an overall roughness of ~ 1 nm.

plane ZnO can be attributed to the growth of a surface oxide layer when exposed to air. The thickness of this Al_2O_3 film is self-limiting and typically depends on the initial thickness of the Al layer [208]. For bulk Al, the Al_2O_3 layer thickness is usually up to 10 nm, but it can be much lower for nanostructures or very thin layers.
From the AFM and SEM measurements it can be concluded, that the surface of these samples is fully covered with a smooth film of Al_2O_3.

5.1.2 Ellipsometry of Al- and Al_2O_3-Coated *a*-plane ZnO

The coating thickness, as well as its composition was determined by ellipsometry, which allows for better resolution than optical spectroscopy, as discussed in section 3.2.2.
The thickness and chemical composition of the nanostructured Al films were modelled by the effective medium theory, where library parameters were used to model the Al_2O_3 layer. To adjust the density of the surface coatings, voids were introduced. Furthermore,

the incorporation of a small percentage of metallic Al in those Al_2O_3 films were modelled using Bruggeman's and Maxwell-Garnett's theories. While Bruggeman's model is typically employed for a mixture of nanoparticles of random shapes and sizes, resulting in a broader plasmon absorption band; the Maxwell-Garnett theory uses isolated nanoparticles, which are randomly distributed in the matrix of Al_2O_3, the resulting plasmon absorption band is narrower for the Maxwell-Garnett model than that modelled with the Bruggeman theory. These two theoretical descriptions are illustrated in fig. 5.2, showing the nanoparticle distribution in the Maxwell-Garnett and the Bruggeman picture in (a) and (b), respectively. Figure 5.2c depicts the core-shell like structure of the nanoparticle surrounded by the second material after Maxwell-Garnett — here, an Al core with an Al_2O_3 shell, while (d) illustrates the nanoparticle consisting of a mixture of the two materials (Bruggeman) [209].

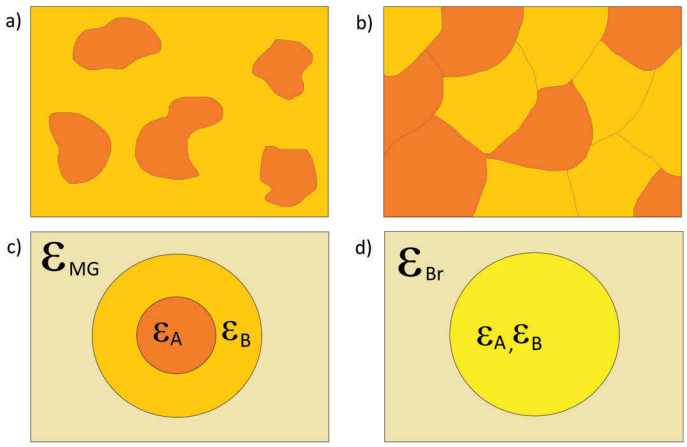

Fig. 5.2: (a) Separated grain structure of material A (orange) and B (yellow) and (b) an aggregated structure of those two materials. (c) shows the isolated nanoparticle in a core-shell structure in the Maxwell-Garnett picture and (d) the mixed structure after Bruggeman
This figure is adopted from [209].

Furthermore, the modelling allows for variation of the shape of the nanoparticles from spherical ($L = 0.33$) to more rod-like shapes ($L = 0.20$), where L is the depolarisation factor. In the case of Al, the nanoparticles' shape can result in a large spectral shift of the LSPR. The optical spectra, typically the extinction spectra, of those structures can be modelled, which allows for comparison with measured optical spectra.
For the samples *Al* and *Al hot*, a composition of small Al nanoparticles embedded in an Al_2O_3 matrix was determined, using the Bruggeman's model. The percentage of metallic Al was calculated to approximately (0.10 ± 0.02)Vol% (*Al*) to (0.20 ± 0.02)Vol% (*Al hot*), respectively, with a coating thickness of (2.80 ± 0.01) nm. The definite size and shape of the Al nanoparticles could not be identified, but a large distribution of different sizes of small nanoparticles, where the fitting suggests that a round-elliptical shape is most

likely. The corresponding extinction spectra, using the fitting parameters obtained from the ellipsometry data, are illustrated in fig. 5.3. The investigated sample consists of a stack of 10 times 2 nm hot deposited Al to allow for better resolution. It can be assumed that each layer in this stack is similar to that of the sample *Al hot*. The oscillator fit used in fig. 5.3 shows the maximum absorption at a wavelength of $\sim 240\,\text{nm}$ (5.17 eV) with a long tail in the visible spectrum. This broad absorption can be explained by a large distribution of different shapes of Al nanoparticles embedded in Al_2O_3. The extinction spectra of differently shaped Al nanoparticles are shown in fig. 5.3 with the parameters varying from spherical nanoparticles ($L = 0.33$) to nanorods ($L = 0.20$), indicating that the surface coating consists of small Al nanoparticles of different sizes and shapes in an Al_2O_3 matrix.

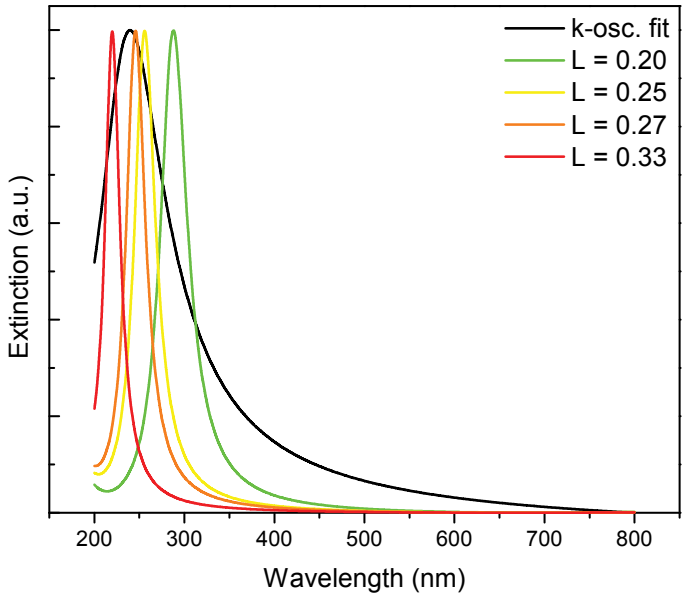

Fig. 5.3: Extinction spectrum of sample *Al hot* fitted with an oscillator model, obtained by ellipsometry (black).
Modelled extinction spectra of differently shaped Al nanoparticles in an Al_2O_3 matrix (coloured lines), where $L = 0.33$ corresponds to a spherical nanoparticle and $L = 0.20$ a nanorod. The other L-values correspond to a more elliptical shape, being between those two L-values, indicating that the sample *Al hot* contains a large distribution of differently shaped Al nanoparticles.

The amount of metallic Al was smaller than expected. However, as will be shown later in this chapter, other characterisation methods also confirm the presence of metallic Al, in particular the difference in the optical properties of the three studied samples. Consequently, it is likely that the metallic Al nanoparticles are located at the filmZnO boundary being sub-nanometre.
The sample *Al oxide* can be fitted with a (2.80 ± 0.01) nm thin Al_2O_3 film using the library

parameters. As expected, no metallic Al could be found in this sample.

5.1.3 Optical Spectroscopy of Al- and Al_2O_3-Coated *a*-plane ZnO

To confirm the results obtained from ellipsometry, transmission spectroscopy was performed.
The three Al-coatings were deposited onto UV-quartz to allow for a larger spectral range in the UV compared with the *a*-plane ZnO, which absorbs light of energies larger than 3.36 eV (i. e. wavelengths > 369 nm). This is necessary as the Al nanoparticles' LSPR is widely spread over the UV part of spectrum depending on the size and shape of Al, as shown in section 5.1.2.
Figure 5.4 depicts the transmission spectra of those Al-coating on UV-quartz, each divided by the reference spectrum of uncoated UV-quartz. The resulting spectrum of the sample *Al oxide* is close to 1 with increased noise level, which indicates no change compared to the reference. The samples *Al* and *Al hot*, however, exhibit a reduced transmission over the entire range of the spectrum. Particularly, sample *Al hot* shows reduced transmission in the UV, which is similar to the ellipsometry results, discussed above.

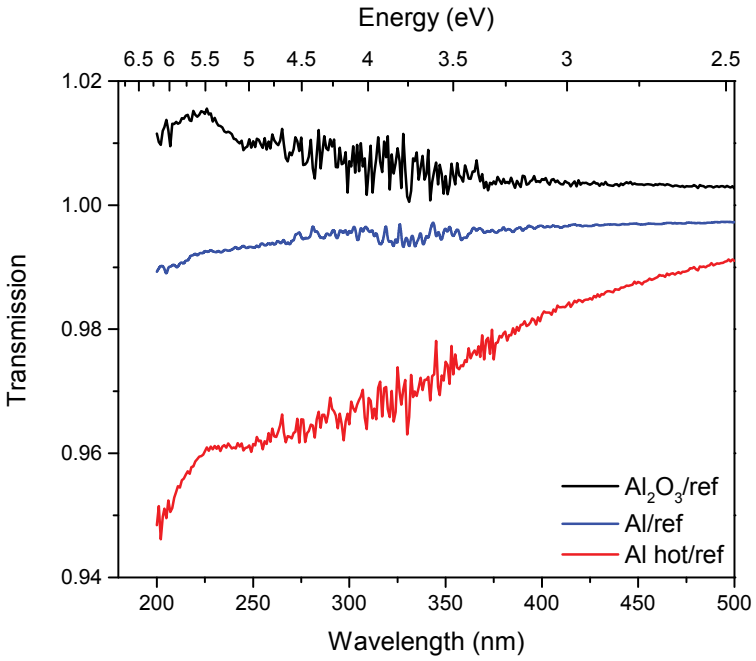

Fig. 5.4: Transmission spectra of the three Al coatings (*Al* in blue, *Al hot* in red and *Al oxide* in black) on UV-quartz divided by the reference spectrum of uncoated UV-quartz, showing LSPR absorption for the samples *Al* and *Al hot*.

Note that in the near-UV range, the spectra show increased noise due to the change of

white light sources in the spectrometer (Agilent Cary 7000 UV/VIS/NIR UMS). Therefore, high-resolution spectra of the reference and the sample *Al hot* were collected, which is presented in fig. 5.5. A reduced transmission from 200 nm to 450 nm in the sample *Al hot* can be seen, indicating a broad LSPR absorption in this range. Although the actual

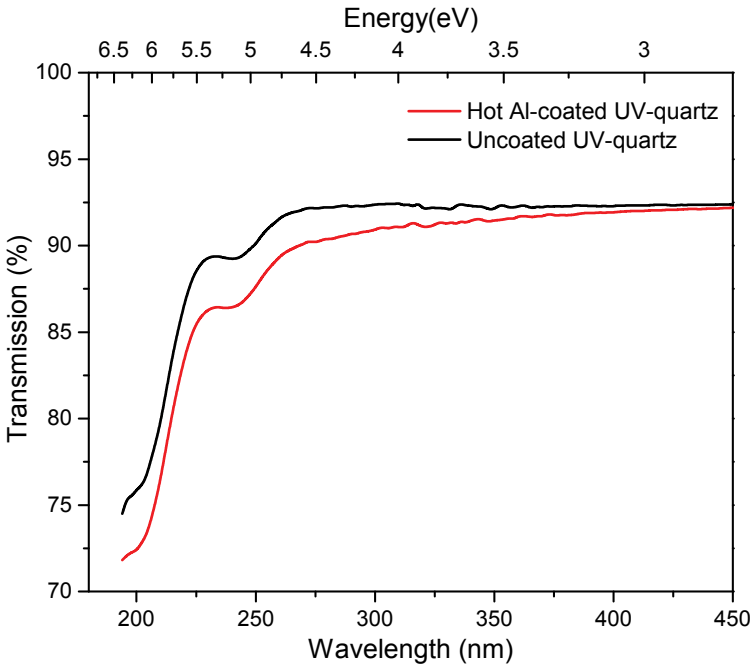

Fig. 5.5: High-resolution transmission spectra of uncoated UV-quartz (black) as a reference and UV-quartz coated with hot deposited Al (sample *Al hot*) in red, indicating a broad LSPR absorption in the UV spectral range.

size and shape of the Al nanoparticles in the samples *Al* and *Al hot* cannot be determined by any of the aforementioned methods, a broad light absorption in the UV can be attributed to the LSPR of small, differently shaped Al nanoparticles [210–212], despite a very low content of approximately (0.10 ± 0.02)Vol% (*Al*) and (0.20 ± 0.02)Vol% (*Al hot*) Al in the (2.80 ± 0.01) nm thin Al_2O_3 film. As mentioned above, the metallic Al nanoparticles are most likely located close to the ZnO-metal film interface, as the Al oxidisation occurs at the surface, where it is exposed to air. The sample *Al oxide* does not show any metallic Al or LSPR, indicating that this film only contains Al_2O_3.

In summary, the morphology of the three Al-coated *a*-plane ZnO samples is difficult to image. From the combination of the different methods discussed above, it can be concluded that the samples *Al* and *Al hot* consist of small Al nanoparticles embedded in a Al_2O_3 matrix, which both have a surface roughness of ~ 1 nm. The sample *Al oxide* consists of a smooth (2.80 ± 0.01) nm thin Al_2O_3 film.

5.1.4 X-Ray Photospectroscopy of Al- and Al_2O_3-Coated *a*-plane ZnO

To study the surface band bending of the uncoated *a*-plane ZnO and the samples *Al*, *Al hot* and *Al oxide*, VB-XPS was performed.
The results are presented in fig. 5.6, showing the Zn $3d$ peak at $\sim 10.2\,\text{eV}$ and two states near the valence band maximum, centered at 7 eV and 5 eV, attributed to hybridised Zn $4s$-O $2p$ and O $2p$ states, respectively (cf. section 4.2). From the valence band edge, shown

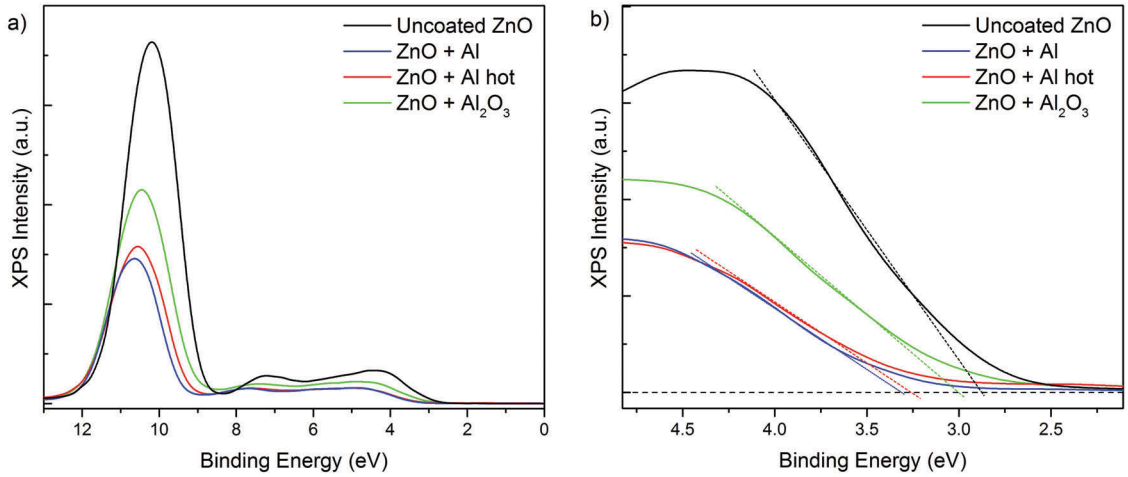

Fig. 5.6: (a) Valence band XPS spectra of the uncoated *a*-plane ZnO and the samples *Al*, *Al hot* and *Al oxide* and (b) close-up of the valence band with linear fits of the valence band onset for each sample.

in fig. 5.6b, the degree of surface band bending can be determined, using the measured ZnO carrier density of $2.7 \times 10^{14}\ \text{cm}^{-3}$, in the eq. (4.1). The calculated V_{BB}, as well as the width of the space charge layer W (cf. eq. (4.4) in section 4.2) and the electric field at the surface E_{S} (eq. (4.5)) of the four samples are listed in table 5.1. It can be seen that the V_{BB}

Table 5.1: Surface band bending of the uncoated, *a*-plane ZnO and the sample *Al*, *Al hot* and *Al oxide*, calculated using eq. (4.1).

Sample	V_{BB} (V)	Direction of V_{BB}	W (nm)	E_{S} (V cm^{-1})
uncoated *a*-plane ZnO	+0.20	upward	840	2.3×10^3
Al	−0.22	downward	880	5.0×10^3
Al hot	−0.15	downward	730	4.1×10^3
Al oxide	+0.08	upward	530	3.0×10^3

is changed from upward for the uncoated *a*-plane ZnO to almost flat bands due to the Al_2O_3-coating, while the small amount of metallic Al in the samples *Al* and *Al hot* results in a downward band bending. Accordingly, the width of the space charge layer varies with the layer being thinnest for the Al_2O_3-coated ZnO.

It can be concluded that the Al-coatings affect the electronic properties of the ZnO surface and results in a change of band bending. This change in band bending can have significant effects on the optical properties of those three samples and will be further discussed in the following sections.
Furthermore, the Al $2p$ core levels of the three samples *Al*, *Al hot* and *Al oxide* were studied with XPS to confirm presence of metallic Al in the coating. All three samples only showed the typical $2p$ level of oxidised aluminium. This is consistent with the ellipsometry results only 0.1 Vol% and 0.2 Vol% for the samples *Al* and *Al hot*, respectively as the detection limit of the laboratory XPS setup is > 0.5 at% (cf. section 5.1.2).

5.2 CL and PL Study of Aluminium-Coated *a*-plane ZnO

In this section, the results of the *a*-plane ZnO coated with 2 nm Al at room temperature (sample *Al*) are discussed. An enhanced UV emission following the Al coating is observed and its origin comprehensively studied by depth-resolved CL, temperature-dependent PL, excitation power-dependent PL and CL and time-resolved PL.

5.2.1 Depth-resolved CL of Al-Coated *a*-plane ZnO

The depth-resolved CL was performed at three different acceleration voltages, 3 kV, 5 kV and 10 kV, which translate into CL excitation depths of approximately 50 nm, 90 nm and 350 nm, respectively. This allows the distribution of luminescence to be probed within the sample *Al* from the near-surface to the bulk.
The full CL-spectra of the sample *Al* at a temperature of 10 K and 80 K are displayed in fig. 5.7a and b, respectively. At 10 K, an increased UV intensity for the Al-coated *a*-plane ZnO at all three acceleration voltages can be seen, with an 1.7-fold enhancement at 3 kV and 5 kV, and a slightly less enhanced UV emission of 1.4 at an acceleration voltage of 10 kV. The NBE emission of the Al-coated *a*-plane ZnO is slightly red-shifted compared to the uncoated side of the sample; the normalised NBE emission of the spectra are depicted in fig. 5.7c. As the NBE of ZnO is comprised of various excitonic transitions, spectrally higher resolution of this region is needed to study the apparent red-shift, following the Al coating. This will be discussed in greater detail below.
The relatively weak and broad DL emission is similarly intense for the uncoated and the Al-coated *a*-plane ZnO, as displayed in fig. 5.7e. The Al-coated *a*-plane ZnO exhibits a narrower DL emission, which is red-shifted from approximately 2.2 eV to 2.0 eV at lower acceleration voltages (3 kV and 5 kV). The green luminescence (GL) centered at 2.3 eV, typically attributed to zinc vacancies (V_{Zn}) in ZnO, is almost invisible in the sample *Al*. However, at 10 kV, the centre of the DL emission blue shifts from 2.0 eV to 2.1 eV and a broadening can be observed with a shoulder close to the reported GL, indicating that the

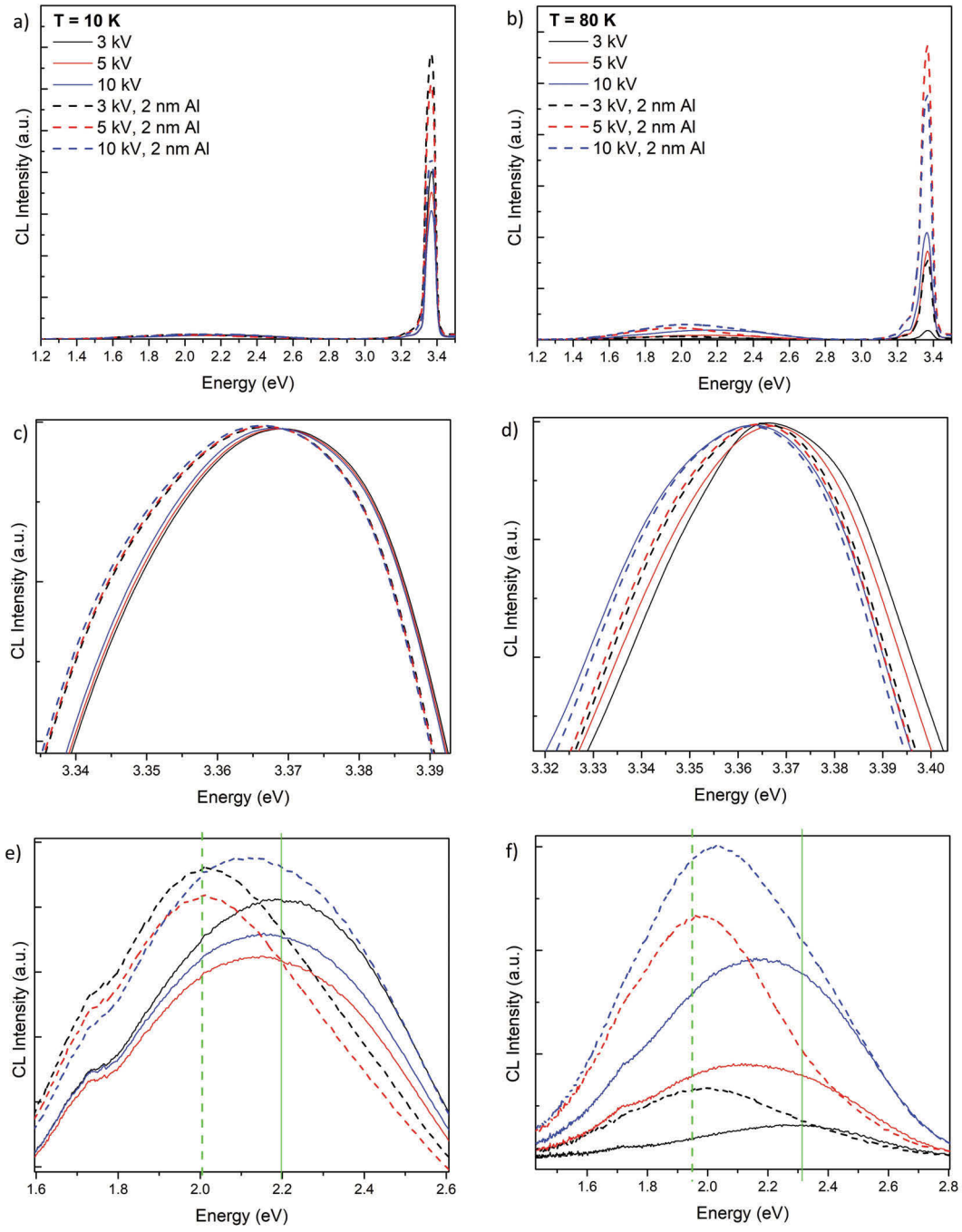

Fig. 5.7: Depth-resolved CL spectra of uncoated (solid lines) and Al-coated (dashed lines) *a*-plane ZnO single crystal at $HV = 3$, 5 and 10 kV at (a) 10 K and (b) 80 K. (c and d) display the normalised NBE emission of the uncoated and the Al-coated *a*-plane ZnO at 10 K and 80 K, respectively; the DL emission of the uncoated and the Al-coated *a*-plane ZnO at both temperatures are shown in (e and f).
$P = 17.5\,\mu$W, scan area $10\,\mu\text{m} \times 10\,\mu\text{m}$.

underlying effect is surface-related (cf. table 2.2).
This depth-dependent change in the DL emission can be possibly due to changes in the V_{Zn} charge state arising from surface charge transfer processes induced by the presence of the Al surface coating.
Another possible explanation is the change of the charge transfer level at the interface of ZnO and Al_2O_3 due to the surface band bending, as discussed in section 5.1.4. Here, the change in surface band bending from upward in the uncoated to downward in the Al-coated *a*-plane ZnO can possibly bend the V_{Zn} charge transfer level below the Fermi level, charging the V_{Zn} charge state. However, due to the small downward bending and low carrier density (i.e. large space charge layer width W; cf. table 5.1), it is unlikely that the band bending would change the charge state of a DL defect.
The depth-resolved CL spectra of the sample *Al* at 80 K are presented in fig. 5.7b. Here, the intensity of the UV emission of the Al-coated *a*-plane ZnO is 8.6 times enhanced at an acceleration voltage of 3 kV, while a smaller enhancement is found at higher acceleration voltages (3.3 times at 5 kV and 2.2 times at 10 kV).
The UV enhancement factors of the sample *Al* at 10 K, 80 K and 300 K are shown in the table 5.2 below. To be more representative of the whole NBE emission, it is integrated from 3.10 eV to 3.45 eV, presented in column 4, while column 3 shows the maximum intensity of the uncoated *a*-plane ZnO divided by that of the Al-coated *a*-plane ZnO. The

Table 5.2: UV enhancement factors of the sample *Al* at three different acceleration voltages at 10 K, 80 K and 300 K. The UV emission was integrated from 3.10 eV to 3.45 eV.

HV (kV)	Temperature (K)	UV enhancement (I)	UV enhancement (Int)
3	10	1.8	1.8
5	10	1.8	1.8
10	10	1.5	1.5
3	80	8.6	8.3
5	80	3.3	3.3
10	80	2.3	2.2
3	300	4.9	5.0
5	300	6.0	5.9
10	300	3.7	4.4

highest integrated enhancement of 8.3 is found at the lowest CL excitation depth (3 kV) at a temperature of 80 K, while the UV emission is less enhanced at 10 K and at room temperature (300 K). Furthermore, a reduced UV enhancement with increasing CL excitation depth at all temperatures is observed, which indicates that the UV enhancement is larger with excitation closer to the surface.
Moreover, at 80 K the red-shift of the NBE emission for Al-coated *a*-plane ZnO is less

pronounced than that at 10 K. This behaviour is likely due to the different degrees of enhancement for each of the DBX excitonic transitions in the NBE. High-resolution luminescence spectra of the NBE are shown below, allowing the study of the apparent red-shift for the Al-coated *a*-plane ZnO, as well as the temperature-dependent enhancement factor in more detail.

The DL emission spectra with increasing CL excitation depth at 80 K are depicted in fig. 5.7f, showing a similar trend to the 10 K-spectra. The DL emission of the Al-coated *a*-plane ZnO at lower acceleration voltages of 3 kV and 5 kV is narrower than that of the uncoated side of the sample, accompanied by a red-shift from approximately 2.3 eV to 1.95 eV. At 10 kV, the DL emission of the sample *Al* is broadened and blue shifted compared to the DL emission at lower acceleration voltages, which is similar to the trend at 10 K. In contrast to the UV enhancement, the depth-dependent change in the DL emission is temperature independent, which is in accordance with possible explanations of surface band bending and surface passivation, discussed above.

To investigate the UV enhancement in greater detail, the high-resolution CL spectra, shown from 3.10 eV to 3.45 eV at 3, 5 and 10 kV at a temperature of 10 K are displayed in fig. 5.8.

It can be seen that the spectra are dominated by the bound excitons, particularly the I_4-line at 3.363 eV, which is typically attributed to hydrogen (cf. table 2.1). The presence of H is not unexpected, as the *a*-plane ZnO crystals are hydrothermally grown, which can introduce hydrogen into the crystal lattice.

The spectra of the Al-coated *a*-plane ZnO exhibit an overall increased NBE emission. However, the I_6 line at an energy of 3.361 eV, assigned to Al impurities (cf. table 2.1), is not more enhanced than the rest of the spectrum. Therefore, the diffusion of Al into ZnO appears to be negligible. This is consistent with a relatively low Al-diffusion coefficient at room temperature, as shown by Thimsen et al. [213].

The enhancement factor as a function of energy for each acceleration voltage is reported in fig. 5.9, which is found by dividing the spectra of the Al-coated *a*-plane ZnO by that of the uncoated *a*-plane ZnO. Note that this ratio is only meaningful if no large change in the peak position, width or shape of the individual emission lines occurs, as this would shift the enhancement drastically.

In fig. 5.9, the lowest acceleration voltage of 3 kV shows the greatest enhancement, which is consistent with the depth-resolved CL spectra shown above (fig. 5.7). It is noteworthy, that the enhancement factor is not equally distributed over the entire energy range, but instead certain emissions are more strongly enhanced than others. To correlate the enhanced emissions to actual transitions in the *a*-plane ZnO sample, the I lines and the DBX-related LO phonon replicas are labelled in green, while FX-related emissions are presented in olive.

Some of the DBX transitions, such as I_0 and I_2 are more enhanced (~ 3 times) than others,

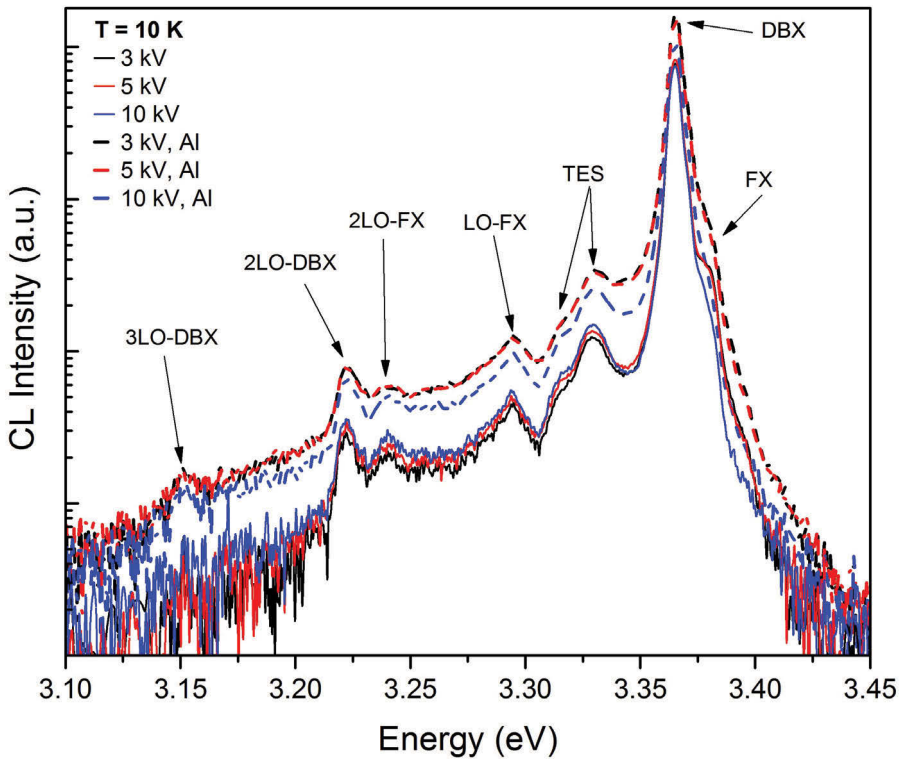

Fig. 5.8: High-resolution depth-resolved CL spectra of uncoated (solid lines) and Al-coated (dashed lines) *a*-plane ZnO with labelled excitonic transitions.
$HV = 3$ (black), 5 (red) and 10 kV (blue), $T = 10$ K, $P = 17.5$ µW, scan area 10 µm × 10 µm.

although their assignment can be difficult as the I lines are spectrally very close to each other. Interestingly, the FX peaks are not very pronounced in the before and after spectral data (cf. fig. 5.8), but they are clearly visible in the enhancement plot (fig. 5.9), despite the DBX being the most efficient recombination channel at 10 K.

Furthermore, a 4-fold enhanced broad emission at 3.343 eV is observed, which seems to be comprised of more than one emission peak. The shoulder at 3.354 eV can be attributed to the first LO-phonon-replica of the FX-C, while the lower energy side of this broad emission has not been reported in the literature and therefore, cannot be assigned to any transitions in ZnO. A thin Al_2O_3 film directly deposited onto a Si substrate did not exhibit any emission in the UV spectral region, indicating that the emission at 3.34 eV is not related to any transitions in Al_2O_3. Therefore, the most probable explanation for this emission is a transition at the interface between ZnO and Al or ZnO and Al_2O_3. Moreover, no emission at 3.343 eV was found in the Au nanoparticle-coated *a*-plane ZnO sample (cf. fig. 4.23), indicating that this emission is only observed in the Al thin films on *a*-plane ZnO.

It is also notable that the features in the enhanced emissions in fig. 5.9 decline with greater

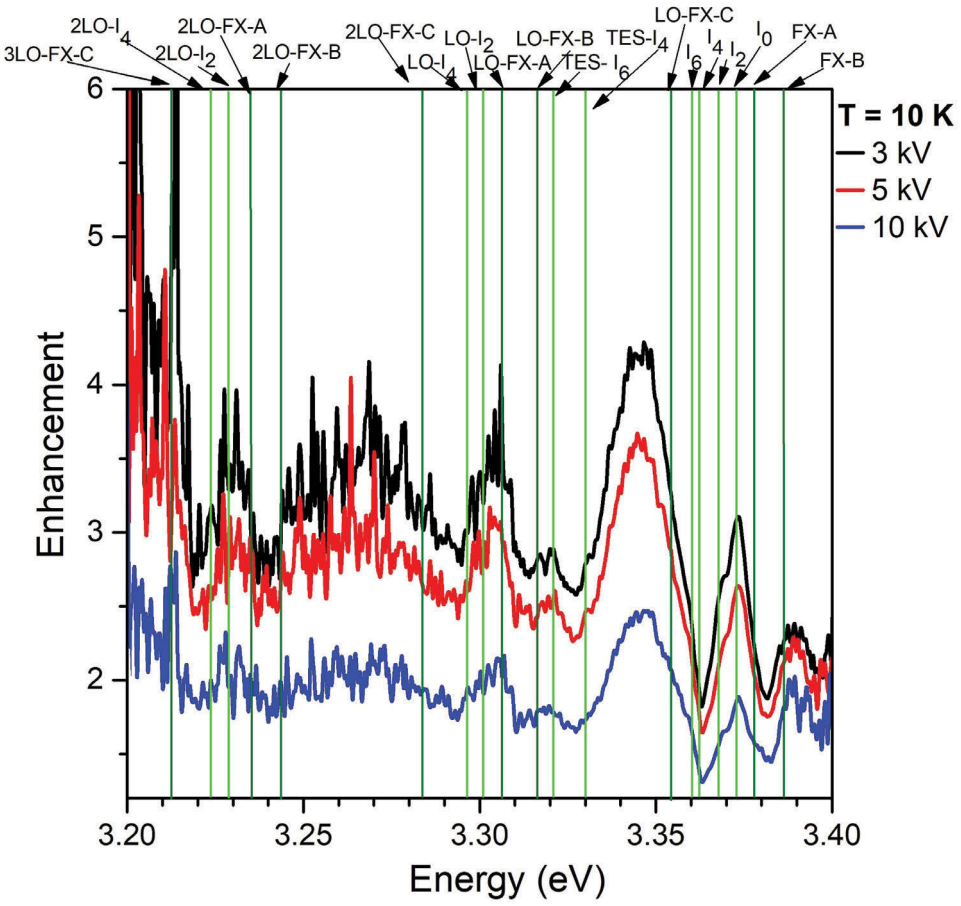

Fig. 5.9: CL enhancement as a function of energy at $HV = 3\,\text{kV}$ (black), 5 kV (red) and 10 kV (blue), showing highest enhancement at the surface. The green labels present the DBX-related emission peaks, while FX emissions are labelled in olive.
$T = 10\,\text{K}$, $P = 17.5\,\mu\text{W}$, scan area $10\,\mu\text{m} \times 10\,\mu\text{m}$.

depth, which is consistent with a process close to the surface, near the Al-ZnO interface. To study the apparent temperature dependence of the enhancement in this sample, the high-resolution depth-resolved CL spectra of the uncoated and Al-coated *a*-plane ZnO sample at 80 K are presented in fig. 5.10. The comparison of the CL-spectra at 80 K (fig. 5.10) with those at 10 K (see fig. 5.8) exhibits more pronounced FX-related emissions due to thermalisation of the DBX emissions at 80 K, as well as a broadening of the individual peaks due to increased phonon interactions.

The enhancement has overall increased at 80 K, which is displayed in fig. 5.11 as a function of energy for each acceleration voltage. Here, a clear enhancement of the I_6 line at 3.359 eV can be seen, which is assigned to Al impurities in ZnO, indicating that some of the sputter-coated Al diffused into the ZnO during the deposition. This Al-doping effect is not visible in the enhancement graph at 10 K (fig. 5.9), which can be explained by

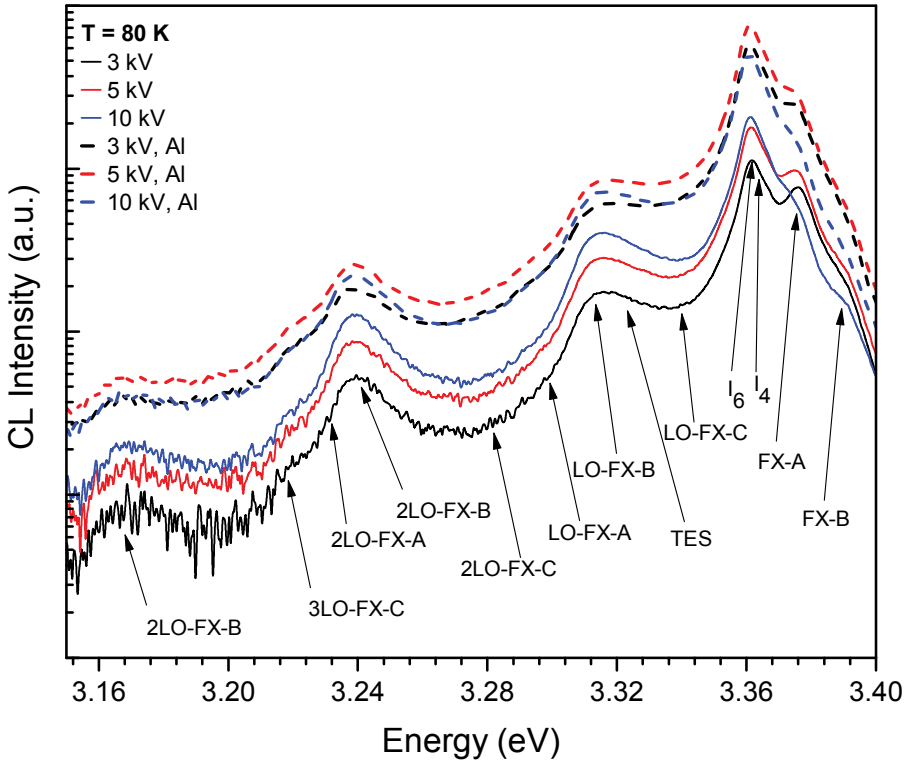

Fig. 5.10: 80 K-high-resolution depth-resolved CL spectra of uncoated (solid lines) and Al-coated (dashed lines) *a*-plane ZnO with labelled excitonic transitions.
$HV = 3$ kV (black), 5 kV (red) and 10 kV (blue), $P = 17.5$ µW, scan area 10 µm × 10 µm.

more efficient recombination channels being used at a lower temperature, possibly the energetically higher I_4. The I_4 line has a lower activation energy of 13 meV than the I_6 line (15 meV), resulting in a dissociation of the I_4-DBX at lower temperatures than that of the I_6 [214]. Hence, the enhancement of the I_6 is more pronounced at 80 K than at 10 K. Furthermore, the coupling of the LSPs in the Al nanoparticles to the DBX, specifically the I_6, is also a possible explanation.

The emission at 3.343 eV, possibly due to interface transitions of ZnO-Al or ZnO-Al_2O_3, is equally strongly enhanced – approximately 4 times – at both temperatures and is most pronounced at low acceleration voltages, when the excitation is close to the surface.

It is noteworthy, that although the FX-A and -B emissions are more visible in the spectra at 80 K than at 10 K (cf. fig. 5.8 and fig. 5.10, respectively), they are similarly enhanced at both temperatures. However, the highest enhancement factors, except for the I_6 line, are achieved at the position of the LO-phonon replicas of the FX-C, separated by 73 meV each, which is consistent with the phonon energy in ZnO. The relatively higher enhancement of the LO-phonon replica of the FX-C can be possibly explained by the energetically higher transition of the FX-C (3.4264 eV; cf. table 2.1) than any other excitonic transition

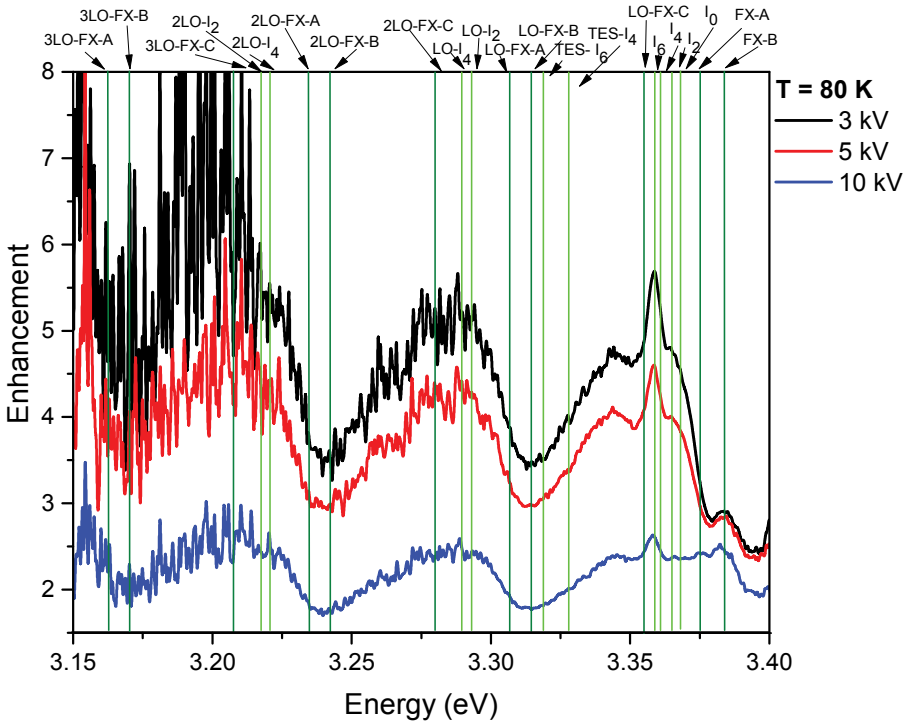

Fig. 5.11: CL enhancement as a function of energy at $HV = 3\,\text{kV}$ (black), 5 kV (red) and 10 kV (blue), showing highest enhancement at the surface. The green labels present the DBX-related emission peaks, while FX emissions are labelled in olive.
$T = 80\,\text{K}$, $P = 17.5\,\mu\text{W}$, scan area $10\,\mu\text{m} \times 10\,\mu\text{m}$.

in ZnO. In the LSP-exciton coupling picture (cf. section 2.5.3), the dipole-dipole coupling between the LSPs in the metal nanoparticles and the excitons in the semiconductor is strongest when the LSPR energy of the metal nanoparticles is close to the energy of the excitonic emission. As shown in section 5.1.2 and section 5.1.3, the maximum of the LSPR of the Al nanoparticles is approximately at 5.17 eV with a long tail into the visible spectrum, which is attributed to a large distribution of sizes and shapes of the Al nanoparticles. The LSP-exciton coupling is believed to be stronger for the largest spectral overlap of the dipoles in the LSPs of the Al nanoparticles and the excitons. In the case of ZnO, the FX-C has the largest spectral overlap with the LSPR of the Al nanoparticles. Therefore, a higher enhancement factor of the FX-C-related emissions is assumed.
Note that the UV enhancement of the Al-coated ZnO cannot be attributed to interband transitions, as discussed in the previous chapter (cf. section 4.7), as the the interband transitions in Al are mainly found in the infrared spectral range [212, 215–217].
In summary, the depth-resolved CL spectra show an overall increased UV emission for the Al-coated *a*-plane ZnO compared with the uncoated side of the sample, with the highest CL enhancement factor closest to the ZnO-Al interface at 3 kV for both temperatures,

10 K and 80 K. With increasing CL excitation depth from 3 to 10 kV, the enhancement factor reduces from 1.6 to 1.4 at 10 K and 4.3 to 1.9 at 80 K ($HV = 3$ kV), showing that the enhancement is not only depth-dependent but also temperature-dependent. Furthermore, at both temperatures, the DL emission narrows and red-shifts following the Al deposition at 3 kV and 5 kV, suppressing the GL emission at 2.3 eV, which is typically attributed to V_{Zn} in the literature. At 10 kV, the DL emission peak position and shape of the Al-coated *a*-plane ZnO appears similar to that of the uncoated *a*-plane ZnO. This depth-dependent change in the DL emission due to the Al-coating can be most likely attributed to defect interactions with the Al, changing the charge transfer mechanism.
The high-resolution CL spectra of the sample *Al* show a similar depth-dependent enhancement effect, as discussed above. At 10 K, mainly the DBX-related emissions are enhanced, as well as a new emission at 3.343 eV, which can be most likely assigned to an interface transition between ZnO and Al or ZnO and Al_2O_3. At 80 K, an increase in the Al-associated I_6 line can be observed, indicating that some Al has diffused into the ZnO during the deposition. Furthermore, the enhancement of the first three LO-phonon replicas of the FX-C is apparent. As the DBX thermalises at temperatures around 80 K, the spectra show increased FX contributions. The coupling of the LSPs in the Al nanoparticles with the FX in ZnO is a possible explanation for the enhanced UV emission in the sample *Al*. As the FX-C is the energetically highest excitonic transition in ZnO at 3.4264 eV (cf. table 2.1), the coupling to the broad LSPR from ~ 2.8 eV to 6.2 eV with its maximum at 5.17 eV is more probable than to energetically lower emissions in ZnO.
This dipole-dipole coupling provides a faster, additional relaxation channel via the LSPs in the Al nanoparticles, enhancing the SER and thereby the UV emission of ZnO.

5.2.2 Temperature-dependent PL and CL Spectroscopy of *a*-plane ZnO Coated with Aluminium

High-resolution PL spectroscopy was performed to further study the NBE-luminescence distribution in the sample *Al* with increasing temperature from 10 K to 250 K, as well as to compare the UV enhancement in PL and CL.
The high-resolution PL spectra of the uncoated and the Al-coated *a*-plane ZnO are shown in fig. 5.12 and fig. 5.13, respectively. As expected, the emission peaks broaden and red-shift with increasing temperature due to thermalisation effects and increased phonon interaction. Furthermore, the DBX emissions thermally dissociate with increasing temperature, which results in a decreased DBX intensity, while the FX emissions become more intense.
The enhancement factor — found by dividing the PL spectra of the Al-coated by that of the uncoated *a*-plane ZnO — as a function of energy for the aforementioned temperature range is displayed in fig. 5.14, graphed together with the high-resolution spectra of the

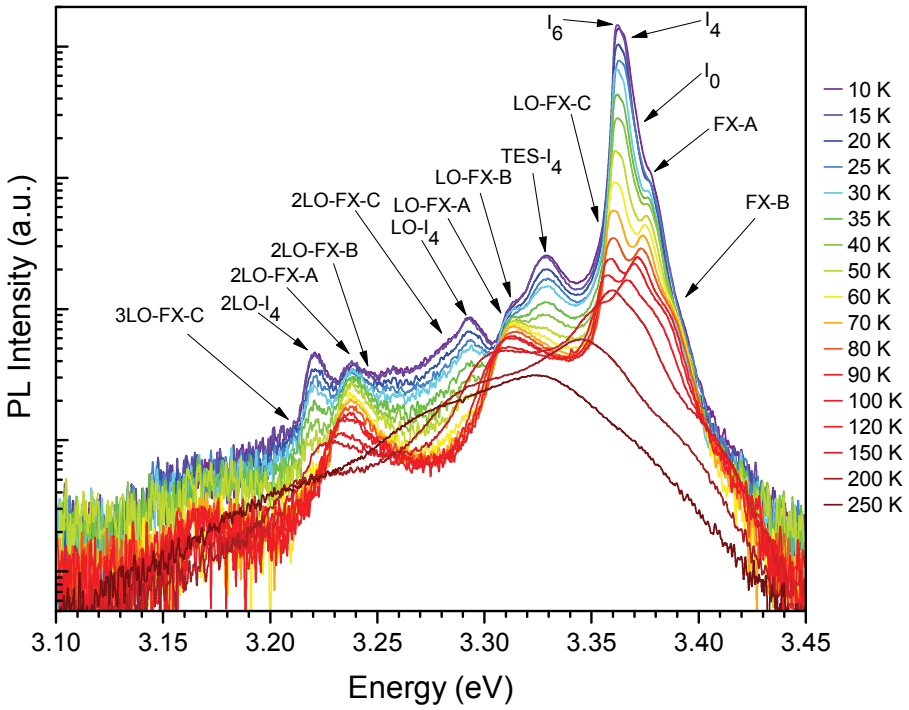

Fig. 5.12: Temperature-dependent high-resolution PL spectra of uncoated *a*-plane ZnO from 10 K to 250 K, with labelled excitonic emission peaks. $\lambda_{exc} = 325$ nm, $P = 2.2$ mW, laser spot ~ 30 µm.

uncoated and the Al-coated *a*-plane ZnO at 10 K to allow the identification of the excitonic transitions in ZnO.

The highest enhancement of ~ 12 is reached at a temperature of 80 K at an energy of approximately 3.354 eV, which can be attributed to the first LO-phonon replica of the the FX-C. The second FX-C LO-phonon replica can be seen at approximately 3.281 eV with an enhancement of ~ 8 times. At 80 K, most of the DBX are thermally dissociated, while the FX-related emissions are more pronounced compared to the DBX. Therefore, a stronger coupling between the LSPs in the Al nanoparticles with the FX in the *a*-plane ZnO is a possible explanation for the maximum enhancement at 80 K, shown in fig. 5.7 and fig. 5.14.

Furthermore, the interface emission between ZnO and Al or ZnO and Al_2O_3, centered at 3.343 eV, is more visible at lower temperatures (10 K to 40 K), as it starts overlapping with the LO-phonon replica of the FX-C in ZnO at temperatures above 60 K, due to the thermalisation of the DBX.

To represent the enhancement of the entire UV and DL emission in the Al-coated *a*-plane ZnO, the integrated PL enhancement of the DL (1.2 eV to 3.0 eV) and the NBE emission (3.00 eV to 3.54 eV) is illustrated as a function of temperature in fig. 5.15b. It shows the

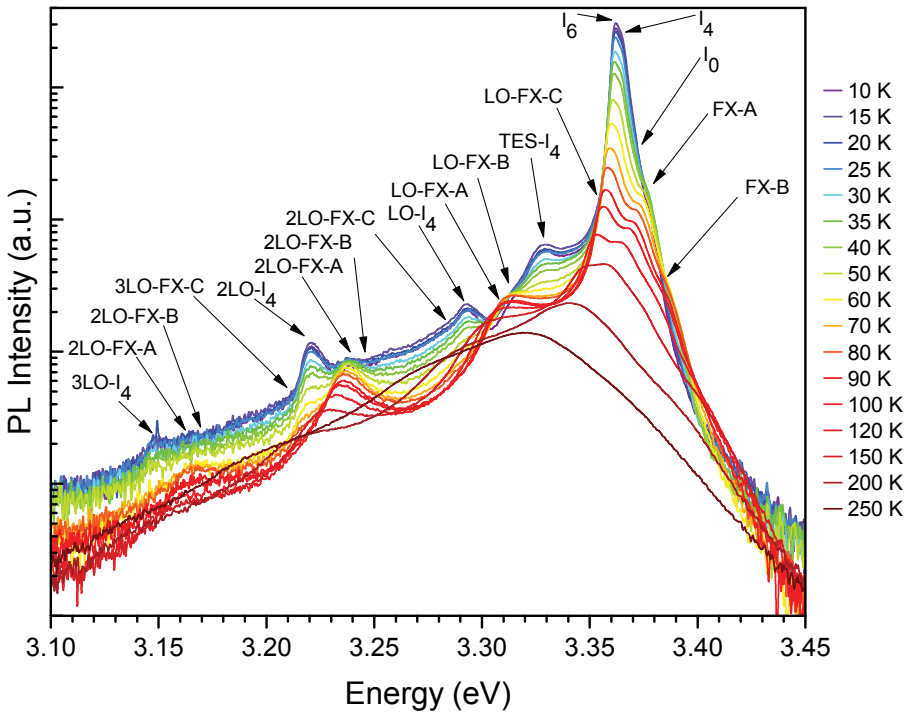

Fig. 5.13: Temperature-dependent high-resolution PL spectra of Al-coated *a*-plane ZnO from 10 K to 250 K, with labelled excitonic emission peaks. $\lambda_{exc} = 325$ nm, $P = 2.2$ mW, laser spot ~ 30 µm.

same trend of the highest UV enhancement of 6.5 at 80 K, while the integrated DL emission is overall decreased for all temperatures.

The enhancement factor in CL as a function of the temperature from 10 K to 110 K is illustrated in fig. 5.15a, showing the enhancement of the integrated DL and NBE emission, respectively. It can be seen that the DL emission is slightly enhanced ($\sim$ 1.4 times) over the entire temperature range, while the NBE shows a temperature-dependent enhancement with its maximum of 3.3 around 70 K. It is striking that the overall enhancement is larger in PL than in CL, which is likely to be due to the different depth distribution of PL and CL excitation. The laser excitation is greatest at the surface, as the energy deposited into the sample follows the Beer-Lambert's Law (cf. eq. (3.11)) with the maximum at the surface. The electron beam excitation has a different energy loss profile with its maximum deeper within the sample (cf. fig. 3.6). Furthermore, the excitation density in CL is approximately 4 orders of magnitude greater than that in PL. The excitation power dependence of the UV enhancement will further discussed in section 5.2.3.

The comparison of the UV enhancement factors as a function of energy in PL and CL is shown in fig. 5.16 at a temperature of 10 K. Here, the green labels correspond to DBX-related emission peaks, while FX-related emission peaks are labelled in olive. Note that the high-resolution CL spectra are collected at an acceleration voltage of 5 kV to assure

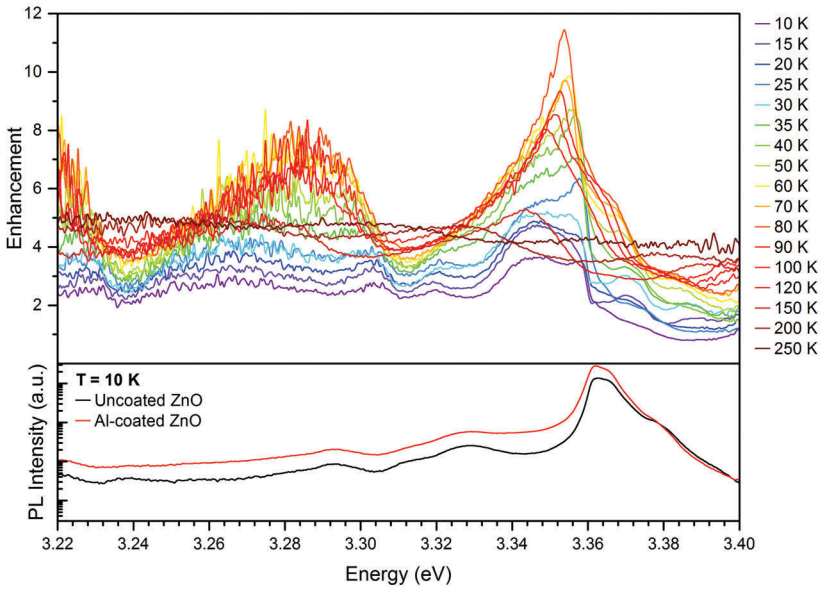

Fig. 5.14: Top: PL enhancement of the Al-coated *a*-plane ZnO as a function of energy, with temperatures from 10 K to 250 K, showing the highest enhancement factor of approximately 12 at 3.354 eV at 80 K.
Bottom: 10 K-PL spectra of uncoated (black) and Al-coated (red) *a*-plane ZnO, graphed on a semi-logarithmic scale.
$\lambda_{exc} = 325$ nm, P =2.2 mW, laser spot $d = 30$ µm.

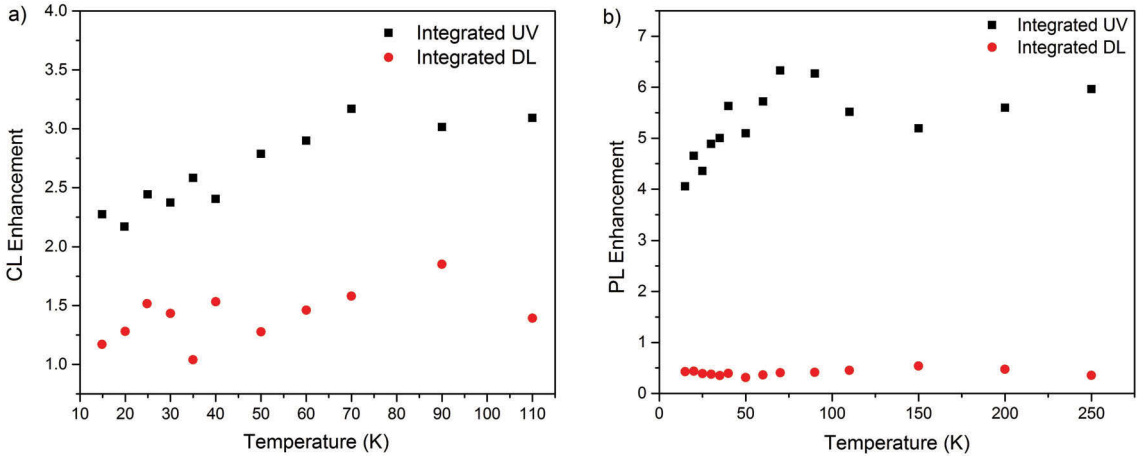

Fig. 5.15: (a) Integrated CL enhancement of the UV emission (black) from 3.00 eV to 3.54 eV and the DL emission (red) from 1.2 eV to 3.0 eV as a function of temperature (10 K to 110 K).
(b) Enhancement of the integrated PL of the UV (black) and DL (red) emission as a function of temperature (10 K to 250 K), with an overall decreased DL emission and a maximum UV enhancement of ~ 6.5 times at 80 K.
CL: $P = 17.5$ microW, $HV = 5$ kV, scan area 10 µm $\times$ 10 µm.
PL: $\lambda_{exc} = 325$ nm, $P = 2.2$ mW, laser spot ~ 30 µm.

a comparable PL and CL excitation depth, as discussed in section 3.2.6. However, the injected carrier density for the electron beam excitation is approximately four orders of magnitude higher than that of the laser excitation (cf. section 3.2.6).
It can be seen that the highest enhancement for both PL and CL, is at the energy of 3.343 eV (labelled in purple), which is most likely associated with a transition at the ZnO-Al or ZnO-Al_2O_3 interface, as discussed above. Furthermore, the CL intensity of the FX-A and -B as well as the energetically lower DBX-transitions, such as I_0 and I_2, is enhanced, while these emissions are almost unchanged in PL, compared with that in the uncoated *a*-plane ZnO. However, the region close to the first LO-phonon FX-C replica ($\sim$ 3.354 eV) is approximately 3 times enhanced in PL, which is less pronounced in CL. Note that the FX-C transition at 3.4264 eV is not observed, due to the poor UV collection efficiency and self-absorption.

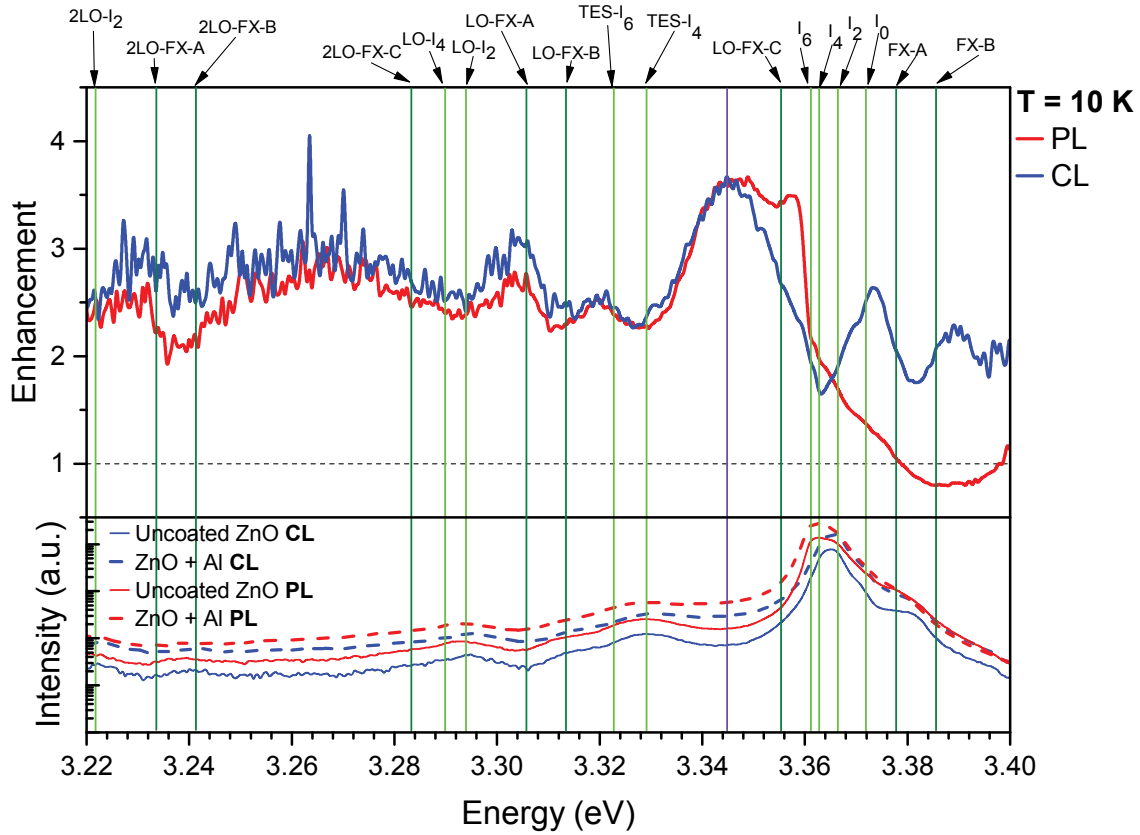

Fig. 5.16: Top: PL (red) and CL (blue) enhancement of Al-coated *a*-plane ZnO as a function of energy. The green labels present the DBX-related emission peaks, while FX emissions are labelled in olive.
Bottom: PL (red) and CL (blue) spectra of uncoated *a*-plane ZnO (solid lines) and Al-coated *a*-plane ZnO (dashed lines) at 10 K, graphed on a semi-logarithmic scale.
PL: $P = 2.2$ mW, laser spot ~ 30 µm
CL: $HV = 5$ kV, $P = 17.5$ µW, scan area 10 µm $\times$ 10 µm.

As mentioned above, an even higher enhancement is achieved at a temperature of 80 K, which is displayed in fig. 5.17. Here, the PL enhancement is greatest – approximately 12 times – for the first LO-phonon replica of the FX-C at 3.354 eV; the second and third LO-phonon FX-C replicas are located at 3.281 eV and 3.208 eV, showing a 7 to 8-fold enhancement. Although the LO-phonon replicas of the FX-C are enhanced in CL, the enhancement factor is only ~ 4 times, which is roughly half of that of PL. The comparison of the PL and CL enhancement of the FX-A and -B leads to a similar enhancement of 3 for both types of excitation. The highest CL enhancement of 4 times is recorded for the Al-associated I_6 line (3.359 eV), as discussed in section 5.2. In PL, the I_6 line is overlapped with the much more intense LO-phonon replica of the FX-C, which results in a shoulder of the broader FX-C LO-phonon replica. Similarly overlapped is the possible ZnO-Al or ZnO-Al_2O_3 interface emission at 3.343 eV for both, PL and CL.

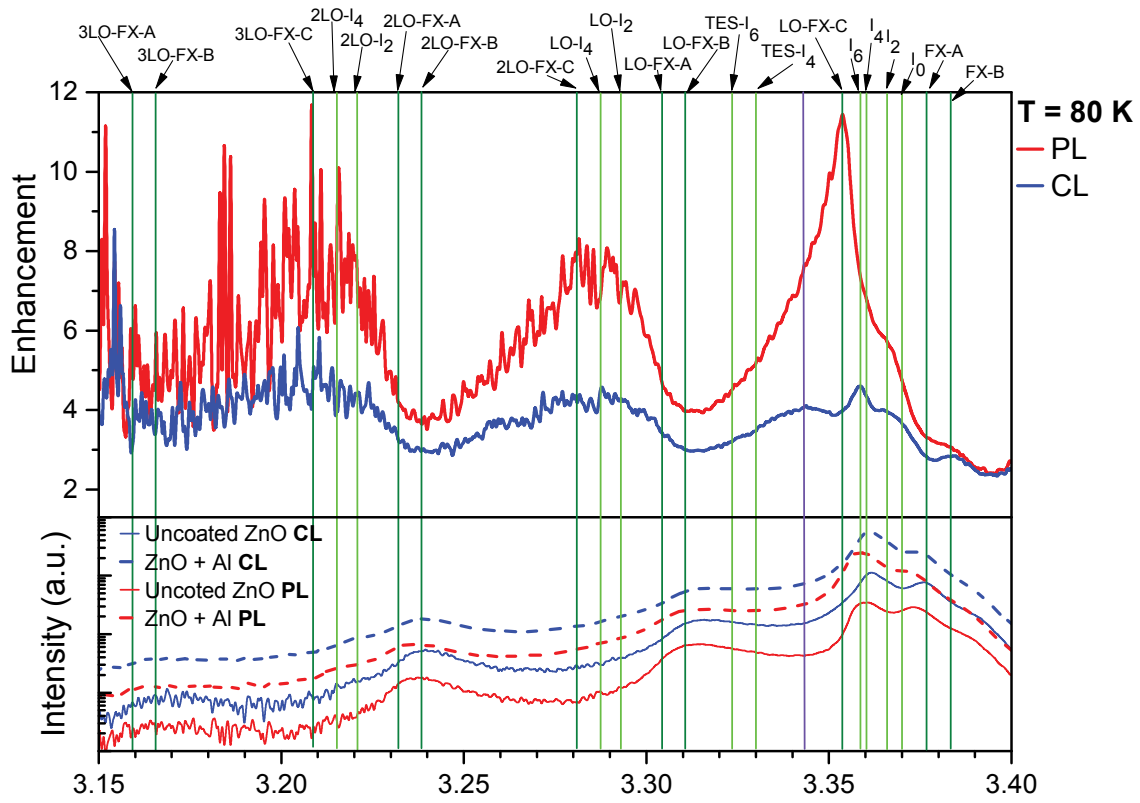

Fig. 5.17: Top: PL (red) and CL (blue) enhancement of Al-coated *a*-plane ZnO as a function of energy. The green labels present the DBX-related emission peaks, while FX emissions are labelled in olive.
Bottom: PL (red) and CL (blue) spectra of uncoated *a*-plane ZnO (solid lines) and Al-coated *a*-plane ZnO (dashed lines) at 80 K, graphed on a semi-logarithmic scale.
PL: $\lambda_{exc} = 325$ nm, $P = 2.2$ mW, laser spot ~ 30 µm
CL: $HV = 5$ kV, $P = 17.5$ µW, scan area 10 µm $\times$ 10 µm.

This temperature-dependent enhancement in PL and CL is in accordance with the aforementioned LSP-exciton coupling, mainly between the FX-C in ZnO and the LSPs in the Al nanoparticles. At low temperatures, such as 10 K, the luminescence spectra are dominated by the bound excitons, which are energetically lower than the free excitons. With increasing temperature the DBX emissions thermalise, so that the spectra are dominated by FX-related emission, peaking at approximately 120 K. A higher contribution of FX allows for increased LSP-exciton coupling, as the FX transitions are energetically higher. Moreover, the FX is more mobile than the localised DBX which also has a lower spatial extent than the FX, with the DBX wave function being localised close to the donor. Therefore, the FX can diffuse close to the ZnO-Al interface for stronger dipole-dipole interaction with the LSPs in the Al nanoparticles, while the intensity enhancement of the BX is defined by the donor/acceptor distribution. However, the highest enhancement is found at 80 K, where the FX emissions are similarly intense to that of the DBX. But a further increase in the temperature also decreases the FX intensity, as well as red-shifts and broadens the FX and LO-phonon replica excitonic emissions in ZnO due to increased phonon interaction, which possibly decreases the spectral overlap between the excitons and LSPs. It can be assumed, that the abundance of mobile FX – mainly FX-C – close to the Al surface coating, as well as their transition energy plays a crucial role for their coupling with the LSPs in the Al nanoparticles. Accordingly, 80 K appears to be the optimum temperature to allow for strongest LSP-exciton coupling.
Furthermore, the less pronounced CL enhancement of the LO-FX-C of 4 times at 80 K is most likely due to PL polarisation excitation effects, which, of course, is not relevant in CL generation with an electron beam. In PL, the laser light is always perpendicular polarised to the k-vector of the light, which is in the plane of the sample surface. This results in a preferred recombination of centres polarised in the same plane as the laser light. In the case of *a*-plane ZnO, the three FX transistions are differently polarised; FX-A and -B are perpendicular polarised to the c-axis, while the FX-C is parallel polarised. Therefore, the recombination through the FX-C-related emissions is preferred, as the FX-C is polarised in the same plane as the laser light. Hence, a higher coupling of the LSPs in the Al nanoparticles to the FX-C in *a*-plane ZnO is more probable when excited with laser light, resulting in a higher enhancement factor of the FX-C-related emissions, as observed in fig. 5.17.

Summarising the temperature-dependent luminescence enhancement in the UV, it can be seen that the highest enhancement is reached at a temperature of 80 K in CL and PL. While the DL emission, integrated from 1.2 eV to 3.0 eV, of the Al-coated *a*-plane ZnO is decreased in PL, it is slightly enhanced in CL to 1.5. The difference in DL emission enhancement in CL and PL is possibly due to the presence of non-radiative surface recombination or different in-depth defect distributions and excitation with CL and PL.

The integrated UV emission (3.00 eV to 3.54 eV) is overall enhanced up to 6.5 in PL and 3.3 in CL, following the Al deposition. The difference of the UV enhancement factor in CL and PL is most likely due to the different interaction area for the two types of excitation. While the light absorption in PL follows Beer-Lambert's Law (eq. (3.11)), injecting most of its energy and electron-hole pairs close to the surface, the energy loss profile of the electron beam has its maximum deeper in the sample (cf. fig. 3.6). Therefore, the laser injects carriers closer to the surface than the electron beam; as a result, the overlap of the dipole-dipole coupling is larger in PL than in CL. Additionally, a difference in excitation power densities in PL and CL can also be responsible for a different UV enhancement factors for both types of excitation, which is discussed in the next section (cf. section 5.2.3). Furthermore, a clear temperature dependence of the UV enhancement is found, peaking at 80 K. Interestingly, at 80 K the luminescence spectra are dominated by the FX, while the intensity of the DBX is considerably reduced due to thermalisation. Particularly in PL, the greatest enhancement of 12 times is found for the first LO-phonon replica of the FX-C at 3.354 eV, which is energetically higher than the FX-B and -A. The most probable explanation for this great enhancement is the larger spectral overlap between the FX-C with the LSPR in the Al nanoparticles (2.8 eV to 6.2 eV with maximum at approximately 5.17 eV), compared with other, energetically lower excitonic emissions in ZnO. Furthermore, a higher excitation selectivity by the laser can be assumed. The electric field of the laser light is perpendicularly polarised to its k-vector, therefore the polarisation of the laser light is parallel to the sample surface. However, the FX-C, which is polarised parallel to the c-axis in ZnO, is in the case of a-plane ZnO also parallel polarised to the sample surface. Hence, the excitation of the FX-C is favourable with laser excitation, allowing for stronger LSP-exciton coupling; while the FX-A and -B are perpendicularly polarised to the c-axis in ZnO. Nevertheless, the CL enhancement of the UV emission of the sample *Al* shows its maximum for the second and third LO-phonon replicas of the FX-C (3.281 eV and 3.208 eV at 80 K), as well as the emission at 3.343 eV, which is most likely from the ZnO-Al or ZnO-Al_2O_3 interface, as discussed above. Furthermore, the Al-related I_6 line is equally highly enhanced ($\sim$ 4 times) as the aforementioned emissions, indicating that the Al has diffused in the ZnO during the deposition process. Therefore, some of the observed UV enhancement can be assigned to Al-doping, which should be, in principle, higher at lower temperatures, as the DBX dissociates at elevated temperatures, while the FX in ZnO are much more stable. The maximum enhancement at 80 K, as well as the greatly enhanced LO-phonon replicas of the FX-C indicate that the LSP-exciton coupling is strongest for the energetically highest FX-C and the LSPs in the Al nanoparticles.

5.2.3 Excitation Power-Dependent CL and PL Study of Al-Coated *a*-plane ZnO

As discussed in section 3.2.6, the excitation power density with the electron beam is approximately four orders of magnitude higher than that of the laser, which could be responsible for the difference in the enhancement factors. A possible excitation power dependence on the enhancement factor in the sample *Al* was investigated and the results are discussed in this section.

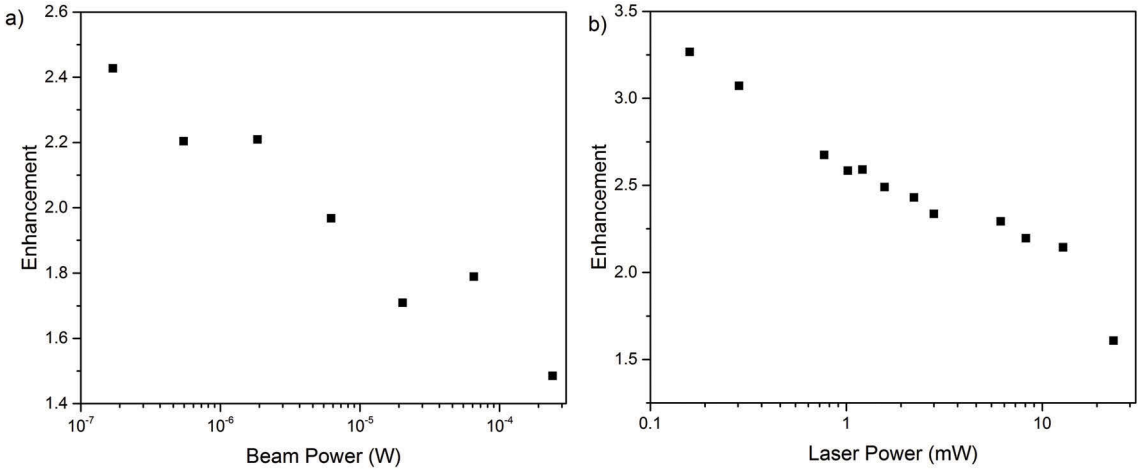

Fig. 5.18: Power-dependent UV enhancement in (a) CL and (b) PL of the Al-coated *a*-plane ZnO, integrated from 3.00 eV to 3.54 eV at 10 K.
CL: $HV = 5$ kV, scan area 15 µm × 15 µm.
PL: $\lambda_{exc} = 325$ nm, spot size ~ 30 µm.

The corresponding CL and PL enhancement factors as a function of electron beam and laser excitation power at 10 K are shown in fig. 5.18 a and b, respectively. It can be seen that the enhancement is highest at lowest excitation power for both CL and PL excitation. An exponential relationship between the enhancement factor and the excitation power (plotted semi-logarithmically) is found.

A closer look at the integrated DL and the UV emission of the uncoated and the Al-coated *a*-plane ZnO as a function of excitation power shows a similar behaviour for the laser and the electron beam excitation, depicted in fig. 5.19. While the integrated UV emission of the Al-coated *a*-plane ZnO as a function of excitation power, logarithmically plotted, has a linear relationship with a power law exponent of (1.01 ± 0.02), the uncoated *a*-plane ZnO shows a super-linear power law exponent (1.10 ± 0.01) for both PL and CL (cf. section 3.2.5.2). The super-linear power law exponent for the uncoated side of the sample *Al* can be explained by the saturation of radiative or non-radiative recombination channels with increasing power, which is not observed in the Al-coated *a*-plane ZnO.

The integrated DL emission of the uncoated *a*-plane ZnO exhibits a sub-linear power law exponent with increasing excitation power, indicating that one or more of the defect-related recombination channels saturate. However, the Al-coated *a*-plane ZnO shows a

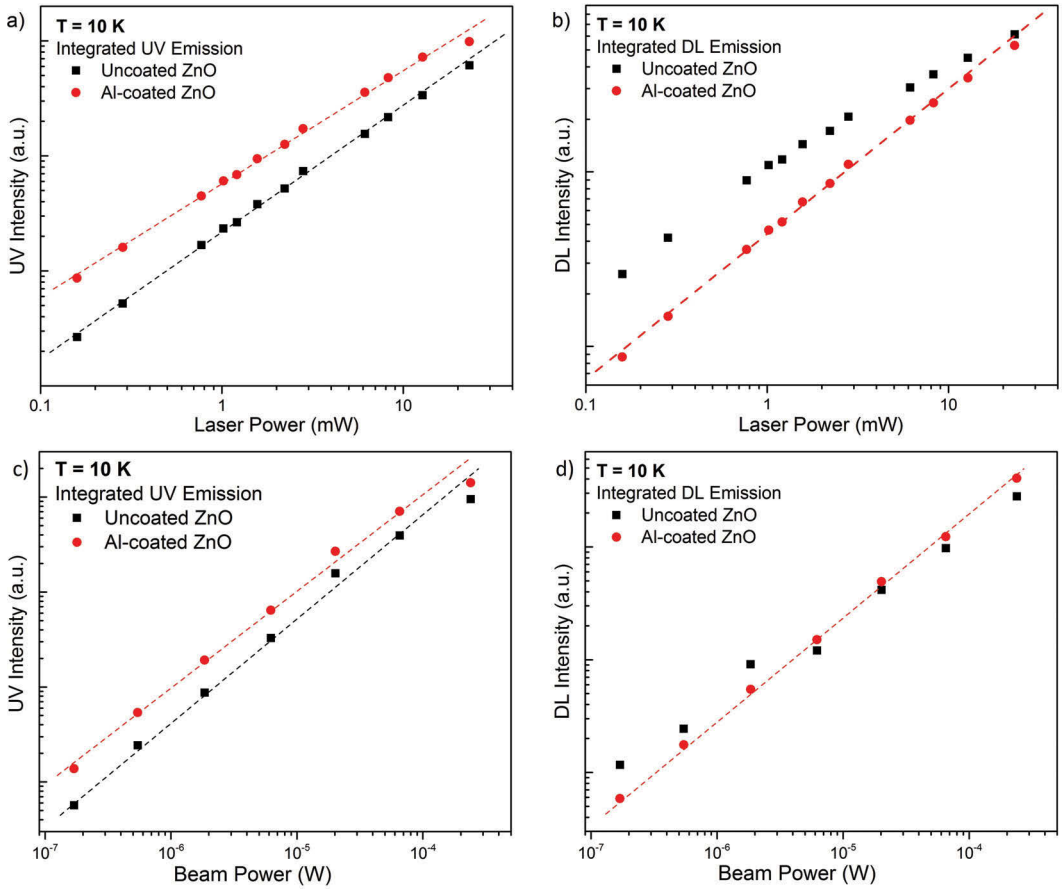

Fig. 5.19: (a) 10 K-power-dependent PL of the UV emission, integrated from 3.00 eV to 3.54 eV and (b) the DL emission, integrated from 1.2 eV to 3.0 eV of the uncoated (black) and the Al-coated *a*-plane ZnO (red), graphed logarithmically. (c) Power-dependent CL of the integrated UV emission and (d) the integrated DL emission. The dashed lines serve as guide to the eye.
PL: $\lambda_{exc} = 325\,nm$, laser spot $\sim 30\,\mu m$
CL: $HV = 5\,kV$, scan area $15\,\mu m \times 15\,\mu m$.

linear relationship with increasing excitation power. This trend can be observed for both the electron beam and the laser excitation.

From the depth-resolved CL spectroscopy in section 5.2.1, it is known that the GL at an acceleration voltage of 5 kV is only present in the uncoated *a*-plane ZnO, but suppressed in the Al-coated *a*-plane ZnO (cf. fig. 5.7 e and f). A similar behaviour can be seen with the laser excitation, presented in fig. 5.20, which has a similar penetration depth into ZnO as the CL excitation depth of the electron beam at an acceleration voltage at 5 kV (see section 3.2.6). A possible explanation of the sub-linear power law exponent in the DL emission with increasing excitation power is that the GL in the uncoated *a*-plane ZnO saturates with increasing excitation power. The lifetime of the GL is on the order of µs, which is several orders of magnitude slower than that of the fast excitonic UV emission

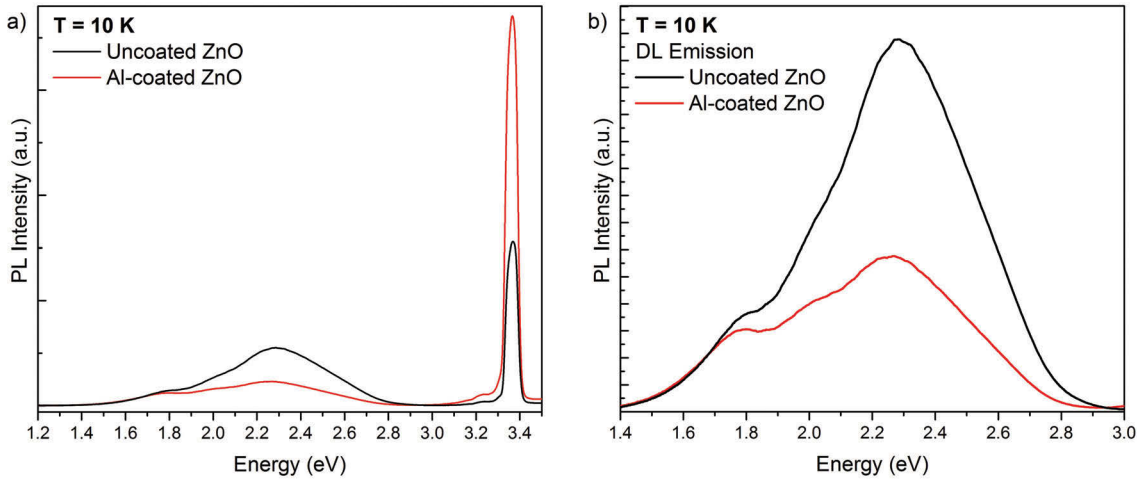

Fig. 5.20: (a) Full PL spectra of the uncoated (black) and the Al-coated *a*-plane ZnO (red) at 80 K. (b) DL emission of the uncoated (black) and the Al-coated *a*-plane ZnO (red), showing reduced green luminescence (GL). $\lambda_{exc} = 325\,nm$, $P = 2.2\,mW$, spot size $\sim 30\,\mu m$.

in ZnO (tens or hundreds of ps)[187, 218]. Therefore, saturation of the slower competitive recombination channel (GL) with increasing excitation power will increase the UV emission at the same time, explaining both the sub-linear DL power law exponent, as well as the super-linear exponent of the UV emission.

Conversely, both the integrated DL and UV emission of the Al-coated *a*-plane ZnO show a linear relationship with increasing excitation power, which indicates that no recombination pathway is saturated or created with increasing power. This excitation power independence is most likely due to the suppressed or at least highly reduced GL in this sample.

A similar power-dependent luminescence trend can be observed at a temperature of 80 K, which is illustrated in fig. 5.21 (a) and (b) for PL and (c) and (d) for CL.

The corresponding UV enhancement in CL and PL at 10 K, 80 K and 300 K is shown in fig. 5.22. These results indicate that the power-dependent enhancement is not temperature dependent, but the enhancement itself, as discussed in section 5.2.2.

The excitation power-dependent enhancement of the Al-coated *a*-plane ZnO sample can possibly explain the difference in the maximum PL and CL enhancement, demonstrated in fig. 5.18. Here, a higher enhancement factor (~ 3.3) can be reached with the laser excitation, while the highest integrated CL enhancement is ~ 2.4. The lower maximum enhancement in CL can be explained by a larger excitation power density by the electron beam (cf. section 3.2.6). Therefore, the lowest effective electron beam power over the entire sample area is greater than that of the laser excitation. Furthermore, the aforementioned different energy loss profile within the sample is different for laser and electron beam excitation, so that PL is, even at a similar penetration depth of $\sim 100\,nm$ like the

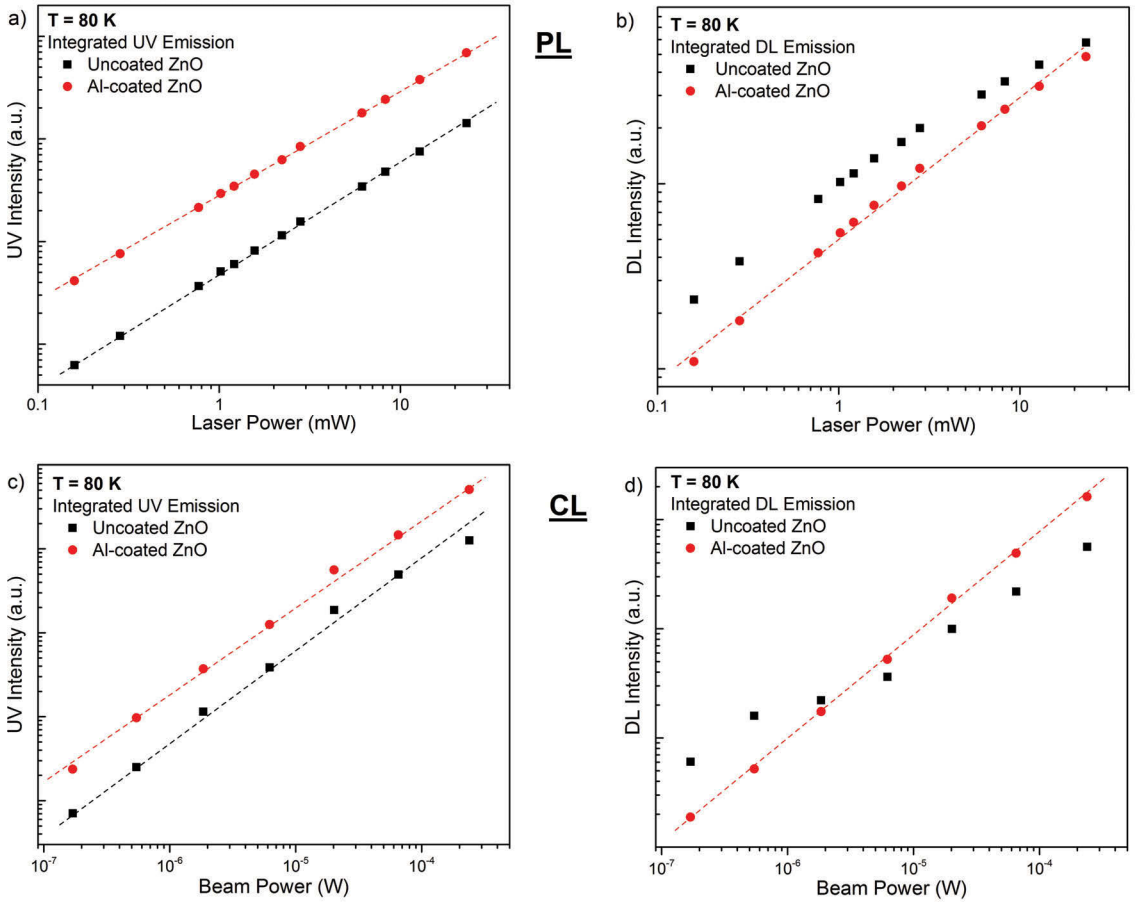

Fig. 5.21: Power-dependent PL at 80 K of (a) the UV emission, integrated from 3.00 eV to 3.54 eV and (b) the DL emission, integrated from 1.2 eV to 3.0 eV of the uncoated (black) and the Al-coated *a*-plane ZnO (red), graphed logarithmically.
Power-dependent CL at 80 K of (c) the UV emission, integrated from 3.00 eV to 3.54 eV and (d) the DL emission, integrated from 1.2 eV to 3.0 eV of the uncoated (black) and the Al-coated *a*-plane ZnO (red), graphed logarithmically. The dashed lines serve as guide to the eye.
CL: $HV = 5\,\text{kV}$, scan area $15\,\mu\text{m} \times 15\,\mu\text{m}$.
PL: $\lambda_{\text{exc}} = 325\,\text{nm}$, spot size $\sim 30\,\mu\text{m}$.

CL excitation depth of approximately 88 nm at an acceleration voltage of 5 kV, a more surface-sensitive technique than CL.

The power law exponents of the UV emission at 10 K, 80 K and 300 K are illustrated in the table 5.3 below.

The power dependence of the UV enhancement, showing the maximum enhancement at the lowest excitation power for both types of excitation, is most likely due to the saturation of the GL in the uncoated *a*-plane ZnO with increasing excitation power, which increases the recombination probability of the excitonic emission at the same time. Conversely, the GL in the Al-coated *a*-plane ZnO is highly reduced, which leads to linear

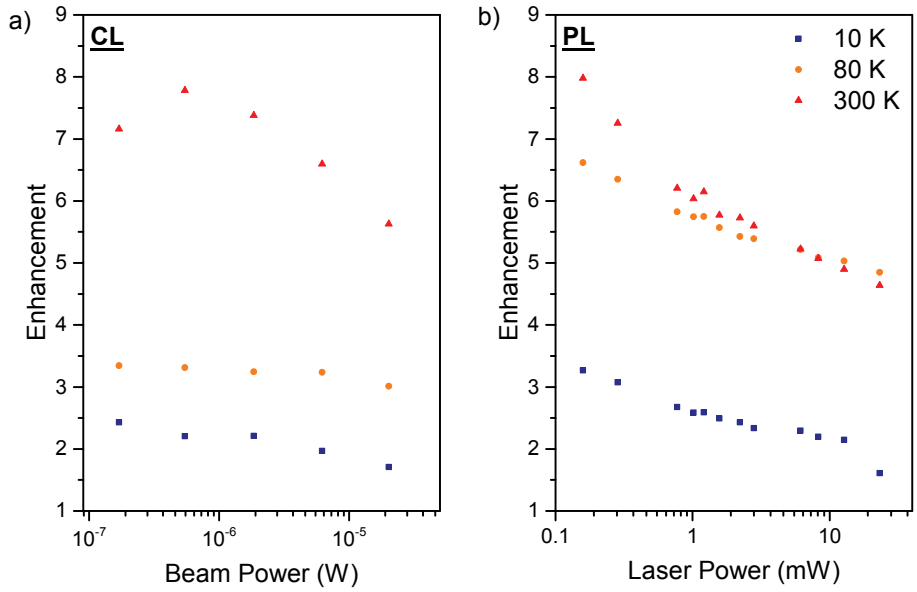

Fig. 5.22: Power-dependent UV enhancement in (a) CL and (b) PL of the Al-coated *a*-plane ZnO, integrated from 3.00 eV to 3.54 eV at 10 K (blue), 80 K (orange) and 300 K (red), graphed logarithmically.
CL: $HV = 5$ kV, scan area 15 µm × 15 µm.
PL: $\lambda_{exc} = 325$ nm, spot size ∼ 30 µm.

Table 5.3: Power law exponents of the UV enhancement of the sample *Al* at 10 K and 80 K.

Sample	Temperature (K)	Power law exponent of the UV emission with increasing laser excitation power
uncoated *a*-plane ZnO	10	(1.10 ± 0.02)
Al-coated *a*-plane ZnO	10	(1.01 ± 0.02)
uncoated *a*-plane ZnO	80	(1.10 ± 0.01)
Al-coated *a*-plane ZnO	80	(1.02 ± 0.01)
uncoated *a*-plane ZnO	300	(1.11 ± 0.01)
Al-coated *a*-plane ZnO	300	(1.01 ± 0.01)

power dependency of both the integrated UV and the DL emission. The changed GL in Al-coated *a*-plane ZnO compared to the uncoated side of the sample is therefore assumed to be responsible for larger UV enhancement factors for lower excitation powers.

This change in GL is depth-dependent, as discussed in section 5.2.1, suggesting that a different excitation power dependence of the UV enhancement factor would apply for greater CL generation depths.

5.2.4 Time-Resolved PL of Al-Coated *a*-plane ZnO

As the LSP-exciton coupling increases the SER by creating an additional, faster relaxation channel through the metal nanoparticle-coating, a reduced minority carrier lifetime is typically be observed (cf. section 2.4.4). To study the lifetime of the uncoated and the Al-coated *a*-plane ZnO sample, time-resolved PL was performed at a temperature of 10 K, which is presented in fig. 5.23. As discussed in section 4.4.4.2, the decay of the mi-

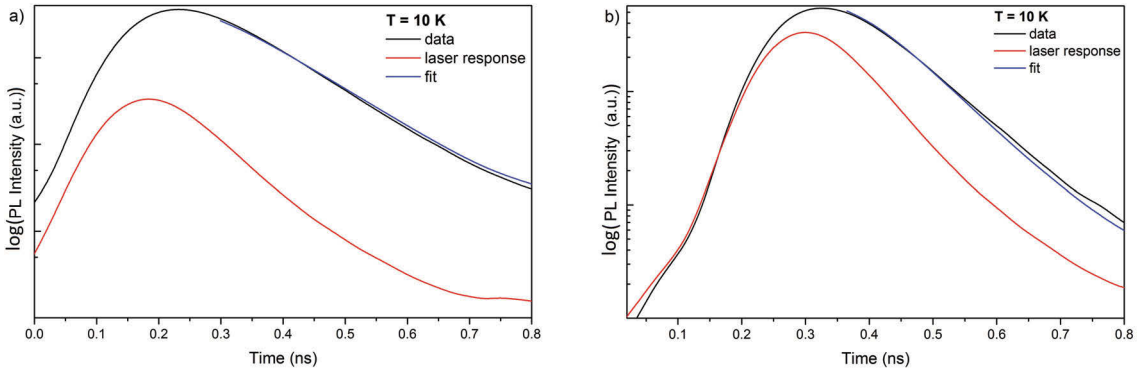

Fig. 5.23: Time-resolved PL at a fixed collection energy of 3.36 eV of (a) the uncoated and (b) the Al-coated *a*-plane ZnO, at 10 K, showing a shortened lifetime from $\tau_{\mathrm{ZnO}} = (161 \pm 4)$ ps to $\tau_{\mathrm{ZnO+Al}} \leq 53$ ps. The uncertainty of $\tau_{\mathrm{ZnO+Al}}$ cannot be determined, as the lifetime is similarly short as the laser response function.

nority carriers in the investigated sample can be fitted with an exponential function — in the case of the ZnO nanorods a bi-exponential fit was needed to account for the non-radiative and radiative lifetime, while the *a*-plane ZnO single crystals can be fitted with a single exponential function. Note that the TR-PL data was deconvoluted with the laser response function, which exhibits a second laser pulse after approximately after 1.1 ns, which is why the TR-PL data is only presented between 0 ns to 0.8 ns.

The corresponding lifetimes, from fig. 5.23, of the uncoated and the Al-coated *a*-plane ZnO are determined to be $\tau_{\mathrm{ZnO}} = (161 \pm 4)$ ps and $\tau_{\mathrm{ZnO+Al}} \leq 53$ ps, respectively. While the uncoated *a*-plane ZnO shows a relatively long lifetime, measured at the energy of the DBX, the Al-coated side of the sample exhibits a shorter lifetime, which is very close to the laser pulse duration. Therefore, it is not possible to confidently fit the data and determine the lifetime, although it can be concluded that lifetime is at least shortened to $\tau_{\mathrm{ZnO+Al}} \leq 53$ ps.

From those lifetimes the Purcell enhancement factor can be calculated, as shown in section 2.4.4.

$$F_{\mathrm{P}} = \frac{\tau_{\mathrm{ZnO}}}{\tau_{\mathrm{ZnO+Al}}} \sim 3.$$

Comparing of the F_{P} with the PL enhancement of the DBX at 10 K in fig. 5.16 shows that they are both in the same order of $\sim$ 2 to 3. However, the lifetime of the various excitonic transitions in ZnO are not the same and it can be assumed that the reduction on the lifetime is dependent on the strength of the LSP-exciton coupling. Therefore, a larger lifetime reduction of the FX-C or its LO-phonon replicas is expected, which is below the resolution of the experimental setup used (cf. section 3.2.7). As the enhancement is highest at 80 K, an even more reduced lifetime is expected for the FX-C-related emissions. In general, a larger number of lifetime measurements of the excitonic transitions in ZnO would be needed to fully characterise the UV enhancement in the Al-coated *a*-plane ZnO, possibly at 10 K as well as 80 K. The performance of these measurements is not only very time-consuming, but also difficult, as the *I* lines in the DBX region are very close to each other and may be overlapping with each other, as well as the temporal resolution of the experimental setup being required to be sub-ps. Nevertheless, the TR-PL results shown above, indicate that the lifetime of the DBX is shortened due to LSP-exciton coupling, which is consistent with the creation of an additional, faster decay pathway via the Al nanoparticles, increasing the SER and subsequently the UV emission of the Al-coated *a*-plane ZnO.

5.2.5 Summary of the Results of Al-coated *a*-plane ZnO

In summary, the sample *Al* exhibits an enhanced UV emission, which shows the greatest enhancement close to the ZnO-Al interface at lowest excitation power, at a temperature of 80 K.

The excitation power dependence of the Al-coated *a*-plane ZnO is most likely due to a decreased GL in the DL emission, compared with the uncoated side of the sample. Here, the GL possibly saturates with increasing excitation power by both the electron beam and the laser light, allowing for increased integrated UV emission at the same time. The Al-coated *a*-plane ZnO with the highly reduced GL has a linear excitation power relationship in both UV and DL emission. Due to higher excitation power density of the electron beam (at 5 kV) compared to that of the laser, a larger UV enhancement in PL is observed than in CL.

Furthermore, the results of the depth-dependent CL, showing the highest UV enhancement at the surface close to the ZnO-Al interface, as well as the temperature dependence of the UV enhancement can most likely be attributed to LSP-exciton coupling between the Al nanoparticles and the FX-C in ZnO. It is known that the coupling strength is highly

dependent on the dipole separation (exciton and LSP), and the physical LSP-exciton separation, as the evanescent field decays exponentially with increasing distance. In the case of the sample *Al*, the energy separation between the LSPs and the excitons is the smallest for the energetically highest transition in ZnO, the FX-C, as the LSPR of the Al nanoparticles is broad (6.2 eV to 2.8 eV) with its maximum around 5.17 eV.
This can be underpinned by the results of the temperature-dependent PL measurements, which show the highest integrated UV enhancement of ~ 6.5 at a temperature of 80 K. At this temperature, the PL spectra exhibit intense FX-related emissions, while the DBX have started to thermalise already. With rising temperatures, the FX emissions are more intense, compared with the DBX, having its maximum at ~ 120 K, but the excitonic emissions in ZnO broaden and red-shift due to phonon interaction at the same time. Therefore, the optimal conditions for LSP-exciton coupling between the excitons in ZnO and the LSPs in Al nanoparticles are reached at a temperature of 80 K.
Additionally, the parallel polarisation of the FX-C to the c-axis of the ZnO — parallel to the sample surface in the case of *a*-plane ZnO — is more likely to be excited by the laser light, which is polarised in the same plane and, therefore, allows for stronger LSP-exciton coupling.
Moreover, a reduced lifetime with a resulting Purcell enhancement factor of at least ~ 3 is found, indicating the creation of a faster, additional relaxation channel via the LSPs in the Al nanoparticles. This results in an increase of the SER and, therefore, enhances the UV emission of the Al-coated *a*-plane ZnO.

5.3 Optical Properties of Hot Al-Coated *a*-plane ZnO

In this section, the results of the optical characterisation of the sample *Al hot* are presented and discussed. The CL and PL spectra of the *a*-plane ZnO deposited with Al at 300 °C show an enhanced UV emission, similar to those at room temperature, discussed in section 5.2. The results in section 5.1.2 and section 5.1.3 suggest that the Al-coating of sample *Al hot* contains more metallic Al than the sample *Al*, indicated by an increase of the LSP absorption in the transmission spectrum. This might lead to an increased LSP-exciton coupling in the sample *Al hot*, compared with the sample *Al*. This section will discuss the similarities and the differences of these two samples.

5.3.1 Depth-Resolved CL Spectroscopy of Hot Al-Coated *a*-plane ZnO

To study the distribution of the luminescence with increasing probing depth, depth-resolved CL spectroscopy was performed. Similarly to the depth-resolved CL results of the sample *Al* (cf. section 5.2.1), it is expected that the enhanced UV emission in the sample *Al hot* shows a depth dependence. Furthermore, the change in the DL emission

with increasing CL excitation depth was investigated.
In fig. 5.24 the depth-resolved CL spectra of the uncoated and hot Al-coated *a*-plane ZnO are displayed, showing an overall increased and slightly red-shifted UV emission following the hot Al-coating.

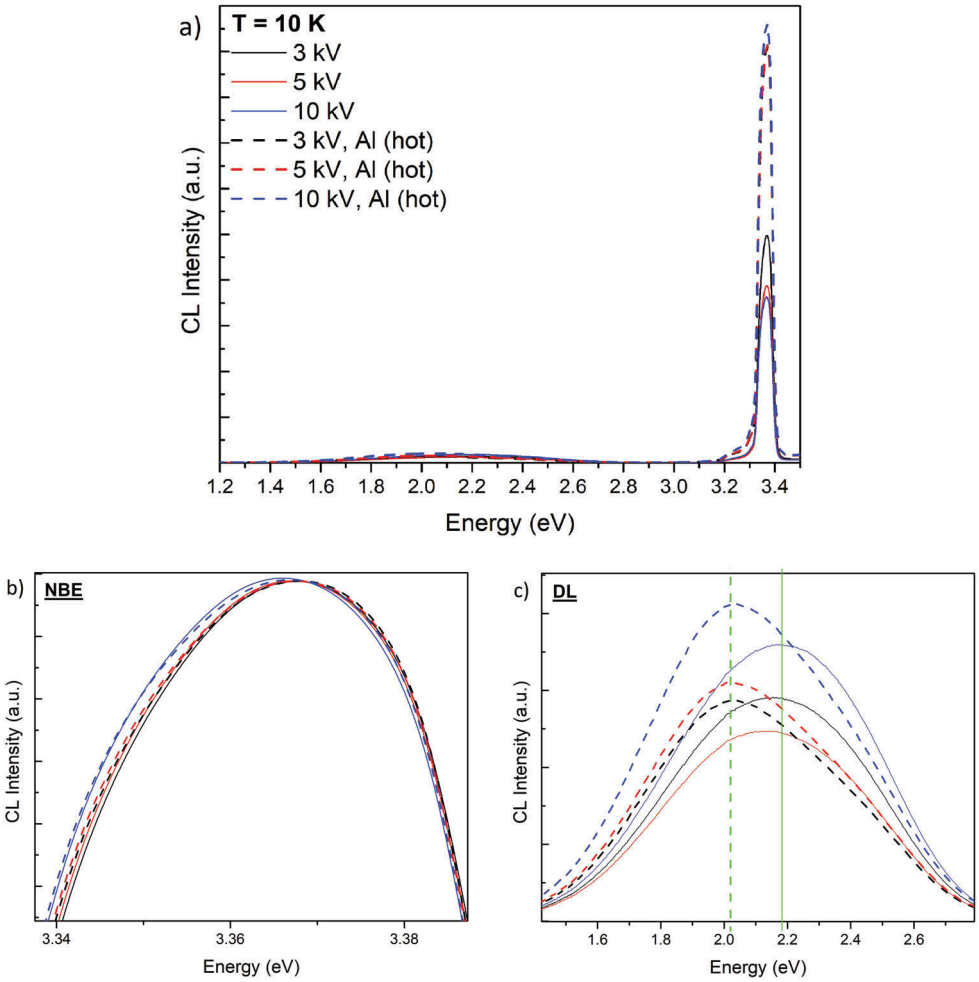

Fig. 5.24: (a) Depth-resolved CL spectra of the uncoated and hot Al-coated *a*-plane ZnO at 10 K. (b) shows the normalised UV emission and (c) the DL emission of the sample *Al hot*.
$HV = 3\,\text{kV}, 5\,\text{kV}$ and $10\,\text{kV}$, $P = 17.5\,\mu\text{W}$, scan area $10\,\mu\text{m} \times 10\,\mu\text{m}$.

Table 5.4 shows the UV enhancement factor, calculated from the maximum intensity of the NBE emission of the uncoated and hot Al-coated *a*-plane ZnO, as well as the enhancement integrated over the entire UV emission (3.10 eV to 3.45 eV). It can be seen that the UV enhancement factor is highest at 10 kV, which is the opposite effect as in the sample *Al*, which showed its highest enhancement at 3 kV, closest to the sample surface. For completeness, the UV enhancement factors at 180 K and 300 K are listed in table 5.4. At 80 K, the UV emission of the hot Al-coated *a*-plane ZnO at 3 kV is even halved compared

Table 5.4: UV enhancement factors of the sample *Al hot* at three different acceleration voltages at 10 K, 80 K and 300 K. The second column presents the UV enhancement, calculated from the highest UV emission, while the third column shows the UV enhancement, integrated from 3.10 eV to 3.45 eV.

HV (kV)	T (K)	UV enhancement (I)	UV enhancement (Int)
3	10	1.9	1.8
5	10	2.4	2.4
10	10	2.6	2.6
3	80	0.6	0.5
5	80	1.6	1.6
10	80	3.2	3.1
3	300	1.1	1.1
5	300	1.4	1.3
10	300	1.3	1.3

to the uncoated side of the sample. This trend is unexpected and is therefore studied in more detail below, showing the high-resolution depth-dependent CL spectra.
The normalised spectra of the NBE emission in the uncoated and the Al-coated *a*-plane ZnO is depicted in fig. 5.24b, showing that the red-shift due to the Al-coating in the sample *Al* is not observed in this sample.
The DL emission in fig. 5.24c shows a similar trend as seen in the sample *Al* (fig. 5.7) with a reduced GL at 2.45 eV at lower acceleration voltages of 3 kV and 5 kV of the hot Al-coated *a*-plane ZnO. At 10 kV, a shoulder at approximately 2.45 eV is visible, indicating that this effect is surface-related. The reduction of the GL in this sample is less pronounced than in the sample *Al*, where the GL is highly reduced at 3 kV. The change in the GL due to the Al-coating can be possibly explained by changes in the V_{Zn} charge transfer mechanisms, as discussed in section 5.2.1. Furthermore, a less pronounced band bending was found in the sample *Al hot*, which can possibly affect the degree of reduction of the GL defect (cf. table 5.1).
The high-resolution depth-resolved CL spectra of the uncoated and hot Al-coated *a*-plane ZnO at the acceleration voltages of 3 kV, 5 kV and 10 kV are presented in fig. 5.25, exhibiting an overall increased UV emission for the Al-coated side of the sample *Al hot*. The excitonic emission peaks are labelled at both temperatures, 10 K and 80 K, showing the thermalisation of the DBX at higher temperature, and peak broadening and red-shifting. Although this trend is similar to that shown in section 5.2.1, the UV enhancement as a function of energy for 3 kV, 5 kV and 10 kV appears to be different. Figure 5.26a and b depict the enhancement at 10 K and 80 K, respectively. It can be seen that the enhancement is depth-dependent with its maximum of approximately 2.8 at 5 kV at a temperature of 10 K, while at 80 K, it shows the largest enhancement ($\sim$ 2.8) at 3 kV. These results are

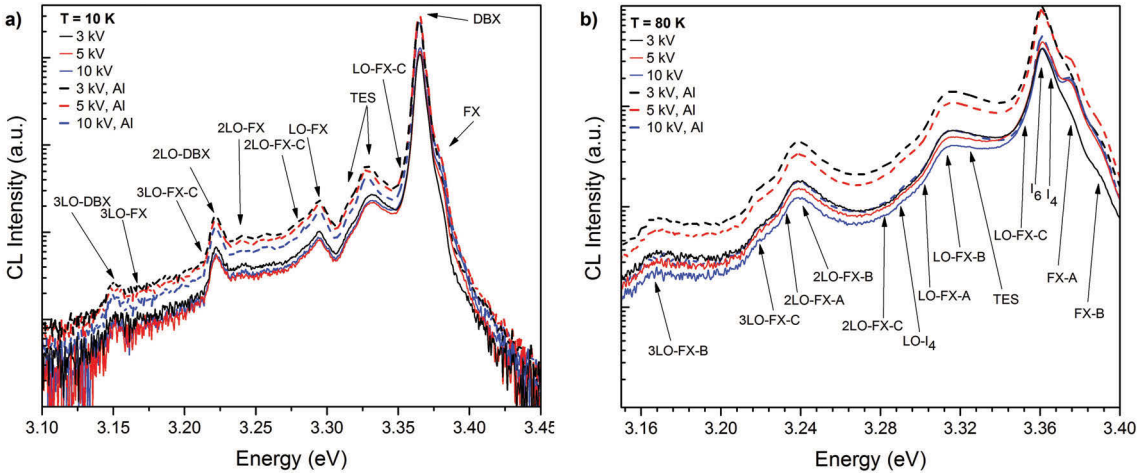

Fig. 5.25: High-resolution depth-resolved CL spectra of the sample *Al hot* at (a) 10 K and (b) 80 K.
$HV = 3$ K, 5 K and 10 K, $P = 17.5$ µW, scan area 10 µm × 10 µm.

different to the integrated UV enhancement, presented in table 5.4, showing the greatest enhancement at 10 kV. As the depth-dependent trend with the maximum UV enhancement at 3 kV, closest to the ZnO-Al interface is also observed in the sample *Al*, it is more likely that the results of the high-resolution depth-resolved CL spectra reflect the LSP-exciton behaviour more accurately than the integrated UV enhancement factors, shown in table 5.4. At both 10 K and 80 K, the maximum enhancement of ~ 2.8 is found for the I_6

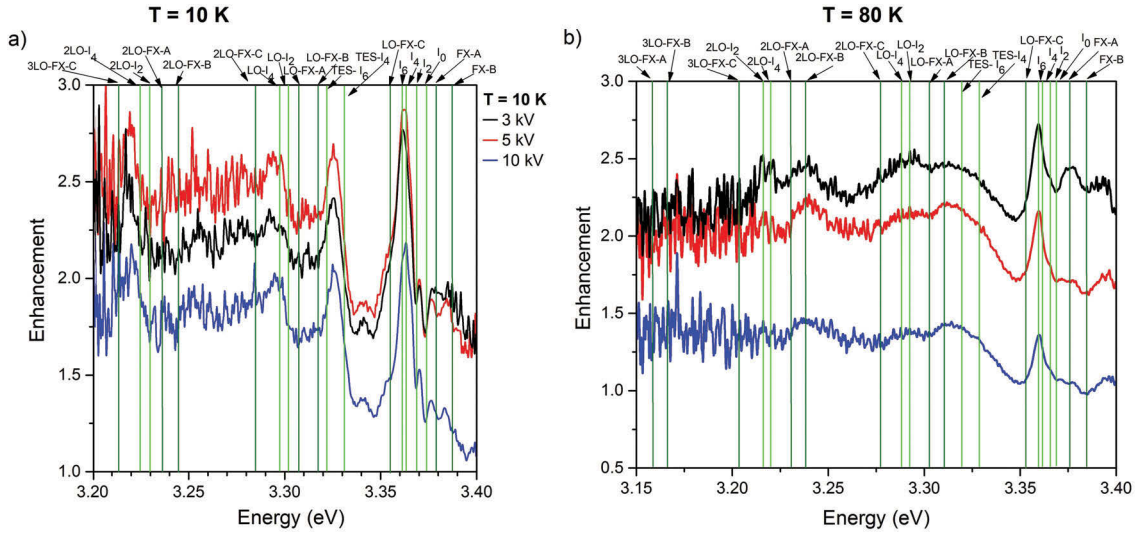

Fig. 5.26: Depth-dependent CL enhancement of the sample *Al hot* as a function of energy at (a) 10 K and (b) 80 K. The green labels present the DBX-related emission peaks, while FX emissions are labelled in olive.
$HV = 3$ kV, 5 kV and 10 kV, $P = 17.5$ µW, scan area 10 µm × 10 µm.

line (fig. 5.26), which is associated with Al (cf. table 2.1). Therefore, it can be assumed that

some Al diffused into ZnO during the deposition, as Al is a well-known donor dopant for ZnO with a signature of a sharp I_6 emission line. Here, this Al-doping is more pronounced than in the sample *Al* (see fig. 5.11), which can be explained by the elevated deposition temperature, allowing for thermally-assisted Al diffusion into ZnO.
Furthermore, the enhancement of the aforementioned interface emission between ZnO and Al or ZnO and Al_2O_3 at $\sim 3.343\,eV$ is visible at 10 K, but it is not as greatly enhanced as the DBX-related emission. At 80 K, the contribution of the FX to the enhancement is higher than at 10 K, as expected, but the FX-C is not as pronounced as in the sample *Al*. Additionally, the enhancement is not as energy-dependent and high as found in the sample *Al*. A possible explanation for this less pronounced enhancement can be either:

1. a less pronounced surface band bending (cf. section 5.1.4) or
2. a higher diffusion of Al into ZnO.

Here, the reduced downward surface band bending possibly does not move the charge transfer level as much as for the sample *Al*, which exhibits a larger surface band bending. This might be the reason why the GL in the DL emission, presented in fig. 5.24c, is less reduced, leading to a lower enhancement factor of the UV emission — this will be further discussed in the excitation power-dependent luminescence section (section 5.3.3).
Furthermore, the increased Al-doping is likely to mainly enhance the Al-associated I_6 line, while effectively less metallic Al is present at the surface to form nanoparticles for plasmonic interaction. Although the results of the ellipsometry measurements and simulations, as well as that of the transmission spectroscopy (cf. section 5.1.2 and section 5.1.3) suggest a higher Al content, this appears not to be the case for the luminescence results, which is possibly due to the Al deposition on different substrates. For the ellipsometry measurements, the Al was deposited at 300 °C onto Si, while for the transmission spectroscopy, it was deposited onto UV-quartz. It is possible that Al diffuses into Si, quartz and ZnO to different extents, as Al is a known dopant for ZnO. Most of the Al deposited diffused in the ZnO substrate and contributes to highly enhanced I_6, while less Al is available for plasmonic coupling with the excitons, which results in a less pronounced overall UV enhancement, as well as a less distinct energy dependence of the enhancement factor.

5.3.2 Temperature-Dependent PL Spectroscopy of Hot Al-Coated *a*-plane ZnO

To further investigate the origin of the enhanced UV emission of the hot Al-coated *a*-plane ZnO, as well as the differences between the sample *Al* and *Al hot*, temperature-dependent PL was performed from 10 K to 250 K.
The resulting spectra of the uncoated and the hot Al-coated *a*-plane ZnO are depicted in fig. 5.27 a and b, respectively. The typical thermalisation effects with increasing tempera-

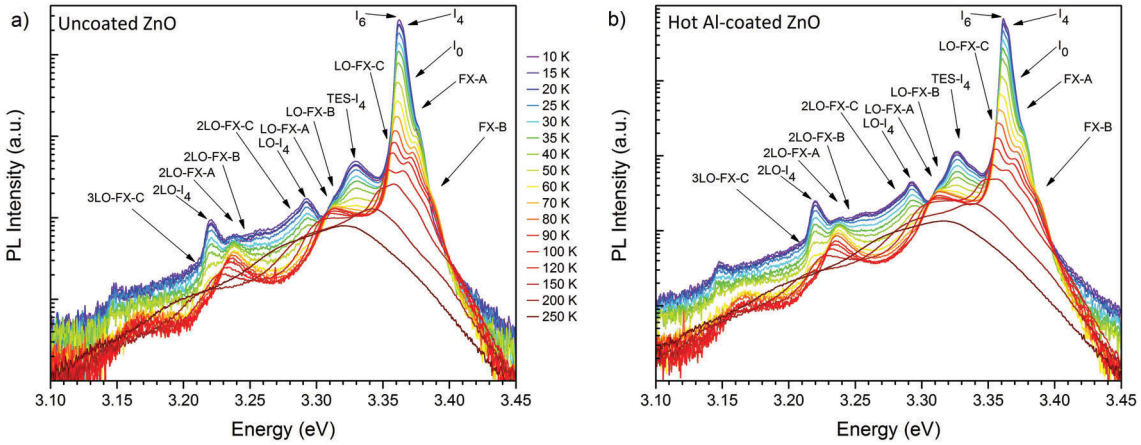

Fig. 5.27: Temperature-resolved PL of (a) uncoated and (b) hot Al-coated *a*-plane ZnO.
$\lambda_{exc} = 325\,\text{nm}$, $P = 2.2\,\text{mW}$, laser spot $d \sim 30\,\mu\text{m}$.

ture can be observed, including reduced intensity of the DBX-related emissions compared to the FX, as well as peak broadening and red-shifting.

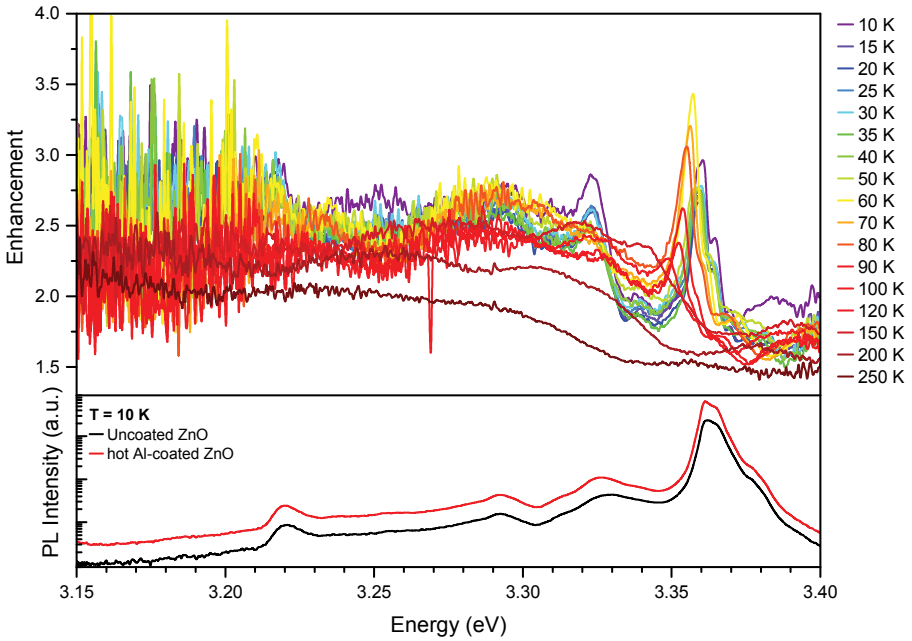

Fig. 5.28: Top: Temperature-resolved PL enhancement of the sample *Al hot* as a function of energy.
Bottom: High-resolution 10 K-PL of uncoated (black) and hot Al-coated *a*-plane ZnO (red), graphed on a semi-logarithmic scale.
$\lambda_{exc} = 325\,\text{nm}$, $P = 2.2\,\text{mW}$, laser spot $\sim 30\,\mu\text{m}$.

The enhancement factor as a function of energy is presented in fig. 5.28, showing the maximum enhancement of approximately 3.5 at 60 K. The enhancement at this particular

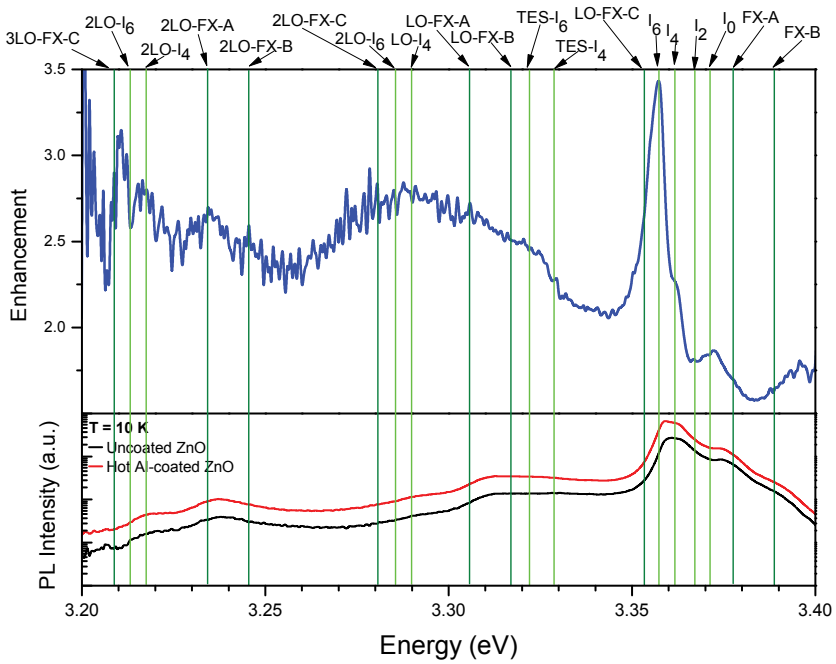

Fig. 5.29: Top: PL enhancement of the sample *Al hot* as a function of energy at 60 K. The green labels present the DBX-related emission peaks, while FX emissions are labelled in olive.
Bottom: High-resolution 10 K-PL of uncoated (black) and hot Al-coated *a*-plane ZnO (red), graphed on a semi-logarithmic scale.
$\lambda_{exc} = 325\,nm$, $P = 2.2\,mW$, laser spot $d \sim 30\,\mu m$.

temperature is depicted in fig. 5.29 with labelled excitonic emission peaks. Similar to the depth-resolved CL results shown in section 5.3.1, the highest enhanced emission is the I_6 line at 3.358 eV, while the broad LO-phonon-replica of the DBX and FX are approximately 2.8 times enhanced. In contrast to the results in section 5.2, the emissions related to the FX-C are not particularly enhanced, suggesting that the LSP-exciton coupling is lower in this sample. The smaller enhancement overall and that of the FX-C-related emissions, can be possibly explained by the lower content of metallic Al in the surface coating, leading to fewer LSPs in the Al nanoparticles to couple to. Moreover, the recombination channel through the I_6 line might be more efficient than the FX-C, resulting in a lower FX-C emission. Therefore, the LSP-exciton coupling strength is likely to be reduced due to fewer LSPs and FX-C.

5.3.3 Excitation Power-Dependent PL and CL Spectroscopy of Hot Al-Coated *a*-plane ZnO

This section discusses the CL and PL enhancement dependence of the excitation power. In section 5.2, an exponential reduction of the UV enhancement with increasing laser and electron beam excitation power is found for the sample *Al*, resulting in different CL and

PL enhancement factors. The power dependence can most likely be attributed to the suppression of the GL in the Al-coated *a*-plane ZnO. The saturation of the GL of the uncoated *a*-plane ZnO at higher excitation power can be explained by the longer GL lifetime, in the order of µs, which leads to an increased UV emission with a much faster lifetime of tens or hundreds of ps.

Figure 5.30 illustrates the integrated DL intensity, from 1.2 eV to 3.0 eV, and UV emission (3.00 eV to 3.54 eV) as a function of laser and electron beam excitation power at 10 K, graphed on a double logarithmic scale. For both types of excitation, the UV emission exhibits a linear relationship — while the hot Al-coated side of the sample has a gradient of (1.01 ± 0.01), the uncoated *a*-plane ZnO shows a super-linear power law exponent with a gradient of (1.12 ± 0.02). However, the DL emission of the uncoated *a*-plane ZnO

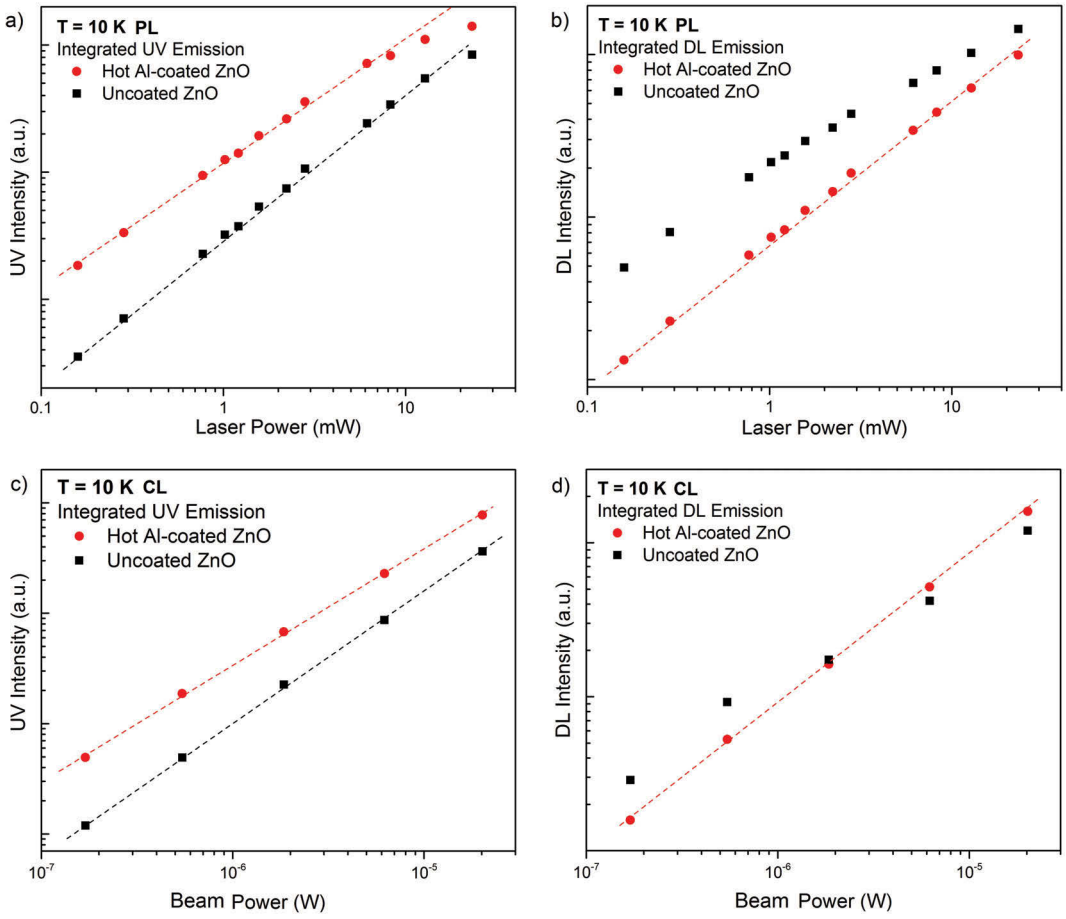

Fig. 5.30: (a and c) Integrated UV (1.2 eV to 3.0 eV) and (b and d) DL emission (3.00 eV to 3.54 eV) of the sample *Al hot* as a function of excitation power; laser (a and b) and electron beam (c and d) excitation. T =10 K, graphed logarithmically. The dashed lines serve as a guide of the eye.
CL: HV = 5 kV, scan area 10 µm × 10 µm
PL: λ_{exc} = 325 nm, laser spot ∼ 30 µm .

clearly saturates with increasing laser and electron beam excitation power; while the hot Al-coated *a*-plane ZnO does not exhibit any saturation effect. These trends can be similarly observed at 80 K and 300 K, whose power law exponents of the UV emission are listed in table 5.5.

Table 5.5: Power law exponents of the UV enhancement of the sample *Al hot* at 10 K and 80 K.

Sample	Temperature (K)	Power law exponent of the UV emission with increasing laser excitation power
uncoated *a*-plane ZnO	10	(1.12 ± 0.02)
Al-coated *a*-plane ZnO	10	(1.01 ± 0.01)
uncoated *a*-plane ZnO	80	(1.15 ± 0.02)
Al-coated *a*-plane ZnO	80	(1.03 ± 0.01)
uncoated *a*-plane ZnO	300	(1.11 ± 0.01)
Al-coated *a*-plane ZnO	300	(1.02 ± 0.01)

The corresponding enhancement factors of the integrated UV and DL emission of the uncoated and the hot Al-coated *a*-plane ZnO at 10 K, 80 K and 300 K are displayed in fig. 5.31. At 10 K, the highest UV enhancement factors of approximately 5.3 in PL and 4.2 in CL are found at the lowest excitation of $\sim$ 0.15 mW and 0.1 µW in PL and CL, respectively. A reduction in the UV enhancement is observed for 80 K and 300 K. The discrepancy in the PL and the CL UV enhancement at each temperature can be explained by the difference in excitation power density, which is approximately four orders of magnitude larger in CL, compared to the laser excitation. Therefore, a smaller reduction of the GL in the uncoated *a*-plane ZnO by the laser excitation is found, which results in a higher UV enhancement. Additionally, the aforementioned difference in types of excitation, with PL being a surface-near excitation and CL having its highest energy loss deeper within the sample, can explain the difference in UV enhancement factors for PL and CL (cf. section 5.2.3).

In fig. 5.31 it can be seen that the enhancement factor at a given excitation power is highest at 10 K and lowest at room temperature. These results further support the aforementioned argument, that the enhanced UV emission in the sample *Al hot* is mainly due to Al-doping and therefore increases the I_6 emission. The I_6 thermalises with increasing temperature, resulting in a reduced intensity, relative to the FX, which is a more effective recombination channel at elevated temperatures than the DBX. However, the LSPs in the Al nanoparticles most efficiently couple to the FX-C in the *a*-plane ZnO, which can possibly explain the effective temperature-dependent UV enhancement behaviour. These two competitive UV enhancement mechanisms exhibit a different temperature dependence,

resulting in the maximum enhancement at a temperature of 60 K.
These power-dependent CL and PL results are similar to that of the sample *Al* (cf. section 5.2.3), and it can therefore be assumed that the saturation of the GL in the uncoated *a*-plane ZnO and the GL reduction due to the Al-coating follows the same explanation.

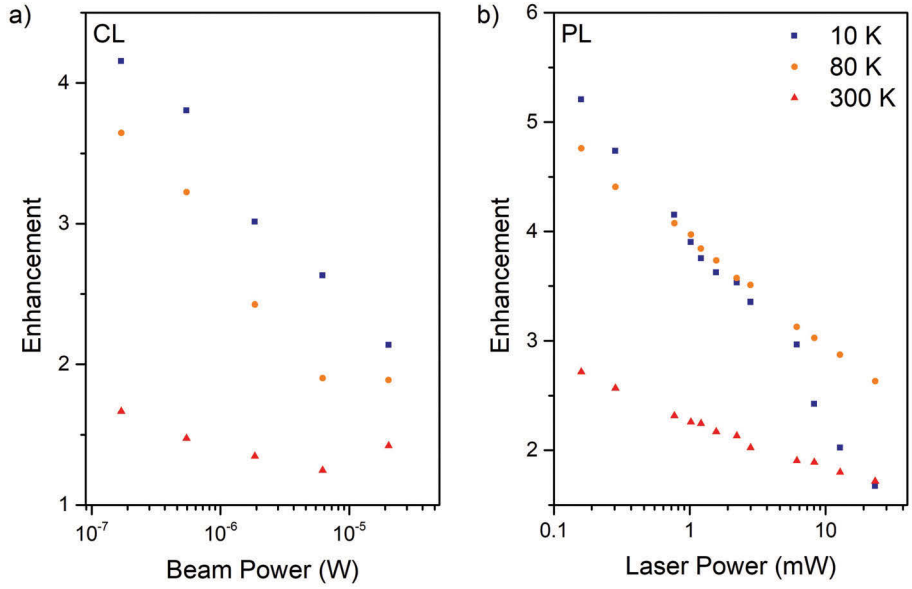

Fig. 5.31: UV enhancement of the sample *Al hot* as a function of electron beam (a) and (b) laser excitation power at 10 K, 80 K and 300 K.
CL: $HV = 5\,\text{kV}$, scan area 15 µm × 15 µm
PL: $\lambda_{\text{exc}} = 325\,\text{nm}$, laser spot ∼ 30 µm.

Surprisingly, at 10 K, the highest PL and CL enhancement factors of the UV emission at the lowest excitation power, 5.3 and 4.2 respectively, are higher than those of the sample *Al* with 2.4 and 3.3 for electron beam and laser excitation, respectively. This could be due to an even greater increase of the I_6 emission in the sample *Al hot*, which might be less affected by the change in temperature than the LSP-coupling to the FX. Thus, a relatively higher UV enhancement of the sample *Al hot*, compared to the sample *Al* is plausible at a temperature of 10 K. At 80 K, the UV enhancement factors of the sample *Al* are increased to 3.3 and 6.5 in CL and PL, respectively, however, in the sample *Al hot* they are decreased to 3.3 and 4.8 in CL and PL, respectively.
This is in accordance with temperature-dependent PL results, showing a higher UV enhancement at a lower temperature of 60 K and a less pronounced overall temperature-dependent UV enhancement than in the sample *Al* with its maximum enhancement at 80 K.

5.3.4 Time-resolved PL of Hot Al-coated *a*-plane ZnO

The lifetimes of the carriers in the sample *Al hot* were not determined, but it is assumed to be similar to that of the sample *Al* (cf. section 5.2.4), as the LSP-exciton coupling mechanism is similar in these two samples; although the Al-doping in the sample *Al hot* is more pronounced than in the sample *Al*. Therefore, a reduction in the lifetime of the PL enhanced transitions in ZnO is expected (cf. fig. 5.29), with a Purcell enhancement factor of the same order. However, the enhancement of the I_6 line is attributed to Al-doping of the *a*-plane ZnO, which is why no change in lifetime is assumed to be observed. As mentioned above (section 5.2.4), the TR-PL measurements of the individual excitonic emission lines in ZnO is challenging, as they are spectrally very close to each other and exhibit relatively short lifetimes on the order of ps, which requires a very short laser pulse duration to resolve them.

5.3.5 Summary of the Results of Hot Al-coated *a*-plane ZnO

In summary, the sample *Al hot* shows similar UV enhancement with a reduced DL emission for low acceleration voltages of 3 kV and 5 kV, similar to the results shown for the sample *Al*. Although the depth-resolved CL spectra exhibit a depth-dependent UV enhancement, it is not as pronounced as in the sample *Al*, discussed above (see section 5.2). Furthermore, the hot deposition of Al leads to an increased diffusion of Al into the ZnO and thereby an enhanced I_6 line. Even though the LO-phonon replica of the FX-C are enhanced in CL and PL, the main enhancement appears to originate from the Al-doping. A less pronounced temperature-dependence with the highest enhancement factor of $\sim$ 3.5 at 60 K is found.

The excitation power dependence of both types of excitation, with highest enhancement at the lowest power, can be possibly explained by the reduced GL in the hot Al-coated *a*-plane ZnO, which saturates in the uncoated side of the sample with increasing power. This trend is similar to that in the sample *Al*. However, higher enhancement factors for laser and electron beam excitation power are achieved for the sample *Al hot*, and a less pronounced temperature dependence, showing the maximum enhancement at 60 K compared to 80 K in the sample *Al*. This is consistent with the I_6 transition being mainly enhanced in the sample *Al hot*.

Finally, the UV enhancement in the sample *Al* is mainly attributed to resonant coupling between the LSPs in Al and the FX-C in ZnO, with the highest integrated enhancement of 6.5 and up to 12 of the first FX-C LO-phonon replica at a temperature of 80 K. The UV enhancement in the sample *Al hot* can be most likely be assigned to a fairly strong Al-doping, as well as a less pronounced LSP-exciton coupling to the FX-C. The maximum

enhancement of 3.5 was reached at 60 K, which might be higher at lower laser excitation power, as shown in the excitation power-dependent measurements with the highest enhancement factor at the lowest excitation power ($\sim$ 5.3 at 10 K).

5.4 Optical Properties of Aluminium Oxide-Coated *a*-plane ZnO

This section presents and discusses the PL and CL results of the Al_2O_3-coated *a*-plane ZnO (sample *Al oxide*). As discussed in section 5.1.2 and section 5.1.3, no evidence of metallic Al could be found in this surface coating. Therefore, it is assumed that the surface coating of the sample *Al oxide* consists only of an approximately 2.8 nm thin Al_2O_3 layer. As a result, no UV enhancement due to LSP-exciton coupling is expected. As above, the depth-resolved CL, temperature-dependent PL, excitation power PL and CL, as well as time-resolved PL were performed to comprehensively study this sample.

5.4.1 Depth-Resolved CL of Al_2O_3-Coated *a*-plane ZnO

The depth-resolved CL spectra of the uncoated and Al_2O_3 *a*-plane ZnO are presented in fig. 5.32 at 10 K and 80 K. At both temperatures, the UV emission is reduced for all acceleration voltages with the exception of 10 kV at 10 K and 80 K, which shows a similar intense emission for both sides of the sample. Furthermore, the NBE emission of the Al_2O_3-coated *a*-plane ZnO appears broader than that of the uncoated side of the sample. This phenomenon will be further investigated with high-resolution CL and PL. The corresponding enhancement factors are listed in table 5.6, calculated from the maximum UV intensity in the second column and the UV emission integrated from 3.30 eV to 3.45 eV in the third column, excluding the new broader emission, which will be discussed below. The table illustrates that at both temperatures, the UV emission is highly reduced close

Table 5.6: UV enhancement factors of the sample *Al oxide* at three different acceleration voltages at 10 K and 80 K. The second column presents the UV enhancement, calculated from the highest UV emission, while the third column shows the UV enhancement, integrated from 3.30 eV to 3.45 eV.

HV (kV)	T (K)	UV enhancement (I)	UV enhancement (Int)
3	10	0.2	0.6
5	10	0.7	0.9
10	10	1.1	1.0
3	80	0.2	0.4
5	80	0.7	0.5
10	80	1.1	1.1

to the surface, while it is close to the value of the uncoated *a*-plane ZnO at 10 kV.

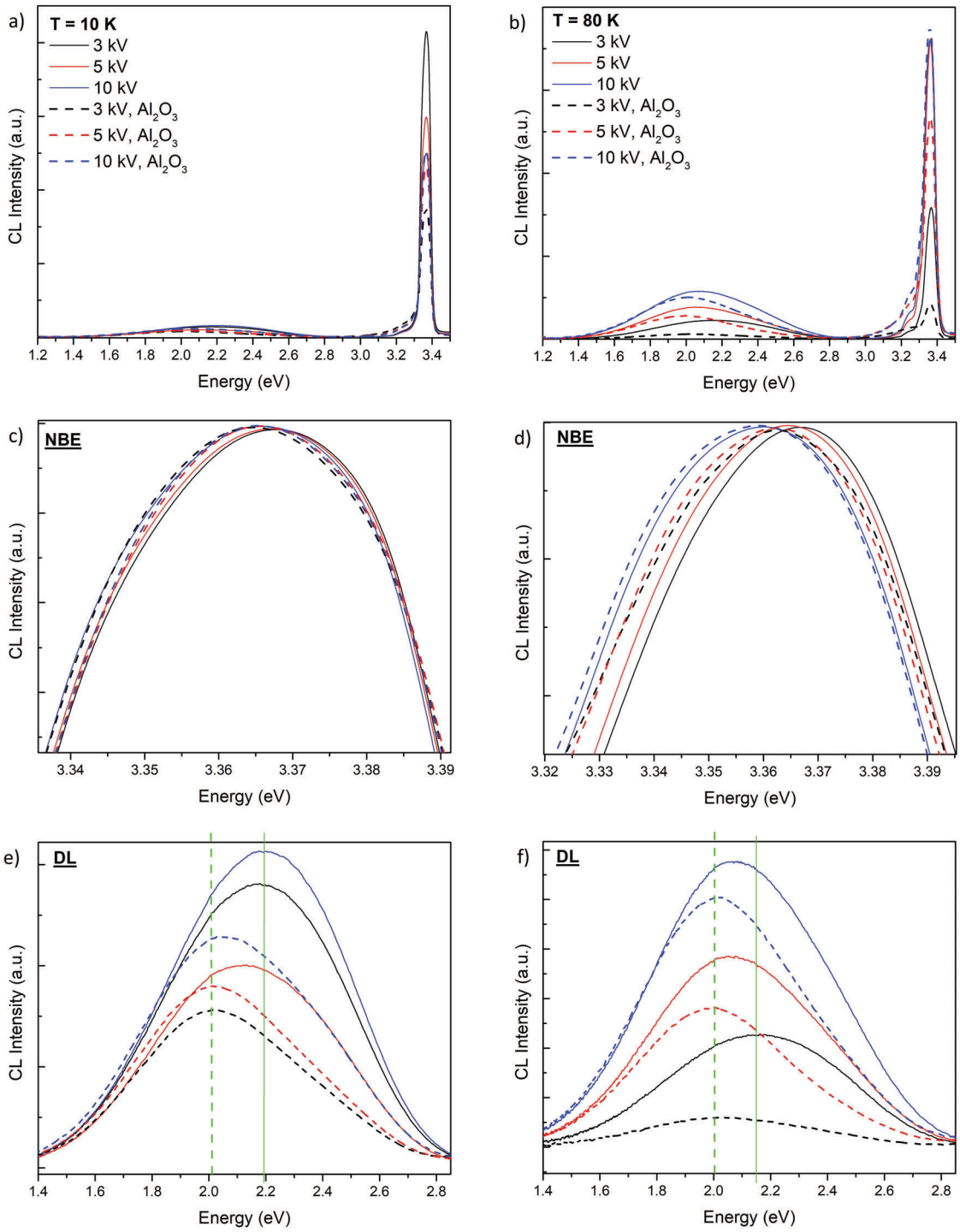

Fig. 5.32: (a and b) Depth-resolved CL spectra of the sample *Al oxide* at 10 K (left) and 80 K (right); (c and d) normalised NBE emission and (e and f) DL emission.
$HV = 3\,\text{kV}, 5\,\text{kV}$ and $10\,\text{kV}$, $P = 17.5\,\mu\text{W}$, scan area $10\,\mu\text{m} \times 10\,\mu\text{m}$.

The normalised NBE emission, shown in fig. 5.32c and d at 10 K and 80 K, respectively, shows the typical red-shift with increasing acceleration voltage; a slight, negligible red-shift for the Al_2O_3-coating is observed.
The DL of the Al_2O_3-coated *a*-plane ZnO, illustrated in fig. 5.32e and f, exhibit a similar change, as discussed in the two sections above for the samples *Al* and *Al hot*. At the lower acceleration voltages of 3 kV and 5 kV, the GL around 2.3 eV is reduced compared to the uncoated side of the sample, which is indicated by the green vertical lines; while at 10 kV, a shoulder of GL is visible. This surface-near effect appears to be temperature-independent, like found for the sample *Al* and *Al hot*. As discussed in detail in section 5.2.1, this can be due to two different effects:

- a decrease in upward band bending at the surface, following the Al_2O_3 deposition, producing a changed position of the charge transfer level section 5.1.4.
- Or changes in the V_{Zn} charge state due to surface charge transfer mechanisms induced by the Al surface layer (section 5.2.1).

To investigate the depth-dependent reduction of the UV emission of the Al_2O_3-coated *a*-plane ZnO, high-resolution depth-resolved CL spectroscopy was performed. The resulting CL spectra of the uncoated and the Al_2O_3-coated *a*-plane ZnO are displayed in fig. 5.33, at a temperature of 10 K and 80 K. The emission lines in the spectra of the un-

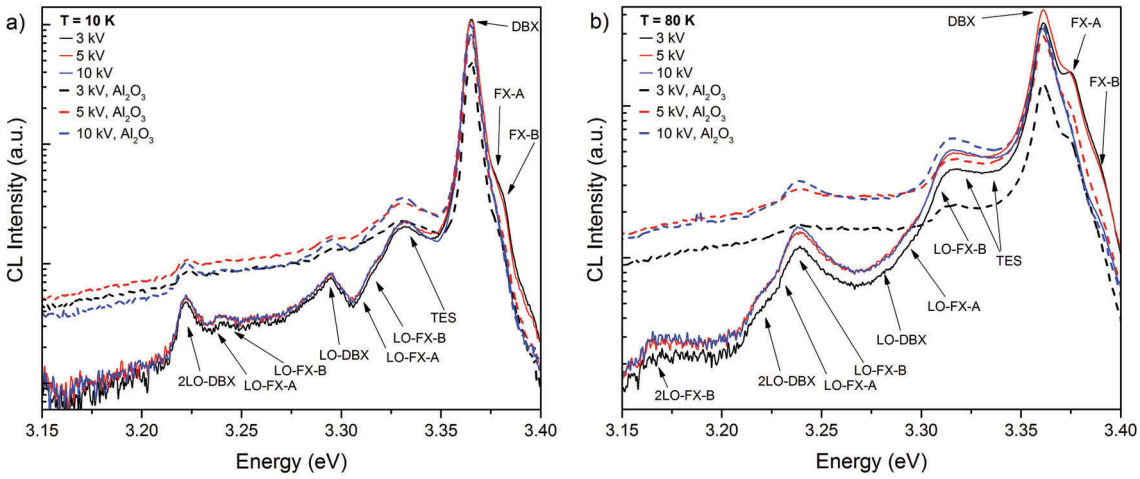

Fig. 5.33: High-resolution depth-resolved CL spectra of the sample *Al oxide* at (a) 10 K and (b) 80 K.
$HV = 3$ kV, 5 kV and 10 kV, $P = 17.5$ µW, scan area 10 µm × 10 µm.

coated *a*-plane ZnO can be labelled, similarly to that of the samples *Al* and *Al hot*, while the Al_2O_3-coated side of the sample shows a very broad emission from approximately 3.10 eV to 3.32 eV. The origin of this emission is still unclear, as it cannot be assigned to any known emission peaks in ZnO or in Al_2O_3. In addition, the deposition of this Al_2O_3-coating onto a Si substrate did not show any of these emissions in this particular region,

which indicates that this broad emission is related to Al_2O_3 on ZnO. The difference in the deposition of the surface coating between the sample *Al oxide* and the samples *Al* and *Al hot* is the additional oxygen as a working gas. Therefore, a control *a*-plane ZnO sample treated with argon-oxygen-plasma under identical conditions as the deposition of the Al_2O_3-coating, was studied with PL and CL. No change in PL or CL is found, compared with the untreated side of the sample, indicating that the additional broad emission at approximately 3.10 eV to 3.32 eV cannot be attributed to the Al_2O_3-coating alone, but is possibly related to the specific radiative defects at the Al_2O_3-*a*-plane ZnO interface
Due to this broad emission, it is difficult to analyse the underlying excitonic emission peaks from ZnO. The typical thermalisation effects and increased phonon interactions with increasing temperature, resulting in decreased intensity of the DBX, red-shifting and broadening of the excitonic emissions, can be seen in fig. 5.33a and b.

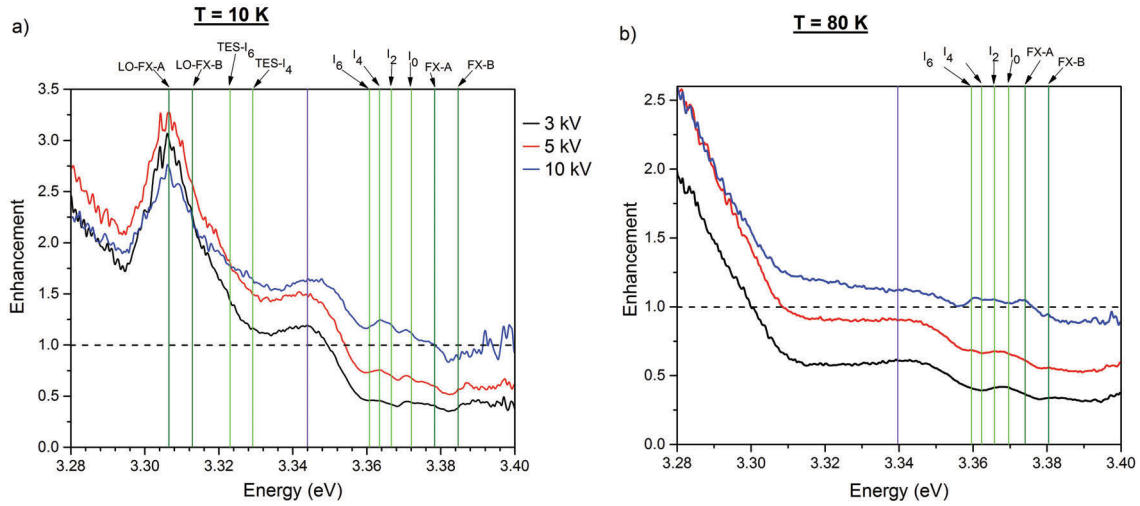

Fig. 5.34: Depth-resolved CL enhancement factor of the sample *Al oxide* as a function of energy at (a) 10 K and (b) 80 K. The green labels present the DBX-related emission peaks, while FX emissions are labelled in olive. $HV = 3$ kV, 5 kV and 10 kV, $P = 17.5$ µW, scan area 30 µm x 30 µm.

The UV enhancement factor as a function of energy is illustrated in fig. 5.34 at 10 K and 80 K. The lower energy region is not shown here, as it strongly overlaps with the aforementioned broad emission. At 10 K (fig. 5.34a), the DBX-related emissions, labelled in green, can be identified, as well as the FX-related emissions (olive). While a clear reduction in the I lines is visible, the first LO-phonon replica of the FX-A and -B are enhanced by approximately 3 times. However, it can be assumed that this is an artifact related to the overlap with the broad emission (3.10 eV to 3.32 eV). At a temperature of 10 K, the FX emissions are typically not very pronounced, as the DBX provide a more efficient recombination pathway due to their higher capture cross section. Furthermore, this observation can be supported by the enhancement as a function of energy at 80 K, shown in fig. 5.34b.

Here, the enhancement factor suddenly increases at an energy of $\sim 3.31\,\text{eV}$ from close to 1 to up to 2.5, while the higher energies above 3.31 eV show an almost constant enhancement factor (~ 0.5 for 3 kV, 0.9 for 5 kV and 1.1 for 10 kV). These depth-dependent enhancement factors are in accordance with the integrated enhancement factors calculated from the spectra in fig. 5.32, listed in table 5.6.
Furthermore, the emission at $\sim 3.343\,\text{eV}$, which is most likely attributed to an emission from the ZnO-Al or ZnO-Al_2O_3 interface for the samples *Al* and *Al hot*, can also be seen in fig. 5.34, labelled in purple. Hence, it can possibly be attributed to an interface emission from the Al_2O_3 and ZnO, rather than the ZnO-Al interface.

5.4.2 Temperature-Dependent PL of Al_2O_3-Coated *a*-plane ZnO

The temperature dependence in PL, ranging from 10 K to 250 K, of the sample *Al oxide* was similarly studied like the samples *Al* and *Al hot* (section 5.2.2 and section 5.3.2).
The temperature-dependent PL spectra of the uncoated and Al_2O_3-coated *a*-plane ZnO are displayed in fig. 5.35, showing the typical peak broadening and red-shifting with increasing temperature. While the uncoated *a*-plane ZnO shows clear excitonic emission

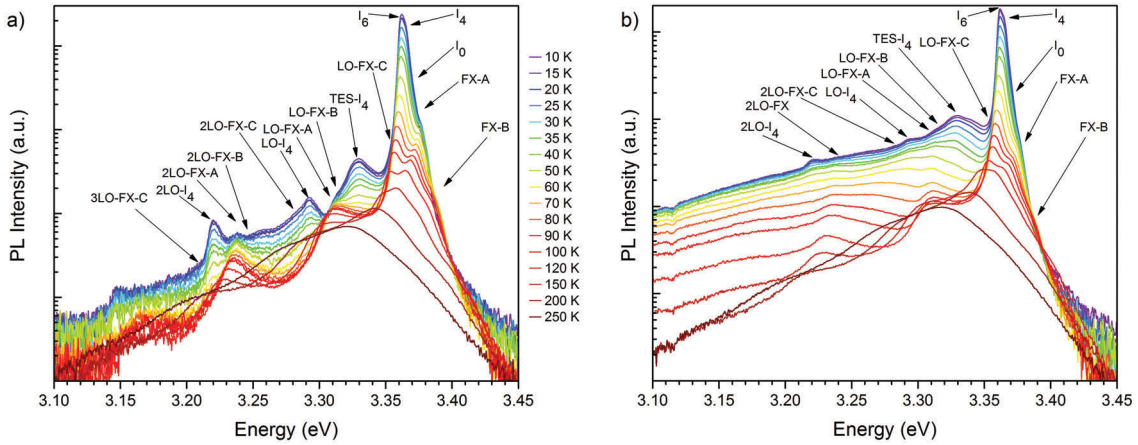

Fig. 5.35: Temperature-resolved PL of (a) uncoated and (b) hot Al_2O_3-coated *a*-plane ZnO.
$P = 2.2\,\text{mW}$, laser spot $\sim 30\,\mu\text{m}$.

peaks, the Al_2O_3-coated side of the sample exhibits the aforementioned broad peak ranging from $\sim 3.10\,\text{eV}$ to 3.32 eV. The enhancement factor as a function of energy is depicted in fig. 5.36; where (a) shows the same full energy range from 3.15 eV to 3.40 eV, which was also shown for the samples *Al* and *Al hot* in section 5.2.2 and section 5.3.2. (b) only presents the energy region in which the broad emission seems not to overlap with the emissions in ZnO. It can be seen that the UV emission in this region is reduced overall, except for higher temperatures from 150 K to 250 K with a slight enhancement of 1.1 to 1.3. No distinct emission peaks can be identified at any temperature. Although only a

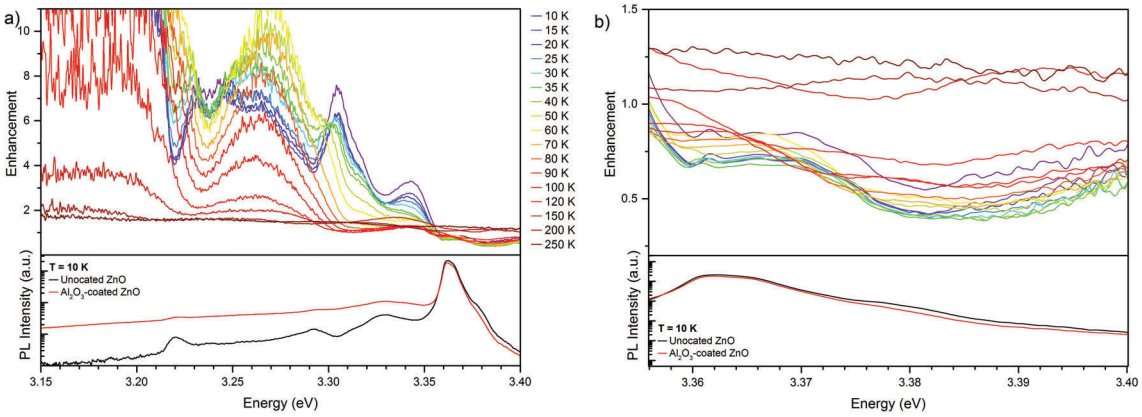

Fig. 5.36: Top: Temperature-resolved PL enhancement of the sample *Al oxide* as a function of energy. Bottom: High-resolution 10 K-PL of uncoated (black) and Al_2O_3-coated *a*-plane ZnO (red), graphed on a semi-logarithmic scale.
$\lambda_{exc} = 325\,nm$, $P = 2.2\,mW$, laser spot $\sim 30\,\mu m$.

small section of the energy range can be analysed, a clear reduction of the UV emission following the Al_2O_3-coating is observed for up to 120 K. The origin of the reduction in the UV emission is difficult to ascertain due to the additional unknown broad emission at approximately 3.10 eV to 3.32 eV, which can possibly act as a more efficient recombination channel than the excitonic transitions in ZnO. From the high-resolution PL spectra at the temperatures ranging from 150 K to 250 K in fig. 5.35, it can be seen that the broad emission is not as pronounced anymore, which might explain the small enhancement seen in fig. 5.36. Although the origin of the broad emission is unknown, a reduction in intensity with increasing temperature can be observed, which suggest the thermalisation of the responsible recombination centre.

5.4.3 Excitation Power-Dependent PL of Al_2O_3-Coated *a*-plane ZnO

The excitation power dependence in the Al_2O_3-coated *a*-plane ZnO was investigated and is discussed in this section. The presented data only shows the UV emission, integrated from 3.32 eV to 3.45 eV to minimise the effect of the overlapping broad emission at $\sim$ 3.10 eV to 3.32 eV. However, a spectral overlap cannot be fully excluded in this case.
The UV enhancement is graphed as function of laser excitation power in fig. 5.37, showing that the UV emission is slightly enhanced at low laser powers of up to 0.8 mW. This is a similar trend to what has been shown in section 5.2.3 and section 5.3.3 for the samples *Al* and *Al hot*, respectively. It can be assumed that the origin of the excitation power dependence in the sample *Al oxide* is the same as in the samples *Al* and *Al hot*, where the GL (2.3 eV) is greatly reduced due the Al_2O_3-coating (section 5.4.1). While the GL in

the uncoated *a*-plane ZnO possibly saturates with increasing power, leading to a super-linear trend of the UV emission with increasing excitation power, all three samples with the Al-coating show a linear behaviour with increasing power. This change in GL in the samples *Al*, *Al hot* and *Al oxide* at low acceleration voltages (3 kV and 5 kV) leads to the presented excitation power dependence.
Note that this enhancement might be due to the spectral overlap between the excitonic emissions in ZnO with the broad emission related to the Al_2O_3-coating on ZnO.

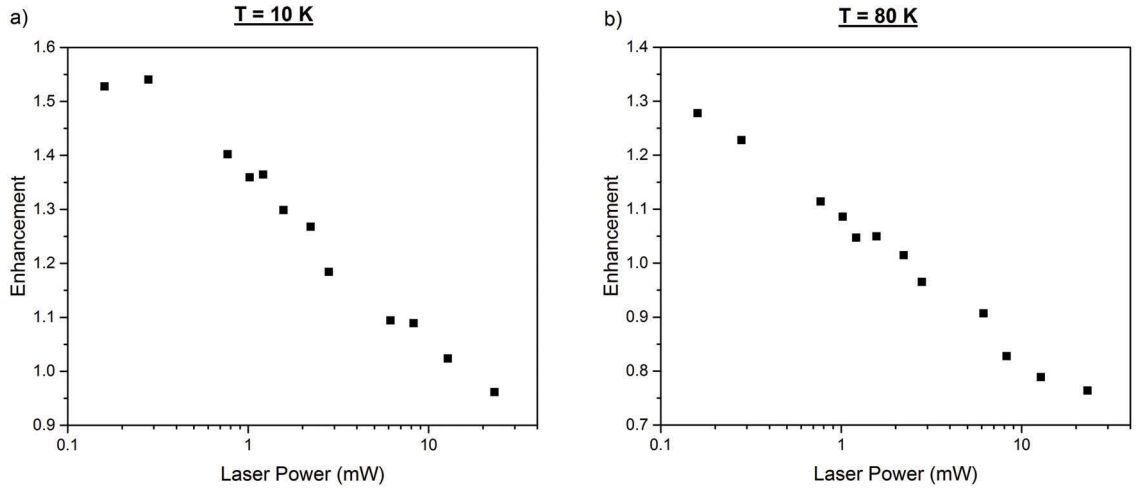

Fig. 5.37: UV enhancement of the sample *Al oxide* as a function of laser excitation power at (a) 10 K and (b) 80 K. The UV emission was integrated from 3.32 eV to 3.45 eV.
PL: $\lambda_{exc} = 325$ nm, laser spot ~ 30 µm.

5.4.4 Time-Resolved PL of Al_2O_3-Coated *a*-plane ZnO

To investigate the lifetimes of the uncoated and Al_2O_3-coated *a*-plane ZnO, time-resolved PL was performed at a temperature of 10 K, displayed in fig. 5.38. It can be seen that the exponential decay at the DBX appears identical, within the range of uncertainties for both sides of the sample, which is reflected in the corresponding lifetimes:
$\tau_{ZnO} = (119 \pm 7)$ ps and $\tau_{ZnO+Al2O3} = (124 \pm 3)$ ps.
This result is consistent with the transmission spectroscopy, as well as the results of the ellipsometry, which did not provide any evidence for metallic Al in this sample. Therefore, no additional, faster relaxation channel is created, which is also in accordance with the reduced UV emission of the Al_2O_3-coated *a*-plane ZnO. It can be concluded that no LSP-exciton coupling is observed in this sample.

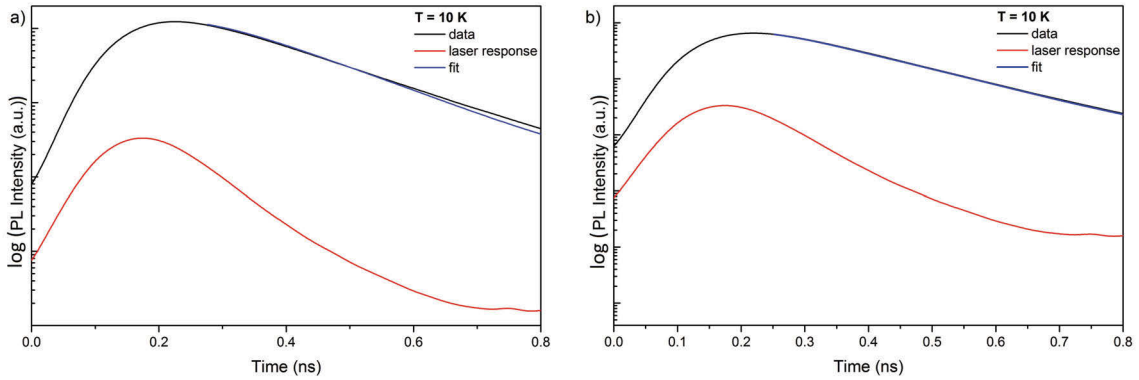

Fig. 5.38: Time-resolved PL at a fixed collection energy at the DBX of (a) the uncoated and (b) Al_2O_3-coated *a*-plane ZnO, at 10 K. The corresponding lifetimes are $\tau_{ZnO} = (119 \pm 7)$ ps and $\tau_{ZnO+Al2O3} = (124 \pm 3)$ ps.

5.4.5 Summary of Al_2O_3-Coated *a*-plane ZnO

In summary, the Al_2O_3-coated *a*-plane ZnO shows a reduction in UV emission compared to the uncoated side of the sample. An additional broad emission at $\sim$ 3.10 eV to 3.32 eV is found, following the Al_2O_3 coating. Although the origin of this emission is unknown, it seems to be related to the Al_2O_3-coating on ZnO, as no emission was found for oxygen-plasma treated *a*-plane ZnO or Al_2O_3-coated Si. This emission spectrally overlaps with the excitonic emissions in ZnO, which makes the analysis and interpretation of the collected data difficult. However, in the energy region where no spectral overlap is visible, a reduction in the UV emission can be seen, with no energy or temperature dependence up to 150 K, where a small enhancement of 1.1 to 1.3 can be observed. This is possibly related to the thermal dissociation around 150 K of the underlying recombination centre of unknown origin.

The reduction of the UV emission is depth-dependent, showing the highest reduction close to the surface at an acceleration voltage of 3 kV. This reduced UV emission might be due to a more efficient recombination pathway through the additional, competitive broad emission channel.

Furthermore, an excitation power dependence is found, which is similar to that in the samples *Al* and *Al hot*. This was attributed to a reduced GL due to the Al_2O_3-coating, most likely due to changes in the V_{Zn} charge transfer mechanism.

It can be concluded that the sample *Al oxide*, consisting of a 2.8 nm thin Al_2O_3 film with no metallic Al, does not show any similar UV enhancement like the sample *Al* (section 5.2) and *Al hot* (section 5.3). Furthermore, no change in lifetime is observed, therefore no evidence for LSP-exciton coupling is found in this sample.

5.5 Effect of Carrier Density on the UV Enhancement *a*-plane ZnO with Al

The dependence of the UV enhancement of Al-coated *a*-plane ZnO on the carrier density in the *a*-plane ZnO was investigated. Here, *a*-plane ZnO single crystals with a large variation in carrier density from 10^{13} to 10^{17} cm^{-3} were coated with Al under similar conditions as sample set *Al* (cf. section 5.1). The PL enhancement of the UV emission at 80 K are presented in fig. 5.39.

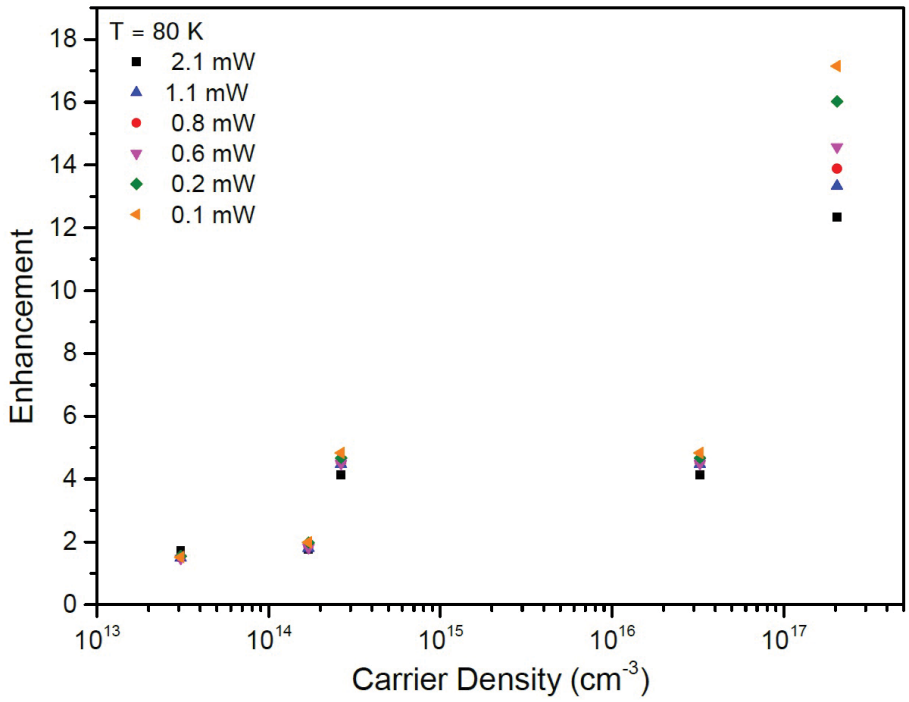

Fig. 5.39: UV enhancement of Al-coated *a*-plane ZnO with different carrier densities from 10^{13} to 10^{17} cm^{-3}, showing different UV enhancement factors. The laser excitation power was varied from 0.103 mW to 2.125 mW. $\lambda_{exc} = 325$ nm, laser spot ~ 30 µm.

Significantly, under identical laser excitation power, a trend of increasing UV enhancement with increasing carrier density can be observed. Furthermore, the dependence of the UV enhancement on the laser excitation is more pronounced for the *a*-plane ZnO samples with the higher carrier densities, compared to that of the lower densities.
The UV enhancement has resulted from a dipole-dipole coupling in the Al nanoparticles *a*-plane ZnO samples. Accordingly, the high carrier densities might be expected to screen this interaction, reducing the UV emission enhancement, however the opposite is observed experimentally. It is well known that as the carrier density in a semiconductor increases, the thickness of the space charge region, W, drastically shrinks. This is described by the full depletion model, as shown in eq. (4.4) and eq. (4.5) (cf. section 4.2).

The width of the space charge region and the electric field, E_S, at the surface are presented in table 5.7 for *a*-plane ZnO with the lowest and highest carrier densities, used in this work. From these calculations it can be seen that while the width of the space charge region is highly reduced for the ZnO with the highest carrier density, the electric field at the surface is approximately two orders of magnitude increased at the same time. As the LSP-exciton coupling is typically attributed to an enhanced surface electric field by the metal nanoparticles, it is possible that this field enhancement effect is higher for larger surface electric fields. This effect would result in a further improved SER of the already enhanced decay channel by the Al-coating and could possibly explain the observed UV enhancement strength on carrier density in the Al-coated *a*-plane ZnO. Additionally, the increased sensitivity of the UV enhancement to the laser power at higher carrier densities suggest that other relaxation channels could also be created. For example, fast Auger recombination pathways that could raise the exciton SER as described in section 2.4.4.

Table 5.7: Calculation of the width of the space charge region W and the surface electric field E_S for the Al-coated *a*-plane ZnO with the lowest and highest carrier densities, used in this work.

Carrier density (cm^{-3})	W (nm)	E_S ($V\,cm^{-1}$)
3.1×10^{13}	2607	8.1×10^3
2.0×10^{17}	37	7.3×10^5

An equivalent effect in Al-coated ZnO nanorods could not be established, as the determination of the carrier density in nanorods is difficult, using Hall measurements on an electrically contacted nanorod ensemble.

5.6 Characterisation of Al-coated ZnO Nanorods

To investigate the effect of a larger surface-to-volume ratio on the LSP-exciton coupling, two differently grown ZnO nanorods were coated with a 2 nm thin Al film (cf. sample *Al* in section 5.1). The results of the CL and PL spectroscopy will be presented in this section.

The larger surface-to-volume ratio of the ZnO nanorods can possibly have an effect on the coupling strength between the LSPs in the Al nanoparticles and the excitons in the ZnO. As this LSP-exciton coupling is a surface-near effect, it can be assumed that a larger surface area can further enhance the UV emission of the Al-ZnO sample.

Furthermore, the diffusion length of the more mobile FX is known to be larger than that of the DBX, which are localised at donor sites, therefore the probability of the FX being close to the surface in a confined structure, such as a nanorod is higher than in a planar ZnO crystal. This can possibly allow for higher enhancement factors, which is studied and

discussed in this section, using PL and CL spectroscopy of two types of ZnO nanorods — hydrothermally-grown and VS-grown. The synthesis of the hydrothermally-grown ZnO nanorods can be found in section 3.1.1, while the VS-grown ZnO nanorods were fabricated by Rahman, as described in [219].
The hydrothermally-grown ZnO nanorods exhibit an average diameter of (40 ± 10) nm and a length of of approximately 700 nm with a random orientation to the surface, as shown in section 4.1. The VS-grown ZnO nanorods have a larger diameter of ~ 100 nm and a length of approximately 1 µm. The orientation of the ZnO nanorods is perpendicular to the substrate surface, which can be seen in fig. 5.49 in section 5.6.3. However, both types of ZnO nanorods grow along the c-axis of ZnO, which leads to an alignment of the FX-C parallel to the length of the nanorods. This is different to the *a*-plane ZnO single crystals, discussed in section 5.2, section 5.3 and section 5.4. In the ZnO crystals, the orientation of the c-axis and thereby the FX-C is parallel to the sample surface. In the VS-grown ZnO nanorods, the c-axis and polarisation of the FX-C is perpendicular to the substrate surface, while it is randomly oriented in the hydrothermally-grown ZnO nanorods, as they are randomly aligned.
The morphology of the Al-coating could not be imaged by SEM, as the secondary electron yield of Al is very low, as previously discussed in section 5.1. The sputter-coating process of Al with a nominal thickness of 2 nm at room temperature is the same as for the *a*-plane ZnO single crystals. Therefore, it is assumed that the resulting Al-coating has the same morphology. This was found to be valid for the Au nanoparticle-coating on a planar surface, as well as on the ZnO nanorods, discussed in section 4.1.

5.6.1 Optical Characterisation of Hydrothermally-Grown ZnO Nanorods Coated with 2 nm Al

This section discusses the results of the PL and CL study on the hydrothermally-grown ZnO nanorods coated with a 2 nm thin Al film.
As discussed in section 4.1, the hydrothermally-grown ZnO nanorods exhibit an average diameter of (40 ± 10) nm and a length of ~ 700 nm. The Al-coating is assumed to be identical to that of the sample *Al*, consisting of an approximately 2.8 nm thin Al_2O_3 film with $0.1 Vol\%$ metallic Al, showing a broad LSP absorption from 2.8 eV to 6.2 eV.

5.6.1.1 Depth-Resolved CL of Al-Coated Hydrothermally-Grown ZnO Nanorods

To study the depth-dependent distribution of luminescence within the uncoated and Al-coated ZnO nanorods, depth-resolved CL spectroscopy was performed at 10 K, 80 K and 300 K.
The corresponding CL spectra of the uncoated and the Al-coated ZnO nanorods at 10 K

and 80 K are shown in fig. 5.40. A large enhancement of the UV emission for all acceleration voltages and for both temperatures is observed. The UV enhancement factors at

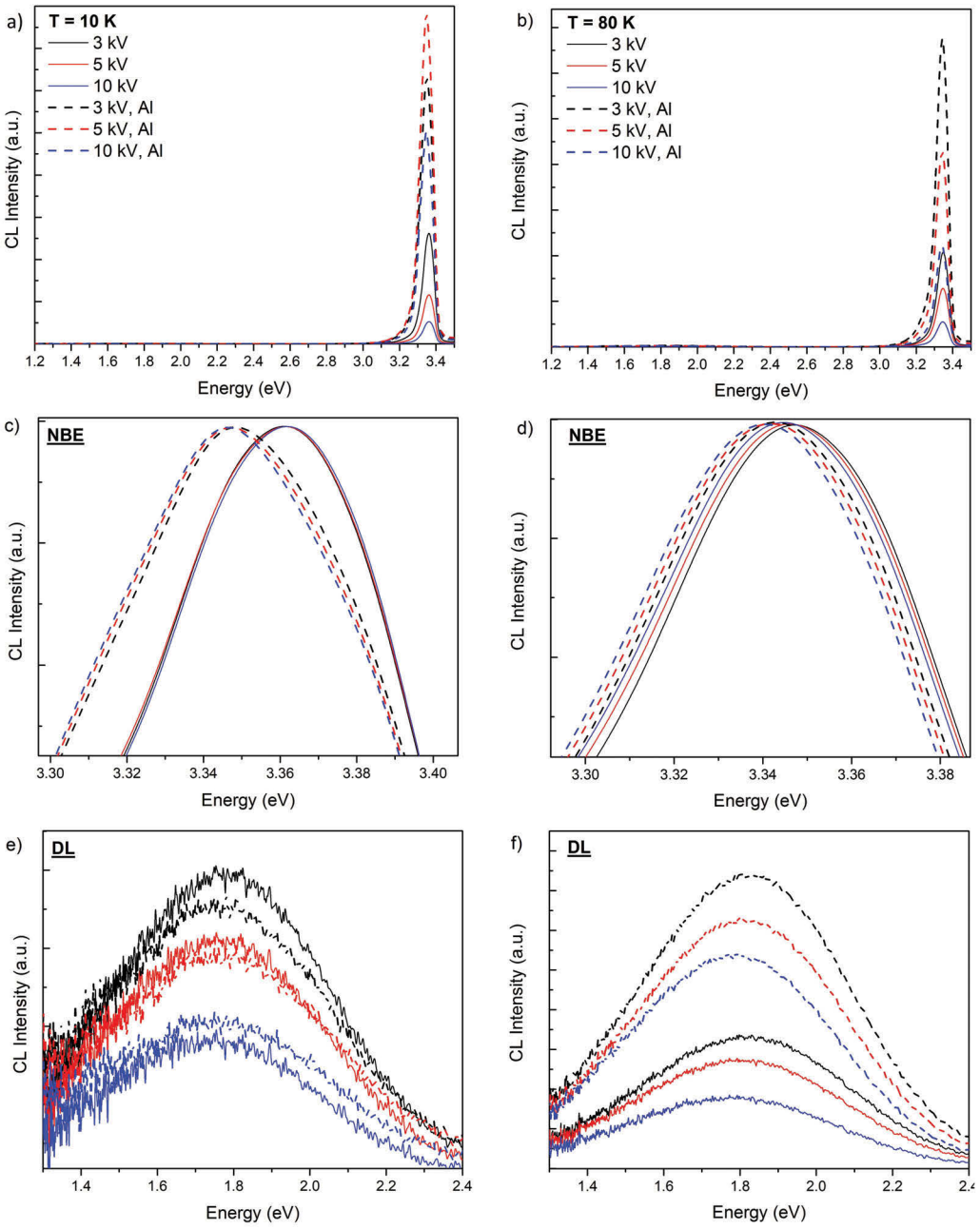

Fig. 5.40: Depth-resolved CL spectra of the uncoated (solid lines) and the Al-coated ZnO nanorods (dashed lines) at (a) 10 K and (b) 80 K. (c and d) Normalised NBE emission and (e and f) DL emission of the uncoated and the Al-coated ZnO nanorods 10 K and (b) 80 K, respectively. $P = 17.5\,\mu W$, scan area $10\,\mu m \times 10\,\mu m$.

the three temperatures and at the three acceleration voltages are listed below in table 5.8.

Here, the third column displays the UV enhancement factor calculated from the maximum intensity of the NBE emission of the uncoated and the Al-coated ZnO nanorods. The fourth column shows the UV enhancement, determined by integrating over the entire NBE emission from 3.10 eV to 3.45 eV. A clear trend of increasing enhancement factor

Table 5.8: UV enhancement factors of the hydrothermally-grown ZnO nanorods coated with Al, at three different acceleration voltages at 10 K, 80 K and 300 K. The UV emission was integrated from 3.10 eV to 3.45 eV.

HV (kV)	T (K)	UV enhancement (I)	UV enhancement (Int.)
3	10	2.4	2.6
5	10	6.8	7.2
10	10	9.2	10.3
3	80	3.3	3.3
5	80	3.6	3.4
10	80	3.9	4.0
3	300	1.4	1.4
5	300	2.5	2.5
10	300	4.0	3.7

with increasing CL excitation depth can be seen, with the highest enhancement of 10.3 at 10 kV at 10 K. At higher temperatures of 80 K and 300 K, an overall reduced enhancement factor is observed, while the depth-dependent trend is unchanged. This is similar to the results of the depth-resolved CL spectroscopy of Au nanoparticle-coated ZnO nanorods at 10 K, discussed in section 4.4.1. However, this depth-dependent CL behaviour is opposite to that of the *a*-plane ZnO single crystals, which shows the highest enhancement closest to the surface, more specifically to the ZnO-Al interface. As the Al-coating is the same on the planar and the nanostructured ZnO samples, the differences in the type of the ZnO sample possibly affect the enhancement:

1. A different mechanism could be responsible for the UV enhancement in the Al-coated *a*-plane ZnO single crystals and the hydrothermally-grown ZnO nanorods coated with Al. This is not impossible, but rather unlikely, which will be discussed in the following sections.

2. Since the LSP-exciton coupling has been shown to be the underlying UV enhancement effect in both types of samples (section 5.2 and section 5.3), the type and concentration of excitons — e.g. FX, DBX, ABX — in the two types of ZnO can be different, which can result in a changed depth- and temperature-dependent CL and PL behaviour. This will be further investigated over a large range of temperatures (10 K to 250 K) in section 5.6.1.2.

3. The random ZnO nanorod orientation can lead to more overall excitation of ZnO at greater CL excitation depths, as the effective surface area of the nanorod ensemble irradiated by the electron beam is larger at higher acceleration voltages, as discussed in section 4.4.1. This is illustrated in fig. 5.41, showing the energy loss within ZnO coated with 2 nm Al simulated with CASINO. Here, the surface area excited by the electron beam, is roughly 25 nm at 3 kV, while it is substantially larger at 10 kV ($\sim$ 350 nm). At an acceleration voltage of 5 kV, the electron beam excitation depths is already larger than the average diameter of the hydrothermally-grown ZnO nanorods. Therefore, more Al-coated ZnO nanorod side wall surfaces can be excited, which probably results in a higher number of LSPs formed in the Al nanoparticles, as well as an increased amount of surface-near FX, resulting in an increased LSP-exciton coupling. Furthermore, forward scattered electrons can possibly excite side wall surfaces on neighbouring ZnO nanorods, further enhancing the UV emission.

4. The possibility of the waveguiding effect in these randomly oriented ZnO nanorods allows for LSP excitation in neighbouring nanorods. This might be more pronounced at higher acceleration voltages, as a larger surface area is excited at 10 kV than at 3 kV.

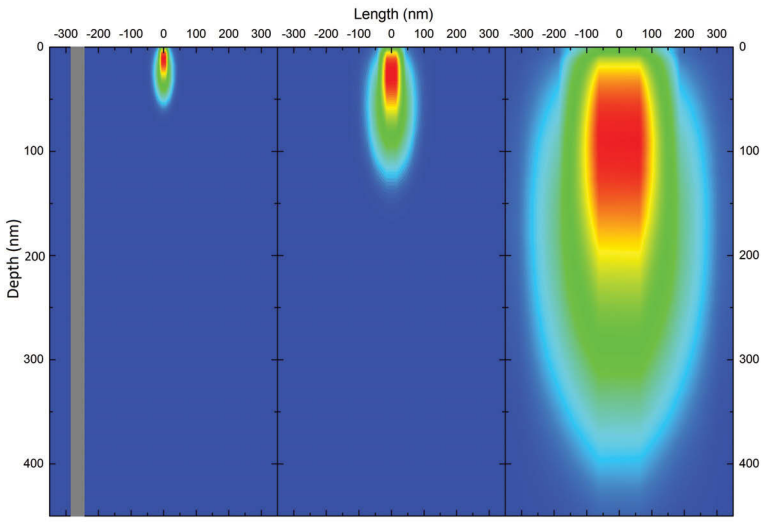

Fig. 5.41: CASINO simulation of the energy loss within ZnO coated with a 2 nm thin Al film at 3 kV, 5 kV and 10 kV. The grey bar on the left indicates an average ZnO nanorod with a diameter of 40 nm, showing that all electrons are injected into a single nanorod at 3 kV and more ZnO nanorods are excited by higher acceleration voltages.

Figure 5.40c and d show the normalised NBE of the uncoated and the Al-coated ZnO

nanorods. While the red-shift of the NBE emission with the Al-coating is very pronounced at 10 K, in the order of 20 meV, it is less visible at 80 K with a red-shift of less than 5 meV. Furthermore, the peak shape at 10 K is changed following the Al coating, to a broader emission peak with a shoulder around 3.37 eV. This will be further investigated below, as higher spectral resolution is required. However, at 80 K, the shape of the NBE emission is very similar for the uncoated and the Al-coated ZnO nanorods. This is most likely due to a less pronounced enhancement of one of the I lines in the DBX at 80 K, compared to 10 K.
At a temperature of 10 K, the DL emission — centered at 1.8 eV and attributed to acceptor-like defects (cf. section 4.4.1) — is comparably intense for the uncoated and the Al-coated ZnO nanorods, see fig. 5.40e. No apparent shift or change in shape can be seen. At 80 K (fig. 5.40f), the DL emission of the Al-coated ZnO nanorods is enhanced compared to the uncoated side of the sample, which is most likely due to quenching of competitive non-radiative recombination channels by the Al-coating.

5.6.1.2 Temperature-Dependent PL of Al-Coated ZnO Nanorods

To investigate the effect of temperature on the luminescence of this sample, PL spectroscopy of the uncoated and the Al-coated ZnO nanorods was performed from 10 K to 250 K. This can give insight into the type of excitons present in this sample and, therefore, the possible underlying coupling mechanism between these excitons and the LSPs in the Al nanoparticles.
The high-resolution PL spectra of the uncoated and the Al-coated ZnO nanorods at 10 K, as well as the enhancement factor as a function of energy is shown in fig. 5.42. It can be seen that the highest enhancement of approximately 9.2 is reached at an energy of 3.324 eV, while the DBX is $\sim$ 5.2 times enhanced. Similar to the high-resolution spectra of the ZnO nanorods coated with Au nanoparticles, shown in fig. 4.8, the excitonic emissions are broad compared to that in the *a*-plane ZnO single crystals, which makes it difficult to identify the I lines in the DBX region.
The broad emission at 3.324 eV is close to the TES of the I_4 and the I_6 line at 3.329 eV and 3.323 eV, respectively (cf. table 2.1). However, three emissions at lower energies are found with the typical spacing of the LO-phonon replica of 73 meV in ZnO (3.253 eV, 3.180 eV and 3.107 eV), indicating that the peak at 3.323 eV is related to a BX emission.
In the literature, excitons bound to defects have been reported in this energy region. A structural defect introduced during the growth of ZnO nanorods, possibly located close to the bottom of the nanorod, has been reported by Richter et al. at an energy of 3.333 eV. The so-called A line or A peak is energetically close to the observed emission in this sample at 3.324 eV [220–222]. The assignment of this emission to the A line with its three

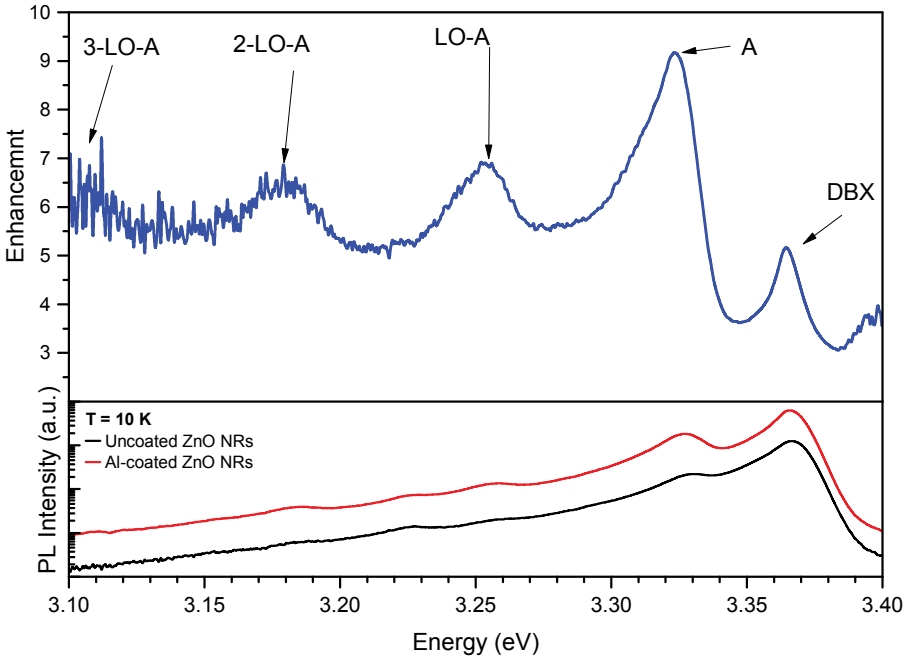

Fig. 5.42: Top: Enhancement of the Al-coated ZnO nanorods as a function of energy. Bottom: High-resolution PL spectra of the uncoated (black) and the Al-coated ZnO nanorods (red) at 10 K, graphed on a semi-logarithmic scale.
$\lambda_{exc} = 325\,nm$, $P = 2.4\,mW$, spot size $\sim 30\,\mu m$.

LO-phonon replicas, is more likely than the TES-I_4 and TES-I_6. Furthermore, this structural defect can possibly be close to the surface of the nanorod, which allows for relatively strong coupling of the defect bound exciton with the LSPs in the Al surface coating. This is consistent with highest enhancement factors at the energy position of the A line and its LO-phonon replicas. Moreover, this is in accordance with the depth-resolved CL, showing a higher enhancement at a greater CL excitation depth of approximately 350 nm at 10 kV, due to a larger excited surface area than at lower acceleration voltages.
The integrated PL emission of the UV and the DL of the uncoated and the Al-coated ZnO nanorods as a function of temperature is shown in fig. 5.43a. Figure 5.43b illustrates the corresponding enhancement of the UV and the DL emission. The DL emission is almost unchanged following the Al coating with close to no temperature dependence, while the UV emission is up to 6 times enhanced with a trend of decreasing enhancement with increasing temperature. These results are similar to those discussed in the depth-resolved CL section (section 5.6.1.1). However, the temperature dependence seems to be more pronounced in CL, which also showed a higher enhancement at 10 K of 7.2 at 5 kV. This is possibly due to the different type of excitation with the laser, which deposits most of its energy close to the sample surface, while the electron beam injects carriers at 88 nm for 5 kV, where the energy loss is maximum within the sample (cf. fig. 5.41 and section 5.2.2).

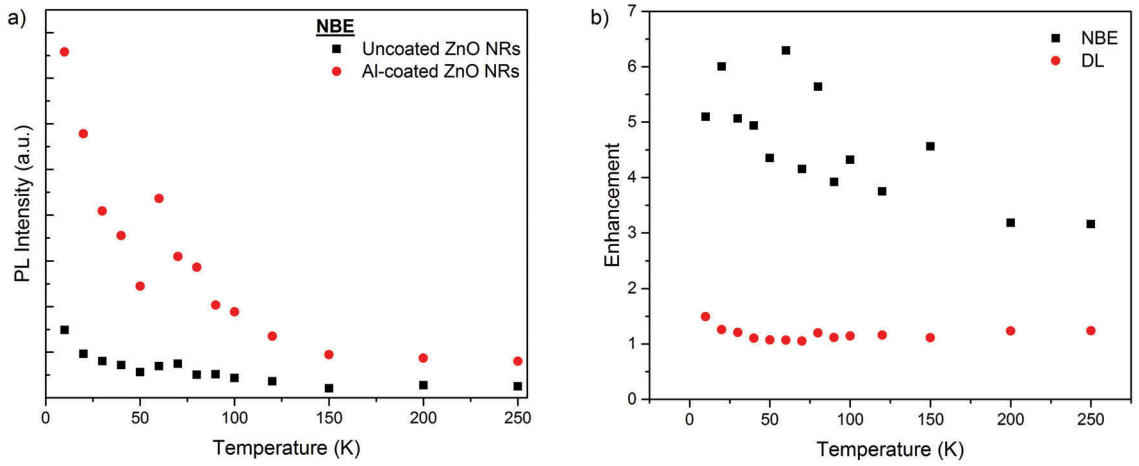

Fig. 5.43: (a) Integrated PL (UV: 3.00 eV to 3.54 eV; DL: 1.2 eV to 2.8 eV) of the uncoated (black) and the Al-coated ZnO nanorods (red) as a function of temperature. (b) PL enhancement of the UV and DL emission as a function of temperature.
$\lambda_{exc} = 325$ nm, $P = 2.4$ mW, spot size ~ 30 µm.

This behaviour is in accordance with the depth-dependent enhancement factor found in section 5.6.1.1, showing the highest enhancement at a greater depth. Furthermore, it is consistent with the assumption that the excitons bound to a structural defect (A) have a higher concentration at the bottom of the ZnO nanorods, which couple to the LSPs in the Al nanoparticles. Therefore, the more surface-sensitive laser excitation of the Al-coated ZnO nanorods results in lower UV enhancement factors than with the electron beam excitation.

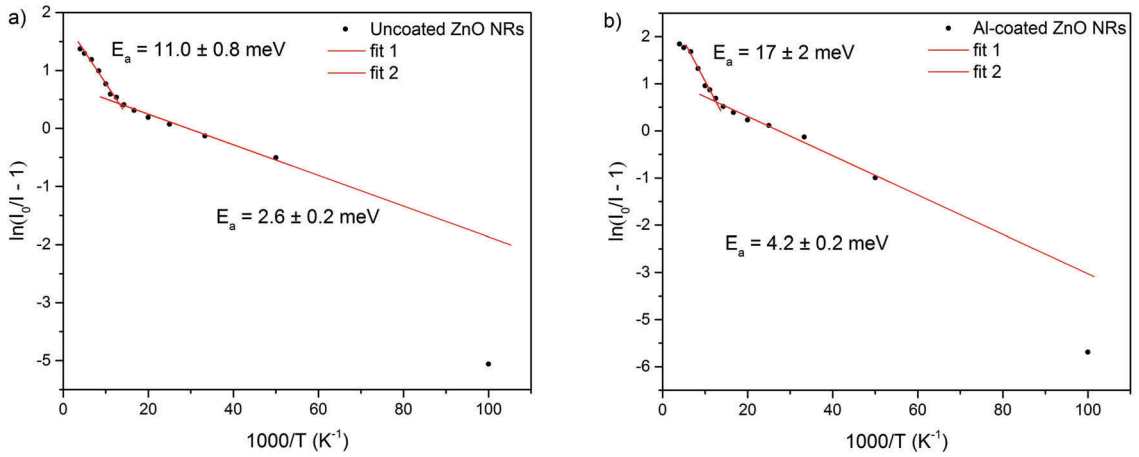

Fig. 5.44: (a) Arrhenius plot of the uncoated ZnO nanorods. Integrated PL from 3.00 eV to 3.54 eV. (b) Arrhenius plot of the Al-coated ZnO nanorods. Integrated PL from 3.00 eV to 3.54 eV.
$\lambda_{exc} = 325$ nm, $P = 2.4$ mW, spot size ~ 30 µm.

The Arrhenius plot of the integrated UV emission of the uncoated and the Al-coated ZnO nanorods is displayed in fig. 5.44a and b, respectively. Here, two gradients can be found in each side of the sample, indicating two main recombination channels with different activation energies (cf. eq. (3.14)). These activation energies are listed below, in table 5.9.

Table 5.9: Activation energies, E_a of the integrated UV emission (3.00 eV to 3.54 eV) of the uncoated and Al-coated ZnO nanorods.

Sample	$E_a(1)$ (meV)	$E_a(2)$ (meV)
Uncoated ZnO nanorods	(11.0 ± 0.8)	(2.6 ± 0.2)
Al-coated ZnO nanorods	(17 ± 2)	(4.2 ± 0.2)

It can be seen that both activation energies are higher for the Al-coated ZnO nanorods than for the uncoated side of the sample, which indicates that non-radiative recombination processes become active at higher temperatures in the Al-coated ZnO nanorods. It can be concluded that the Al-coating has improved the radiative recombination properties of the ZnO nanorods.

5.6.1.3 Excitation Power-Dependent PL of Al-Coated ZnO Nanorods

To investigate the UV enhancement of the Al-coated ZnO nanorods as a function of the excitation power, power-dependent PL measurements were performed at 10 K and 80 K. The results are shown in fig. 5.45. Here, the integrated UV (3.00 eV to 3.54 eV) and the integrated DL emission (1.2 eV to 2.8 eV) are illustrated as a function of laser excitation power. At both temperatures, the UV and the DL emission show a linear power law relationship with increasing laser excitation power, in both, the uncoated and Al-coated nanorods.

This trend is different to the Al-coated *a*-plane ZnO single crystals, as discussed in section 5.2.3, section 5.3.3 and section 5.4.3, where the integrated DL emission of the uncoated *a*-plane ZnO exhibits a sub-linear power-dependent power law, while the integrated UV emission shows a super-linear trend with increasing excitation power. The Al-coated *a*-plane ZnO, however, has a linear excitation power-dependent relationship, resulting in an overall power-dependent UV enhancement. The change in the power law can be attributed to the reduction of GL (at 2.3 eV) with the Al-coating, possibly due to surface interactions with the Al or surface band bending, resulting in a change of the charge transfer level for this GL. However, the presented uncoated and Al-coated ZnO nanorods do not exhibit any GL, but only orange (OL) and red luminescence (RL) — typically attributed to acceptor-like defects, as discussed in section 4.4.1. This suggests that the GL in *a*-plane ZnO saturates with increasing excitation power, which is not observed for the OL or RL.

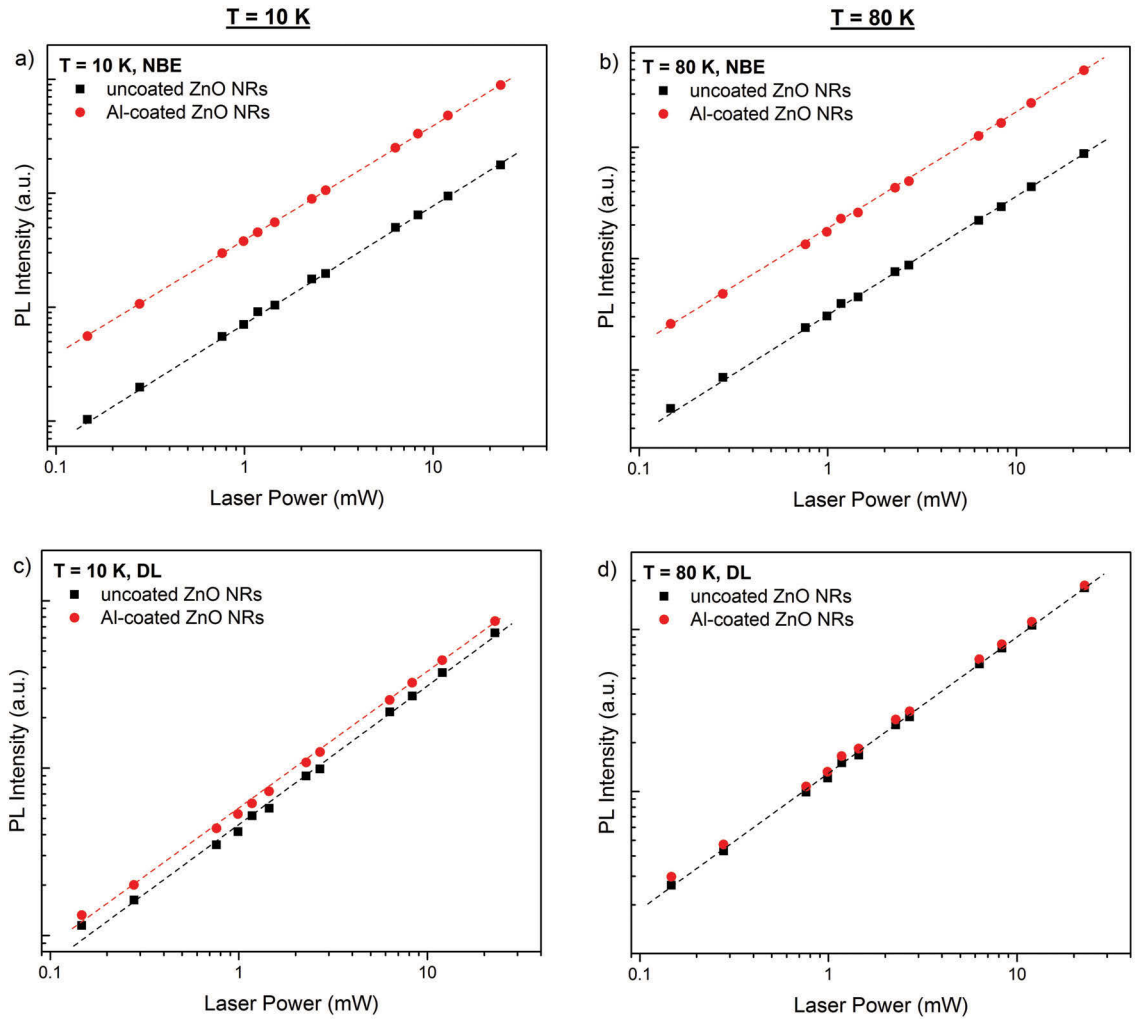

Fig. 5.45: UV PL of the uncoated (black) and the Al-coated ZnO nanorods (red), integrated from 3.00 eV to 3.54 eV, as a function of laser excitation power at (a) 10 K and (b) 80 K, graphed logarithmically. (c and d) Logarithmically plotted integrated DL emission from 1.2 eV to 2.8 eV as a function of laser excitation power at 10 K and 80 K, respectively. The dashed lines serve as guide to the eye.
$\lambda_{exc} = 325$ nm, spot size ~ 30 µm.

The UV and DL enhancement of the Al-coated ZnO nanorods as a function of laser excitation power at 10 K, 80 K and 300 K are illustrated in fig. 5.46. No laser excitation power dependence can be found, which is similar to the excitation power-dependent results in the Au nanoparticle-coated ZnO nanorods, discussed in section 4.4.3. This independence of laser excitation power can be possibly attributed to the defect-related DL emission in the ZnO nanorods, which is unaffected by the Al-coating.

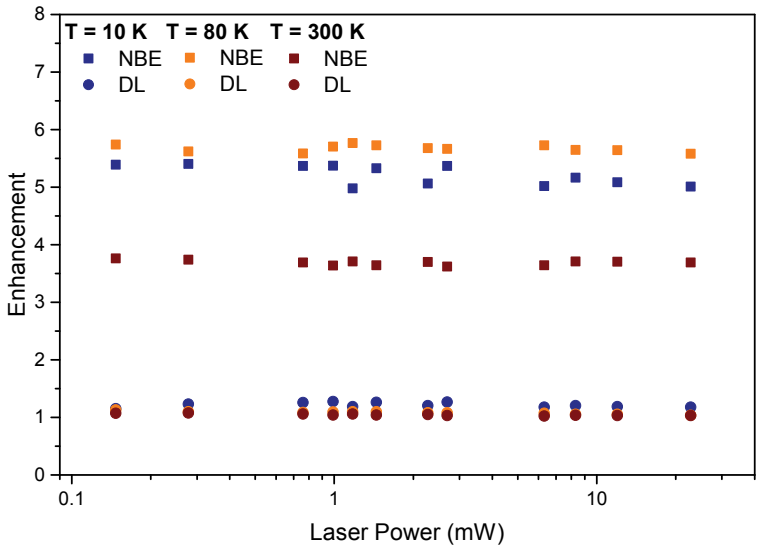

Fig. 5.46: Enhancement of the integrated UV PL (3.00 eV to 3.54 eV; squares) and the DL PL (1.2 eV to 2.8 eV; circles) of the Al-coated ZnO nanorods as a function of laser excitation power at 10 K (blue), 80 K (orange) and 300 K (wine).
$\lambda_{exc} = 325$ nm, spot size ~ 30 µm.

5.6.1.4 Time-Resolved PL of Hydrothermally-Grown Al-Coated ZnO Nanorods

The TR-PL measurements of the uncoated and the Al-coated ZnO nanorods were performed at the DBX at a temperature of 10 K, shown in fig. 5.47 and at the energy of the A-line at 80 K, presented in fig. 5.48. The enhancement of the DBX at 10 K is approximately 5.2, as shown in fig. 5.42. It is assumed that the LSPs in the Al nanoparticles couple to the DBX, although the coupling to the bound-exciton A appears to be stronger, resulting in an enhancement of 9.2 times. An approximate 4.5-fold reduction in lifetime of the DBX is expected.

From the fit of the longer exponential decay in the uncoated ZnO nanorods, typically attributed to the radiative recombination, a lifetime of $\tau_{\text{ZnO NRs}} = (135 \pm 3)$ ps is observed. The Al-coated ZnO nanorods exhibit an approximately 2.2 times reduced lifetime of $\tau_{\text{ZnO NRs+Al}} = (62 \pm 5)$ ps. It is noteworthy that this lifetime is most likely below the resolution of the laser response function, which makes an unequivocal determination of the lifetime difficult. However, a shortened lifetime of at least 2.2 can be found.

At 80 K, the lifetime of the highly enhanced exciton bound to a structural defect (A line) can be determined to be $\tau_{\text{ZnO NRs, 80K}} = (108 \pm 2)$ ps for the uncoated ZnO nanorods, see fig. 5.48. The Al-coated side of the sample exhibits an extremely short decay, which has the a similar shape as the laser response function, shown fig. 5.48b. Therefore, the actual lifetime cannot be determined, however, a great lifetime reduction is observed, which indicates that the LSPs in the Al nanoparticles couple relatively strongly to the A line in

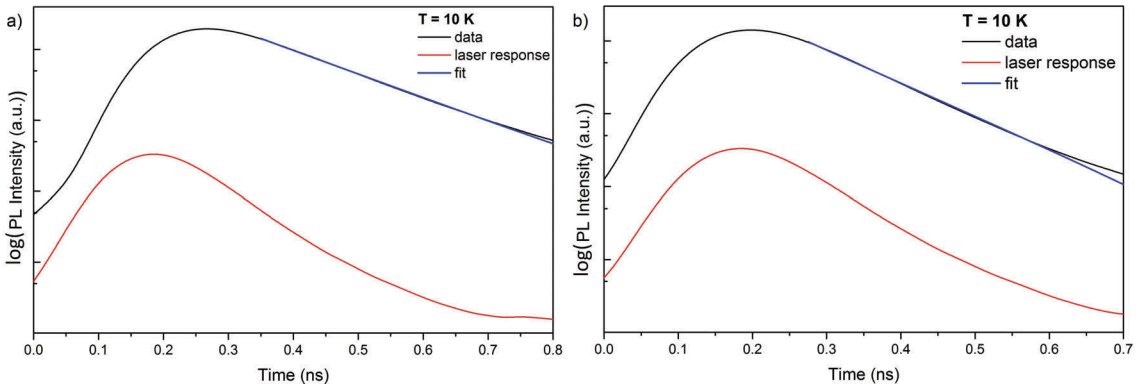

Fig. 5.47: Time-resolved PL at a fixed collection energy at the DBX of (a) the uncoated and (b) Al-coated hydrothermally-grown ZnO nanorods, at 10 K. The corresponding lifetimes are $\tau_{\text{ZnO NRs}} = (135 \pm 3)$ ps and $\tau_{\text{ZnO NRs+Al}} = (62 \pm 5)$ ps, which is already close to the laser response function.

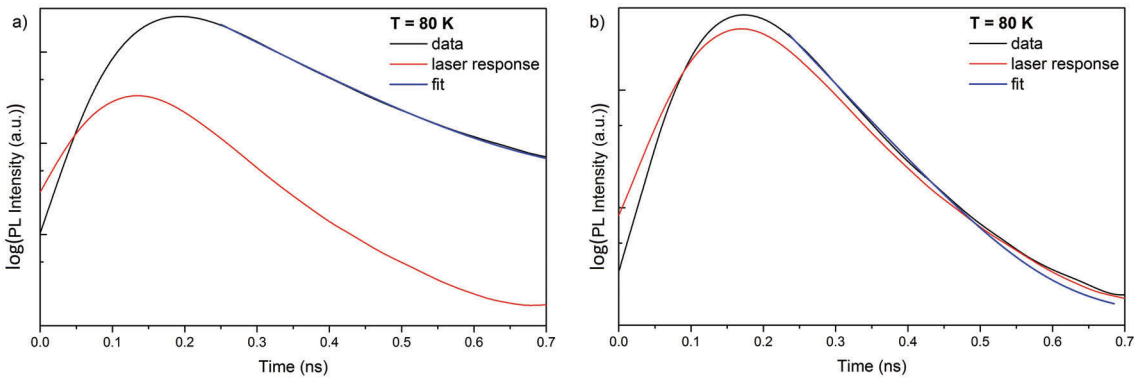

Fig. 5.48: Time-resolved PL at a fixed collection energy at the A line of (a) the uncoated and (b) Al-coated hydrothermally-grown ZnO nanorods, at 80 K. The corresponding lifetimes are $\tau_{\text{ZnO NRs, 80K}} = (108 \pm 2)$ ps, while $\tau_{\text{ZnO NRs+Al, 80K}}$ is at least as short as the laser pulse.

the ZnO nanorods. The SER in this sample is highly increased, resulting in an enhanced emission of up to 9.2 times.

5.6.2 Summary of Hydrothermally-Grown Al-Coated ZnO Nanorods

In summary, the Al-coated ZnO nanorods show an enhanced UV emission in PL and CL, compared with the uncoated side of the sample. This UV enhancement is found to be excitation power-independent, which can be attributed the absence of the GL of the DL in the ZnO nanorods.

Furthermore, the UV enhancement is depth-dependent, showing the highest enhancement of 10.3 at the greatest CL excitation depth ($HV = 10$ kV, $T = 10$ K). This is likely due to a larger surface area irradiated by the electron beam, resulting in a greater excited

surface area at 10 kV compared with that at 3 kV. Therefore, in the LSP-exciton mechanism, more LSPs in the Al nanoparticles can be excited by the 10 kV-electron beam than at lower acceleration voltages. Moreover, a waveguiding effect in the neighbour nanorods can possibly further increase the emission in the ZnO nanorods. The highly enhanced A line and its LO-phonon replicas in this sample can most likely be attributed to a structural defect, introduced during the growth, which is commonly closer to the bottom of the ZnO nanorods than the top. This further supports the results of the depth-resolved CL, showing the highest enhancement at 10 kV.
A slightly lower UV enhancement factor of 6 was found in PL, compared with that in CL (up to 10.3). This is most likely due to the different type of excitation, as the laser mainly loses its energy close to the surface (eq. (3.11)), while the energy loss profile of the electron beam has its maximum deeper within the sample. This is consistent with the results of the depth-resolved CL measurements with the highest UV enhancement at 10 kV.
Furthermore, a reduced lifetime of the DBX, as well as the A line in the Al-coated ZnO nanorods is observed, compared with the uncoated side of the sample. The actual lifetimes in the Al-coated ZnO nanorods cannot be determined due to the limitations of the experimental setup, which only allows for lifetime measurements down to ~ 70 ps.
The difference in the UV enhancement in PL and CL, as well as strongly-enhanced A line and its LO-phonon replica, suggest that the excitons bound to a surface-near structural defect, introduced during the ZnO nanorod growth, mainly couples to the LSPs in the Al nanoparticles. Furthermore, the UV enhancement of the Al-coated ZnO nanorods shows a temperature dependence with the highest enhancement at the lowest temperature of 10 K (7.2 at 5 kV in CL and 6 in PL). This is likely due to a higher number of stable A excitons at lower temperatures than at higher temperatures, where it possibly thermalises. In this sample, no FX-related emissions are found in the high-resolution spectra or in the enhancement, graphed as a function of energy (fig. 5.42). This result suggests that the LSP-exciton coupling in Al-coated ZnO might be more dependent on the concentration, the location and the polarisation of excitons in the studied ZnO sample than the properties of the Al-coating itself, such as the LSPR of the Al nanoparticles. Although, the type of the deposition of the Al can affect the degree of the diffusion and the oxidation of the Al surface coating.

5.6.3 Morphology of VS-Grown ZnO Nanorods Coated with 2 nm Al

The VS-grown ZnO nanorods exhibit approximately double the diameter of the hydrothermally-grown ZnO nanorods (~ 100 nm) and an approximate length of 1 µm, which is displayed in fig. 5.49. This results in a smaller surface-volume-ratio than that of the hydrothermally-grown ZnO nanorods, which might affect the coupling strength between the excitons in those ZnO nanorods and the LSPs in the Al nanoparticles in the surface

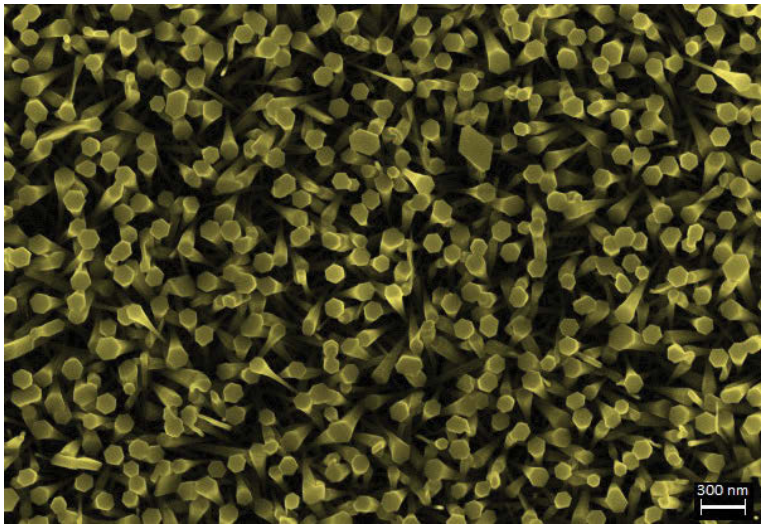

Fig. 5.49: Typical SE image of the VS-grown ZnO nanorods.
$HV = 5\,\text{kV}$.

coating. Assuming that the LSPs in the Al nanoparticles couple to the FX in the VS-grown ZnO nanorods, the diffusion of the relatively mobile FX to the ZnO nanorod surface is more probable than in the *a*-plane ZnO single crystals, which theoretically allows for a larger numbers of the FX to couple to the LSPs.
Furthermore, the VS-grown ZnO nanorods are well-aligned with an orientation perpendicular to the substrate, which leads to a well-defined ZnO crystal orientation. Here, the nanorods grow along the *c*-axis and due to the parallel polarisation of the FX-C to the *c*-axis, the FX-C is perpendicular to the surface, but parallel to the laser direction. However, the FX-A and -B are polarised perpendicular to the *c*-axis and lie thereby in the same plane as the laser electric field. Therefore, it is assumed that the LSPs in the Al nanoparticles might couple more strongly to the FX-A and -B in these Al-coated ZnO nanorods. This is the opposite polarisation as in the Al-coated *a*-plane ZnO single crystals (section 5.2, section 5.3 and section 5.4) and different to the hydrothermally-grown ZnO nanorods with no favourable crystal orientation due to their random alignment with respect to the substrate surface (section 5.6.1).
The morphology of the Al-coating cannot be determined due to the aforementioned low SE yield of the Al and the presence of the Al_2O_3. However, it is assumed that the surface coating is similar to that on the Si substrate, discussed in section 5.1, as the deposition was carried out under identical conditions.

5.6.4 Optical Characterisation of VS-Grown ZnO Nanorods Coated with Al

The optical properties of the VS-grown ZnO nanorods coated with Al were studied using PL and CL at a temperature of 80 K.

The depth-resolved CL spectra of the uncoated and the Al-coated ZnO nanorods are shown in fig. 5.50. Following the Al-coating, an enhanced UV emission of up to 2.3 is

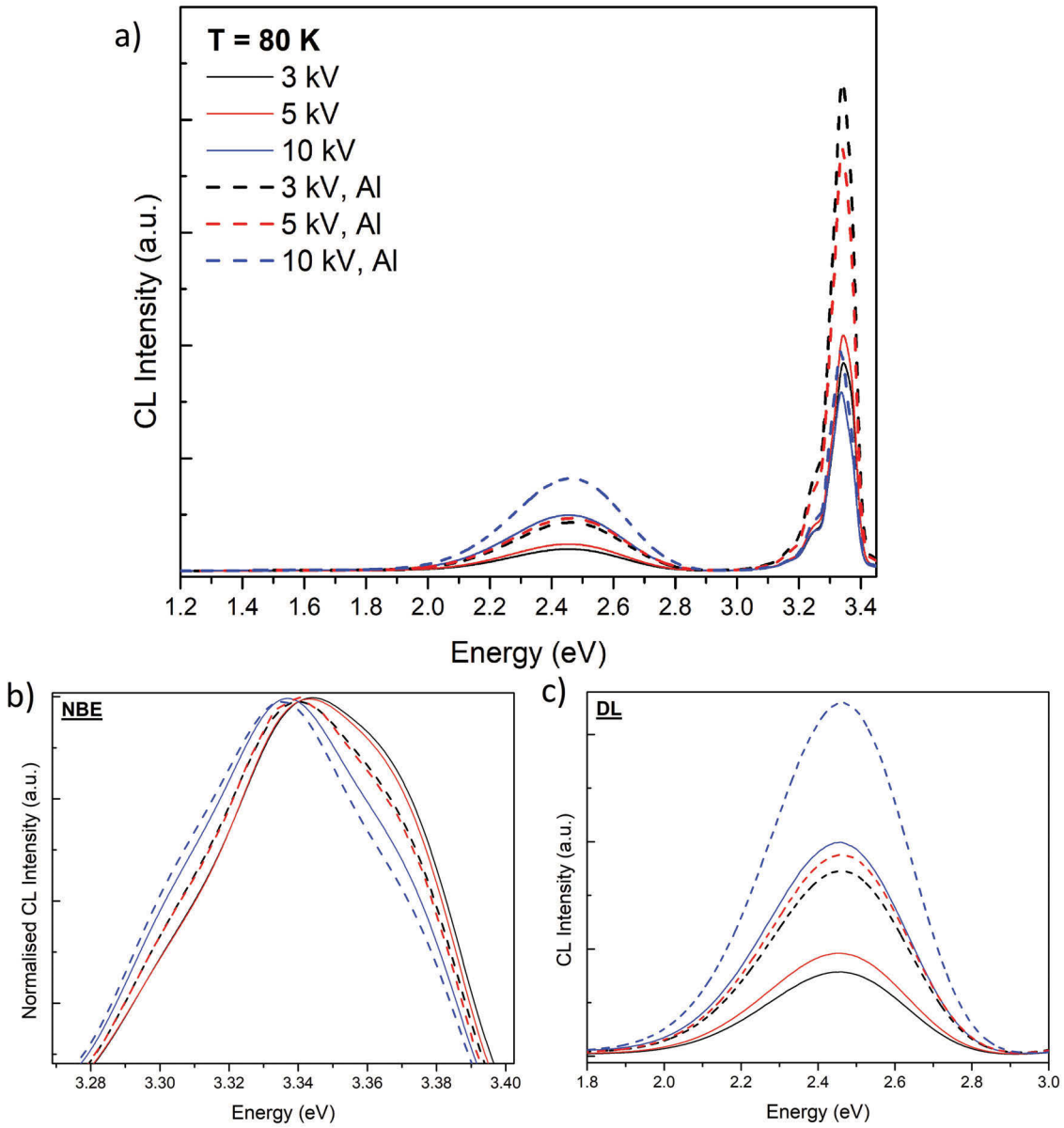

Fig. 5.50: (a) Depth-resolved CL of the uncoated (solid lines) and the Al-coated (dashed lines) ZnO nanorods (VS-grown) at 3 kV, 5 kV and 10 kV at 80 K. (b) Normalised NBE emission and (c) DL emission of uncoated and Al-coated ZnO nanorods.
CL: $P = 17.5\,\mu W$, scan area $10\,\mu m \times 10\,\mu m$.

observed (at 3 kV), as well as $\sim$ 1.7-fold enhanced DL emission. However, the UV enhancement decreases with increasing CL excitation depth, as shown in table 5.10.

Table 5.10: UV enhancement factors of the VS-grown ZnO nanorods coated with Al, at three different acceleration voltages at 80 K. The UV emission was integrated from 3.10 eV to 3.45 eV.

HV (kV)	UV enhancement (I)	UV enhancement (Int.)
3	2.3	2.3
5	1.8	1.8
10	1.2	1.2

This depth-dependent CL enhancement is similar to that observed for the Al-coated *a*-plane ZnO (cf. section 5.2.1 and section 5.3.1), while it is opposite to the hydrothermally-grown ZnO nanorods, discussed above (section 5.6.1.1).
It can be assumed that at an acceleration voltage of 3 kV the electron beam only excites one single ZnO nanorod, as the average diameter is 100 nm, which is larger than the CL excitation depth of $\sim$ 50 nm. For higher acceleration voltages, the CL excitation depth increases to approximately 90 nm (5 kV) and 350 nm (10 kV), exciting possibly more than one ZnO nanorod; while the 3 kV-electron beam mainly excites the top of the single ZnO nanorod. As the electron beam scans over an area of 10 µm $\times$ 10 µm, the CL spectra are always collected from an ensemble of ZnO nanorods. At 3 kV, most of the CL is coming from the top surface of the ZnO nanorods, while at higher acceleration voltages the CL emission is mainly from the bulk.
Moreover, the high density of the parallel aligned VS-grown ZnO nanorods might affect the Al deposition, as the deep side walls are not efficiently coated, resulting in a higher density of Al nanoparticles on the top of the ZnO nanorods, rather than on the side walls. Therefore, this shadowing effect results in a depth-dependent UV enhancement like that observed in the Al-coated *a*-plane ZnO, as mainly the surface of the ZnO nanorods effectively contributes to the LSP-exciton coupling. For the deeper CL excitation depths, at 5 kV and 10 kV, the less Al-coated side walls of the ZnO nanorods are being excited by the electron beam without contributing much to the overall UV enhancement. This depth-dependent behaviour is different to that in the randomly aligned hydrothermally-grown ZnO nanorods, which are most likely evenly covered with Al due to their oblique axis alignment to the substrate. This is consistent with the even distribution of the Au nanoparticles on the Au nanoparticle-coated ZnO nanorods (cf. section 4.1), which is assumed to be identical to the Al deposition on the hydrothermally-grown ZnO nanorods.
Figure 5.50b depicts the normalised NBE emission of the uncoated and the Al-coated ZnO nanorods, showing a slight red-shift and narrowing in the peak width. This will be discussed in more detail below, as a higher spectral resolution is required to identify individual excitonic transitions.
The DL emission, presented in fig. 5.50c, centered at approximately 2.45 eV (GL_1), shows

an enhancement in the presence of the Al surface coating, but no obvious change in peak shape or position can be seen. The enhancement of the DL is most likely due to a change in the charge transfer level by surface band bending or passivation of non-radiative recombination channels, possibly surface states, which is not further studied in this work. The GL_1 at 2.45 eV is typically attributed to V_O in ZnO, indicating that the DL emission of the VS-grown ZnO nanorods is substantially different to that in the *a*-plane ZnO, as well as the hydrothermally-grown ZnO nanorods (cf. table 2.2).

The high-resolution depth-resolved CL spectra of the uncoated and the Al-coated ZnO nanorods at 80 K is displayed in fig. 5.51, allowing the study of the luminescence distribution with increasing CL excitation depth in more detail. Although the FX transitions

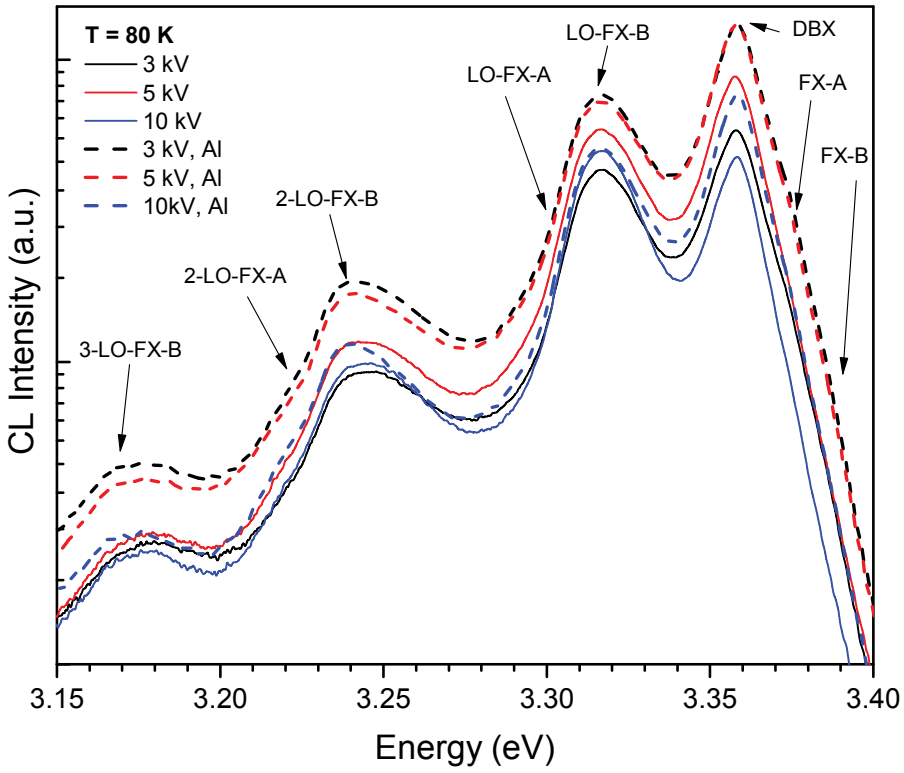

Fig. 5.51: High-resolution depth-resolved CL of the uncoated and the Al-coated ZnO nanorods (VS-grown) at 3 kV, 5 kV and 10 kV, graphed on a semi-logarithmic scale.
$T = 80$ K, $P = 17.5$ µW, scan area 10 µm × 10 µm.

and their LO-phonon replicas can be labelled in these high-resolution CL spectra, the individual I lines in the broad DBX are difficult to identify. However, a trend of greater enhancement of the Al-coated ZnO nanorods at lower CL excitation depth is observed, consistent with the results shown above.

The UV enhancement as a function of energy is illustrated in fig. 5.52 at 3 kV, 5 kV and 10 kV. Here, the assignment of the excitonic transitions is easier, however, the labelled I

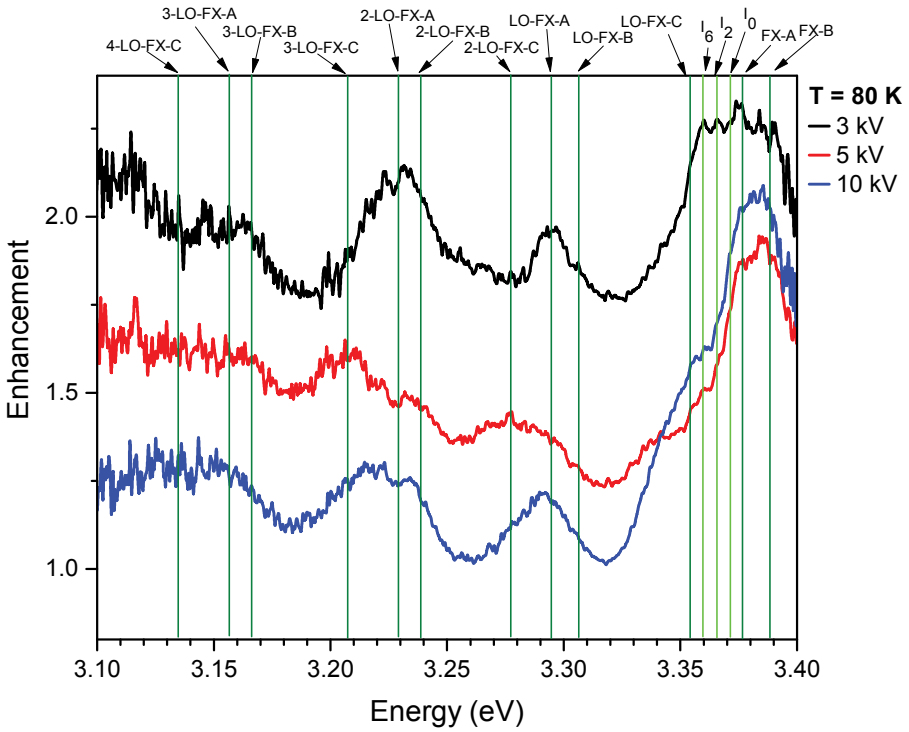

Fig. 5.52: UV enhancement of the Al-coated ZnO nanorods (VS-grown) at 3 kV, 5 kV and 10 kV as a function of energy, showing highest enhancement closest to the surface. The green labels present the DBX-related emission peaks, while FX emissions are labelled in olive.
$T = 80$ K, $P = 17.5$ µW, scan area 10 µm × 10 µm.

lines in the DBX region are shown for completeness and to allow for the comparison with the *a*-plane ZnO samples, discussed above (section 5.2, section 5.3, section 5.4). Nevertheless, the highest enhancement is found at 3 kV with its maximum of 2.6 in the DBX region and at the energy of the FX-A and -B. The enhancement of the first LO-phonon replica of the FX-C is less pronounced — a 2-fold enhanced shoulder at 3.353 eV — while the LO-phonon replica of the FX-A are more strongly enhanced.
For greater CL excitation depths, the UV enhancement is reduced, showing the same depth-dependent trend as the Al-coated *a*-plane ZnO single crystals (cf. section 5.2.1).

To also compare the PL results with that of the Al-coated *a*-plane ZnO and hydrothermally-grown ZnO nanorods, high-resolution PL was performed at 80 K. The corresponding spectra, as well as the enhancement factor as a function of energy are presented in fig. 5.54. The UV enhancement profile in PL is different to that in CL, showing the highest enhancement of 7.5 at 3.357 eV, which is attributed to the Al-associated I_6 line. Therefore, the diffusion of Al into the ZnO nanorods is the most likely explanation, even though a

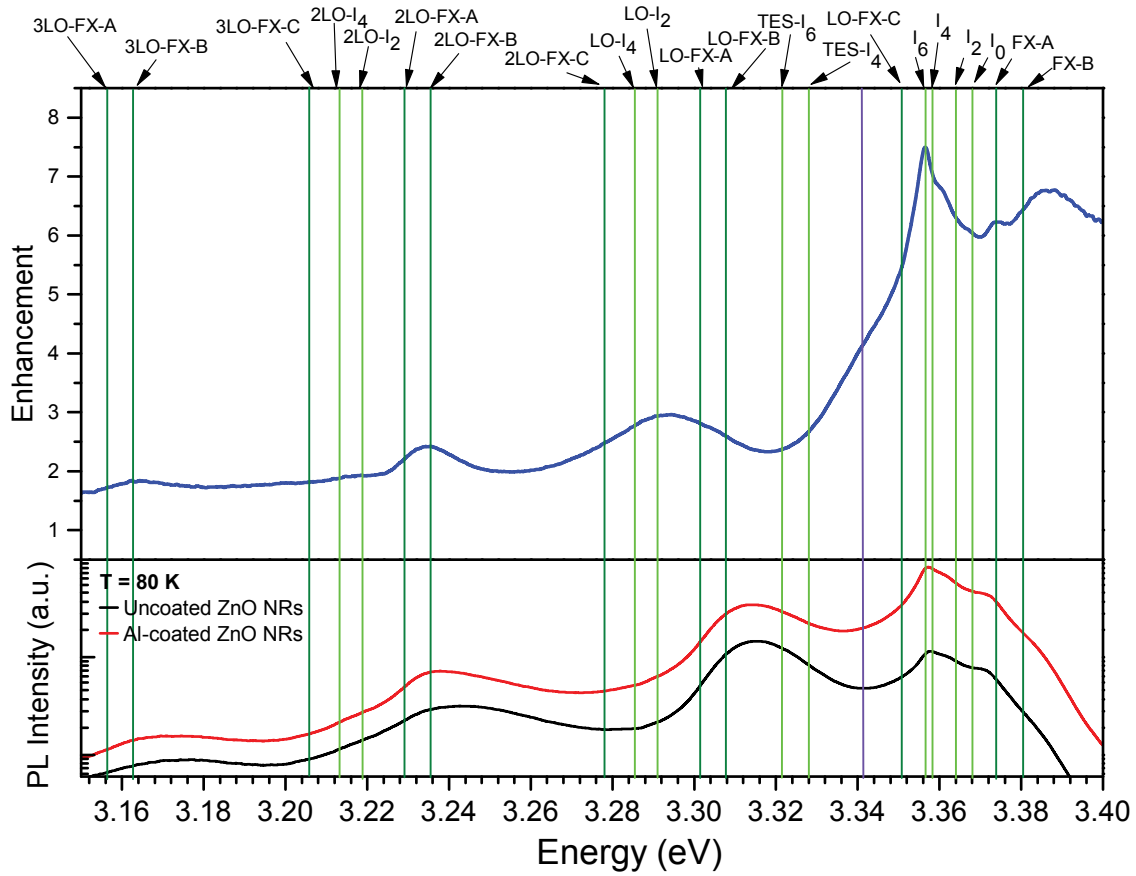

Fig. 5.53: Top: UV enhancement of the Al-coated ZnO nanorods (VL-grown) at 80 K. The green labels present the DBX-related emission peaks, while FX emissions are labelled in olive.
Bottom: High-resolution PL spectra of the uncoated and Al-coated ZnO nanorods at 80 K, graphed on a semi-logarithmic scale.
PL: $\lambda_{exc} = 325$ nm, spot size ~ 30 µm.

similarly high enhancement of 6.8 of the FX-A and -B (at 3.74 eV and 3.383 eV, respectively) is observed. Furthermore, the LO-phonon replicas of the FX-A and -B are clearly visible in the enhancement, which suggests that the UV enhancement of the Al-coated ZnO nanorods can be attributed to a combination of the Al-doping and the LSP-exciton coupling between the LSPs in the Al nanoparticles and possibly the FX-A and -B.
The difference in the CL and the PL enhancement is likely due to the more surface-near excitation with the laser light, as both types of enhancement — Al-doping and LSP-exciton coupling — take place close to the surface. The electron beam has a greater excitation depth and excites less CL in the very top of the ZnO nanorods.
The LSPs in the Al nanoparticles most likely couple to the FX-A and -B, as they are highly enhanced as well as their LO-phonon replicas, while the LO-phonon replicas of the FX-C are not particularly enhanced. This is consistent with the polarisation match of the FX-A

and -B, being polarised perpendicular to the c-axis in ZnO and therefore aligned along the short axis of the ZnO nanorods. This orientation of the FX-A and -B results in a higher excitation probability with the laser, which is polarised in the same plane. Therefore, a stronger coupling between the LSPs in the Al nanoparticles with the FX-A and -B is possible, resulting in a higher PL enhancement than in CL.

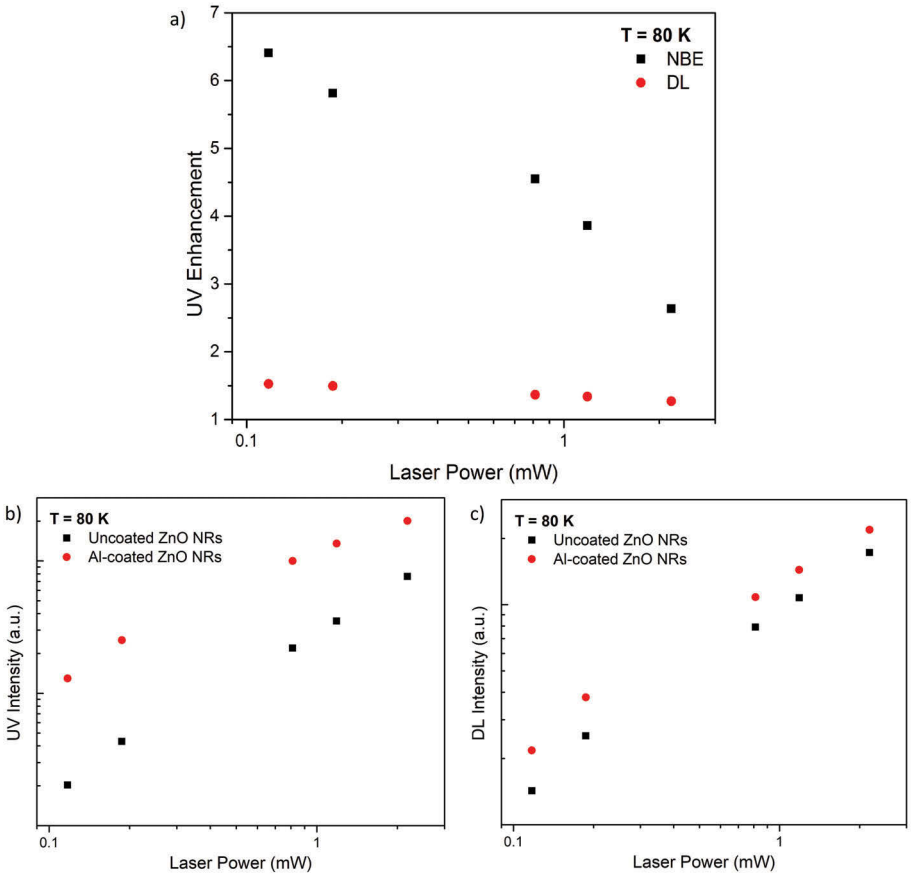

Fig. 5.54: (a) UV emission integrated from 3.00 eV to 3.54 eV of the uncoated (black) and the Al-coated (red) ZnO nanorods (VS-grown) as a function of laser excitation power, graphed logarithmically. (b) UV and (c) DL enhancement of the Al-coated ZnO nanorods as a function of laser excitation power.
$T = 80\,\mathrm{K}$, $\lambda_{\mathrm{exc}} = 325\,\mathrm{nm}$, $P = 117\,\mu\mathrm{W}$, spot size $\sim 30\,\mu\mathrm{m}$.

The UV enhancement dependence on the excitation power was studied by power-dependent PL at 80 K, which is shown in fig. 5.54. In (a), it can be seen that the UV enhancement of the Al-coated ZnO nanorods is highly dependent on the excitation power, with the maximum enhancement of 6.5 at the lowest laser excitation power of 0.12 mW.
The integrated UV emission (3.00 eV to 3.54 eV), illustrated in fig. 5.54b, shows a superlinear trend for the uncoated ZnO nanorods with a gradient of (1.20 ± 0.02), while the

gradient of the Al-coated side of the sample is decreased. The super-linearity of the uncoated ZnO was also found in the uncoated *a*-plane ZnO single crystals, which is likely due to the saturation of the GL (2.3 eV) in the DL, allowing for an increased recombination through the NBE. The Al-coating on the *a*-plane ZnO single crystals, however, reduced the GL, resulting in a linear relationship in the DL and the UV emission with increasing excitation power. In the Al-coated VS-grown ZnO nanorods, the excitation power dependence of the UV and the DL emission is different to the Al-coated *a*-plane ZnO, which is possibly due to different defect-related recombination centres in the DL.
The integrated DL emission (1.2 eV to 3.0 eV) is depicted in fig. 5.54c, showing a sub-linear behaviour with increasing laser excitation power for both sides of the sample. The corresponding gradients are determined to be 0.83 and 0.77 for the uncoated and Al-coated ZnO nanorods, respectively. It can be assumed that the DL emission is comprised of more than one defect-related emission, where one exhibits a faster saturation with increasing power than the others. In comparison with the DL in the *a*-plane ZnO single crystals, which shows the GL at 2.3 eV, as well as an intense the yellow luminescence. The present ZnO nanorods exhibit a different defect-related DL emission, with mainly GL_1 at 2.45 eV. The lifetimes of these luminescence centres can vary depending on the defect centres in the ZnO sample, and therefore lead to a different saturation behaviour with increasing excitation power [45]. It is conceivable that the Al-coating on these ZnO nanorods similarly reduces the aforementioned GL at 2.3 eV, while another recombination channel becomes more favourable. However at this stage, it is not possible to draw unequivocal conclusions, as the chemical origin of the DL emission in ZnO is still highly controversial in the literature and a large variety of measurements would be needed to reliably assign the defects to specific defect centres.
The power-dependent UV emission of the Al-coated ZnO nanorods cannot be fully explained, as they show a different DL emission than the hydrothermally-grown ZnO nanorods and the *a*-plane ZnO single crystals. However, the UV enhancement of the Al-coated ZnO nanorods is highly dependent on the laser excitation power, which could therefore possibly explain the different enhancement factors in CL and PL.

5.6.5 Summary of VS-Grown ZnO Nanorods Coated with 2 nm Al

Summarising the results of the VS-grown ZnO nanorods coated with Al, a depth-dependent UV enhancement is observed with the highest enhancement of 2.3 at 3 kV, followed by a reduced UV enhancement with increasing CL excitation depth. This trend is similar to that in the Al-coated *a*-plane ZnO (cf. section 5.2.1 and section 5.3.1), but opposite to that in the hydrothermally-grown ZnO nanorods (see section 5.6.1). This can be explained by the parallel alignment of the VS-grown ZnO nanorods, which most likely leads to a shadowing effect during the Al deposition, leading to an Al-coating mainly on

the top of the ZnO nanorods with poor coverage of the ZnO nanorods' side walls. Effectively, this is similar to a surface coating on a planar sample, while the random alignment of the hydrothermally-grown ZnO nanorods exhibit an evenly distributed surface coating, shown for the Au nanoparticle-coated ZnO nanorods in section 4.1.
The high-resolution CL and PL spectra show an enhanced I_6 line, indicating Al diffusion into the ZnO nanorods, as well as a large contribution of the FX-A and -B. It can be assumed that the UV enhancement is due to Al-doping, as well as LSP-exciton coupling between the LSPs in the Al nanoparticles with mainly the FX-A and -B, which is more pronounced in the PL spectra with an approximate enhancement of 6.8 compared with that of CL (1.8). This difference in the PL and the CL enhancement is most likely due to the more surface-sensitive laser excitation, as well as its polarisation being in the same plane as the FX-A and -B in the VS-grown ZnO nanorods. Furthermore, the excitation density with the electron beam is approximately four orders of magnitude larger than that of the laser, which is consistent with strong power-dependent UV enhancement with the laser excitation power, showing the greatest enhancement at the lowest power.
In conclusion, the behaviour of the UV enhancement of the Al-coated VS-grown ZnO nanorods in CL and PL is similar to that found in the Al-coated *a*-plane ZnO. In PL, a stronger LSP-exciton coupling to the FX-A and -B is observed, which is most likely due to the polarisation of the laser light being in the same plane as that of the FX-A and -B in the ZnO nanorods. This results in the creation of a faster, additional relaxation channel through the LSPs in the Al nanoparticles, increasing the SER and thereby enhancing the UV emission of the Al-coated VS-grown ZnO nanorods.

5.7 Discussion

This section provides a summary of the findings of the conducted experiments, presented above, and a critical discussion. The LSP-exciton coupling in three types of ZnO samples coated with three different Al surface coatings were comprehensively studied, using various experimental techniques to determine the morphology of the coatings and to optically characterise these samples. A combination of ellipsometry and transmission spectroscopy was used to obtain the information on the morphology and composition of the Al-coating. The optical characteristics of the different samples were investigated by depth-resolved CL, temperature- and excitation-dependent PL and time-resolved PL from 10 K to 300 K. Table 5.11 lists the different types of samples and their morphologies, investigated in this work.
Summarising the results of the samples *Al*: a highly enhanced UV emission of the Al-coated side of the sample was observed compared with the uncoated *a*-plane ZnO, where the maximum enhancement of 8.3 was observed at the lowest CL excitation depth (3 kV) at a temperature of 80 K. The UV enhancement was found to decrease with increasing

Table 5.11: Overview of the samples studied in this work.

Sample	Crystal orientation	Al deposition	Al coating
Al	*a*-plane ZnO single crystal	2 nm Al in Ar at RT	$\sim$ 2.8 nm thin Al_2O_3 layer with 0.1 Vol% metallic Al
Al hot	*a*-plane ZnO single crystal	2 nm Al in Ar at 300 °C	$\sim$ 2.8 nm thin Al_2O_3 layer with 0.2 Vol% metallic Al
Al oxide	*a*-plane ZnO single crystal	2 nm Al in Ar and O at RT	$\sim$ 2.8 nm thin Al_2O_3 layer (no metallic Al)
Hydrothermally-grown ZnO nanorods	grown along *c*-axis, randomly aligned	2 nm Al in Ar at RT	$\sim$ 2.8 nm thin Al_2O_3 layer with 0.1 Vol% metallic Al
VS-grown ZnO nanorods	grown along *c*-axis, parallel aligned	2 nm Al in Ar at RT	$\sim$ 2.8 nm thin Al_2O_3 layer with 0.1 Vol% metallic Al

CL excitation depth, indicating that the origin of the UV enhancement is a near surface effect. Furthermore, a temperature dependence of the UV enhancement was found in CL and PL, peaking at 80 K. The high-resolution luminescence spectra revealed that a maximum enhancement of 12 was achieved at the energy of 3.354 eV, assigned to the first LO-phonon replica of the FX-C. As the temperature increases from 10 K to approximately 120 K, the intensity of the FX emissions increases, as the BX peaks quench due to their thermal dissociation. Therefore, the depth-resolved CL and the temperature-dependent CL and PL results are consistent with a relatively strong coupling between the LSPs in the Al nanoparticles and the FX-C. This is reasonable as the FX are more mobile than the DBX. As they can move freely, the probability of the FX diffusing to the ZnO-Al interface and coupling to the LSPs in the Al nanoparticles is higher than that of the less mobile, spatially localised DBX. In addition, the FX-C has the highest FX transition energy in ZnO, and accordingly the greatest spectral overlap with the broad LSPR energy (2.8 eV to 6.2 eV), allowing, in principle, for relatively stronger LSP-exciton coupling. Furthermore, a higher UV enhancement factor was observed in PL than in CL, which is in accordance with the Al-LSP coupling to the FX-C in ZnO, as the laser is polarised in the same plane as the FX-C in *a*-plane ZnO. An approximately 3 times shortened lifetime for the Al-coated *a*-plane ZnO, compared with the uncoated side of the sample provides additional evidence for the LSP-exciton coupling mechanism in this sample. These results indicate that the SER is increased due to the creation of an additional, faster relaxation pathway via excitation of LSPs in the Al nanoparticles.

An excitation power dependence with the maximum UV enhancement at the lowest excitation power was found, which can be attributed to a highly reduced GL at 2.3 eV, possibly related to V_{Zn}, due to the Al-coating. In the uncoated *a*-plane ZnO, the DL emission exhibited a sub-linear power law exponent with increasing power, while the NBE emission showed a super-linear behaviour in the Al-coated side of the sample. Here, both DL and NBE emissions have a linear relationship with increasing excitation power, indicating that the GL shows saturation effects and therefore results in a power-dependent UV enhancement of the Al-coated *a*-plane ZnO. The reduction of the GL, found in the depth-resolved CL spectra at 3 kV and 5 kV, is most likely due to a change in the charge transfer level introduced by the surface band bending from upward in the uncoated side to downward in the Al-coated *a*-plane ZnO. Al surface in-diffusion is another possible explanation for the reduced GL at the surface of the Al-coated *a*-plane ZnO, where the Al occupies V_{Zn} sites. Furthermore, the difference in UV enhancement factors in CL and PL can be explained by: (i) an approximately four orders of magnitude higher excitation power density by the electron beam and (ii) that the greatest PL excitation by the laser occurs at the surface, following the Beer-Lambert's Law (cf. eq. (3.11)) with an approximate penetration depth of 100 nm, compared to that in CL, where the maximum injection occurs at a depth of approximately one third of the electron range ($\sim$ 90 nm).
Moreover, a slightly enhanced I_6 line was observed, which can be attributed to Al diffusion into the surface of the *a*-plane ZnO. Therefore, it can be concluded that the up to 12-fold UV enhancement in the sample *Al* can be explained by Al-doping to a certain extent, as well as a strong coupling between the LSPs in the Al nanoparticles and mainly the FX-C in the *a*-plane ZnO.
Similar results were found for the sample *Al hot*, where an overall lower UV enhancement of 2.8 in CL and 3.5 in PL was observed. Although the ellipsometry results suggested a higher percentage of 0.2 % metallic Al than in the sample *Al*, the PL and CL results show an increased Al-doping effect, indicated by an 3.5-fold enhanced I_6 emission. This is possibly due to the higher deposition temperature of 300 °C, allowing for easier diffusion of Al into ZnO. However, an enhanced emission of the LO-phonon replicas of the FX-C can also be observed, which indicates that the UV enhancement of the hot Al-coated *a*-plane ZnO can be attributed to Al-doping, as well as LSP-exciton coupling between the LSPs in the Al nanoparticles and the FX-C in the *a*-plane ZnO. This is similar to the result in the sample *Al*, but it can be assumed that a larger part of the UV enhancement is due to the diffusion of Al into ZnO, while the LSP-exciton coupling is less pronounced, as less metallic Al is present to form Al nanoparticles. This is also reflected in the temperature-dependent PL results, showing the maximum UV enhancement at 60 K — compared to 80 K in the sample *Al*. As the I_6 transition is expected to thermally dissociate with increasing temperature, the highest enhancement due to Al-doping can be assumed to occur at low temperature; whereas the FX-related emissions are much more stable at elevated

temperature and therefore provide a greater contribution to the UV enhancement of the LSP-exciton coupling at higher temperatures. Here, the optimum conditions for the combination of those two enhancement mechanisms — Al-doping and LSP-exciton coupling to the FX-C — is reached at a temperature of 60 K.

The Al_2O_3-coating of the sample *Al oxide*, where no metallic Al was found, shows very different CL and PL results. Here, an overall reduced UV emission was observed, as well as an additional broad emission at 3.10 eV to 3.32 eV, which was confirmed not to be due to the oxygen-plasma treatment or the Al_2O_3-coating itself. As this emission overlaps with a large part of the excitonic transitions in ZnO, the identification of the individual DBX- and FX-related emission peaks was difficult, complicating the interpretation of the PL and CL data. However, the depth-resolved CL measurements revealed a greater UV reduction close to the surface, while at 10 kV the integrated UV emission exhibited a similar intensity for both sides of the sample. Furthermore, the temperature-dependent PL data showed that no distinct transition in ZnO was reduced or enhanced by the Al_2O_3-coating.

The excitation power dependence, observed in the samples *Al* and *Al hot*, can be similarly found in the sample *Al oxide*, which suggest that the reduced surface band bending from 0.28 V for the uncoated *a*-plane ZnO to 0.15 V in the Al_2O_3-coated side of the sample is possibly responsible to sufficiently change the charge transfer level to quench the GL in the Al- or Al_2O_3-coated *a*-plane ZnO. However, due to the low carrier density in the *a*-plane ZnO, i. e. a wide space charge region, it is unlikely that the surface band bending would change the charge state of the GL defect. The in-diffusion of Al is another possible explanation for the reduction of the GL in the Al- and Al_2O_3-coated *a*-plane ZnO, however, the Al-diffusion coefficient in Al_2O_3 is much higher than that in Al.

Furthermore, the time-resolved PL measurements revealed an identical lifetime for both sides of the sample *Al oxide*, indicating that no additional, faster relaxation pathway was created. As expected, no LSP-exciton coupling occurred in the sample *Al oxide*. In fact, no UV enhancement was found, indicating that even a small percentage of metallic Al is sufficient to create LSPs, which can then efficiently couple to the excitons in ZnO. In the case of *a*-plane ZnO, the FX-C is more favourable, particularly with laser excitation, than the energetically lower FX-A and -B.

The VS-grown ZnO nanorods, with an average diameter of $\sim$ 100 nm and 1 µm length, coated with Al exhibited an up to 2.3-fold CL enhancement of the UV emission. A similar depth dependence of the UV enhancement as the Al-coated *a*-plane ZnO samples was found, with the maximum at 3 kV. This can be explained by a shadowing effect during the Al deposition due to the parallel alignment of the ZnO nanorods to each other. Therefore, the top of the nanorods can possibly have a denser Al nanoparticle-coating than the nanorods' side walls, which results in a higher contribution from the top of the ZnO nanorods to the LSP-exciton coupling.

A greater UV enhancement factor was achieved with laser excitation, which is most likely due to the maximum laser excitation being closer to the surface, compared with the electron beam. This is consistent with the results of the power-dependent PL measurements, showing the greatest UV enhancement at lowest excitation power. Although, this trend appears similar to that in the Al-coated *a*-plane ZnO, a different DL emission behaviour was observed in the VS-grown ZnO nanorods, with the highest contribution being due to V_O-related defects, which was not affected by the Al-coating. The V_O defect is unlikely to be quenched by Al in-diffusion with being donor type defects in ZnO. The excitation power dependence of the UV emission in the VS-grown ZnO nanorods cannot be unequivocally attributed at this stage.

Similar to the sample *Al*, some diffusion of Al can also be found in this sample, indicated by a PL enhanced I_6 emission of ~ 7.5 times at 80 K. However, similarly high PL enhancement of the FX-A and -B can be observed, as well as their LO-phonon replicas, indicating that the LSPs in the Al nanoparticles mainly couple to the FX-A and -B. This is opposite to the results of the Al-coated *a*-plane ZnO with the most efficient LSP-exciton coupling to the FX-C. As mentioned before, the VS-grown ZnO nanorods grow along the *c*-axis perpendicular to the substrate. As a result, the FX-A and -B, which are perpendicular polarised to the *c*-axis in ZnO, lie in the same polarisation plane as the laser light. This allows for a higher excitation of the FX-A and -B relative to the FX-C. Therefore, it can be concluded that the LSP-exciton coupling is not exclusively limited by the LSPR of the Al nanoparticles, but also by the orientation of the ZnO sample and the polarisation of the different FX.

The hydrothermally-grown ZnO nanorods exhibit an average diameter of 40 nm and a length of 700 nm, and therefore have a larger surface-to-volume ratio than the VS-grown ZnO nanorods. This is a large advantage of the ZnO nanorods over the planar ZnO crystals, as the diffusion of the FX to the surface in the ZnO nanorods is more probable than in the *a*-plane ZnO single crystals. However, due to the shadowing effect in the VS-grown ZnO nanorods, no advantage of the larger surface-to-volume ratio was observed. In contrast, the random orientation of the ZnO nanorods allows for a more evenly distributed Al-coating along the entire length of the nanorods, similar to the Au nanoparticle-coating shown in section 4.1. Interestingly, the results of the depth-resolved CL spectroscopy showed the opposite trend of UV enhancement, with the maximum UV enhancement of 10.3 at 10 kV, while being smaller at lower CL excitation depths. This was attributed to a larger side wall surface area being excited by the electron beam at 10 kV than at 3 kV, allowing for greater excitation of LSPs in the Al nanoparticles and excitons in ZnO. Moreover, a waveguiding effect in the neighbouring ZnO nanorods can possibly further enhance the UV emission.

Furthermore, a different temperature dependence of the UV emission was observed, showing the highest enhancement at 10 K. The high-resolution PL spectra revealed the

highest enhancement of 9.2 at an energy of 3.324 eV, which was attributed to an exciton bound to a structural defect (A line), introduced during the ZnO nanorod-growth. Although the DBX is approximately 5.2-fold enhanced, no DBX-related LO-phonon replicas were found; while LO-phonon replicas of the A line were found with the typical spacing of 73 meV in ZnO. The more pronounced LSP-exciton coupling to the A line than to other transitions in ZnO can be explained by a larger abundance of structural defects and the possibility that these centres lie naturally closer to the surface of the ZnO nanorods. This structural defect is reported to be closer to the bottom of the ZnO nanorods, which is consistent with the results of the depth-resolved CL measurements, where greater acceleration voltages (10 kV) showed a higher enhancement. This is also in accordance with the maximum UV enhancement at 10 K, as the thermalisation effects reduce its intensity with increasing temperature. The high-resolution PL spectra did not exhibit any FX-related emissions, which explains why no LSP-coupling to the FX in ZnO was found. Furthermore, due to the random orientation of the hydrothermally-grown ZnO nanorods, no polarisation of the FX transitions is favoured by the laser excitation.

In addition, no excitation power dependence on the UV enhancement was observed in Al-coated hydrothermally-grown ZnO nanorods. This is most likely due to the DL emission, comprised of OL and RL, while no GL was found. Furthermore, no change of the DL emission with increasing CL excitation depth was observed. This suggests that the GL in the uncoated *a*-plane ZnO samples, assigned to the acceptor-like V_{Zn}, is responsible for the sub-linear power-law exponent in the DL and super-linear in the NBE emission with increasing excitation power. A change in the charge transfer level by a reduced surface band bending or in-diffused Al occupying V_{Zn} centres are possible explanations for the quenching of the GL in the Al-coated *a*-plane ZnO.

The higher UV enhancement in CL than in PL can therefore only be attributed to larger excitation depth by the electron beam, which has an energy loss profile with the maximum deeper in the sample at $\frac{R_{\mathrm{e}}}{3}$, compared with the laser excitation being greatest at the surface.

In summary, the Al-coated hydrothermally-grown ZnO nanorods show a large UV enhancement, which is mainly attributed to the LSP-exciton coupling between the LSPs in the Al nanoparticles and the excitons bound to the surface-near structural defect (A), introduced during the ZnO nanorod growth. This can be further supported by the at least 4 times reduced lifetime of the A line of the Al-coated ZnO nanorods, compared with the uncoated side of the sample.

The main results of the studied samples are presented in table 5.12.

In conclusion, the deposition of a thin Al film onto ZnO results in a large enhancement of the UV emission of up to 12 times, which can be mainly attributed to LSP-exciton coupling of the Al nanoparticles and the excitons in ZnO. An elevated temperature during the Al deposition increases the Al diffusion into ZnO, which reduces the amount of

Table 5.12: Overview of the results of the investigated samples.

Sample	Max. enh.	Temp. of max. enh.	Depth-dep. enh.	Enh. mechanisms
Al	CL: 8.3, PL: 8.0	80 K	↘ with CL depth	mainly LSP-exciton coupling with FX-C; Al-doping
Al hot	CL: 2.8, PL: 3.5	60 K	↘ with CL depth	mainly Al-doping; LSP-exciton coupling with FX-C
Al oxide	reduced UV emission	None	reduction ↘ with CL depth	N/A
Hydrothermally-grown ZnO nanorods	CL: 10.3, PL: 5.8	10 K	↗ with CL depth	mainly LSP-exciton coupling with the A line; Al-doping
VS-grown ZnO nanorods	CL: 2.3, PL: 6.5	N/A	↘ with CL depth	mainly LSP-exciton coupling with FX-A and -B; Al-doping

metallic Al on the surface for plasmonic coupling. Therefore, a reduced coupling strength between the LSPs in the Al nanoparticles and the excitons in ZnO in the sample *Al hot* was found. The Al-doping was observed by a highly enhanced Al-associated I_6 emission in ZnO, although a coupling of the LSPs in the Al nanoparticles with the I_6 cannot be fully excluded. However, the DBX of the uncoated *a*-plane ZnO exhibited mainly the slightly energetically higher I_4 emission, which was not found to be similarly as highly enhanced as the I_6 emission. Therefore, the increase of the I_6 emission of the Al-coated *a*-plane ZnO is possibly due to diffusion of Al into the ZnO.

In general, the coupling of LSPs in the Al nanoparticles to various excitonic transitions in ZnO is possible, as the LSPR energy of the Al nanoparticles ranges from 2.8 eV to 6.2 eV, which covers the entire NBE emission of ZnO. However, the results of the five samples investigated in this work show that the LSPs are more likely to couple to the FX. This can be explained by the larger spatial extent of the FX compared to the DBX. Furthermore, the FX can freely move in all directions in the crystal lattice, which can result in a higher abundance at the surface than the more localised BX, whose distribution is determined by the distribution, location and concentration of the acceptors and donors in the sample. Moreover, the FX transitions in ZnO are energetically higher than those of the DBX, which possibly allows for a higher spectral overlap with the LSPR of the Al nanoparticles.

Due to the split valence band in ZnO, three energetically different FX transitions are

found in ZnO (cf. section 2.2.1). While the energetically lower FX-A and -B are perpendicular polarised to the c-axis in ZnO, the energetically highest transition of the FX-C is polarised parallel to the c-axis. Therefore, the LSP-coupling to the FX-C is most likely favourable over that to the energetically lower FX-A and -B, as the spectral overlap is larger for the FX-C. Furthermore, the crystal orientation of the sample with respect to the laser excitation, which is naturally polarised in the plane parallel to the sample surface, can allow selective coupling to one or the other polarisation of the FX more strongly. In the Al-coated *a*-plane ZnO samples, the FX-C lies in the same polarisation plane as the laser, which resulted in highly enhanced LO-phonon replicas of the FX-C. It can be assumed that the increased SER, caused by the LSP-exciton coupling, in the FX-C equally affects the LO-phonon replicas of this transition. This is consistent with the results of the Al-coated VS-grown ZnO nanorods, where the FX-A and -B are polarised in the same plane as the laser and showed the highest PL enhancement. Although the electron beam excitation has no polarisation-like dependence compared with the laser, higher concentration of recombination centres with a high capture cross-section make certain recombination pathways more efficient than others. Therefore, the enhancement of the different FX transitions in the aforementioned samples was found to be less selective in CL, which resulted in different UV enhancement factors for the two types of excitation. Furthermore, the LSP-exciton coupling strength is not only dependent on the spectral overlap between the LSPs and the excitons, but also their spatial overlap. Therefore, the surface-near laser excitation showed a larger enhancement for the Al-coated *a*-plane ZnO as well as the VS-grown ZnO nanorods, as the electron beam deposits most of its energy further into the sample rather than in the surface, despite the similar penetration or excitation depth of the laser ($\sim$ 100 nm) and the electron beam at an acceleration voltage of 5 kV ($\sim$ 88 nm). Conversely, the Al-coated hydrothermally-grown ZnO nanorods exhibited a UV enhancement with the opposite excitation depth dependence, as well as the highest LSP-exciton coupling to a different type of exciton than the FX. It is believed that excitons bound to a structural defect (A line) is mainly coupling to the LSPs in the Al nanoparticles. This structural defect, introduced during the growth, is reported to be more abundant at the bottom of the ZnO nanorods, which explains the maximum UV enhancement at the highest CL excitation depth. Moreover, the random alignment of the hydrothermally-grown ZnO nanorods allowed for a more even Al-coating than on the VS-grown ZnO nanorods, as well as a larger surface area excited by a 10 kV-electron beam than by 3 kV. The high-resolution spectra of this sample did not exhibit a strong FX contribution, which explains why the coupling of the LSPs in the Al nanoparticles was not found to couple to the FX in the ZnO nanorods, but the excitons to the more abundant A line.

Therefore, it can be concluded that the LSPs in the Al nanoparticles favourably couple to

the more mobile and spatially larger FX than to the more localised DBX, which is furthermore dependent on the abundance of the FX or other excitons in the ZnO.

6 Conclusion

Large UV enhancement factors of Al and Au nanoparticle-coated ZnO have been reported in the literature. Although the samples appear identical, the reported results are not consistent with orders of magnitude variation in the measured enhancement factors. Additionally, significantly different models have been proposed to explain the observed increase in the UV light output. One due to LSP-exciton coupling and the other involving the injection of hot carriers into the ZnO via the decay of Au plasmons into elementary energetic electron-hole pairs, where the latter explanation is usually supported by the correlative DL visible emission. However, it is difficult to directly compare these results and to critically evaluate these literature explanations, as many of the papers reporting an UV enhancement using the coupling model do not include any data on the accompanying changes in the intensity of the ZnO defect peaks in the visible spectral region. For this reason, a broad range of ZnO-samples with Al and Au metal nanoparticle-coatings were systemically investigated in this work.

In the case of Au nanoparticle-coated ZnO, two types of ZnO samples — *a*-plane ZnO single crystals and ZnO nanorods — were coated with a Au nanoparticle film and comprehensively studied, using mainly CL and PL, as well as novel concurrent CL-PL techniques. Expectedly, an enhanced UV emission of the Au nanoparticle-coated ZnO samples was found, with a higher enhancement factor of up to 3.8 of the ZnO nanorods, compared to 2.0 for the single crystals. A greater surface-to-volume ratio of the ZnO nanorods is believed to allow for an effectively larger surface area coated with Au nanoparticles and subsequently higher overall UV enhancement.

As mentioned above, the charge transfer of hot electrons in the Au nanoparticles, created due to decay of LSPs into hot carriers, into the conduction band of the ZnO is one of the widely reported UV enhancement mechanisms, which involves the excitation of LSPs in the Au nanoparticles by the defect-related emission of ZnO. The use of a concurrent excitation with the electron beam and the laser light ($\lambda_{\mathrm{exc}} = 532\,\mathrm{nm}$), assuring additional excitation of the LSPs in the Au nanoparticles, was particularly designed to probe this charge transfer mechanism. However, no further UV enhancement was found, indicating that no hot electrons were transferred into the ZnO conduction band. The other UV enhancement mechanism found in the literature is the LSP-exciton coupling, a resonant dipole-dipole coupling between the LSPs in the Au nanoparticles and the excitons in the

ZnO, increasing the SER and therefore enhancing the UV emission in the Au nanoparticle-coated ZnO. This typically involves a lifetime reduction of the same order of the UV enhancement factor, quantified by the Purcell enhancement factor, F_{P}. The results of the time-resolved PL indeed showed a shortened lifetime for the Au nanoparticle-coated ZnO samples, however, the corresponding F_{P} was much lower than the actual UV enhancement. Furthermore, the LSPR energy of the Au nanoparticle ($E_{\mathrm{LSP}} = 2.25\,\mathrm{eV}$) has little to no spectral overlap with the exciton energy in ZnO ($\sim 3.37\,\mathrm{eV}$). Neither of the two reported mechanisms can be responsible for the UV enhancement in these samples. However, the interband transitions of Au in the UV spectral range, from the $5d$ band to the partly filled $6sp$ conduction band, can possibly be excited by the exciton emissions in ZnO via a type of resonance energy transfer mechanism and therefore, create an additional, faster relaxation channel, enhancing the UV emission of Au nanoparticle-coated ZnO.

The ZnO samples, *a*-plane ZnO single crystals and two differently-grown ZnO nanorods, coated with a thin Al film showed an up to 12-fold UV enhancement, and its origin was extensively investigated by different CL and PL techniques. The UV enhancement was attributed to both the diffusion of the Al into the ZnO and the LSP-exciton coupling. Due to the broad LSPR of the Al nanoparticles, their spectral overlap with the excitons in the ZnO is large — conversely to the Au nanoparticle-coated ZnO samples — which allows for relatively strong LSP-exciton coupling. It was found that the LSPs in the Al nanoparticles couple more favourably to the FX in the ZnO than to the DBX. This can be explained by the larger spatial extent of the wave function of the FX and their greater diffusion length, compared to the DBX, which is localised at the donor sites. Additionally, for a given temperature, the FX density is only dependent on the type and the strength of the excitation, PL or CL, while the DBX is limited by the concentration and spatial distribution of the donors near the surface of the sample. The high-resolution PL spectra of the Al-coated ZnO also revealed that the LSP-coupling to one of the three FX in ZnO is dependent on the crystal orientation and thereby the polarisation of the FX-A , FX-B and FX-C in ZnO with respect to the incident laser light; the LSPs in the Al nanoparticles couple preferably to the FX polarised in the same plane as the laser. The excitation density of the excitons in the ZnO sample plays a crucial role, as the more abundant excitons are more likely to couple to the LSPs in the Al nanoparticles at a specific temperature. Furthermore, the strength of the LSP-exciton coupling was found to be dependent on the carrier concentration of ZnO, showing a greater UV enhancement for higher carrier concentrations, possibly due to a surface electric field enhancement of the ZnO exciton-Al LSP coupling.

It can be concluded that the LSP-exciton coupling is highly dependent on the ZnO sample itself, as well as the Al-deposition conditions. While the Al diffusion into the ZnO for room temperature-deposited Al was relatively low, it increased at elevated temperatures

(here 300 °C), resulting in a reduced LSP-exciton coupling strength at the same time. The UV enhancement due to the Al-diffusion into ZnO was found to be commonly ignored in the literature, however, the results of this work show that the in-diffusion of Al is not negligible.

In conclusion, ZnO samples coated with Au nanoparticles and Al thin films resulted in a higher UV enhancement, arising from two different mechanisms. Where the UV enhancement of the Au nanoparticle-coated ZnO samples was attributed to interband transitions in the Au nanoparticles, the origin of the UV enhancement of the Al-coated ZnO samples was assigned to LSP-exciton coupling preferably to the FX in ZnO.

These results show that a more profound understanding of the origin of the UV enhancement of metal nanoparticle-coated ZnO is essential to utilise these metal-ZnO sample nanostructures in actual devices. Although ZnO is relatively cheap and nanostructures can be easily grown, *p*-type doping is still challenging and therefore ZnO-based devices can only be grown in heterostructures as yet. As a result, the implementation of GaN-based devices, for instance, is much better developed than that of ZnO. However, ZnO and GaN have similar optical and electronic properties, such as the excitonic structure of the NBE, as well as the type of defects in the DL emission. Therefore, the results and conclusions in this work can be used as a platform to understand the fundamentals of the metal nanoparticle-coatings on other technologically important wide bandgap semiconductors. Particularly, the deeper insight in the LSP-exciton coupling in the Al-coated ZnO samples can be possibly adapted for GaN-based devices.

Furthermore, anti-reflection coatings consisting of ZnO nanorods or ZnO thin films coated with metal nanoparticles, such as Au or Al, can be possibly applied on UV-LEDs or solar cells to enhance their currently low LEE.

Bibliography

[1] Shuji Nakamura, Takashi Mukai, and Masayuki Senoh. “Candela-class high-brightness InGaN/AlGaN double-heterostructure blue-light-emitting diodes”. In: *Applied Physics Letters* 64.13 (1994), p. 1687.

[2] *The 2014 Nobel Prize in Physics - Press Release*.

[3] Yu-Hsuan Hsiao et al. “Light extraction enhancement with radiation pattern shaping of LEDs by waveguiding nanorods with impedance-matching tips”. In: *Nanoscale* 6.5 (2014), pp. 2624–2628.

[4] Mitsuo Fukuda. *Opticl Semiconductor Dvices*. Wiley Series in Mircowave and Optical Engineering. Wiley Interscience Publication, New York, 1999.

[5] E. Fred Schubert and Jong Kyu Kim. “Solid-state light sources getting smart”. In: *Science* 308.5726 (2005), pp. 1274–1278.

[6] T. Fujii et al. “Increase in the extraction efficiency of GaN-based light-emitting diodes via surface roughening”. In: *Applied Physics Letters* 84.6 (2004), p. 855.

[7] Ming-Lung Tu et al. “Violet electroluminescence from poly(N-vinylcarbazole)/ZnO-nanrod composite polymer light-emitting devices”. In: *Synthetic Metals* 161.5-6 (2011), pp. 450–454.

[8] Sheng Chu et al. “Electrically pumped waveguide lasing from ZnO nanowires”. In: *Nature Nanotechnology* 6.8 (2011), pp. 506–510.

[9] Zhen Guo et al. “The ultralow driven current ultraviolet-blue light-emitting diode based on n-ZnO nanowires/i-polymer/p-GaN heterojunction”. In: *Applied Physics Letters* 97.17 (2010), p. 173508.

[10] Alice Sandmann, Christian Notthoff, and Markus Winterer. “Continuous wave ultraviolet-laser sintering of ZnO and TiO_2 nanoparticle thin films at low laser powers”. In: *Journal of Applied Physics* 113.4 (2013), p. 044310.

[11] Nargis Bano. “Fabrication and characterization of ZnO nanorods based intrinsic white light emitting diodes (LEDs)”. PhD thesis. Nörrköping: Department of Science and Engineering, Linköpings universitete, 2011.

[12] Meng Ding et al. “The ultraviolet laser from individual ZnO microwire with quadrate cross section”. In: *Optics Express* 20.13 (2012), p. 13657.

[13] Sheng Xu et al. “Ordered Nanowire Array Blue/Near-UV Light Emitting Diodes”. In: *Advanced Materials* 22.42 (2010), pp. 4749–4753.

[14] Jing-Jing Dong et al. “Highly ordered ZnO nanostructure arrays: Preparation and light-emitting diode application”. In: *Japanese Journal of Applied Physics* 53.5 (2014), p. 055201.

[15] Li Su and Ni Qin. “A facile method for fabricating Au-nanoparticles-decorated ZnO nanorods with greatly enhanced near-band-edge emission”. In: *Ceramics International* 41.2 (2015), pp. 2673–2679.

[16] Yang Zhang, Xuehong Li, and Xijun Ren. “Effects of localized surface plasmons on the photoluminescence properties of Au-coated ZnO films”. In: *Optics express* 17.11 (2009), pp. 8735–8740.

[17] Narendar Gogurla et al. “Multifunctional Au-ZnO Plasmonic Nanostructures for Enhanced UV Photodetector and Room Temperature NO Sensing Devices”. In: *Scientific Reports* 4 (2014), p. 6483.

[18] C. W. Cheng et al. “Surface plasmon enhanced band edge luminescence of ZnO nanorods by capping Au nanoparticles”. In: *Applied Physics Letters* 96.7 (2010), p. 071107.

[19] Moumita Mahanti and Durga Basak. “Highly enhanced UV emission due to surface plasmon resonance in Ag–ZnO nanorods”. In: *Chemical Physics Letters* 542 (2012), pp. 110–116.

[20] Veeradasan Perumal et al. “Thickness Dependent Nanostructural, Morphological, Optical and Impedometric Analyses of Zinc Oxide-Gold Hybrids: Nanoparticle to Thin Film”. In: *PloS one* 10.12 (2015), e0144964.

[21] Veeradasan Perumal et al. “Characterization of Gold-Sputtered Zinc Oxide Nanorods—a Potential Hybrid Material”. In: *Nanoscale Research Letters* 11.1 (2016).

[22] Trilok Singh, D.K. Pandya, and R. Singh. “Surface plasmon enhanced bandgap emission of electrochemically grown ZnO nanorods using Au nanoparticles”. In: *Thin Solid Films* 520.14 (2012), pp. 4646–4649.

[23] Saji Thomas Kochuveedu et al. “Surface-Plasmon-Enhanced Band Emission of ZnO Nanoflowers Decorated with Au Nanoparticles”. In: *Chemistry - A European Journal* 18.24 (2012), pp. 7467–7472.

[24] Andrea Pescaglini et al. “Hot-Electron Injection in Au Nanorod–ZnO Nanowire Hybrid Device for Near-Infrared Photodetection”. In: *Nano Letters* 14.11 (2014), pp. 6202–6209.

[25] Dongyan Zhang et al. “Photoluminescence modulation of ZnO via coupling with the surface plasmon resonance of gold nanoparticles”. In: *Applied Physics Letters* 103.9 (2013), p. 093114.

[26] Da-Ren Hang et al. “Full Solution-Processed Synthesis and Mechanisms of a Recyclable and Bifunctional Au/ZnO Plasmonic Platform for Enhanced UV/Vis Photocatalysis and Optical Properties”. In: *Chemistry - A European Journal* 22.42 (2016), pp. 14950–14961.

[27] Toshio Nishida, Hisao Saito, and Naoki Kobayashi. “Efficient and high-power AlGaN-based ultraviolet light-emitting diode grown on bulk GaN”. In: *Applied Physics Letters* 79.6 (2001), p. 711.

[28] D. G. Thomas. “The exciton spectrum of zinc oxide”. In: *Journal of Physics and Chemistry of Solids* 15.1-2 (1960), pp. 86–96.

[29] Ü. Özgür et al. “A comprehensive review of ZnO materials and devices”. In: *Journal of Applied Physics* 98.4 (2005), p. 041301.

[30] Paul Miller. “Zinc Oxide: A spectroscopic investigation of bulk crystals and thin films.” In: (2008).

[31] B.G. Yacobi. *Semiconductor Materials: An Introduction to Basic Principles*. Microdevices Series. Kluwer Academic Pub, 2003.

[32] Daniel S. Chemla et al. “Room Temperature Excitonic Nonlinear Absorption and Refraction in GaAs/AIGaAs Multiple Quantum Well Structures”. In: *IEEE Journal of Quantum Electronics* QE-20.3 (1984).

[33] A. A. Toropov et al. “Temperature-dependent polarized luminescence of exciton polaritons in a ZnO film”. In: *physica status solidi (a)* 202.3 (2005), pp. 392–395.

[34] A. Mang and K. Reimann. “Band gaps, crystal-field splitting, spin-orbit coupling, and exciton binding energies in ZnO under hydrostatic pressure”. In: *Solid state communications* 94.4 (1995), pp. 251–254.

[35] J. M. Calleja and Manuel Cardona. “Resonant raman scattering in ZnO”. In: *Physical Review B* 16.8 (1977), p. 3753.

[36] Markus Raphael Wagner. “Fundamental properties of excitons and phonons in ZnO: A spectroscopic study of the dynamics, polarity, and effects of external fields”. PhD Thesis. Technische Universität Berlin, 2010.

[37] W. Y. Liang and A. D. Yoffe. “Transmission spectra of ZnO single crystals”. In: *Physical Review Letters* 20.2 (1968), p. 59.

[38] Y. J. Fang et al. “Behind the change of the photoluminescence property of metal-coated ZnO nanowire arrays”. In: *Applied Physics Letters* 98.3 (2011), p. 033103.

[39] C. Ton-That, L. Weston, and M. R. Phillips. "Characteristics of point defects in the green luminescence from Zn- and O-rich ZnO". In: *Physical Review B* 86.11 (2012).

[40] T. Moe Børseth et al. "Identification of oxygen and zinc vacancy optical signals in ZnO". In: *Applied Physics Letters* 89.26 (2006), p. 262112.

[41] Jinpeng Lv and Chundong Li. "Evidences of V_O, V_{Zn}, and O_i defects as the green luminescence origins in ZnO". In: *Applied Physics Letters* 103.23 (2013), p. 232114.

[42] F. H. Leiter et al. "The oxygen vacancy as the origin of a green emission in undoped ZnO". In: *physica status solidi (b)* 226.1 (2001), R4–R5.

[43] R. Dingle. "Luminescent Transitions Associated with Divalent Copper Impurites and the Green Emission from Semiconducting Zinc Oxide". In: *Physical Review Letters* 23.11 (1969).

[44] D.M. Hofmann et al. "Properties of the oxygen vacancy in ZnO". In: *Applied Physics A* 88.1 (2007), pp. 147–151.

[45] Michael A. Reshchikov et al. "About the Cu-related green luminescence band in ZnO". In: *Journal of Vacuum Science & Technology B: Microelectronics and Nanometer Structures* 27.3 (2009), p. 1749.

[46] Yuanda Liu et al. "Cu related doublets green band emission in ZnO:Cu thin films". In: *Journal of Applied Physics* 108.11 (2010), p. 113507.

[47] N. Y. Garces et al. "Role of copper in the green luminescence from ZnO crystals". In: *Applied Physics Letters* 81.4 (2002), pp. 622–624.

[48] Bixia Lin, Zhuxi Fu, and Yunbo Jia. "Green luminescent center in undoped zinc oxide films deposited on silicon substrates". In: *Applied Physics Letters* 79.7 (2001), pp. 943–945.

[49] Amir R. Gheisi et al. "O_2 adsorption dependent photoluminescence emission from metal oxide nanoparticles". In: *Phys. Chem. Chem. Phys.* 16.43 (2014), pp. 23922–23929.

[50] X. L. Wu et al. "Photoluminescence and cathodoluminescence studies of stoichiometric and oxygen-deficient ZnO films". In: *Applied Physics Letters* 78.16 (2001), pp. 2285–2287.

[51] Vinod Kumar et al. "Origin of the red emission in zinc oxide nanophosphors". In: *Materials Letters* 101 (2013), pp. 57–60.

[52] Xiang Liu et al. "Growth mechanism and properties of ZnO nanorods synthesized by plasma-enhanced chemical vapor deposition". In: *Journal of Applied Physics* 95.6 (2004), pp. 3141–3147.

[53] Cheol Hyoun Ahn et al. "A comparative analysis of deep level emission in ZnO layers deposited by various methods". In: *Journal of Applied Physics* 105.1 (2009), p. 013502.

[54] A. Escobedo-Morales and U. Pal. "Defect annihilation and morphological improvement of hydrothermally grown ZnO nanorods by Ga doping". In: *Applied Physics Letters* 93.19 (2008), p. 193120.

[55] Suranan Anantachaisilp et al. "Nature of red luminescence in oxygen treated hydrothermally grown zinc oxide nanorods". In: *Journal of Luminescence* 168 (2015), pp. 20–25.

[56] Suranan Anantachaisilp et al. "Tailoring Deep Level Surface Defects in ZnO Nanorods for High Sensitivity Ammonia Gas Sensing". In: *The Journal of Physical Chemistry C* 118.46 (2014), pp. 27150–27156.

[57] Z. Zhang et al. "Thermal process dependence of Li configuration and electrical properties of Li-doped ZnO". In: *Applied Physics Letters* 100.4 (2012), p. 042107.

[58] D. Zwingel. "Trapping and recombination processes in the thermoluminescence of Li-doped ZnO single crystals". In: *Journal of Luminescence* 5.6 (1972), pp. 385–405.

[59] Magnus Willander. *Zinc Oxide Nanostructures*.

[60] Alex BF Martinson et al. "ZnO nanotube based dye-sensitized solar cells". In: *Nano letters* 7.8 (2007), pp. 2183–2187.

[61] A. Zainelabdin et al. "Deposition of Well-Aligned ZnO Nanorods at 50 °C on Metal, Semiconducting Polymer, and Copper Oxides Substrates and Their Structural and Optical Properties". In: *Crystal Growth & Design* 10.7 (2010), pp. 3250–3256.

[62] Suo Bai et al. "High-Performance Integrated ZnO Nanowire UV Sensors on Rigid and Flexible Substrates". In: *Advanced Functional Materials* 21.23 (2011), pp. 4464–4469.

[63] C. Soci et al. "ZnO Nanowire UV Photodetectors with High Internal Gain". In: *Nano Letters* 7.4 (2007), pp. 1003–1009.

[64] Seung Hwan Ko et al. "Nanoforest of Hydrothermally Grown Hierarchical ZnO Nanowires for a High Efficiency Dye-Sensitized Solar Cell". In: *Nano Letters* 11.2 (2011), pp. 666–671.

[65] Honghui Guo et al. "White-Light-Emitting Diode Based on ZnO Nanotubes". In: *The Journal of Physical Chemistry C* 113.28 (2009), pp. 12546–12550.

[66] Chi Hwan Lee, Dong Rip Kim, and Xiaolin Zheng. "Fabrication of Nanowire Electronics on Nonconventional Substrates by Water-Assisted Transfer Printing Method". In: *Nano Letters* 11.8 (2011), pp. 3435–3439.

[67] Hannes Kind et al. "Nanowire ultraviolet photodetectors and optical switches". In: *Advanced materials* 14.2 (2002), p. 158.

[68] Z. D. Fu et al. "Study on the quantum confinement effect on ultraviolet photoluminescence of crystalline ZnO nanoparticles with nearly uniform size". In: *Applied Physics Letters* 90.26 (2007), p. 263113.

[69] Aleksandra B. Djurišić and Yu Hang Leung. "Optical Properties of ZnO Nanostructures". In: *Small* 2.8-9 (2006), pp. 944–961.

[70] C. Klingshirn. "ZnO: From basics towards applications". In: *physica status solidi (b)* 244.9 (2007), pp. 3027–3073.

[71] Abhilash Sugunan et al. "Zinc oxide nanowires in chemical bath on seeded substrates: Role of hexamine". In: *Journal of Sol-Gel Science and Technology* 39.1 (2006), pp. 49–56.

[72] Shrok Al-lami and Halima Jaber. "Controlling ZnO Nanostructure Morphology on Seedless Substrate by Tuning Process Parameters and Additives". In: *Chemistry and Materials Research* 6.4 (2014), pp. 101–109.

[73] N. H. Alvi et al. "The origin of the red emission in n-ZnO nanotubes/p-GaN white light emitting diodes". In: *Nanoscale research letters* 6.1 (2011), p. 130.

[74] Jinmin Wang and Lian Gao. "Wet chemical synthesis of ultralong and straight single-crystalline ZnO nanowires and their excellent UV emission properties". In: *Journal of Materials Chemistry* 13.10 (2003), p. 2551.

[75] N. E. Hsu, W. K. Hung, and Y. F. Chen. "Origin of defect emission identified by polarized luminescence from aligned ZnO nanorods". In: *Journal of Applied Physics* 96.8 (2004), p. 4671.

[76] I. C. Robin et al. "Evidence for low density of nonradiative defects in ZnO nanowires grown by metal organic vapor-phase epitaxy". In: *Applied Physics Letters* 91.14 (2007), p. 143120.

[77] Kwun Nam Hui et al. "Enhanced Light Extraction Efficiency of GaN-Based LED with ZnO Nanorod Grown on Ga-Doped ZnO Seed Layer". In: *ECS Solid State Letters* 2.6 (2013), Q43–Q46.

[78] Sung Jin An et al. "Enhanced light output of GaN-based light-emitting diodes with ZnO nanorod arrays". In: *Applied Physics Letters* 92.12 (2008), p. 121108.

[79] Lionel Vayssieres. "Growth of arrayed nanorods and nanowires of ZnO from aqueous solutions". In: *Advanced Materials* 15.5 (2003), pp. 464–466.

[80] Lori E. Greene et al. “Low-Temperature Wafer-Scale Production of ZnO Nanowire Arrays”. In: *Angewandte Chemie International Edition* 42.26 (2003), pp. 3031–3034.

[81] Lori E. Greene et al. “General Route to Vertical ZnO Nanowire Arrays Using Textured ZnO Seeds”. In: *Nano Letters* 5.7 (2005), pp. 1231–1236.

[82] Sheng Xu et al. “Optimizing and Improving the Growth Quality of ZnO Nanowire Arrays Guided by Statistical Design of Experiments”. In: *ACS Nano* 3.7 (2009), pp. 1803–1812.

[83] Peidong Yang et al. “Controlled growth of ZnO nanowires and their optical properties”. In: *Advanced Functional Materials* 12.5 (2002), p. 323.

[84] R B M Cross, M M De Souza, and E M Sankara Narayanan. “A low temperature combination method for the production of ZnO nanowires”. In: *Nanotechnology* 16.10 (2005), pp. 2188–2192.

[85] C. B. Tay et al. “Empirical Model for Density and Length Prediction of ZnO Nanorods on GaN Using Hydrothermal Synthesis”. In: *Journal of The Electrochemical Society* 154.9 (2007), K45.

[86] Zhaolin Yuan et al. “Well-aligned ZnO nanorod arrays from diameter-controlled growth and their application in inverted polymer solar cell”. In: *Journal of Materials Science: Materials in Electronics* 22.11 (2011), pp. 1730–1735.

[87] C.B. Soh et al. “Optimization of hydrothermal growth ZnO Nanorods for enhancement of light extraction from GaN blue LEDs”. In: *Journal of Crystal Growth* 312.11 (2010), pp. 1848–1854.

[88] G. J. Lin et al. “Efficiency Enhancement of InGaN-Based Multiple Quantum Well Solar Cells Employing Antireflective ZnO Nanorod Arrays”. In: *IEEE Electron Device Letters* 32.8 (2011), pp. 1104–1106.

[89] K. Takanezawa et al. “Efficient Charge Collection with ZnO Nanorod Array in Hybrid Photovoltaic Devices”. In: *Journal of Physical Chemistry C* 111.19 (2007), pp. 7218–7223.

[90] Shuji Sakohara, Masahiro Ishida, and Marc A. Anderson. “Visible Luminescence and Surface Properties of Nanosized ZnO Colloids Prepared by Hydrolyzing Zinc Acetate”. In: *The Journal of Physical Chemistry B* 102.50 (1998), pp. 10169–10175.

[91] Eric A. Meulenkamp. “Synthesis and Growth of ZnO Nanoparticles”. In: *The Journal of Physical Chemistry B* 102.29 (1998), pp. 5566–5572.

[92] Claudia Pacholski, Andreas Kornowski, and Horst Weller. “Site-Specific Photodeposition of Silver on ZnO Nanorods”. In: *Angewandte Chemie* 116.36 (2004), pp. 4878–4881.

[93] N. Bano et al. "ZnO-organic hybrid white light emitting diodes grown on flexible plastic using low temperature aqueous chemical method". In: *Journal of Applied Physics* 108.4 (2010), p. 043103.

[94] Gul Amin. "ZnO and CuO nanostructures: low temperature growth, characterization, their optoelectronic and sensing applications". PhD thesis. 2012.

[95] Afsal Manekkathodi et al. "Direct Growth of Aligned Zinc Oxide Nanorods on Paper Substrates for Low-Cost Flexible Electronics". In: *Advanced Materials* 22.36 (2010), pp. 4059–4063.

[96] Ray-Hua Horng et al. "High performance of Ga-doped ZnO transparent conductive layers using MOCVD for GaN LED applications". In: *Optics Express* 21.12 (2013), p. 14452.

[97] J. S. Xia et al. "Strong resonant luminescence from Ge quantum dots in photonic crystal microcavity at room temperature". In: *Applied Physics Letters* 89.20 (2006), p. 201102.

[98] Jun Ho Son et al. "Design Rule of Nanostructures in Light-Emitting Diodes for Complete Elimination of Total Internal Reflection". In: *Advanced Materials* 24.17 (2012), pp. 2259–2262.

[99] S. J. Chang et al. "Nitride-based light emitting diodes with indium tin oxide electrode patterned by imprint lithography". In: *Applied Physics Letters* 91.1 (2007), p. 013504.

[100] J. K. Sheu et al. "Enhancement in output power of blue gallium nitride-based light-emitting diodes with omnidirectional metal reflector under electrode pads". In: *Applied Physics Letters* 93.10 (2008), p. 103507.

[101] Jong Kyu Kim et al. "GaInN light-emitting diode with conductive omnidirectional reflector having a low-refractive-index indium-tin oxide layer". In: *Applied Physics Letters* 88.1 (2006), p. 013501.

[102] J. K. Kim et al. "Light-Extraction Enhancement of GaInN Light-Emitting Diodes by Graded-Refractive-Index Indium Tin Oxide Anti-Reflection Contact". In: *Advanced Materials* 20.4 (2008), pp. 801–804.

[103] Cheng-Yi Fang et al. "Nanoparticle Stacks with Graded Refractive Indices Enhance the Omnidirectional Light Harvesting of Solar Cells and the Light Extraction of Light-Emitting Diodes". In: *Advanced Functional Materials* 23.11 (2013), pp. 1412–1421.

[104] K. McGroddy et al. "Directional emission control and increased light extraction in GaN photonic crystal light emitting diodes". In: *Applied Physics Letters* 93.10 (2008), p. 103502.

[105] Min-Ki Kwon et al. "Enhanced emission efficiency of GaN÷InGaN multiple quantum well light-emitting diode with an embedded photonic crystal". In: *Applied Physics Letters* 92.25 (2008), p. 251110.

[106] Aurlien David, Henri Benisty, and Claude Weisbuch. "Optimization of Light-Diffracting Photonic-Crystals for High Extraction Efficiency LEDs". In: *Journal of Display Technology* 3.2 (2007), pp. 133–148.

[107] Elison Matioli et al. "High extraction efficiency light-emitting diodes based on embedded air-gap photonic-crystals". In: *Applied Physics Letters* 96.3 (2010), p. 031108.

[108] Dong-Ho Kim et al. "Enhanced light extraction from GaN-based light-emitting diodes with holographically generated two-dimensional photonic crystal patterns". In: *Applied Physics Letters* 87.20 (2005), p. 203508.

[109] A Chen et al. "Fabrication of sub-100 nm patterns in SiO_2 templates by electron-beam lithography for the growth of periodic III–V semiconductor nanostructures". In: *Nanotechnology* 17.15 (2006), pp. 3903–3908.

[110] D.G Stavenga et al. "Light on the moth-eye corneal nipple array of butterflies". In: *Proceedings of the Royal Society B: Biological Sciences* 273.1587 (2006), pp. 661–667.

[111] Seung-Yeol Han, Brian K. Paul, and Chih-hung Chang. "Nanostructured ZnO as biomimetic anti-reflective coatings on textured silicon using a continuous solution process". In: *Journal of Materials Chemistry* 22.43 (2012), pp. 22906–22912.

[112] S.J. Wilson and M.C. Hutley. "The Optical Properties of 'Moth Eye' Antireflection Surfaces". In: *Optica Acta: International Journal of Optics* 29.7 (1982), pp. 993–1009.

[113] Hyun Jeong et al. "Light-extraction enhancement of a GaN-based LED covered with ZnO nanorod arrays". In: *Nanoscale* 6.8 (2014), pp. 4371–4378.

[114] Yun-Ju Lee et al. "ZnO Nanostructures as Efficient Antireflection Layers in Solar Cells". In: *Nano Letters* 8.5 (2008), pp. 1501–1505.

[115] Yen-Chun Chao et al. "Light scattering by nanostructured anti-reflection coatings". In: *Energy & Environmental Science* 4.9 (2011), p. 3436.

[116] Young Min Song et al. "Bioinspired Parabola Subwavelength Structures for Improved Broadband Antireflection". In: *Small* 6.9 (2010), pp. 984–987.

[117] Yongshu Tian et al. "ZnO Pyramidal Arrays: Novel Functionality in Antireflection". In: *The Journal of Physical Chemistry C* 114.22 (2010), pp. 10265–10269.

[118] Yu Tian et al. "Synthesis, characterization and photoluminescence properties of ZnO hexagonal pyramids by the thermal evaporation method". In: *Physica E: Low-dimensional Systems and Nanostructures* 43.1 (2010), pp. 410–414.

[119] Taejoon Son et al. “Improved light extraction efficiency and leakage characteristics in light-emitting diodes by nanorod arrays formed on hexagonal pits”. In: *Materials Science in Semiconductor Processing* 29 (2015), pp. 380–385.

[120] Do-Hyun Kim, Dong Su Shin, and Jinsub Park. “Enhanced light extraction from GaN based light-emitting diodes using a hemispherical NiCoO lens”. In: *Optics Express* 22.S4 (2014), A1071.

[121] Gabriel Lozano et al. “Plasmonics for solid-state lighting: enhanced excitation and directional emission of highly efficient light sources”. In: *Light: Science & Applications* 2.5 (2013), e66.

[122] editorial. “Beyond the diffraction limit”. In: 3 (2009).

[123] Dmitri K. Gramotnev and Sergey I. Bozhevolnyi. “Plasmonics beyond the diffraction limit”. In: *Nature Photonics* 4.2 (2010), pp. 83–91.

[124] Stefan A. Maier. *Plasmonics: Fundamentals and Applications*.

[125] H. Raether. *Surface plasmons on smooth surfaces*.

[126] J M Pitarke et al. “Theory of surface plasmons and surface-plasmon polaritons”. In: *Reports on Progress in Physics* 70.1 (2007), pp. 1–87.

[127] U. Schröter and D. Heitmann. “Grating couplers for surface plasmons excited on thin metal films in the Kretschmann-Raether configuration”. In: *Physical Review B* 60.7 (1999), p. 4992.

[128] Yashu Zang et al. “Band edge emission enhancement by quadrupole surface plasmon–exciton coupling using direct-contact Ag/ZnO nanospheres”. In: *Nanoscale* 5.2 (2013), pp. 574–580.

[129] Q J Ren et al. “Evidence for coupling between exciton emissions and surface plasmon in Ni-coated ZnO nanowires”. In: *Nanotechnology* 23.42 (2012), p. 425201.

[130] Junfeng Lu et al. “Direct Resonant Coupling of Al Surface Plasmon for Ultraviolet Photoluminescence Enhancement of ZnO Microrods”. In: *ACS Applied Materials & Interfaces* 6.20 (2014), pp. 18301–18305.

[131] Mark Fox. *Quantum Optics - An Introduction*. 2006.

[132] Koichi Okamoto et al. “Surface-plasmon-enhanced light emitters based on InGaN quantum wells”. In: *Nature Materials* 3.9 (2004), pp. 601–605.

[133] Koichi Okamoto et al. “Surface plasmon enhanced spontaneous emission rate of InGaN÷GaN quantum wells probed by time-resolved photoluminescence spectroscopy”. In: *Applied Physics Letters* 87.7 (2005), p. 071102.

[134] Chu-Young Cho et al. “Surface plasmon-enhanced light-emitting diodes with silver nanoparticles and SiO2 nano-disks embedded in p-GaN”. In: *Applied Physics Letters* 99.4 (2011), p. 041107.

[135] C. C. Kao et al. “Localized Surface Plasmon-Enhanced Nitride-Based Light-Emitting Diode With Ag Nanotriangle Array by Nanosphere Lithography”. In: *IEEE Photonics Technology Letters* 22.13 (2010), pp. 984–986.

[136] Min-Ki Kwon, Ja-Yeon Kim, and Seong-Ju Park. “Enhanced emission efficiency of green InGaN/GaN multiple quantum wells by surface plasmon of Au nanoparticles”. In: *Journal of Crystal Growth* 370 (2013), pp. 124–127.

[137] Chu-Young Cho et al. “Surface plasmon enhanced light emission from AlGaN-based ultraviolet light-emitting diodes grown on Si (111)”. In: *Applied Physics Letters* 102.21 (2013), p. 211110.

[138] Yuanhao Jin et al. “Enhanced optical output power of blue light-emitting diodes with quasi-aligned gold nanoparticles”. In: *Nanoscale research letters* 9.1 (2014), pp. 1–6.

[139] Kwang-Geol Lee, Ki-Young Choi, and Seok-Ho Song. “Optimal design of green InGaN/GaN LEDs mediated by surface-plasmon gratings”. In: *Current Applied Physics* 14.12 (2014), pp. 1771–1774.

[140] Kai Huang et al. “Top- and bottom-emission-enhanced electroluminescence of deep-UV light-emitting diodes induced by localised surface plasmons”. In: *Scientific Reports* 4 (2014).

[141] Shih-Hao Chuang et al. “Transparent Conductive Oxide Films Embedded with Plasmonic Nanostructure for Light-Emitting Diode Applications”. In: *ACS Applied Materials & Interfaces* 7.4 (2015), pp. 2546–2553.

[142] Wenkai Zhang et al. “Localized surface plasmon resonance enhanced blue light-emission of polyfluorene copolymer”. In: *Journal of Physics and Chemistry of Solids* 75.12 (2014), pp. 1340–1346.

[143] Jurgis Kundrotas et al. “Enhanced light emission in nanostructures”. In: *Lithuanian Journal of Physics* 51.4 (2011).

[144] Kwang-Geol Lee, Ki-Young Choi, and Seok-Ho Song. “Experimental observation of a practical limit on enhancement of the spontaneous emission rate in blue GaN-LEDs by mediating surface plasmons”. In: *Current Applied Physics* 14.12 (2014), pp. 1639–1642.

[145] Craig Hillman et al. “Silver and sulfur: case studies, physics and possible solutions”. In: *SMTA Inter., October* (2007).

[146] Melek Erol et al. "SERS Not To Be Taken for Granted in the Presence of Oxygen". In: *Journal of the American Chemical Society* 131.22 (2009), pp. 7480–7481.

[147] Davy Gerard and Stephen K. Gray. "Aluminium plasmonics". In: *Journal of Physics D: Applied Physics* (2014).

[148] E. J. Guidelli, O. Baffa, and D. R. Clarke. "Enhanced UV Emission From Silver/ZnO And Gold/ZnO Core-Shell Nanoparticles: Photoluminescence, Radioluminescence, And Optically Stimulated Luminescence". In: *Scientific Reports* 5 (2015), p. 14004.

[149] Jun Yin et al. "Effect of the surface-plasmon–exciton coupling and charge transfer process on the photoluminescence of metal–semiconductor nanostructures". In: *Nanoscale* 5.10 (2013), p. 4436.

[150] Weizhen Liu et al. "Effect of SiO_2 Spacer-Layer Thickness on Localized Surface Plasmon-Enhanced ZnO Nanorod Array LEDs". In: *ACS Applied Materials & Interfaces* 8.3 (2016), pp. 1653–1660.

[151] Junfeng Lu et al. "Plasmon-enhanced Electrically Light-emitting from ZnO Nanorod Arrays/p-GaN Heterostructure Devices". In: *Scientific Reports* 6.1 (2016).

[152] Junfeng Lu et al. "Improved UV photoresponse of ZnO nanorod arrays by resonant coupling with surface plasmons of Al nanoparticles". In: *Nanoscale* 7.8 (2015), pp. 3396–3403.

[153] H. Y. Lin et al. "Enhancement of band gap emission stimulated by defect loss". In: *Optics express* 14.6 (2006), pp. 2372–2379.

[154] R. Udayabhaskar et al. "Enhanced multi-phonon Raman scattering and nonlinear optical power limiting in ZnO:Au nanostructures". In: *RSC Adv.* 5.18 (2015), pp. 13590–13597.

[155] Zao Yi et al. "Surface-Plasmon-Enhanced Band Emission and Enhanced Photocatalytic Activity of Au Nanoparticles-Decorated ZnO Nanorods". In: *Plasmonics* (2015).

[156] William Chamorro et al. "Local Structure-Driven Localized Surface Plasmon Absorption and Enhanced Photoluminescence in ZnO-Au Thin Films". In: *The Journal of Physical Chemistry C* 120.51 (2016), pp. 29405–29413.

[157] Moumita Mahanti and Durga Basak. "Enhanced emission properties of Au/SiO2/ZnO nanorod layered structure: effect of SiO2 spacer layer and role of interfacial charge transfer". In: *RSC Advances* 4.30 (2014), p. 15466.

[158] Moumita Mahanti and Durga Basak. "Enhanced ultraviolet photoresponse in Au/ZnO nanorods". In: *Chemical Physics Letters* 612 (2014), pp. 101–105.

[159] Li Wang et al. "Strongly Enhanced Ultraviolet Emissions of an Au@SiO2/ZnO Plasmonic Hybrid Nanostructure". In: *Nanoscale* (2016).

[160] Monan Liu et al. “Tuning the influence of metal nanoparticles on ZnO photoluminescence by atomic-layer-deposited dielectric spacer”. In: *Nanophotonics* 2.2 (2013).

[161] Lori E. Greene et al. “Solution-Grown Zinc Oxide Nanowires”. In: *Inorganic Chemistry* 45.19 (2006), pp. 7535–7543.

[162] Mark N. Lockrey. “Investigation into the effects of electron-beam irradiation on III-nitride based LED devices”. PhD Thesis. 2015.

[163] Dominique Drouin et al. “CASINO V2. 42—A Fast and Easy-to-use Modeling Tool for Scanning Electron Microscopy and Microanalysis Users”. In: *Scanning* 29.3 (2007), pp. 92–101.

[164] M. Toth and M. R. Phillips. “Monte Carlo modeling of cathodoluminescence generation using electron energy loss curves”. In: *Scanning: The Journal of Scanning Microscopies* 20.6 (1998), pp. 425–432.

[165] O. Gelhausen, M. R. Phillips, and M. Toth. “Depth-resolved cathodoluminescence microanalysis of near-edge emission in III-nitride thin films”. In: *Journal of Applied Physics* 89.6 (2001), pp. 3535–3537.

[166] B.G. Yacobi and D.B. Holt. *Cathodoluminescence microscopy of inorganic solids*. Plenum Press, New York, 1990.

[167] B. K. Meyer et al. “Bound exciton and donor–acceptor pair recombinations in ZnO”. In: *physica status solidi (b)* 241.2 (2004), pp. 231–260.

[168] P. L. Washington et al. “Determination of the optical constants of zinc oxide thin films by spectroscopic ellipsometry”. In: *Applied Physics Letters* 72.25 (1998), pp. 3261–3263.

[169] J. F. Muth et al. “Excitonic structure and absorption coefficient measurements of ZnO single crystal epitaxial films deposited by pulsed laser deposition”. In: *Journal of Applied Physics* 85.11 (1999), pp. 7884–7887.

[170] D. V. O’Connor, W. R. Ware, and J. C. Andre. “Deconvolution of fluorescence decay curves. A critical comparison of techniques”. In: *Journal of Physical Chemistry* 83.10 (1979), pp. 1333–1343.

[171] Kane S. Yee. “Numerical Solution of Initial Boundary Value Problems Involving Maxwell’s Equations in Isotropic Media”. In: *IEEE Transactions on Antennas and Propagation* AP-14.3 (1966).

[172] J. W. Chiou et al. “Correlation between Electronic Structures and Photocatalytic Activities of Nanocrystalline-(Au, Ag, and Pt) Particles on the Surface of ZnO Nanorods”. In: *The Journal of Physical Chemistry C* 115.6 (2011), pp. 2650–2655.

[173] R. T. Girard et al. "Electronic structure of ZnO (0001) studied by angle-resolved photoelectron spectroscopy". In: *Surface Science* 373.2-3 (1997), pp. 409–417.

[174] Cuong Ton-That et al. "Surface electronic properties of ZnO nanoparticles". In: *Applied Physics Letters* 92.26 (2008), p. 261916.

[175] Guoqiang Li et al. "Factors impacted on anisotropic photocatalytic oxidization activity of ZnO: Surface band bending, surface free energy and surface conductance". In: *Applied Catalysis B: Environmental* 158-159 (2014), pp. 280–285.

[176] M. W. Allen et al. "Polarity effects in the x-ray photoemission of ZnO and other wurtzite semiconductors". In: *Applied Physics Letters* 98.10 (2011), p. 101906.

[177] Alex M. Lord et al. "Surface state modulation through wet chemical treatment as a route to controlling the electrical properties of ZnO nanowire arrays investigated with XPS". In: *Applied Surface Science* 320 (2014), pp. 664–669.

[178] Suranan Anantachaisilp. "The effect of surface defects on the optical and electrical properties of ZnO nanorods". PhD Thesis. 2015.

[179] Sachindra Nath Das et al. "Junction properties of Au/ZnO single nanowire Schottky diode". In: *Applied Physics Letters* 96.9 (2010), p. 092111.

[180] Yow-Jon Lin. "Application of the thermionic field emission model in the study of a Schottky barrier of Ni on p-GaN from current–voltage measurements". In: *Applied Physics Letters* 86.12 (2005), p. 122109.

[181] American National Standards Institute and NCSL International. *American national standard for calibration: U.S. guide to the expression of uncertainty in measurement*. OCLC: 423557213. Boulder, Colo.: NCSL International, 2008.

[182] M. S. Tyagi. "Physics of Schottky Barrier Junctions". In: *Metal-Semiconductor Schottky Barrier Junctions and Their Applications*. Ed. by B. L. Sharma. Boston, MA: Springer US, 1984, pp. 1–60.

[183] Marius Grundmann. *The Physics of Semiconductors*. Graduate Texts in Physics. Cham: Springer International Publishing, 2016.

[184] Jakub Siegel et al. "Properties of gold nanostructures sputtered on glass". In: *Nanoscale research letters* 6.96 (2011), p. 9.

[185] Gregory Kalyuzhny et al. "Transmission Surface-Plasmon Resonance (T-SPR) Measurements for Monitoring Adsorption on Ultrathin Gold Island Films". In: *Chemistry-A European Journal* 8.17 (2002), pp. 3849–3857.

[186] X. D. Li et al. "Influence of localized surface plasmon resonance and free electrons on the optical properties of ultrathin Au films: a study of the aggregation effect". In: *Optics Express* 22.5 (2014), p. 5124.

[187] Addy van Dijken et al. "The Kinetics of the Radiative and Nonradiative Processes in Nanocrystalline ZnO Particles upon Photoexcitation". In: *The Journal of Physical Chemistry B* 104.8 (2000), pp. 1715–1723.

[188] Weizhen Liu et al. "Effect of SiO $_2$ Spacer-Layer Thickness on Localized Surface Plasmon-Enhanced ZnO Nanorod Array LEDs". In: *ACS Applied Materials & Interfaces* 8.3 (2016), pp. 1653–1660.

[189] Qing-Hua Ren et al. "Surface-plasmon mediated photoluminescence enhancement of Pt-coated ZnO nanowires by inserting an atomic-layer-deposited Al $_2$ O $_3$ spacer layer". In: *Nanotechnology* 27.16 (2016), p. 165705.

[190] Taeho Shin et al. "Exciton Recombination, Energy-, and Charge Transfer in Single- and Multilayer Quantum-Dot Films on Silver Plasmonic Resonators". In: *Scientific Reports* 6 (2016), p. 26204.

[191] Purcell. "Proceedings of the American Physical Society". In: *Physical Review* 69.11-12 (1946), pp. 674–674.

[192] Wei Zhen Liu et al. "Enhanced ultraviolet emission and improved spatial distribution uniformity of ZnO nanorod array light-emitting diodes via Ag nanoparticles decoration". In: *Nanoscale* 5.18 (2013), p. 8634.

[193] Chul Huh et al. "Improved light-output and electrical performance of InGaN-based light-emitting diode by microroughening of the p-GaN surface". In: *Journal of Applied Physics* 93.11 (2003), p. 9383.

[194] Yi-Zhu Lin and Shun-Wen Xiao. "Theoretical analysis of quasi-random roughened surface on light extraction enhancement and optical field properties of GaN LED". In: *Optik - International Journal for Light and Electron Optics* 126.23 (2015), pp. 4625–4627.

[195] B. Balamurugan and Toshiro Maruyama. "Evidence of an enhanced interband absorption in Au nanoparticles: Size-dependent electronic structure and optical properties". In: *Applied Physics Letters* 87.14 (2005), p. 143105.

[196] V. P. Zhukov et al. "Corrected local-density approximation band structures, linear-response dielectric functions, and quasiparticle lifetimes in noble metals". In: *Physical Review B* 64.19 (2001).

[197] Anatoliy Pinchuk, Gero von Plessen, and Uwe Kreibig. "Influence of interband electronic transitions on the optical absorption in metallic nanoparticles". In: *Journal of Physics D: Applied Physics* 37.22 (2004), pp. 3133–3139.

[198] R. Lässer and N.V. Smith. "Interband optical transitions in gold in the photon energy range 2–25 eV". In: *Solid State Communications* 37.6 (1981), pp. 507–509.

[199] Stéphane Berciaud et al. “Observation of Intrinsic Size Effects in the Optical Response of Individual Gold Nanoparticles”. In: *Nano Letters* 5.3 (2005), pp. 515–518.

[200] T. Goetz et al. “Characterization of large supported metal clusters by optical spectroscopy”. In: *Zeitschrift fuer Physik D Atoms, Molecules and Clusters* 33.2 (1995), pp. 133–141.

[201] Daniel Werner, Shuichi Hashimoto, and Takayuki Uwada. “Remarkable Photothermal Effect of Interband Excitation on Nanosecond Laser-Induced Reshaping and Size Reduction of Pseudospherical Gold Nanoparticles in Aqueous Solution”. In: *Langmuir* 26.12 (2010), pp. 9956–9963.

[202] N. Egede Christensen and B. O. Seraphin. “Relativistic Band Calculation and the Optical Properties of Gold”. In: *Physical Review B* 4.10 (1971), pp. 3321–3344.

[203] E. Dulkeith et al. “Plasmon emission in photoexcited gold nanoparticles”. In: *Physical Review B* 70.20 (2004).

[204] Mark W. Knight et al. “Aluminum Plasmonic Nanoantennas”. In: *Nano Letters* 12.11 (2012), pp. 6000–6004.

[205] Christoph Langhammer et al. “Localized Surface Plasmon Resonances in Aluminum Nanodisks”. In: *Nano Letters* 8.5 (2008), pp. 1461–1471.

[206] Atsushi Taguchi et al. “Tailoring plasmon resonances in the deep-ultraviolet by size-tunable fabrication of aluminum nanostructures”. In: *Applied Physics Letters* 101.8 (2012), p. 081110.

[207] Joseph I Goldstein et al. *Scanning Electron Microscopy and X-ray Microanalysis: Third Edition*. OCLC: 864219011. Boston, MA: Springer US : Imprint : Springer, 2003.

[208] N Cabrera and N F Mott. “Theory of the oxidation of metals”. In: *Reports on Progress in Physics* 12.1 (1949), pp. 163–184.

[209] G. A. Niklasson, C. G. Granqvist, and O. Hunderi. “Effective medium models for the optical properties of inhomogeneous materials”. In: *Applied Optics* 20.1 (1981), p. 26.

[210] K. Lance Kelly et al. “The Optical Properties of Metal Nanoparticles: The Influence of Size, Shape, and Dielectric Environment”. In: *The Journal of Physical Chemistry B* 107.3 (2003), pp. 668–677.

[211] George H. Chan et al. “Localized Surface Plasmon Resonance Spectroscopy of Triangular Aluminum Nanoparticles”. In: *The Journal of Physical Chemistry C* 112.36 (2008), pp. 13958–13963.

[212] Y. Ekinci, H. H. Solak, and J. F. Löffler. “Plasmon resonances of aluminum nanoparticles and nanorods”. In: *Journal of Applied Physics* 104.8 (2008), p. 083107.

[213] Elijah Thimsen et al. “High electron mobility in thin films formed via supersonic impact deposition of nanocrystals synthesized in nonthermal plasmas”. In: *Nature Communications* 5.1 (2014).

[214] M. R. Wagner et al. “Bound excitons in ZnO: Structural defect complexes versus shallow impurity centers”. In: *Physical Review B* 84.3 (2011).

[215] George H. Chan et al. “Localized Surface Plasmon Resonance Spectroscopy of Triangular Aluminum Nanoparticles”. In: *The Journal of Physical Chemistry C* 112.36 (2008), pp. 13958–13963.

[216] E. Petri and A. Otto. “Direct Nonvertical Interband and Intraband Transitions in Al”. In: *Physical Review Letters* 34.20 (1975), pp. 1283–1286.

[217] Keun-Ho Lee and K. J. Chang. “First-principles study of the optical properties and the dielectric response of Al”. In: *Physical Review B* 49.4 (1994), pp. 2362–2367.

[218] V.V. Travnikov, A. Freiberg, and S.F. Savikhin. “Surface excitons in ZnO crystals”. In: *Journal of Luminescence* 47.3 (1990), pp. 107–112.

[219] M. Azizar Rahman et al. “Charge state switching of Cu acceptors in ZnO nanorods”. In: *Applied Physics Letters* 110.12 (2017), p. 121907.

[220] J-P Richters et al. “Enhanced surface-excitonic emission in ZnO/Al_2O_3 core–shell nanowires”. In: *Nanotechnology* 19.30 (2008), p. 305202.

[221] Tobias Voss and Lars Wischmeier. “Recombination Dynamics of Surface-Related Excitonic States in Single ZnO Nanowires”. In: *Journal of Nanoscience and Nanotechnology* 8.1 (2008), pp. 228–232.

[222] Yuanping Sun et al. “Synthesis and characterization of twinned flower–like ZnO structures grown by hydrothermal methods”. In: *Ceramics International* 42.8 (2016), pp. 9648–9652.